IMT School for Advanced Studies, Lucca
Lucca, Italy

Thermoelastic and Fracture Responses of Periodic Materials: Theory and Applications to Laminates and Triply Periodic Minimal Surfaces

PhD Program in Institutions, Markets and Technologies

Curriculum in Computer Science and Systems Engineering

XXXIV Cycle

By

Deison Teixeira Préve

2022

The dissertation of Deison Teixeira Préve is approved.

PhD Program Coordinator: Alberto Bemporad, IMT School for Advanced Studies Lucca

Advisor: Prof. Marco Paggi, IMT School for Advanced Studies Lucca

Co-Advisor: Prof. Pietro Lenarda, IMT School for Advanced Studies Lucca

The dissertation of Deison Teixeira Préve has been reviewed by:

Prof. Maria Laura De Bellis, Università degli Studi "G. D'Annunzio" Chieti - Pescara

Prof. Francesco Dal Corso, Università di Trento

Prof. Alberto Giuseppe Sapora, Politecnico di Torino

IMT School for Advanced Studies Lucca
2022

To that existence which is devoid of duality, formless, neither free nor captive, neither attached nor detached. Neither the experienced, nor the experience.

To that which is not.

Contents

List of Figures

List of Tables

Acknowledgements

Firstly, I feel truly honored to be guided by Prof. Marco Paggi during my PhD path, all my gratitude to him. He was always available for any kind of discussion, either online or in person. He was always concerned about the progress of the work, always giving great insights to be dug. Most importantly, when the time came, when I expected the worst, he was the most genteel and kind person I would have never imagined, he was very supportive, and helped me to find new perspectives for our final goal. Moreover, I am very thankful to him for giving me the opportunity to work right aside you, by which I could learn tons of new knowledge and improved other hundreds of skills. For the ones that have Prof. Marco Paggi as a guide, consider yourselves lucky to have one of the best advisors you could ever have.

I would like to offer my special thanks to my Co-Advisor Dr. Pietro Lenarda, which had embarked on this ship half way of the journey, for all the support he gave me, without him this present thesis would not be possible. I thank Dr. Ian Maskery for receiving me as his student under his guidance during my visiting period in Nottingham. He always demonstrated interest on my research endeavours, either indicating ideas via emails or providing me the tools to tackle the topics for the research. I also would like to thank Dr. Andrea Bacigalupo, for all the acquired personal and professional knowledge that I learned from him.

I would like to acknowledge the research funding from the Italian Ministry of Education, University and Research to the Research Project of National Interest (PRIN "XFAST-SIMS: Extra fast and accurate simulation of complex structural systems" (Grant Agreement no. 20173C478N). I gratefully acknowledge as well the financial support co-funded by the Erasmus+ Programme of the European Union for the traineeship, no. 2020-1-IT02-KA103-078114, utilized at the University of Nottingham (United Kingdom) initiated in September 2021.

My warmest thanks to my closest IMT colleagues. Only the ones that have lived and live the same journey can understand the brightest and

darkest sides of this trip. Particularly, I express my appreciation to Pavan Kumar for all the relaxing time (river and beach) spent together, all the amazing conversations over all sort of subjects, for all the research brainstorming, for the gym partnership, and most of all, for the great friendship built throughout these years, thank you mate! I want to thank Nicolò Morando for having been the awesome roommate that you were, the best one that I could have ever had, great travels, great drinkings, amazing memories, you are a great friend, thank you for the laughs together! I also thank Chinmay Siwach and Evgeniia Volosova, I had wonderful times playing board games along side you two, and in the meantime nice and stimulating chats about every single thing, those times will be missed. I thank Francis John and Liang Wu for the friendship, and for enhancing the experiences we shared. Thank you very much, Afroditi Giannakopoulou for the support during critical periods, and the great laughs shared and heard though the streets and corridors, I found a great friend at the end of this journey, thank you, darling! Lastly, thank you Surya Soman for all the dances and drinks we had together.

My enduring and sincere thanks to my close and supportive circle of friends all around the globe, my PhD road was paved by you all. There would not be enough pages to mention each one of you here and to share my gratitude to you all. However, bear in mind that I am not forgetting, and I will not forget any of you, I am very obliged to have you all as friends.

I want to extend my heartfelt thanks to my beloved Alessandra Dos Reis, who has decided to embark on this life cruise not long ago, providing me pleasant moments, feeling her love, care and affection. You have brought new purposes to my life journey, thank you. I love you dearly!

Last but not least, I want to thank my parents Vanderlei Préve and Nilsa Préve, and my sister Cíntia Préve, for their care, love, encouragement and belief in me. Without you three, this journey would have never been sought, and it is just getting started. Thank you very much!

Publications

1. **Preve, Deison**, Andrea Bacigalupo, and Marco Paggi. "Variational-asymptotic homogenization of thermoelastic periodic materials with thermal relaxation." International Journal of Mechanical Sciences 205 (2021): 106566.
   doi:https://doi.org/10.1016/j.ijmecsci.2021.106566
2. **Preve, Deison**, Pietro Lenarda, Ian Maskery and Marco Paggi. "A comprehensive characterization of fracture in unit cell open foams generated from Triply Periodic Minimal Surfaces", Engineering Fracture Mechanics (2022): 108949.
   doi:https://doi.org/10.1016/j.engfracmech.2022.108949

Abstract

In order to provide better quality on a variety of equipment, services and new technologies to the community, periodic materials as laminates and periodic structures as foams are constantly gaining more attention worldwide, due to the fact that these structures present suitable mechanical behaviours, enhanced physical properties and are yet low-cost. Therefore, it is crucial to understand how these structures respond for different physical and mechanical problems. The present thesis exploits how certain periodic structures behave and respond under thermo-mechanical loading and fracture phenomena.

In the first part of the thesis, a multi-scale variational-asymptotic homogenization method for periodic microstructured materials for thermoelastic problems with one relaxation time is exploited. The asymptotic expansions of the micro-displacement and the micro-temperature fields are rewritten on the transformed Laplace space and expressed as power series of the microstructural length scale, leading to a set of recursive differential problems over the periodic unit cell. The solution of such cell problems leads to the perturbation functions. Up-scaling and down-scaling relations are then defined, and the latter allow expressing the microscopic fields in terms of the macroscopic ones and their gradients. The variational-asymptotic scheme to establish an equivalence between the equations at macro-scale and micro-scale is developed. Average field equations of infinite order are also derived. The efficiency of the proposed technique was tested in relation to a bi-dimensional orthotropic layered bodies with orthotropy axis parallel to the direction of the layers, where the mechanical and temperature constitutive properties were well established. The dispersion curves of the homogenized medium, truncated at the first order are compared with the dispersion curves of the heterogeneous continuum obtained by the Floquet-Bloch theory. The results obtained with the two different approaches show a very good agreement.

The second part of the thesis is focused on assessing the occurrence of

fracture in Triply Periodic Minimal Surfaces (TPMS) foams subjected to compressive loading. TPMS, described by the mathematics community, may be exploited as a backbone for developing a new class of foams with open porosity for a wide range of engineering and biomedical applications. Therefore, a comprehensive analysis of their fracture response is fundamental and is herein attempted. To this aim, a 3D phase field model is outlined and applied to TPMS foam structures under compression, with the goal to predict critical points for crack nucleation, potential crack paths, and the stiffness and maximum compressive stress of the unit cell, which can be related to the apparent Young's modulus and apparent strength of a macro-scale composite made of such TPMS unit cells. A careful mesh sensitivity analysis was conducted on the specimens, to provide guidelines on how to identify the optimal finite element discretization consistent with the internal length scale parameter of the phase field approach to fracture. The major predicted mechanical properties for five different TPMS open foams, and for different levels of porosity, are summarized in Ashby plots. The predicted trends are in agreement with previous results on TPMS taken from the literature and show that TPMS can outperform standard Aluminium open foams.

Chapter 1

Introduction

1.1 Periodic materials

Periodic structures, such as composite laminates consisting of substructures periodically arranged, have been drawn attention because of their inherent characteristics that the periodicity attribute bring. For instance, periodic layered materials present unique dynamical features which make them act as mechanical filters in wave propagation. Apart from man-made materials and motivated by Richard's Feynman quote *"We are not to tell nature what she's gotta be... She's always got better imagination than we have."*, nature provides fundamental structures that, once they are unrevealed by science, they might be utilized and replicated for our own purposes. So much so, soap films, as known as minimal surfaces, and the periodic minimal surfaces structures, have been widely identified and applied in a broad range of scientific fields. Overall, the present thesis addresses some physical and mechanical problems, mathematically modelling them using some cutting-edge techniques in thermoelastic wave propagation and fracture mechanics, which the capability of the models are assessed over materials with periodic features. This section mainly concerns to a brief discussion on these periodic materials (partially taken from [16, 17]).

1.1.1 Layered materials and applications

A layered material, or simply a laminate, is an example of a composite material which is made of a combination of materials stacked on each other to form a new material system, which will present enhanced chemical resistance and tailoring properties compared with the conventional materials one by one separately, as raw steel

[18]. A notorious example from history that can be cited is the Japanese Samurai swords. Samurai warriors combined laminated metals to forge their swords, these combinations allow designing desired shapes and contours, and aside from aesthetics, these combinations were aimed to produce structural advantages as, low weight and high stiffness at the same time, which leads to less susceptibility to breakage upon impact, and even more affordable swords. With the fast industrial development, composite materials are being currently used in the components of aircraft, helicopters, satellites, space shuttles, automotive vehicles, among other applications [19], some examples are displayed in Fig. 1. It has been analyzed the dynamical characteristics of wave propagation in periodic layered materials, where they work as mechanical filters for the frequency bands [20].

(a) Automotive vehicles engineering. Source [21].

(b) Aerospace engineering. Source [22].

Figure 1: Industrial applications of laminated composites.

Composite materials, as well as laminates, can be viewed from their physical properties which are classified either the microscopic and macroscopic level to describe the scale of material characterization. The term macroscopic is related to the properties of the bulk, in other words, it concerns to the overall behaviour of the system, in the context of the present work, to the layered material as a whole, meaning that a macromechanical analysis considers the averaged properties of the composite. Whereas, the term microscopic deals with the constituents properties and elements of the composite, it refers to the fundamental structure of the matter. Thus, a micromechanical analysis recognizes the heterogeneity of the material, and calculated properties from this analysis might serve as basis for input into the analysis for predicting macrostructural properties. Naturally, from the definition of anisotropy, an orthotropic continuum means that the mechanical, physical, thermal and electrical properties of the material are different in three mutually orthogonal directions [23].

Nowadays, material availability, economics and market competitiveness are dic-

tating the role laminate composites are playing in engineering design by the optimization of the cost-effective manufacturing process. In fact, for some aircraft structural components, more than 30% weight savings in existing metal structures are achieved by using composite materials, representing impressive performance gains [1]. Fig. 2 shows an example of a laminate periodic-like composite used in aircraft fuselage skin. Additionally, modeling combined phenomena as elasticity and heat transfer on multiphase materials containing a periodic microstructure, such as laminates, is a topic of vast importance in modern applications, such as aerospace, aircraft, biomedical and electronics [24–28]. Laminates are also often engaged in photovoltaic modules. Regarding to thermoelastic phenomenon, thermo-elastic deformations in photovoltaic laminates have been analytically investigated in [29]. Nonetheless, a plethora of problems are assumed on heterogeneous continuum with a small accuracy over the microstructural length scale. Furthermore, deriving the solution of standard physical phenomena, as the governing thermoelastic partial differential equation with one relaxation time tackled in Chapter 2, may be cumbersome both analytically and numerically, due to the periodicity of the media [30, 31].

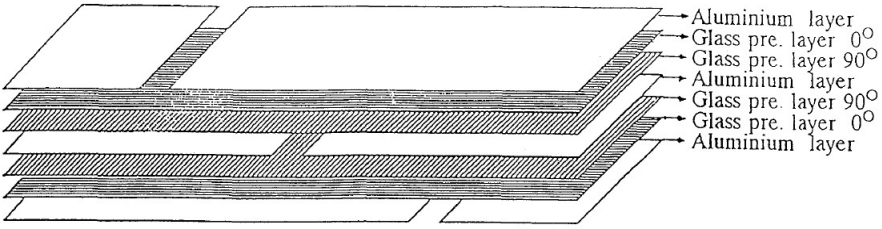

Figure 2: Laminated panel in aircraft fuselage skin. Taken from [1].

In order to provide a novel perspective to approach the solution of several phenomena within composite materials, specially layered medias, the multi-scale variational asymptotic homogenization arises among them, which has been well established in earlier works [32–35]. Multi-scale variational asymptotic homogenization show themselves as effective tools for determining the responses of the microscopic phases on the overall properties of the composites, by replacing the heterogeneous continuum by an equivalent homogenized model, whose solutions are good approximations of the real ones, but are characterized by constitutive tensors not affected by the fast variable which gives rapid oscillations due to the underlying microstructure. Therefore, such procedure is computationally effective [36, 37].

1.1.2 Triply Periodic Minimal Surfaces and their applications

As it will be seen forthcoming in Chapter 3, Section 3.1.1, a minimal surface can be interpreted as a surface that is locally area minimizing when a boundary curve is given, specifically they may also be defined as surfaces with zero mean curvature [38, 39], i.e. the arithmetic average of the principal curvatures vanishes everywhere on the surface. Started by Plateau's experiments over surface tension with soap films in the mid of the 19th Century [40], those experiments had demonstrated the existence of stable surfaces with least area bounded by a closed curve, and known nowadays as Plateau's Problem. Lately, resolving Plateau's problem regards to the minimization of the energetic cost of the surface, since the total interfacial energy depends on the amount of interface, and hence, on the principal curvatures [41].

Intuitively, a legitimate question rises, beside soap films, whether such behaviour is reproduced by nature. Indeed, minimal surfaces are frequently seen in natural objects, for instance, in beetle shells, weevils exoskeletons [2, 3] (see Fig. 3), crustacean skeletons [42–45], trabecular bone [46, 47], whose interface presents mean curvature near to zero everywhere. Figs. 4 and 5 show minimal surfaces structures in butterfly wing scales [4, 5, 48], where interestingly the blue color seen over the butterfly wing in Fig. 5 is particularly patterned by the mathematical geometry of a minimal surface, rather than other biological-chemical feature [6]. In what concerns to engineering applications, minimal surfaces have been widely used in several areas of knowledge. The engineer Otto Frei designed the Olympic stadium, depicted in Fig. 6, in Munich for the 1972 Summer Olympics based on minimal surfaces [49].

In this context, Triply Periodic Minimal Surfaces (TPMS) are minimal surfaces which have periodicity throughout the three space dimensions. TPMS struts are flourishing as objects of great interest to physicists, biologists, and mathematicians [50, 51]. From the standing point of mechanics, it has proved TPMS are not only geometrically extremal but extremal for heat and mass transport, electric conduction, leading to applications involving chemical reactions, permeability (see Fig. 7a), catalytic converters, fuel cells, batteries electrodes (Fig. 7b) and heat exchangers [52–58].

Studies demonstrate that TPMS sheet solids are a type of scaffold architecture with significant potential benefits for tissue engineering and bone replacement, as illustrated in Fig. 8 [8, 60, 61], and most recently for osseo-integration in root implant [62]. On this regard, thanks to developed automated assembly and additive manufacturing (AM) techniques [63–66], progress have been made in manufacturing TPMS cellular materials for engineering applications for orthopedic applications

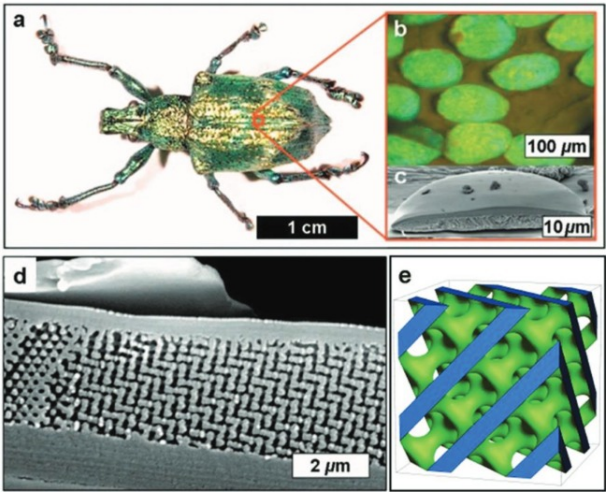

Figure 3: Weevil Lamprocyphus Augustus exoskeleton. Adapted from [2, 3].

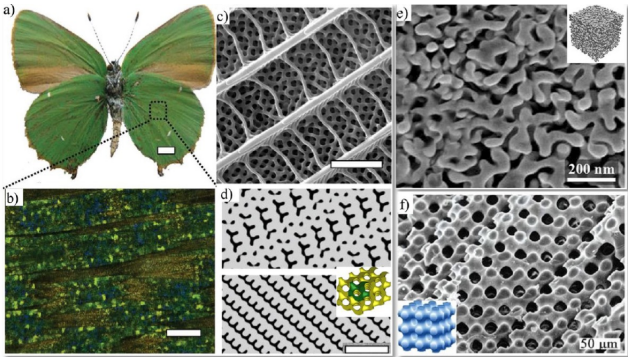

Figure 4: Callophrys Rubi butterfly wing scales. Adapted from [4, 5].

[59, 67–70]. They also showed enhanced mechanical properties when compared to other cellular structures, and thus are promising candidates for various technological applications regarding compressive and tensile regimes [71, 72].

On one hand, analysis from experimental tests of TPMS geometries in quasi-static compressional regimes are being pursuit. On the other hand, fewer studies are exploiting numerical models on TPMS structures to assess fracture behaviour and deformation mechanism (see for example [73–75]). Consequently, as good headway is being made on developing, implementing and analyzing methods for brittle fracture

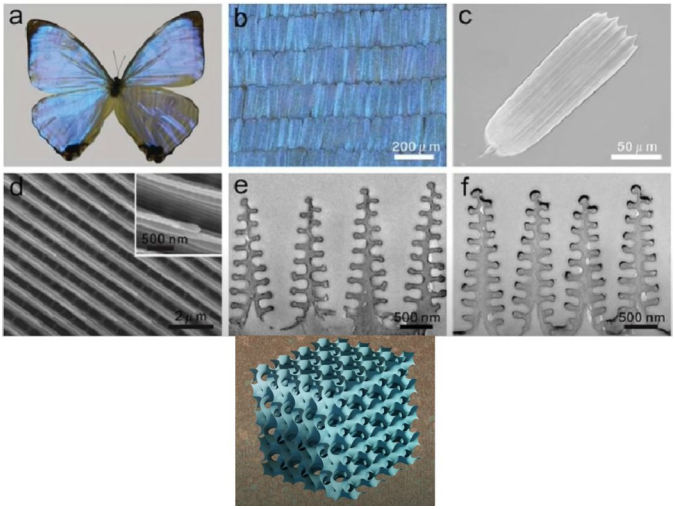

Figure 5: Morpho Sulkowskyi butterfly wing scales. Adapted from [6].

Figure 6: Olympic Stadium in Munich. Source [7]

for solid shells [76], fiber composites [77, 78], and for surfaces with complex topologies [79], Chapter 3 evidences the numerical phase field model applied to open foams TPMS like structures.

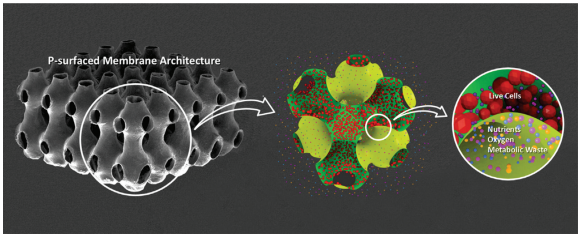

(a) Nonclogging scaffold composed of a semipermeable membrane with Primitive design. Taken from [59].

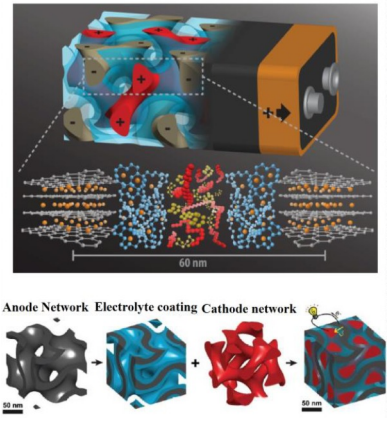

(b) Energy storage nano-3D Li-ion/sulfur system made of functional anode and cathode nanonetworks separated by a Gyroid-like electrolyte phase within a single 3D nanostructure. Adapted from [53].

Figure 7: Usage of TPMS structures in different engineering applications.

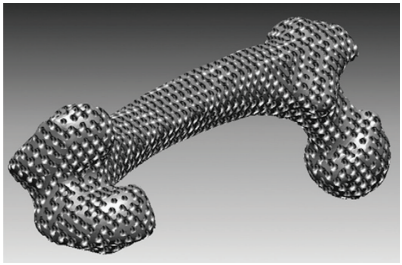

(a) Femur bone scaffold composed of Diamond internal architecture.

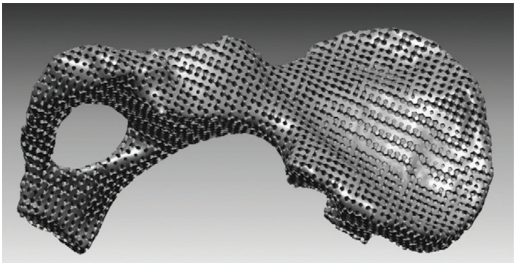

(b) Iliac bone scaffold composed of Primitive internal architecture

Figure 8: TPMS scaffolds bone engineering. Adapted from [8].

1.2 Generalized thermoelasticity theory and homogenization techniques

The thermoelasticity phenomenon bonds together a set of theories [80]. Namely, the general theory of heat conduction, thermal stresses, and strains set up by thermal flow in elastic bodies, and the reverse effect of temperature distribution caused

by the elastic deformation itself leading to thermoelastic energy dissipation. The generalized thermoelastic theory to be tackled forthcoming in Chapter 2 (partially taken from [16]), plays a relevant role when wave propagation is being analysed and reported in certain specific regimes, where the traditional theory lacks to describe experimental observations. Furthermore, given the fact that deriving the solution of the generalized thermoelastic problem on a material with periodic micro-structure by analytical and/or numerical methods can be worrisome, an homogenization technique for the generalized thermoelastic problem is further derived, opening another path for obtaining the solution.

1.2.1 Thermoelastic problem with one thermal relaxation time

The main theory of thermoelasticity based on Fourier's law of heat conduction, leaves thermal perturbations propagate at infinite velocity in a diffusive manner, once the coupled displacement-temperature governing equation is a parabolic-type partial differential equation [80–82]. In practical terms, this means that when a temperature gradient is suddenly produced in some region of the sample, this entails in an instantaneous disturbance at each point of the material [83, 84]. However, there are some experimental observations, as [85] pinpointed, where the temperature acts like a wave propagating through the body with finite speed, commonly referred to as second sound [86, 87]. The pattern of the heat wave propagation has been observed in superfluids, inhomogeneous materials like sand and processed meat, [88, 89], and in pure crystals, [90]. Moreover, this factor contradicts the physical affirmation that for a finite time interval a disturbance of bounded support may only generate the response of a bounded support [85, 91, 92].

In order to overcome such a paradox above described, recent developments were made as [93] mentions, and a couple of generalized thermoelastic theories have flourished. The idea of a generalized thermoelasticity with one relaxation time was introduced in [94] by Lord-Shulman, originally proposed by Maxwell [95] in the context of theory of gases, and later by Cattaneo [96] in the context of heat conduction in rigid bodies [85]. In this theory, a modified law of heat conduction including both the heat flux and its time derivative replaces the conventional Fourier's law [97]. The heat equation associated to this theory becomes hyperbolic and hence eliminates the paradox of the propagation of thermal signals with an infinite speed. The equations of motion and constitutive relations, remain the same for both theories of thermoelasticity, the uncoupled theory and the coupled one [94].

1.2.2 Variational-Asymptotic homogenization on materials with periodic microstructure

At this stage, it must be highlighted that various homogenization methods have being applied to study the overall properties of multi-phase periodic materials, which may be classified in asymptotic technique [98–102], variational asymptotic schemes [37, 103–106], analytical paths [107–111], and computational approaches [100, 112–120]. In what concerns to periodic materials in presence of thermoelastic effects, as seen in [121–123], the homogenization method has been investigate therein, and developed in the context of thermoelastic periodic material with pertinent physical applications highlighted in [124]. Furthermore, a variational-asymptotic technique for thermoelastic periodic materials was brought in [125].

As a matter of fact, cutting edge research regarding asymptotic homogenization techniques, variational-asymptotic approaches and computational methods are being made along several multi-phase materials in presence of certain phenomena. For instance, the asymptotic homogenization technique over piezoelectric composite materials may be found in [126–129] and on thermal-piezoelectric materials with a periodic microstructure via asymptotic schemes can be checked in [130]. Also, multiscale homogenization schemes have been applied to characterize the behaviour and the global constitutive properties of viscoelastic heterogeneous materials with periodic microstructure [131–134]. Particularly, in the latter case, the variational-asymptotic homogenization method was proposed in order to characterize the propagation of dispersive waves in viscoelastic materials with periodic microstructure. Likewise, the homogenization approach for describing the elastic, thermal and diffusive properties of periodic materials on periodic layered materials in presence of thermal-diffusion has been explored by [135–137]. Effective analysis on heterogeneous continuum in presence of thermal-mechanical and thermal-magneto-electro-elastic deformations have been studied by [138–140] and [141], respectively.

1.3 Phase Field to brittle fracture

In the field of Fracture Mechanics, Phase Field to brittle fracture theory approximates the crack discontinuity sharp edges incorporating a continuous variable, called the phase field function, by which a continuous and well behaved transition describes the solid phases during some loading regime between the fully broken and intact states. Postulated by Griffith in 1921 [142], his approach is based on the equilibrium of the energy of the system. Expressly, Griffith introduced the concept of energy

release rate $\mathcal{G}$ as being the energy released per unit area by a crack in brittle elastic materials. It was also noted by him that failure of a quasi-static crack occurs when the energy release rate reaches a critical value dissipated by the surface for any rate of evolution of the area ($\mathcal{G} = \mathcal{G}_c$), named the critical energy release rate $\mathcal{G}_c$, considered as a material property, and the crack grows monotonic and continuously in time. In fact, as long as $\mathcal{G} < \mathcal{G}_c$, the system remains stable, i.e. the crack length does not change, since the energy released is less than energy required to occur the propagation of the crack tip. A *posteriori*, it was postulated the irreversibility criterion of the fracture process and the evolution of the crack area $\dot{A}$ [143–146]. Thus, the modified/generalized Griffith' criteria can be condensed as

$$\begin{cases} \dot{A} \geq 0 & \text{Irreversibility} \\ (\mathcal{G}_c - \mathcal{G}) \leq 0 & \text{Griffith's criterion} \\ \dot{A}(\mathcal{G}_c - \mathcal{G}) = 0 & \text{Energy Conservation} \end{cases}, \tag{1.1}$$

known also as Kuhn-Tucker conditions [147].

Having established that, such a procedure, which will be outlined in Chapter 3 Sec. 3.2, is then presented and detailed so the fracture mechanisms of TPMS topologies can be derived by the implementation of a finite element method for phase field, which states the framework among compressive experimental works. The progress that have been made in these regards are briefly introduced in this section (partially taken from [17]).

1.3.1 Quasi-static uniaxial compressive Phase Field modelling to TPMS

The pioneering formulation of phase field theory from Griffith's energy-based criterion is particularly attractive by the ability to elegantly simulate complicated quasi-static fracture processes including crack nucleation, propagation and branching of cracks The theory is governed by a minimization problem of an energy functional as a function of the displacement field and the crack surface, where the crack surface is battered by a function that regularizes the discontinuity of the original energy functional, as described by Francfort [148]. The minimization of this functional of the solid results in a set of admissible cracks and displacement fields on the material. Nonetheless, this problem is rather cumbersome to be tackled since the crack surface is not known a *priori*. Driven by this issue, the phase field approximation emerged, which regularizes the variational formulation, i.e., overcomes the crack discontinuity, and thus eases the numerical implementation of the problem. The regularization,

initially presented in [149] for image segmentation, was applied by Bourdin et al. [143] to fracture in brittle materials. This regularization replaces the use of the crack surface as a variable by a continuous scalar field, called crack phase field, which interpolates continuously and smoothly between the state of intact material and the state of fully damaged material. Such an approximation regularizes the topology of a crack surface through the so-called crack surface density function, governed by the new variable set by a regularization parameter responsible for controlling the width of the damaged region.

Experimental studies in quasi-static compressional regimes have been proposed [13, 68, 150–153] to assess stiffness, strength, energy absorption, and also permeability of TPMS structures (see for instance Fig. 9). The effect of the volume fraction (also defined as the complement to unity of porosity) has also been scrutinized [154–157]. Numerical results by [158] have shown that a volume fraction of 30% is desirable or cell in-growth in bone tissue engineering. The energy absorption ability of some graded and uniform open foam TPMS specimens made via AM were discussed in [12, 64], whereby also micro-cracks were registered during compression tests.

Mechanical properties were derived through AM fabricated TPMS lattices having Titanium alloy Ti–6Al–4V [159–161], and Aluminium alloy Al–Si10–Mg [13, 162], as main materials. In the latter, it was stated that choosing a small unit cell size can avoid low-strain structural failure caused by localized fracture and crack propagation. In addition, thereby it has been stated that due to the complex geometry, the crack initiation site is difficult to be spotted, as well as the crack paths were complicated to be determined. At this point, it is worthy noting that inherent problems of different AM techniques and different microstructure properties of the material might lead to different crack patterns, where inevitable micro defects from the fabrication process might serve as nucleation sites, as well as contribute to smaller volume fraction values of the manufactured lattices compared with the effective volume fractions of the TPMS original CAD models, see for example Fig. 10 [9, 163]. For instance, in [164], it was noted that excess of Ti–6Al–4V alloy powders adhered to the surface of the sample led to a thicker sheet, affecting the geometry accuracy and roughness of the fabricated specimens. In [68], microscopic images showed crack formation sites at manufacturing imperfections and at small pores in the bulk. Besides, due to the TPMS continuous rate of curvature, TPMS cells do not have notches (sharp zones), which can act as stress concentrators, minimizing crack nucleation sites from staircase effect inherent to AM techniques, as seen in Fig. 11 [10]. By so, TPMS tend

to present improved fatigue resistance in comparison to other conventional lattice structures (truss-based) with the same volume fraction.

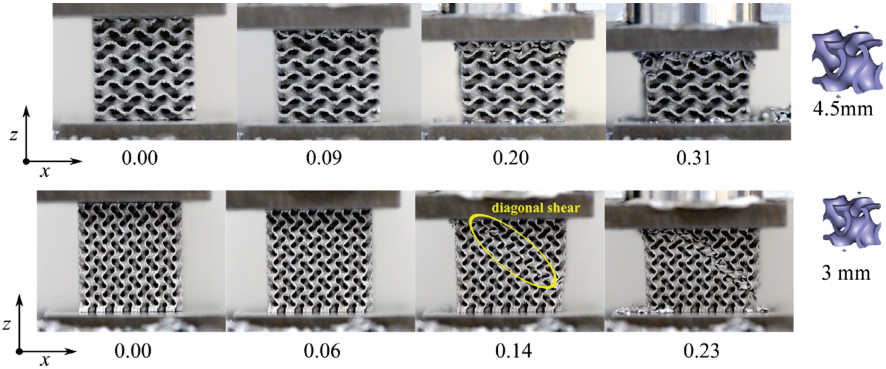

(a) Aluminium alloy TPMS sheet networks additively manufactured under compression. Adapted from [13].

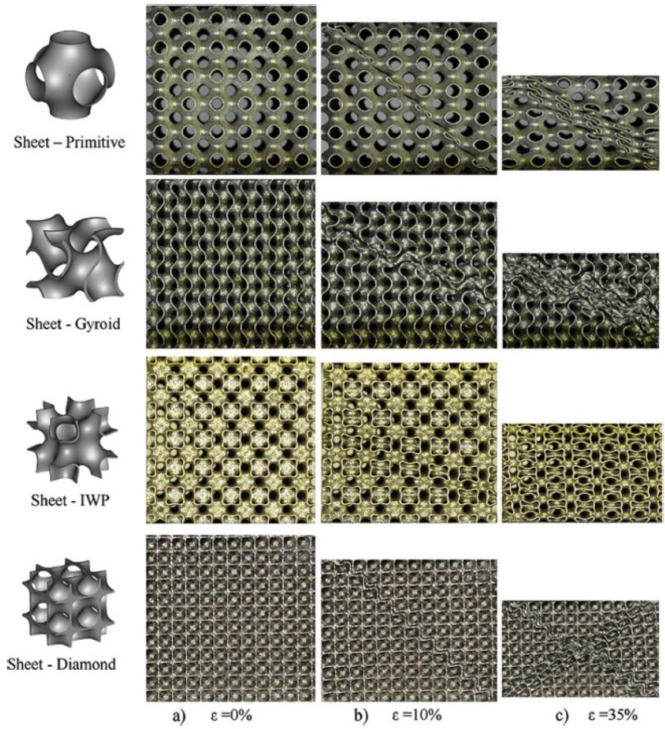

(b) Maraging steel TPMS sheet networks additively manufactured under compression. Taken from [151].

Figure 9: TPMS metal based lattices fabricated using AM techniques under compressive loading.

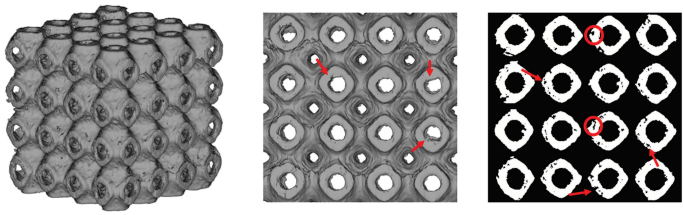

(a) Primitive cluster lattice.

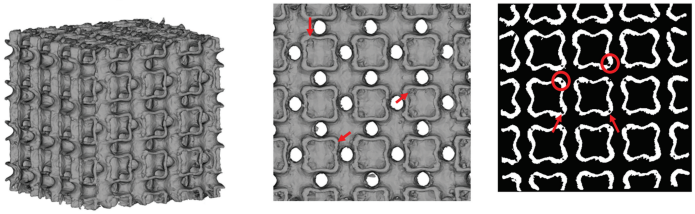

(b) IWP cluster lattice.

Figure 10: Micro defects identification from scanned and reconstructed TPMS lattices additively manufactured. Taken from [9].

So far, the majority of simulation work for structural integrity analysis of TPMS has been confined to the identification of elastic instabilities and plasticity [9, 150, 158, 165]. On that account, the present work exploits the phase field approach to fracture to numerically tackle and characterize the above open issues, assessing/estimating brittle fracture, crack sites, nucleation, propagation and branching under uniaxial compressive loads of TPMS unit cell open foams. Furthermore, such a characterization will be advantageous in understanding how the damage pattern might correlate to the TPMS geometry and their aforementioned mechanical properties, advancing on the researches made to date.

1.4 Aims and structure of the dissertation

Inspired by those studies where the mechanical and physical phenomena are exploited on periodic material, this work presents novel contributions on these regards. More precisely, the work presents an original theoretical framework to characterize the overall properties, namely elastic and thermal, of multi-phase periodic materials governed by Lord-Shulman generalized thermoelasticity equation via variational-asymptotic homogenization. The procedure replaces the heterogeneous continuum

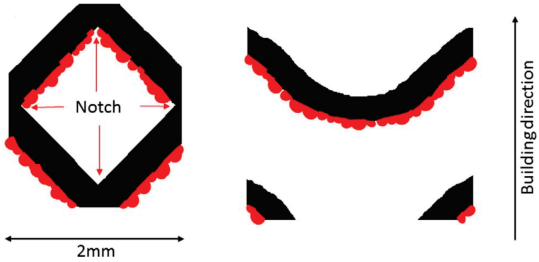

(a) Octahedron truss based.

(b) Gyroid sheet network based.

Figure 11: Illustration of residual particles attached after AM processing technique. Adapted from [10].

by some homogeneous model led by an homogenization approach, combining the generalized theory of thermoelasticity with periodic spatially dependent one time relaxation with the homogenization technique in periodic laminated materials, which are in constant growth on a plethora of applications in engineering and in overall technology. Moreover, from the studies and results over fracture mechanics aforementioned, it is suffice to say that robust breakthrough relationships between TPMS cell geometries and their numerical performances from phase field theory must be established. Thus, the objective towards this endeavour is also modelling fracture over TPMS by means of phase field, furnishing to the academia a powerful tool to characterize and estimate the evolution of damage caused by the crack propagation over TPMS foam topologies.

Throughout Chapter 2, the Lord-Shulman generalized thermoelastic governing equations are homogenized and applied to the laminated periodic material. In the following, Section 2.1 recalls the fundamentals of thermoelasticity with one relaxation time at the micro-scale, which describe the non-homogeneous medium, in the time domain. Subsequently, the generalized thermoelasticity with one relaxation time is transformed by the bi-lateral Laplace transform, once the relaxation time varies within the material phase. Such a strategy takes the real time dependent input to the Laplace domain (complex frequency domain), aiming the separation of the fast from the slow variables in a periodic media and by so separating as well the time relaxation time from the partial derivative in time contained in the differential operator induced by Maxwell-Cattaneo law. In Sections 2.2 and 2.3, the micro-displacement and micro-temperature fields are rewritten as power series

expansions of the microstructural length scale, such that a cascade of recursive non-homogeneous differential problems is defined over the periodic unit cell. From this point, the solvability conditions are imposed to these recursive differential problems, arising from the down-scaling relations, which are written in terms of the perturbation functions. Sections 2.4 deals with the substitution of the down-scaling relations into the microscopic field equations, producing the governing equations at infinite order given in closed form in terms of the microscopic constitutive properties and the perturbation functions. The variational-asymptotic to establish an equivalence between the equations at macro-scale and micro-scale procedure and the zeroth order truncation is tackled in Section 2.5. Thereby, truncating the average field equation of infinite at the zeroth order, and by a variational problem over the power-like functional, the global constitutive tensors are defined.

Some analytical applied examples are stated in Section 2.6. Whereby, wave propagation analysis from related dispersion functions are reported, in order to assess the capability of the method through the study of thermal wave propagation over a two-dimensional bi-layered continuum with a periodic microstructure with orthotropic phases and axis of orthotropy parallel to the direction of layering. The overall mechanical and thermal properties are analytically determined in terms of the physico-mechanical parameters of the microstructure, which are dependent on the relaxation time. By determining the frequency equation, it furnishes the necessary tools to obtain the frequency spectrum of the material in order to analyse and compare the wave propagation of the variational-asymptotic homogenized model with the heterogeneous media via Bloch waves. So much so, throughout Section 2.7, the method is applied for studying the overall properties of two-dimensional bi-layered orthotropic composites. Specifically, the overall elastic, thermal dilatation and thermal conduction tensors are determined in their analytic form, a benchmark and some analysis are pursuit. In addition, it has been analysed the behaviour of the absence of the relaxation time, comparing with different scenarios containing it. Needless to say that, the generalized Lord-Shulman thermoelastic problem studied becomes the conventional thermoelastic problem in presence of a vanishing relaxation time.

Further mathematical details exploring the Euler-Lagrange equation via power-like functional at micro-scale are outlined in Appendix A. The derivation of frequency spectrum and ad hoc background via Floquet-Bloch theory within the heterogeneous continuum, as well as the dispersion relations through the transfer matrix theory, which allows the benchmark analysis against the homogenized model, have been substantially developed in Appendices B, C and D.

Subsequently, a consistent quasi-static uniaxial compressive Phase Field model using spectral diagonalization of the strain tensor has been proposed, among a clear definition of Minimal Surfaces, as well as the concept of Triply Periodic Minimal Surfaces, and their derivation/generation in CAD models are exploited in Chapter 3. Furthermore, the novelty application of the phase field scheme in TPMS unit cell foams is exhaustively dealt and contrasted with existing literature, analyzing fracture mechanics in TPMS on compressive regimes. To this aim, Section 3.1 is dedicated in establishing the mathematical concept of a minimal surface and TPMS from some different theoretical standing points, presenting as well a brief overview of some notorious historical minimal surfaces and their shaped soap films. Section 3.2 presents the phase-field variational approximation to brittle fracture theory. Moreover, thereof the mathematical background in which the phase field finite element method has been derived, is shown in Section 3.2. The finite element model has been developed and implemented on the open-source software `FEniCS` [166], seen in Section 3.3. Still, by assigning a thickness to the thin minimal surfaces, CAE-CAD models of TPMS are designed utilizing either the software `Mathematica` [167], or by the software developed at the University of Nottingham, `FlattPack`, they have been imported into the phase field FEM. Also throughout Section 3.3, by setting the boundary conditions and material properties, an extensive mesh sensitivity analysis has been conducted over the unit cells of the following TPMS geometries: Primitive, Gyroid, IWP, Diamond and Neovius. Ultimate compressive stresses and the apparent Young's moduli in compression are calculated via the stress-strain curves predicted by the phase field simulations. Section 3.4 delineates the characterization of the fracture patterns and the deformation behaviour of the five TPMS unit cell foams studied. Ultimately, in Section 3.5, the estimated mechanical properties of the five types of TPMS unit cells, for different porosity values, have been reported on Ashby charts [152, 168, 169], describing the relationship among them. Moreover, in order to provide also quantitative indications to materials scientists for further research and applications of TPMS in different fields, Section 3.5 confronts and compares those properties with the ones from open cell aluminium alloy foams, and TPMS sheet networks of several different metallic alloys, available in the literature up to date.

The main conclusions achieved in this research thesis are beheld in Chapter 4. Furthermore, future developments are summarized as well.

Chapter 2

Variational-Asymptotic Homogenization of Lord-Shulman Thermoelastic Equation in Bi-Dimensional Laminated Material

As previously mentioned, this Chapter derives the variational asymptotic homogenization scheme for the Lord-Shulman thermoelastic equation. Later, the homogenized model is applied to bi-dimensional periodic laminated material with an orthotropy axis parallel to the layering direction, whose thermal, compressional-thermal and shear waves are derived from the dispersion relations and compared with the results from the heterogeneous continuum via Floquet-Bloch theory, which is outlined in Appendix 4.2. The content of this Chapter is mainly taken from [16].

2.1 Derivation of thermoelasticity with one relaxation time in the Laplace domain

Throughout this Section, the generalized Lord-Shulman thermoelasticity theory is recalled, in relation to an heterogeneous periodic composite material, which will be taken to the Laplace domain.

Let consider an heterogeneous composite material $\mathfrak{L}$, Fig. 12, under the assumption of small strains (for instance a stretching load), which leads to a process of exchanging mechanical energy into thermal energy under the action of externally applied thermal-mechanical loadings. Such procedure is then followed by temperature variances and strains within the body, all of which vanish upon the removal of the mentioned thermal-mechanical loadings. The continuum $\mathfrak{L}$ is described as a linear thermoelastic Cauchy medium [85, 91, 92] under stresses induced by body forces and temperature changes due to heat source.

On each point of the material is endowed with a displacement field $\boldsymbol{u}(\mathbf{x},t) = u_i \boldsymbol{e}_i$ and a relative temperature field $\theta(\mathbf{x},t) = T(\mathbf{x},t) - T_0$, where $T(\mathbf{x},t)$ is the absolute temperature, T_0 is a reference stress-free temperature. The coupled constitutive relations link the stress tensor $\boldsymbol{\sigma}(\mathbf{x},t) = \sigma_{ij}\boldsymbol{e}_i \otimes \boldsymbol{e}_j$, the heat flux vector $\mathbf{q}(\mathbf{x},t) = q_{ij}\boldsymbol{e}_i \otimes \boldsymbol{e}_j$, and the entropy per unit of volume $\boldsymbol{\eta}(\mathbf{x},t) = \eta_{ij}\boldsymbol{e}_i \otimes \boldsymbol{e}_j$, to the aforementioned relevant fields $\boldsymbol{u}(\mathbf{x},t)$, $\theta(\mathbf{x},t)$, that is

$$\boldsymbol{\sigma}(\mathbf{x},t) = \mathfrak{C}(\mathbf{x})\boldsymbol{\varepsilon}(\mathbf{x},t) - \boldsymbol{\alpha}(\mathbf{x})\theta(\mathbf{x},t)\,, \tag{2.1a}$$

$$\mathbf{q}(\mathbf{x},t) + \tau(\mathbf{x})\frac{\partial \mathbf{q}(\mathbf{x},t)}{\partial t} = -\bar{\mathbf{K}}(\mathbf{x})\nabla\theta(\mathbf{x},t)\,, \tag{2.1b}$$

$$\boldsymbol{\eta}(\mathbf{x},t) = \boldsymbol{\alpha}(\mathbf{x})\boldsymbol{\varepsilon}(\mathbf{x},t) + \frac{C_E}{T_0}\theta(\mathbf{x},t)\,, \tag{2.1c}$$

where $\boldsymbol{\varepsilon}(\mathbf{x},t) = \varepsilon_{ij}\boldsymbol{e}_i \otimes \boldsymbol{e}_j$ is the strain tensor, $\mathfrak{C} = C_{ijhk}\mathbf{e}_i \otimes \mathbf{e}_j \otimes \mathbf{e}_h \otimes \mathbf{e}_k$ is the fourth-order elastic tensor, $\bar{\mathbf{K}} = \bar{K}_{ij}\mathbf{e}_i \otimes \mathbf{e}_j$ is the second-order thermal conductivity tensor, $\boldsymbol{\alpha} = \alpha_{ij}\mathbf{e}_i \otimes \mathbf{e}_j$ is the second-order stress-temperature tensor, C_E is the specific heat at zero strain, and for convenience we define $p = C_E/T_0$. The Eqs. ẽqref are symmetric, due to the symmetries of the tensor given by the microscopic orthotropy structure of the material. Besides, as aforementioned, to avoid the physical paradox of infinite speed for the propagation of heat signal in the classical thermoelastic equations [92], which are parabolic, a space dependent relaxation time τ is introduced, known as the Maxwell-Cattaneo law replacing the Fourier law for thermal conduction, in order to transform them into hyperbolic equations.

As the material is under the effect of small displacements, then the micro-strain tensor is defined as

$$\boldsymbol{\varepsilon}(\mathbf{x},t) = \frac{1}{2}\left(\nabla\boldsymbol{u}(\mathbf{x},t) + \nabla^T\boldsymbol{u}(\mathbf{x},t)\right), \tag{2.2}$$

where $\nabla\boldsymbol{u}$ is the gradient of the micro-displacement $\boldsymbol{u}(\mathbf{x},t)$.

The following balance equations hold

$$\nabla \cdot (\boldsymbol{\sigma}(\mathbf{x},t)) + \mathbf{b}(\mathbf{x},t) = \rho(\mathbf{x})\ddot{\mathbf{u}}(\mathbf{x},t), \tag{2.3a}$$

$$\nabla \cdot (\mathbf{q}(\mathbf{x},t)) - \bar{r}(\mathbf{x},t) = -T_0\dot{\boldsymbol{\eta}}(\mathbf{x},t)\,, \tag{2.3b}$$

with $\mathbf{b} = b_i\mathbf{e}_i$ being the body forces, $\bar{r}$ the heat source per unit time per unit volume and ρ is the mass density. Throughout, t stands for the time coordinate, the superimposed dot denotes the derivative in relation to time, and consider $\bar{r} = r/T_0$.

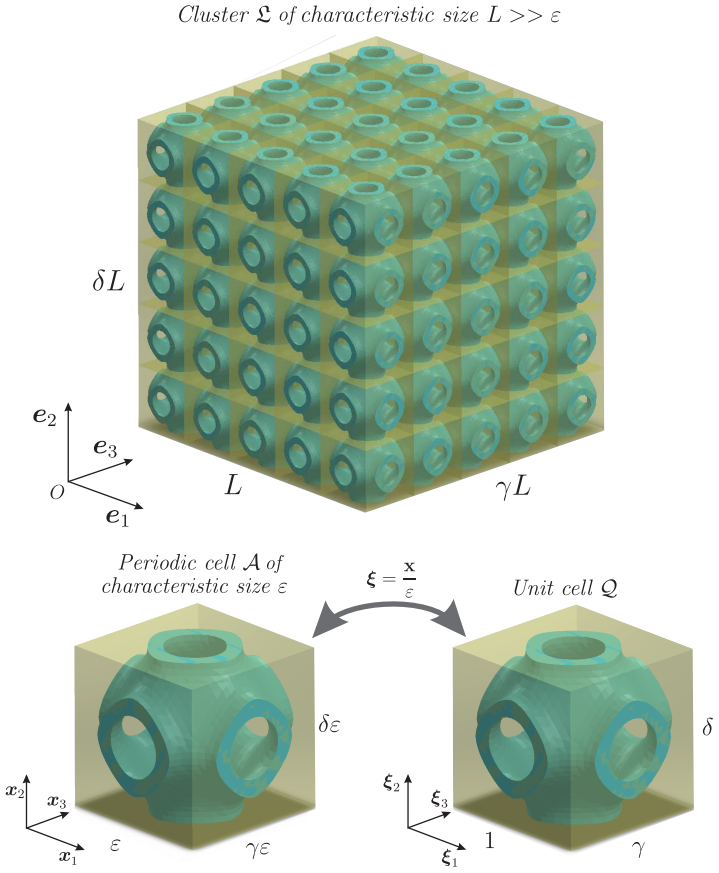

Figure 12: $3D$ continuum domain $\mathfrak{L}$ with periodic cell $\mathcal{A}$ and its dimensionless unit cell $\mathcal{Q}$.

With the thermoelasticity constitutive equations and equilibrium equations well

established, we may thus introduce the periodic microstructure of an heterogeneous composite material theory [170]. Let a point be identified by the position vector $\mathbf{x} = x_1\boldsymbol{e}_1 + x_2\boldsymbol{e}_2 + x_3\boldsymbol{e}_3 \in \mathbb{R}^3$ related to a system of coordinates with origin at point O and written in terms of the orthogonal base $\{\boldsymbol{e}_1, \boldsymbol{e}_2, \boldsymbol{e}_3\}$, on the three-dimensional heterogeneous material $\mathfrak{L}$ characterized by a certain periodic microstructure. Let also $\mathcal{A} = [0, \epsilon] \times [0, \delta\epsilon] \times [0, \gamma\epsilon]$ be a periodic cell with characteristic size ϵ defined by three orthogonal periodic vectors $\boldsymbol{v}_1$, $\boldsymbol{v}_2$ and $\boldsymbol{v}_3$, written as $\boldsymbol{v}_1 = d_1\boldsymbol{e}_1 = \epsilon\boldsymbol{e}_1$, $\boldsymbol{v}_2 = d_2\boldsymbol{e}_2 = \delta\epsilon\boldsymbol{e}_2$ and $\boldsymbol{v}_3 = d_3\boldsymbol{e}_3 = \gamma\epsilon\boldsymbol{e}_3$. The material domain is set up by attaching three-dimensionally the cell $\mathcal{A}$ in accordance to the directions $\boldsymbol{v}_1$, $\boldsymbol{v}_2$ and $\boldsymbol{v}_3$, see Fig. 12.

Due to the periodicity of the material, throughout the work the superscript m refers to the micro-scale. Therefore, $\mathfrak{C}^m(\mathbf{x}, t) = C^m_{ijhk}\mathbf{e}_i \otimes \mathbf{e}_j \otimes \mathbf{e}_h \otimes \mathbf{e}_k$ is the fourth-order micro-elastic tensor, $\bar{\mathbf{K}}^m(\mathbf{x}, t) = \bar{K}^m_{ij}\mathbf{e}_i \otimes \mathbf{e}_j$ is the second-order micro-thermal-conductivity tensor, $\boldsymbol{\alpha}^m(\mathbf{x}, t) = \alpha^m_{ij}\mathbf{e}_i \otimes \mathbf{e}_j$ is the second-order micro-stress temperature tensor, $\rho^m(\mathbf{x})$ is the material density, $p^m(\mathbf{x})$ is the specific heat at zero micro strain, and $\tau^m(\mathbf{x})$ is the micro relaxation time. Furthermore, they obey the following conditions

$$\mathfrak{C}^m(\mathbf{x} + \boldsymbol{v}_i) = \mathfrak{C}^m(\mathbf{x}), \tag{2.4a}$$
$$\bar{\mathbf{K}}^m(\mathbf{x} + \boldsymbol{v}_i) = \bar{\mathbf{K}}^m(\mathbf{x}), \tag{2.4b}$$
$$\boldsymbol{\alpha}^m(\mathbf{x} + \boldsymbol{v}_i) = \boldsymbol{\alpha}^m(\mathbf{x}), \tag{2.4c}$$
$$\rho^m(\mathbf{x} + \boldsymbol{v}_i) = \rho^m(\mathbf{x}), \tag{2.4d}$$
$$p^m(\mathbf{x} + \boldsymbol{v}_i) = p^m(\mathbf{x}), \tag{2.4e}$$
$$\tau^m(\mathbf{x} + \boldsymbol{v}_i) = \tau^m(\mathbf{x}), \tag{2.4f}$$

where $i = 1, 2, 3$, for all $\mathbf{x} \in \mathcal{A}$.

In the following derivation, let us define L and ϵ as the macroscopic length and the microstructural length, respectively, where $L >> \epsilon$, which gives the condition where the scales might be separated since the macroscopic length is taken to be much larger than the microstructural one. Let us also suppose that the heterogeneous material undergoes to $\mathfrak{L}$-periodic body forces $\boldsymbol{b}(\mathbf{x}, t)$, having zero mean values over the continuum $\mathfrak{L} = [0, L] \times [0, \delta L] \times [0, \gamma L]$, hence $\mathfrak{L}$ defined as above represents a portion of the continuum. Now, regarding the dimensionless cell, let us rescale the periodic cell $\mathcal{A}$ by a factor equals to the characteristic length ϵ, this implies that the non-dimensional cell model of the periodic microstructure is then $\mathcal{Q} = [0, 1] \times$

$[0,\delta]\times[0,\gamma]$. Moreover, from such rescaling process it arises two variables namely, the macroscopic (or slow) variable $\mathbf{x}\in\mathcal{A}$ in charge of measuring the slow oscillations within the continuum, and the microscopic (or fast) variable $\boldsymbol{\xi}=\mathbf{x}/\epsilon\in\mathcal{Q}$ responsible in evaluating the fast heat propagation wave within the composite [34, 35, 98, 171]. Thanks to cell $\mathcal{Q}$, the properties presented in (2.4) are now redefined as $\mathcal{Q}$-periodic over $\mathcal{Q}$ so the terms can be expressed by the microscopic variable $\boldsymbol{\xi}$ as

$$\mathbb{C}^m(\mathbf{x})=\mathbb{C}^m\left(\mathbf{x},\boldsymbol{\xi}=\frac{\mathbf{x}}{\epsilon}\right), \tag{2.5a}$$
$$\bar{\mathbf{K}}^m(\mathbf{x})=\bar{\mathbf{K}}^m\left(\mathbf{x},\boldsymbol{\xi}=\frac{\mathbf{x}}{\epsilon}\right), \tag{2.5b}$$
$$\boldsymbol{\alpha}^m(\mathbf{x})=\boldsymbol{\alpha}^m\left(\mathbf{x},\boldsymbol{\xi}=\frac{\mathbf{x}}{\epsilon}\right), \tag{2.5c}$$
$$\rho^m(\mathbf{x})=\rho^m\left(\mathbf{x},\boldsymbol{\xi}=\frac{\mathbf{x}}{\epsilon}\right), \tag{2.5d}$$
$$p^m(\mathbf{x})=p^m\left(\mathbf{x},\boldsymbol{\xi}=\frac{\mathbf{x}}{\epsilon}\right), \tag{2.5e}$$
$$\tau^m(\mathbf{x})=\tau^m\left(\mathbf{x},\boldsymbol{\xi}=\frac{\mathbf{x}}{\epsilon}\right). \tag{2.5f}$$

Along with the $\mathcal{Q}$-periodicity assumptions made for the relations (2.4), regarding the micro-scale, the governing equations are finally obtained by plugging the micro-scale constitutive Eqs (2.1a) to (2.2) into the micro-scale balance Eqs. (2.3a) and (2.3b), also hiding the arguments for a cleaner notation, one provides

$$\nabla\cdot(\mathbb{C}^m\nabla\mathbf{u}-\boldsymbol{\alpha}^m\theta)+\mathbf{b}=\rho^m\ddot{\mathbf{u}}\,, \tag{2.6a}$$
$$\mathbf{q}+\tau^m\dot{\mathbf{q}}=-(T_0)^{-1}\bar{\mathbf{K}}^m\nabla\theta\,, \tag{2.6b}$$
$$\nabla\cdot\mathbf{q}+\boldsymbol{\alpha}^m\nabla\dot{\mathbf{u}}+p^m\dot{\theta}=r\,. \tag{2.6c}$$

In the particular scenario where the relaxation time $\tau^m(\mathbf{x},\boldsymbol{\xi})=\tau>0$ is assumed as a constant, the governing Eqs. (2.6a) and (2.6b) result into

$$\nabla\cdot(\mathbb{C}^m\nabla\mathbf{u}-\boldsymbol{\alpha}^m\theta)+\mathbf{b}=\rho^m\ddot{\mathbf{u}}\,, \tag{2.7a}$$
$$\nabla\cdot\left(-(T_0)^{-1}\bar{\mathbf{K}}^m\nabla\theta\right)+\boldsymbol{\alpha}^m\mathcal{D}(\nabla\dot{\mathbf{u}})+p^m\mathcal{D}(\dot{\theta})=\mathcal{D}(r)\,, \tag{2.7b}$$

where the differential operator $\mathcal{D}=1+\tau^m\partial/\partial t$ depending on the relaxation time τ^m is introduced.

At this point it must be highlighted that, since the periodic cell $\mathcal{Q}$ is composed by two different phase materials, the relaxation time τ^m must be considered as space dependent, which means $\tau(\mathbf{x}, \boldsymbol{\xi})$ is a $\mathcal{Q}$-periodic function and hence varies within the composite material. For this reason, rather than continuing with the Eq. (2.6*b*), we apply the time bilateral Laplace transform, or analogously the Fourier transform with complex argument [172, 173] to the Eqs. (2.1*b*), (2.1*c*), (2.6*a*) and (2.6*c*), in order to separate the time relaxation τ^m from the partial derivative in time contained in the differential operator $\mathcal{D}$.

To clarify ideas, the time bilateral Laplace transform of a function $f : \mathbb{R} \to \mathbb{R}$ is defined as [172],

$$\mathcal{L}\{f(t)\} = \hat{f}(s) = \int_{-\infty}^{+\infty} f(t)\mathrm{e}^{-st}\mathrm{d}t, \quad s \in \mathbb{C}, \tag{2.8}$$

where the Laplace argument s and the Laplace transform $\hat{f}$ are complex valued (i.e. $\hat{f} : \mathbb{C} \to \mathbb{C}$). Whereas from an analytical standing point in [172], the inverse Laplace transform of a function $\hat{f}(s)$ is defined as

$$\mathcal{L}^{-1}\left\{\hat{f}(s)\right\} = f(t) = \frac{1}{2\pi\mathrm{i}} \int_{x-\mathrm{i}\infty}^{x+\mathrm{i}\infty} \mathrm{e}^{ts}\hat{f}(s)\mathrm{d}s, \tag{2.9}$$

where the integration is along the vertical line $\Re s = x$ inside the region of convergence. The Laplace transform of the $n-$th derivative of f with respect to t is given by the identity $\mathcal{L}\{\partial^n f(t)/\partial t^n\} = s^n \hat{f}(s)$. The convolution between two functions f_1 and f_2 is defined as $(f_1(t) * f_2(t)) = \int_{-\infty}^{\infty} f_1(u) f_2(t-\omega)\mathrm{d}\omega$, and it follows that the Laplace transform convolution rule of two time dependent functions f_1 and f_2 is given as $\mathcal{L}\{f_1(t) * f_2(t)\} = \mathcal{L}\{f_1(t)\}\mathcal{L}\{f_2(t)\}$.

Having established this, the governing equations on the transform space are

$$\nabla \cdot \left(\mathbb{C}^m \nabla\hat{\mathbf{u}} - \boldsymbol{\alpha}^m\hat{\theta}\right) + \hat{\mathbf{b}} = \rho s^2 \hat{\mathbf{u}}\,, \tag{2.10a}$$

$$\hat{\mathbf{q}} + \tau^m s\hat{\mathbf{q}} = -(T_0)^{-1}\bar{\mathbf{K}}^m \nabla\hat{\theta}\,, \tag{2.10b}$$

$$\nabla \cdot \hat{\mathbf{q}} + \boldsymbol{\alpha}^m \nabla\hat{\mathbf{u}} + p^m s\hat{\theta} = \hat{r}\,, \tag{2.10c}$$

where s is the unknown complex angular frequency ($s \in \mathbb{C}$), and $\hat{\mathbf{u}}$, $\hat{\theta}$, $\hat{\mathbf{q}}$, $\hat{\mathbf{b}}$, $\hat{r}$, are respectively, the bilateral Laplace transformed of the micro-displacement field, the micro-temperature field, the heat flux, the body forces and the heat source.

Proceeding with the substitutions, Eqs. (2.6*a*), (2.6*b*) and (2.6*c*) become on the Laplace transform space,

$$\nabla \cdot \left(\mathbb{C}^m \nabla \hat{\mathbf{u}} - \boldsymbol{\alpha}^m \hat{\theta} \right) + \hat{\mathbf{b}} = \rho^m s^2 \hat{\mathbf{u}} \,, \tag{2.11a}$$

$$\nabla \cdot \left(-\mathbf{K}^m \nabla \hat{\theta} \right) + s \boldsymbol{\alpha}^m \nabla \hat{\mathbf{u}} + p^m s \hat{\theta} = \hat{r} \,, \tag{2.11b}$$

where, due the plugging we assume

$$\mathbf{K}^m \left(\mathbf{x}, \boldsymbol{\xi}, s \right) = \frac{\bar{\mathbf{K}}^m (\mathbf{x}, \boldsymbol{\xi})}{(1 + \tau^m (\mathbf{x}, \boldsymbol{\xi}) s) T_0}, \tag{2.12}$$

with a $\mathbf{K}^m$ well behaved over the defined domain.

The interface Σ between two different phases i and j in the periodic cell $\mathcal{A}$, holds the jump of the values of function f at it, written as $[[f]] = f^i(\Sigma) - f^j(\Sigma)$, follows that

$$[[\hat{\boldsymbol{u}}]]\big|_{\mathbf{x} \in \Sigma} = \mathbf{0}, \tag{2.13a}$$

$$\left[\left[\left(\mathbb{C}^m \nabla \hat{\boldsymbol{u}} - \boldsymbol{\alpha}^m \hat{\theta} \right) \cdot \mathbf{n} \right] \right] \Big|_{\mathbf{x} \in \Sigma} = \mathbf{0}, \tag{2.13b}$$

$$\left[\left[\hat{\theta} \right] \right] \Big|_{\mathbf{x} \in \Sigma} = \mathbf{0}, \tag{2.13c}$$

$$\left[\left[-\mathbf{K}^m \nabla \hat{\theta} \cdot \mathbf{n} \right] \right] \Big|_{\mathbf{x} \in \Sigma} = \mathbf{0}, \tag{2.13d}$$

representing the conditions of continuity for a bounded interface, where the outward normal to the interface Σ is indicated by the vector $\mathbf{n}$. In case that τ^m is constant within the phases of the material, and applying Laplace inverse transform we arrive in Eqs. (2.7a) and (2.7b) again.

On behalf of the time domain t, let us apply the inverse Laplace transform to the field Eqs. (2.11a) and (2.11b), and due to the dependency on the variable s that $\mathbf{K}$ holds on Eq. (2.12), which gives

$$\mathcal{L}^{-1} \left\{ \mathbf{K}^m \nabla \hat{\theta} \right\} = \mathcal{L}^{-1} \left\{ \mathbf{K}^m \right\} * \nabla \theta, \tag{2.14}$$

the field equations (2.7a) and (2.7b), might be rewritten as an integral-differentiable form, therefore

$$\nabla \cdot (\mathbb{C}^m \nabla \mathbf{u} - \boldsymbol{\alpha}^m \theta) + \mathbf{b} = \rho^m \ddot{\mathbf{u}} \,, \tag{2.15a}$$

$$\nabla \cdot \left(\mathcal{L}^{-1} \left\{ \mathbf{K}^m \right\} * \nabla \theta - \boldsymbol{\alpha}^m \dot{\boldsymbol{u}} \right) + r = p^m \dot{\theta} \tag{2.15b}$$

known also as the field equations of a continuum with one time relaxation of first order.

We must point out here that, from the $\mathcal{Q}$-periodicity of microscopic constitutive tensors in Eqs. (2.5), (2.11a), (2.11b), and bearing in mind the $\mathcal{L}$-periodicity of the body forces, the micro-fields, displacement and temperature (either both Laplace transformed or not) are dependent on the fast variable $\boldsymbol{\xi}$ and the slow one $\mathbf{x}$, besides both fields may be written as $\hat{\boldsymbol{u}} = \hat{\boldsymbol{u}}\left(\mathbf{x}, \boldsymbol{\xi} = \frac{\mathbf{x}}{\epsilon}\right)$ and $\hat{\theta} = \hat{\theta}\left(\mathbf{x}, \boldsymbol{\xi} = \frac{\mathbf{x}}{\epsilon}\right)$. In addition, given the fact of the $\mathcal{Q}$-periodicity of their coefficients, any attempt in deriving the solution of the set of PDEs $(2.11a)$ and $(2.11b)$ might be rather cumbersome both analytically and numerically. Nevertheless, the homogenization technique arrives in this context to barter the microstructured continuum by an equivalent homogeneous one, where the solutions will be an approximation to those from $(2.11a)$ and $(2.11b)$, however on this scenario the coefficients will not be affected by the fast variable $\boldsymbol{\xi}$, which gives rapid oscillations led by the underlying microstructure previously held, and overall such procedure might be quite effective computationally.

Forward to the next Section, the homogenization technique on a bi-phase periodic microstructure composite subjected to thermal sources and periodic body forces will be applied over the equations of thermoelasticity with one time relaxation on the Laplace transformed domain, namely Eqs. $(2.11a)$ and $(2.11b)$.

2.2 Asymptotic expansions of microscopic field equations in the Laplace domain

The micro-displacement $\boldsymbol{u}$ and micro-temperature θ, inspired by the asymptotic approach developed in [32, 34, 35, 105], are expressed as power series in terms of ϵ, as well known as the asymptotic expansions in terms of ϵ that separates the fast variable $\boldsymbol{\xi} = \mathbf{x}/\epsilon$ from the slow one $\mathbf{x}$, i.e. in the hypothesis of scale separation, diving into the components, follows that

$$
\begin{aligned}
u_h\left(\mathbf{x}, \frac{\mathbf{x}}{\epsilon}, t\right) &= \sum_{l=0}^{+\infty} \epsilon^l u_h^{(l)} = u_h^{(0)}\left(\mathbf{x}, \frac{\mathbf{x}}{\epsilon}, t\right) + \epsilon u_h^{(1)}\left(\mathbf{x}, \frac{\mathbf{x}}{\epsilon}, t\right) \\
&+ \epsilon^2 u_h^{(2)}\left(\mathbf{x}, \frac{\mathbf{x}}{\epsilon}, t\right) + \mathcal{O}(\epsilon^3),
\end{aligned}
\tag{2.16a}
$$

$$\theta\left(\mathbf{x},\frac{\mathbf{x}}{\epsilon},t\right)=\sum_{l=0}^{+\infty}\epsilon^l\theta^{(l)}=\theta^{(0)}\left(\mathbf{x},\frac{\mathbf{x}}{\epsilon},t\right)+\epsilon\theta^{(1)}\left(\mathbf{x},\frac{\mathbf{x}}{\epsilon},t\right)$$
$$+\epsilon^2\theta^{(2)}\left(\mathbf{x},\frac{\mathbf{x}}{\epsilon},t\right)+\mathcal{O}(\epsilon^3). \tag{2.16b}$$

The Laplace transform (2.8) is applied to Eqs. (2.16a) and (2.16b), which leads to

$$\mathcal{L}\left(u_h\left(\mathbf{x},\frac{\mathbf{x}}{\epsilon},t\right)\right)=\sum_{l=0}^{+\infty}\epsilon^l\hat{u}_h^{(l)}=\hat{u}_h^{(0)}\left(\mathbf{x},\frac{\mathbf{x}}{\epsilon},s\right)+\epsilon\hat{u}_h^{(1)}\left(\mathbf{x},\frac{\mathbf{x}}{\epsilon},s\right)$$
$$+\epsilon^2\hat{u}_h^{(2)}\left(\mathbf{x},\frac{\mathbf{x}}{\epsilon},s\right)+\mathcal{O}(\epsilon^3), \tag{2.17a}$$

$$\mathcal{L}\left(\theta\left(\mathbf{x},\frac{\mathbf{x}}{\epsilon},t\right)\right)=\sum_{l=0}^{+\infty}\epsilon^l\hat{\theta}^{(l)}=\hat{\theta}^{(0)}\left(\mathbf{x},\frac{\mathbf{x}}{\epsilon},s\right)+\epsilon\hat{\theta}^{(1)}\left(\mathbf{x},\frac{\mathbf{x}}{\epsilon},s\right)$$
$$+\epsilon^2\hat{\theta}^{(2)}\left(\mathbf{x},\frac{\mathbf{x}}{\epsilon},s\right)+\mathcal{O}(\epsilon^3). \tag{2.17b}$$

It is noteworthy that both asymptotic expansions above are equivalent to the asymptotic expansions on the time domain t, (2.16a) and (2.16b).

Now, let us consider the formulas coming from the chain rule of differentiation

$$\frac{D}{Dx_k}\hat{\boldsymbol{u}}\left(\mathbf{x},\boldsymbol{\xi}=\frac{\mathbf{x}}{\epsilon}\right)=\left[\frac{\partial\hat{u}_h(\mathbf{x},\boldsymbol{\xi})}{\partial x_k}+\frac{\partial\hat{u}_h(\mathbf{x},\boldsymbol{\xi})}{\partial\xi_k}\frac{\partial\xi_k}{\partial x_k}\right]\Bigg|_{\boldsymbol{\xi}=\frac{\mathbf{x}}{\epsilon}}=$$
$$=\left[\frac{\partial}{\partial x_k}\hat{u}_h(\mathbf{x},\boldsymbol{\xi})+\frac{1}{\epsilon}\hat{u}_{h,k}\right]\Bigg|_{\boldsymbol{\xi}=\frac{\mathbf{x}}{\epsilon}}, \tag{2.18a}$$

$$\frac{D}{Dx_j}\hat{\theta}\left(\mathbf{x},\boldsymbol{\xi}=\frac{\mathbf{x}}{\epsilon}\right)=\left[\frac{\partial\hat{\theta}(\mathbf{x},\boldsymbol{\xi})}{\partial x_j}+\frac{\partial\hat{\theta}(\mathbf{x},\boldsymbol{\xi})}{\partial\xi_j}\frac{\partial\xi_j}{\partial x_j}\right]\Bigg|_{\boldsymbol{\xi}=\frac{\mathbf{x}}{\epsilon}}=$$
$$=\left[\frac{\partial}{\partial x_j}\hat{\theta}(\mathbf{x},\boldsymbol{\xi})+\frac{1}{\epsilon}\hat{\theta}_{,j}\right]\Bigg|_{\boldsymbol{\xi}=\frac{\mathbf{x}}{\epsilon}}, \tag{2.18b}$$

which introduces the macroscopic derivatives $\partial\hat{u}_h/\partial x_k$, $\partial\hat{\theta}/\partial x_j$, and the microscopic derivatives $\hat{u}_{h,k}$, $\hat{\theta}_{,j}$ on the transformed Laplace domain. Applying them to the asymptotic expansions (2.17a) and (2.17b), one leads to

$$\frac{D}{Dx_k}\hat{\boldsymbol{u}}\left(\mathbf{x},\boldsymbol{\xi}=\frac{\mathbf{x}}{\epsilon}\right)=\left[\left(\frac{\partial\hat{u}_h^{(0)}}{\partial x_k}+\epsilon\frac{\partial\hat{u}_h^{(1)}}{\partial x_k}+\epsilon^2\frac{\partial\hat{u}_h^{(2)}}{\partial x_k}+\cdots\right)+\right.$$
$$\left.+\frac{1}{\epsilon}\left(\hat{u}_{h,k}^{0}+\epsilon\hat{u}_{h,k}^{(1)}+\epsilon^2\hat{u}_{h,k}^{(2)}+\cdots\right)\right]\Big|_{\boldsymbol{\xi}=\frac{\mathbf{x}}{\epsilon}}, \tag{2.19a}$$

$$\frac{D}{Dx_j}\hat{\theta}\left(\mathbf{x},\boldsymbol{\xi}=\frac{\mathbf{x}}{\epsilon}\right)=\left[\left(\frac{\partial\hat{\theta}^{(0)}}{\partial x_j}+\epsilon\frac{\partial\hat{\theta}^{(1)}}{\partial x_j}+\epsilon^2\frac{\partial\hat{\theta}^{(2)}}{\partial x_j}+\cdots\right)+\right.$$
$$\left.+\frac{1}{\epsilon}\left(\hat{\theta}_{,j}^{0}+\epsilon\hat{\theta}_{,j}^{(1)}+\epsilon^2\hat{\theta}_{,j}^{(2)}+\cdots\right)\right]\Big|_{\boldsymbol{\xi}=\frac{\mathbf{x}}{\epsilon}}. \tag{2.19b}$$

The homogenization procedure of the Eqs. (2.11a) and (2.11b) searches for solutions of the micro-displacement $\hat{u}_h$ and micro-temperature $\hat{\theta}$, as decompositions of increasing powers of the microscopic length ϵ. In order to do so, the replacement of the asymptotic expansions (2.17a) and (2.17b) must be done into the microscopic field equations on the Laplace domain (2.11a) and (2.11b), respectively. Rearranging properly the terms with equal powers ϵ, and taking advantage of the derivative Eqs, (2.19a) and (2.19b), yield to the following asymptotic field equations

$$\left(\epsilon^{-2}\left(C_{ijhk}^m\hat{u}_{h,k}^{(0)}\right)_{,j}+\epsilon^{-1}\left[\left(C_{ijhk}^m\left(\frac{\partial\hat{u}_h^{(0)}}{\partial x_k}+\hat{u}_{h,k}^{(1)}\right)\right)_{,j}+\right.\right.$$
$$+\frac{\partial}{\partial x_j}\left(C_{ijhk}^m\hat{u}_{h,k}^{(0)}\right)-\left(\alpha_{ij}^m\hat{\theta}^{(0)}\right)_{,j}\Big]+\epsilon^0\left[\left(C_{ijhk}^m\left(\frac{\partial\hat{u}_h^{(1)}}{\partial x_k}+\hat{u}_{h,k}^{(2)}\right)\right)_{,j}+\right.$$
$$+\frac{\partial}{\partial x_j}\left(C_{ijhk}^m\left(\frac{\partial\hat{u}_h^{(0)}}{\partial x_k}+\hat{u}_{h,k}^{(1)}\right)\right)-\left(\alpha_{ij}^m\hat{\theta}^{(1)}\right)_{,j}+$$
$$-\frac{\partial}{\partial x_j}\left(\alpha_{ij}^m\hat{\theta}^{(0)}\right)+\hat{b}_i-\rho^m s^2u_h^{(0)}\Big]+\epsilon\left[\left(C_{ijhk}^m\left(\frac{\partial\hat{u}_h^{(2)}}{\partial x_k}+\hat{u}_{h,k}^{(3)}\right)\right)_{,j}+\right.$$
$$+\frac{\partial}{\partial x_j}\left(C_{ijhk}^m\left(\frac{\partial\hat{u}_h^{(1)}}{\partial x_k}+\hat{u}_{h,k}^{(2)}\right)\right)-\left(\alpha_{ij}^m\hat{\theta}^{(2)}\right)_{,j}-\frac{\partial}{\partial x_j}\left(\alpha_{ij}^m\hat{\theta}^{(1)}\right)-\rho^m s^2\hat{u}_h^{(1)}\Big]+$$
$$\left.\left.+\ \mathcal{O}(\epsilon^2)\right)\right|_{\boldsymbol{\xi}=\frac{\mathbf{x}}{\epsilon}}=0, \tag{2.20a}$$

$$
\begin{aligned}
&\left(\epsilon^{-2}\left(K_{ij}^{m}\hat{\theta}_{,j}^{(0)}\right)_{,i}+\epsilon^{-1}\left[\left(K_{ij}^{m}\left(\frac{\partial\hat{\theta}^{(0)}}{\partial x_j}+\hat{\theta}_{,j}^{(1)}\right)\right)_{,i}+\frac{\partial}{\partial x_i}\left(K_{ij}^{m}\hat{\theta}_{,j}^{(0)}\right)+\right.\right.\\
&-\left.\left(\alpha_{ij}^{m}s\hat{u}_{i,j}^{(0)}\right)\right]+\epsilon^{0}\left[\left(K_{ij}^{m}\left(\frac{\partial\hat{\theta}^{(1)}}{\partial x_j}+\hat{\theta}_{,j}^{(2)}\right)\right)_{,i}+\frac{\partial}{\partial x_i}\left(K_{ij}^{m}\left(\frac{\partial\hat{\theta}^{(0)}}{\partial x_j}+\hat{\theta}_{,j}^{(1)}\right)\right)+\right.\\
&\left.-\alpha_{ij}^{m}s\left(\frac{\partial\hat{u}_i^{(0)}}{\partial x_j}+\hat{u}_{i,j}^{(1)}\right)\hat{r}-p^{m}s\hat{\theta}^{(0)}\right]+\epsilon\left[\left(K_{ij}^{m}\left(\frac{\partial\hat{\theta}^{(2)}}{\partial x_j}+\hat{\theta}_{,j}^{(3)}\right)\right)_{,i}+\right.\\
&+\frac{\partial}{\partial x_i}\left(K_{ij}^{m}\left(\frac{\partial\hat{\theta}^{(1)}}{\partial x_j}+\hat{\theta}_{,j}^{(2)}\right)\right)-\alpha_{ij}^{m}s\left(\frac{\partial\hat{u}_i^{(1)}}{\partial x_j}+\hat{u}_{i,j}^{(2)}\right)-p^{m}s\hat{\theta}^{(1)}\Bigg]+\\
&+\left.\left.\mathcal{O}(\epsilon^{2})\right]\right)\Big|_{\boldsymbol{\xi}=\frac{\mathbf{x}}{\epsilon}}=0,
\end{aligned}
\tag{2.20b}
$$

where the Eq. (2.20a) is the homogenized micro-displacement field, and the Eq. (2.20b) is the homogenized micro-temperature field.

Recalling the interface conditions $(2.13a)-(2.13d)$, they may be rewritten in terms of the components, thus

$$
\left[\left[\hat{u}_h\right]\right]\Big|_{\mathbf{x}\in\Sigma}=0, \tag{2.21a}
$$

$$
\left[\left[\left(C_{ijhk}^{m}\frac{D\hat{u}_h}{Dx_k}-\alpha_{ij}^{m}\hat{\theta}\right)n_j\right]\right]\Big|_{\mathbf{x}\in\Sigma}=0, \tag{2.21b}
$$

$$
\left[\left[\hat{\theta}\right]\right]\Big|_{\mathbf{x}\in\Sigma}=0, \tag{2.21c}
$$

$$
\left[\left[-K_{ij}^{m}(s)\frac{D\hat{\theta}}{Dx_j}n_i\right]\right]\Big|_{\mathbf{x}\in\Sigma}=0. \tag{2.21d}
$$

Also, once the micro fields $\hat{\boldsymbol{u}}(\mathbf{x},\boldsymbol{\xi},s)$, and $\hat{\theta}(\mathbf{x},\boldsymbol{\xi},s)$ are supposed to be $\mathcal{Q}$-periodic regular functions of the variable $\mathbf{x}$, it is then possible to write the interface conditions $(2.21a)$ to $(2.21d)$ in terms of the fast variable $\boldsymbol{\xi}$. [34]. Therefore the asymptotic expansions $(2.16a)$ and $(2.16b)$, among the derivative formulae (2.19a) and (2.19b), and the interface conditions $(2.21a)$ and $(2.21b)$ are rewritten in terms of ϵ as

$$
\begin{aligned}
&\left[\left[\hat{u}_h^{(0)}\right]\right]\Big|_{\boldsymbol{\xi}\in\Sigma_1} + \epsilon\left[\left[\hat{u}_h^{(1)}\right]\right]\Big|_{\boldsymbol{\xi}\in\Sigma_1} + \epsilon^2\left[\left[\hat{u}_h^{(2)}\right]\right]\Big|_{\boldsymbol{\xi}\in\Sigma_1} + \mathcal{O}(\epsilon^3) = 0,\\
&\frac{1}{\epsilon}\left[\left[\left(C_{ijhk}^m\,\hat{u}_{h,k}^{(0)}\right)n_j\right]\right]\Big|_{\boldsymbol{\xi}\in\Sigma_1} +\\
&+\epsilon^0\left[\left[\left(C_{ijhk}^m\left(\frac{\partial\hat{u}_h^{(0)}}{\partial x_k}+\hat{u}_{h,k}^{(1)}\right)-\alpha_{ij}^m\,\hat{\theta}^{(0)}\right)n_j\right]\right]\Big|_{\boldsymbol{\xi}\in\Sigma_1} +\\
&+\epsilon\left[\left[\left(C_{ijhk}^m\left(\frac{\partial\hat{u}_h^{(1)}}{\partial x_k}+\hat{u}_{h,k}^{(2)}\right)-\alpha_{ij}^m\,\hat{\theta}^{(1)}\right)n_j\right]\right]\Big|_{\boldsymbol{\xi}\in\Sigma_1} +\\
&+\epsilon^2\left[\left[\left(C_{ijhk}^m\left(\frac{\partial\hat{u}_h^{(2)}}{\partial x_k}+\hat{u}_{h,k}^{(3)}\right)-\alpha_{ij}^m\,\hat{\theta}^{(2)}\right)n_j\right]\right]\Big|_{\boldsymbol{\xi}\in\Sigma_1} + \mathcal{O}(\epsilon^3) = 0,
\end{aligned}
\tag{2.22}
$$

and the interface conditions (2.21c) and (2.21d) become

$$
\begin{aligned}
&\left[\left[\hat{\theta}^{(0)}\right]\right]\Big|_{\boldsymbol{\xi}\in\Sigma_1} + \epsilon\left[\left[\hat{\theta}^{(1)}\right]\right]\Big|_{\boldsymbol{\xi}\in\Sigma_1} + \epsilon^2\left[\left[\hat{\theta}^{(2)}\right]\right]\Big|_{\boldsymbol{\xi}\in\Sigma_1} + \mathcal{O}(\epsilon^3) = 0,\\
&\frac{1}{\epsilon}\left[\left[\left(K_{ij}^m\,\hat{\theta}_{,j}^{(0)}\right)n_i\right]\right]\Big|_{\boldsymbol{\xi}\in\Sigma_1} + \epsilon^0\left[\left[\left(K_{ij}^m\left(\frac{\partial\hat{\theta}^{(0)}}{\partial x_j}+\hat{\theta}_{,j}^{(1)}\right)\right)n_i\right]\right]\Big|_{\boldsymbol{\xi}\in\Sigma_1} +\\
&+\epsilon\left[\left[\left(K_{ij}^m\left(\frac{\partial\hat{\theta}^{(1)}}{\partial x_j}+\hat{\theta}_{,j}^{(2)}\right)\right)n_i\right]\right]\Big|_{\boldsymbol{\xi}\in\Sigma_1} +\\
&+\epsilon^2\left[\left[\left(K_{ij}^m\left(\frac{\partial\hat{\theta}^{(2)}}{\partial x_j}+\hat{\theta}_{,j}^{(3)}\right)\right)n_i\right]\right]\Big|_{\boldsymbol{\xi}\in\Sigma_1} +\\
&+\mathcal{O}(\epsilon^3) = 0,
\end{aligned}
\tag{2.23}
$$

where Σ_1 denotes the interface between two different phases in the unit cell $\mathcal{Q}$.

In fact, the fields (2.20a) and (2.20b), as power series obtained from the homogenization asymptotic process, usually have the following structure,

$$
\frac{1}{\epsilon^2}f_i^{(0)}(\mathbf{x}) + \frac{1}{\epsilon}f_i^{(1)}(\mathbf{x}) + \epsilon^0 f_i^{(2)}(\mathbf{x}) + \epsilon f_i^{(3)}(\mathbf{x}) + \cdots + \epsilon^l f_i^{(l+2)}(\mathbf{x}) + \hat{b}_i(\mathbf{x}) = 0, \tag{2.24a}
$$

$$
\frac{1}{\epsilon^2}g^{(0)}(\mathbf{x}) + \frac{1}{\epsilon}g^{(1)}(\mathbf{x}) + \epsilon^0 g^{(2)}(\mathbf{x}) + \epsilon g^{(3)}(\mathbf{x}) + \cdots + \epsilon^l g^{(l+2)}(\mathbf{x}) + \hat{r}(\mathbf{x}) = 0, \tag{2.24b}
$$

where the set of functions $f_i^{(0)},\cdots,f_i^{(l+2)}$ and $g^{(0)},\cdots,g^{(l+2)}$, with $l\in\mathbb{N}$, are such that the dependency goes only over the slow variable $\mathbf{x}$, and are determined imposing the solvability conditions (seen in Sec. 2.3) on the class of the $\mathcal{Q}$-periodic functions.

2.3 Recursive differential problems and their solutions

The asymptotic field Eqs. (2.20a) and (2.20b) produce a cascade of recursive differential problems that determine sequentially the solutions of the displacements $\hat{\boldsymbol{u}}^{(0)}$, $\hat{\boldsymbol{u}}^{(1)}$,..., and also solutions of the temperature $\hat{\theta}^{(0)}$, $\hat{\theta}^{(1)}$..., respectively. For this matter, at the order ϵ^{-2}, the differential problems that arise from Eqs. (2.20a) and (2.20b) are, respectively,

$$\left(C^m_{ijhk}\hat{\boldsymbol{u}}^{(0)}_{h,k}\right)_{,j} = f^{(0)}_i(\mathbf{x}), \tag{2.25a}$$

$$\left(K^m_{ij}\hat{\theta}^{(0)}_{,j}\right)_{,i} = g^{(0)}(\mathbf{x}), \tag{2.25b}$$

with interface conditions

$$\left[\left[\hat{u}^{(0)}_h\right]\right]\Big|_{\boldsymbol{\xi}\in\Sigma_1} = 0, \tag{2.26a}$$

$$\left[\left[\left(C^m_{ijhk}\,\hat{u}^{(0)}_{h,k}\right)n_j\right]\right]\Big|_{\boldsymbol{\xi}\in\Sigma_1} = 0, \tag{2.26b}$$

$$\left[\left[\hat{\theta}^{(0)}\right]\right]\Big|_{\boldsymbol{\xi}\in\Sigma_1} = 0, \tag{2.26c}$$

$$\left[\left[\left(K^m_{ij}\hat{\theta}^{(0)}_{,j}\right)n_i\right]\right]\Big|_{\boldsymbol{\xi}\in\Sigma_1} = 0. \tag{2.26d}$$

As matter of fact, since we are searching for solutions in the class of $\mathcal{Q}$-periodic solutions $\hat{u}^{(0)}_h$ and $\hat{\theta}^{(0)}$, it can be checked [34, 35] that there exists a unique solution of the Eqs. (2.25a) and (2.25b), up to a constant, more specifically, since they are elliptic differential equations in the divergence forms, with vanishing mean values of the source terms over the unit cell $\mathcal{Q}$, implies the existence of a $\mathcal{Q}$-periodic regular solution. Such result gives rise to the also known as solvability condition for these differential problems, implying that the source terms are $f^{(0)}_i(\mathbf{x}) = 0$ and $g^{(0)}(\mathbf{x}) = 0$, therefore the differential problems (2.25a) and (2.25b), take the form

$$\left(C^m_{ijhk}\hat{u}^{(0)}_{h,k}\right)_{,j} = 0, \tag{2.27a}$$

$$\left(K^m_{ij}\hat{\theta}^{(0)}_{,j}\right)_{,i} = 0. \tag{2.27b}$$

Hence, the solution of the first term of the macroscopic displacement expansion field transformed is given by

$$\hat{u}_h^{(0)}(\mathbf{x},\boldsymbol{\xi},s) = \hat{U}_h^M(\mathbf{x},s), \tag{2.28}$$

and the solution for the first term of the macroscopic temperature expansion field is given by

$$\hat{\theta}^{(0)}(\mathbf{x},\boldsymbol{\xi},s) = \hat{\Theta}^M(\mathbf{x},s). \tag{2.29}$$

It is important to notice here that both solutions $\hat{U}_h^M(\mathbf{x},s)$ and $\hat{\Theta}^M(\mathbf{x},s)$ are no longer dependent on the fast variable.

Proceeding with the succeeding terms related to ϵ^{-1} in Eqs., (2.20a) and (2.20b), and using recursively the two solutions above obtained, it follows that

$$\left(C_{ijhk}^m \hat{u}_{h,k}^{(1)}\right)_{,j} + C_{ijhk,j}^m \frac{\partial \hat{U}_h^M}{\partial x_k} - \alpha_{ij,j}^m \hat{\Theta}^M = f_i^{(1)}(\mathbf{x}), \tag{2.30a}$$

$$\left(K_{ij}^m \hat{\theta}_{,j}^{(1)}\right)_{,i} + K_{ij,i}^m \frac{\partial \hat{\Theta}^M}{\partial x_j} = g^{(1)}(\mathbf{x}), \tag{2.30b}$$

since $\hat{U}_{h,k}^M = 0$ and $\hat{\Theta}_{,j}^M = 0$. The interface conditions are, respectively,

$$\left[\left[\hat{u}_h^{(1)}\right]\right]\Big|_{\boldsymbol{\xi}\in\Sigma_1} = 0, \tag{2.31a}$$

$$\left[\left[\left(C_{ijhk}^m \left(\frac{\partial \hat{U}_h^M}{\partial x_k} + \hat{u}_{h,k}^{(1)}\right) - \alpha_{ij}^m \hat{\Theta}^M\right) n_j\right]\right]\Big|_{\boldsymbol{\xi}\in\Sigma_1} = 0, \tag{2.31b}$$

$$\left[\left[\hat{\theta}^{(1)}\right]\right]\Big|_{\boldsymbol{\xi}\in\Sigma_1} = 0, \tag{2.31c}$$

$$\left[\left[\left(K_{ij}^m \left(\frac{\partial \hat{\Theta}^M}{\partial x_j} + \hat{\theta}_{,j}^{(1)}\right)\right) n_i\right]\right]\Big|_{\boldsymbol{\xi}\in\Sigma_1} = 0. \tag{2.31d}$$

Likewise, the solvability condition on the class of $\mathcal{Q}$-periodic functions guarantees that

$$f_i^{(1)}(\mathbf{x}) = \langle f_i^{(1)}(\mathbf{x})\rangle = \langle C_{ijhk,j}^m\rangle \frac{\partial \hat{U}_h^M}{\partial x_k} - \langle \alpha_{ij,j}^m\rangle \hat{\Theta}^M, \tag{2.32a}$$

$$g^{(1)}(\mathbf{x}) = \langle g^{(1)}(\mathbf{x})\rangle = \langle K_{ij,i}^m\rangle \frac{\partial \hat{\Theta}^M}{\partial x_j}, \tag{2.32b}$$

where $\langle(\cdot)\rangle = \frac{1}{|\mathcal{Q}|}\int_{\mathcal{Q}}(\cdot)d\boldsymbol{\xi}$ and $|\mathcal{Q}| = \delta\gamma$ gives the mean value over the unit cell $\mathcal{Q}$. Moreover, the $\mathcal{Q}$-periodicity of the components C^m_{ijhk}, α^m_{ij} and K^m_{ij}, along with the divergence theorem, entail both $f^{(1)}_i(\mathbf{x}) = 0$ and $g^{(1)}(\mathbf{x}) = 0$, thus the differential problems

$$\left(C^m_{ijhk}\hat{u}^{(1)}_{h,k}\right)_{,j} + C^m_{ijhk,j}\frac{\partial\hat{U}^M_h}{\partial x_k} - \alpha^m_{ij,j}\hat{\Theta}^M = 0, \quad \forall\frac{\partial\hat{U}^M_h}{\partial x_k}, \hat{\Theta}^M \tag{2.33a}$$

$$\left(K^m_{ij}\hat{\theta}^{(1)}_{,j}\right)_{,i} + K^m_{ij,i}\frac{\partial\hat{\Theta}^M}{\partial x_j} = 0, \quad \forall\frac{\partial\hat{\Theta}^M}{\partial x_j} \tag{2.33b}$$

have the following solutions, respectively

$$\hat{u}^{(1)}_h(\mathbf{x},\boldsymbol{\xi},s) = N^{(1,0)}_{hpq_1}(\boldsymbol{\xi})\frac{\partial\hat{U}^M_p}{\partial x_{q_1}} + \tilde{N}^{(1,0)}_h(\boldsymbol{\xi})\hat{\Theta}^M, \tag{2.34a}$$

$$\hat{\theta}^{(1)}(\mathbf{x},\boldsymbol{\xi},s) = M^{(1,0)}_{q_1}(\boldsymbol{\xi},s)\frac{\partial\hat{\Theta}^M}{\partial x_{q_1}}, \tag{2.34b}$$

where $N^{(1,0)}_{hpq_1}$, $\tilde{N}^{(1,0)}_h$ and $M^{(1,0)}_{q_1}$, are the perturbation functions, which each of them depends on the fast variable $\boldsymbol{\xi}$. On Sec. 2.3.1, in order to impose uniqueness of the homogenized solutions $\hat{u}_h$ and $\hat{\theta}$, the perturbation functions must be supposed to have zero mean value over the unit cell $\mathcal{Q}$ and so $N^{(1,0)}_{hpq_1}$, $\tilde{N}^{(1,0)}_h$ and $M^{(1,0)}_{q_1}$ comply with the normalization condition, which means that

$$\langle N^{(1,0)}_{hpq_1}\rangle = \frac{1}{|\mathcal{Q}|}\int_{\mathcal{Q}} N^{(1,0)}_{hpq_1}(\boldsymbol{\xi})d\boldsymbol{\xi} = 0, \tag{2.35a}$$

$$\langle \tilde{N}^{(1,0)}_h\rangle = \frac{1}{|\mathcal{Q}|}\int_{\mathcal{Q}} \tilde{N}^{(1,0)}_h(\boldsymbol{\xi})d\boldsymbol{\xi} = 0, \tag{2.35b}$$

$$\langle M^{(1,0)}_{q_1}\rangle = \frac{1}{|\mathcal{Q}|}\int_{\mathcal{Q}} M^{(1,0)}_{q_1}(\boldsymbol{\xi},s)d\boldsymbol{\xi} = 0. \tag{2.35c}$$

At order ϵ^0, the differential problems are

$$\left(C^m_{ijhk}\left(\frac{\partial \hat{u}^{(1)}_h}{\partial x_k}+\hat{u}^{(2)}_{h,k}\right)\right)_{,j}+\frac{\partial}{\partial x_j}\left(C^m_{ijhk}\left(\frac{\partial \hat{u}^{(0)}_h}{\partial x_k}+\hat{u}^{(1)}_{h,k}\right)\right)-\left(\alpha^m_{ij}\hat{\theta}^{(1)}\right)_{,j}+$$
$$-\frac{\partial}{\partial x_j}\left(\alpha^m_{ij}\hat{\theta}^{(0)}\right)-\rho^m s^2\hat{u}^{(0)}_i=f^{(2)}_i(\mathbf{x}), \tag{2.36a}$$

$$\left(K^m_{ij}\left(\frac{\partial \hat{\theta}^{(1)}}{\partial x_j}+\hat{\theta}^{(2)}_{,j}\right)\right)_{,i}+\frac{\partial}{\partial x_i}\left(K^m_{ij}\left(\frac{\partial \hat{\theta}^{(0)}}{\partial x_j}+\hat{\theta}^{(1)}_{,j}\right)\right)+$$
$$-\alpha^m_{ij}\left(\frac{\partial \hat{u}^{(0)}_i}{\partial x_j}+\hat{u}^{(1)}_{i,j}\right)-\rho^m s\hat{\theta}^{(0)}=g^{(2)}(\mathbf{x}). \tag{2.36b}$$

Considering the solutions (2.28), (2.34a) at order ϵ^{-2} and ϵ^{-1}, respectively, from the displacement expansion, and the solutions (2.29), (2.34b), at order ϵ^{-2} and ϵ^{-1}, respectively, from the temperature expansion, the differential problems (2.36a) and (2.36b) are turned into

$$\left(C^m_{ijhk}\hat{u}^{(2)}_{h,k}\right)_{,j}+\left(\left(C^m_{ijhk}N^{(1,0)}_{hpq_1}\right)_{,j}+C^m_{iq_1pk}+\left(C^m_{ikhj}N^{(1,0)}_{hpq_1,j}\right)\right)\frac{\partial^2\hat{U}^M_p}{\partial x_{q_1}\partial x_k}+$$
$$+\left(\left(C^m_{ijhk}\tilde{N}^{(1,0)}_h\right)_{,j}+C^m_{ikhj}\tilde{N}^{(1,0)}_{h,j}-\left(\alpha^m_{ij}M^{(1,0)}_k\right)_{,j}-\alpha^m_{ik}\right)\frac{\partial\hat{\Theta}^M}{\partial x_k}+ \tag{2.37a}$$
$$-\rho^m s^2\hat{U}^M_i=f^{(2)}_i(\mathbf{x}),$$

$$\left(K^m_{ij}\hat{\theta}^{(2)}_{,j}\right)_{,i}+\left(\left(K^m_{ij}M^{(1,0)}_{q_1}\right)_{,i}+K^m_{q_1j}+\left(K^m_{ji}M^{(1,0)}_{q_1,i}\right)\right)\frac{\partial^2\hat{\Theta}^M}{\partial x_{q_1}\partial x_j}+$$
$$-\left(\alpha^m_{ij}N^{(1,0)}_{ipq_1,j}+\alpha^m_{pq_1}\right)s\frac{\partial\hat{U}^M_p}{\partial x_{q_1}}-\left(\alpha^m_{ij}\tilde{N}^{(1,0)}_{i,j}+p^m\right)s\hat{\Theta}^M=g^{(2)}(\mathbf{x}), \tag{2.37b}$$

with interface conditions

$$
\begin{aligned}
&\left[\left[\hat{u}_h^{(2)}\right]\right]\Big|_{\boldsymbol{\xi}\in\Sigma_1} = 0,\\
&\left[\left[\left(C_{ijhk}^m\left(N_{hpq_1,j}^{(1,0)}\frac{\partial^2\hat{U}_p^M}{\partial x_{q_1}\partial x_k} + \tilde{N}_h^{(1,0)}\frac{\partial\hat{\Theta}^M}{\partial x_k} + \hat{u}_{h,k}^{(2)}\right)\right.\right.\right.\\
&\left.\left.\left. - \;\alpha_{ij}^m M_{q_1}^{(1,0)}\frac{\partial\hat{\Theta}^M}{\partial x_{q_1}}\right)n_j\right]\right]\Big|_{\boldsymbol{\xi}\in\Sigma_1} = 0,
\end{aligned}
\tag{2.38a}
$$

$$
\begin{aligned}
&\left[\left[\hat{\theta}^{(2)}\right]\right]\Big|_{\boldsymbol{\xi}\in\Sigma_1} = 0,\\
&\left[\left[\left(K_{ij}^m\left(M_{q_1}^{(1,0)}\frac{\partial^2\hat{\Theta}^M}{\partial x_{q_1}\partial x_j} + \hat{\theta}_{,j}^{(2)}\right)\right)n_i\right]\right]\Big|_{\boldsymbol{\xi}\in\Sigma_1} = 0.
\end{aligned}
\tag{2.38b}
$$

Simmetrizing the terms with the derivative of second order on the two differential problems (2.37a) and (2.37b), and once again, from the solvability condition of differential problem on the class of $\mathcal{Q}$-periodic functions and the divergence theorem lead to, respectively,

$$
\begin{aligned}
f_i^{(2)}(\mathbf{x}) =& \frac{1}{2}\left\langle C_{iq_1pk}^m + C_{ikhj}^m N_{hpq_1,j}^{(1,0)} + C_{ikpq_1}^m + C_{iq_1hj}^m N_{hpk,j}^{(1,0)}\right\rangle\frac{\partial^2\hat{U}_p^M}{\partial x_{q_1}\partial x_h} +\\
&+\left\langle C_{ikhj}^m\tilde{N}_{h,j}^{(1,0)} - \alpha_{ik}^m\right\rangle\frac{\partial\hat{\Theta}^M}{\partial x_k} - \left\langle\rho^m\right\rangle s^2\hat{U}_i^M,
\end{aligned}
\tag{2.39a}
$$

$$
\begin{aligned}
g^{(2)}(\mathbf{x}) =& \frac{1}{2}\left\langle K_{q_1j}^m + K_{ji}^m M_{q_1,i}^{(1,0)} + K_{jq_1}^m + K_{q_1i}^m M_{j,i}^{(1,0)}\right\rangle\frac{\partial^2\hat{\Theta}^M}{\partial x_{q_1}\partial x_j} -\\
&+\left\langle\alpha_{ij}^m N_{ipq_1,j}^{(1,0)} + \alpha_{pq_1}^m\right\rangle s\frac{\partial\hat{U}_p^M}{\partial x_{q1}} - \left\langle\alpha_{ij}^m\tilde{N}_{i,j}^{(1,0)} + p^m\right\rangle s\hat{\Theta}^M.
\end{aligned}
\tag{2.39b}
$$

Note that, even though the interface conditions (2.38a) and (2.38b) are simetrized as well, they are kept hidden on this regard.

Consequently, the solution for each $\hat{U}_p^M$, $\hat{\Theta}^M$ and their derivatives of the differential problems above, at the order ϵ^0, are

$$
\hat{u}_h^{(2)}(\mathbf{x},\boldsymbol{\xi},s) = N_{hpq_1q_2}^{(2,0)}(\boldsymbol{\xi})\frac{\partial^2\hat{U}_p^M}{\partial x_{q_1}\partial x_{q_2}} + \tilde{N}_{hq_1}^{(2,1)}(\boldsymbol{\xi})\frac{\partial\hat{\Theta}^M}{\partial x_{q_1}} + s^2 N_{hq_1}^{(2,2)}(\boldsymbol{\xi})\hat{U}_p^M, \tag{2.40a}
$$

$$
\hat{\theta}^{(2)}(\mathbf{x},\boldsymbol{\xi},s) = M_{q_1q_2}^{(2,0)}(\boldsymbol{\xi})\frac{\partial^2\hat{\Theta}^M}{\partial x_{q_1}\partial x_{q_2}} + s\tilde{M}_{pq_1}^{(2,1)}(\boldsymbol{\xi})\frac{\partial\hat{U}_p^M}{\partial x_{q_1}} + sM^{(2,1)}(\boldsymbol{\xi})\hat{\Theta}^M, \tag{2.40b}
$$

where $N^{(2,0)}_{hpq_1q_2}$, $\tilde{N}^{(2,1)}_{hq_1}$, $N^{(2,2)}_{hq_1}$, $M^{(2,0)}_{q_1q_2}$, $\tilde{M}^{(2,1)}_{pq_1}$ and $M^{(2,1)}$ are the perturbation functions depending on the parameters $\boldsymbol{\xi}$ and s.

2.3.1 Cell problems and perturbation functions

The solutions of Eqs. (2.11a) and (2.11b) provide that the inhomogeneous cell problems at the different orders of ϵ can be expanded in terms of the perturbation functions. In regards to them, such perturbation functions depend exclusively on the microstructure features such as, material geometry and mechanical properties, where the last one influences the displacements and temperature due to the heterogeneity of the material. Despite the existence of the homogenized solution $\mathcal{Q}$-periodic holds without any other assumption [33, 34, 174], it is noteworthy that imposing the normalization conditions (2.35a) – (2.35c) to the cell problems, sooner established on this section, the uniqueness of the perturbation functions is also held.

At this stage, the structure of these cell problems is exploited at the different orders of ϵ, for elasticity and thermal diffusion problems. For this purpose, the recursive differential problems of the elastic and thermal fields will be treated separately for each order of ϵ.

On behalf of the elastic problem at the order ϵ^{-1}, plugging the Eq. (2.34a) of the solution $u^{(1)}_k$, into the differential problem (2.30a), lead to two cell problems:

$$\left(C^m_{ijhk}\, N^{(1,0)}_{hpq_1,k}\right)_{,j} + C^m_{ijpq_1,j} = 0, \tag{2.41a}$$

$$\left(C^m_{ijhk}\tilde{N}^{(1,0)}_{h,k}\right)_{,j} - \alpha^m_{ij,j} = 0. \tag{2.41b}$$

Similarly, from Eq. (2.30b) and in consideration of the solution (2.34b), after substitution, the cell problem at the order ϵ^{-1} takes the form

$$\left(K^m_{ij} M^{(1,0)}_{q_1,j}\right)_{,i} + K^m_{iq_1,i} = 0. \tag{2.42}$$

Therefore, for the terms at the order ϵ^{-1}, we obtain the following set of cell problems

$$\left(C^m_{ijhk}\, N^{(1,0)}_{hpq_1,k}\right)_{,j} + C^m_{ijpq_1,j} = 0, \tag{2.43a}$$

$$\left(C^m_{ijhk}\tilde{N}^{(1,0)}_{h,k}\right)_{,j} - \alpha^m_{ij,j} = 0, \tag{2.43b}$$

$$\left(K^m_{ij} M^{(1,0)}_{q_1,j}\right)_{,i} + K^m_{iq_1,i} = 0, \tag{2.43c}$$

with interface conditions expressed in terms of perturbation functions $N^{(1,0)}_{hpq_1}$, $\tilde{N}^{(1,0)}_{h}$, $M^{(1,0)}_{q_1}$ as

$$\left[\left[N^{(1,0)}_{hpq_1}\right]\right]\Big|_{\boldsymbol{\xi}\in\Sigma_1} = 0, \tag{2.44a}$$

$$\left[\left[\left(C^m_{ijhk}\left(\delta_{hp}\,\delta_{kq_1} + N^{(1,0)}_{hpq_1,k}\right)\right)n_j\right]\right]\Big|_{\boldsymbol{\xi}\in\Sigma_1} = 0, \tag{2.44b}$$

$$\left[\left[\tilde{N}^{(1,0)}_{h}\right]\right]\Big|_{\boldsymbol{\xi}\in\Sigma_1} = 0, \tag{2.44c}$$

$$\left[\left[\left(C^m_{ijhk}\left(\tilde{N}^{(1,0)}_{h,k} - \alpha^m_{ij}\right)\right)n_j\right]\right]\Big|_{\boldsymbol{\xi}\in\Sigma_1} = 0, \tag{2.44d}$$

$$\left[\left[M^{(1,0)}_{q_1}\right]\right]\Big|_{\boldsymbol{\xi}\in\Sigma_1} = 0, \tag{2.44e}$$

$$\left[\left[\left(K^m_{ij}\left(M^{(1,0)}_{q_1,j} + \delta_{jq_1}\right)\right)n_i\right]\right]\Big|_{\boldsymbol{\xi}\in\Sigma_1} = 0, \tag{2.44f}$$

where the symmetries from the respective tensors are passed to the perturbation functions, for instance $N^{(1,0)}_{hpq_1} = N^{(1,0)}_{hq_1p}$, since $C^m_{ijpq_1,j} = C^m_{ijq_1p,j}$.

Once the perturbation functions $N^{(1,0)}_{hpq_1}$, $\tilde{N}^{(1,0)}_{h}$ and $M^{(1)}_{q_1}$ are determined, from the differential problem (2.36a) and recalling the solution $u^{(2)}_k$ in Eq. (2.40a), one derives the three following cell problems, at the order ϵ^0, and symmetrizing with respect to indices q_1 and q_2, leads to

$$\begin{aligned}&\left(C^m_{ijhk}\,N^{(2,0)}_{hpq_1q_2,k}\right)_{,j} + \frac{1}{2}\left[\left(C^m_{ijhq_2}\,N^{(1,0)}_{hpq_1}\right)_{,j} + C^m_{iq_1pq_2} + C^m_{iq_2hj}\,N^{(1,0)}_{hpq_1,j} + \right.\\ &\left. + \left(C^m_{ijhq_1}\,N^{(1,0)}_{hpq_2}\right)_{,j} + C^m_{iq_2pq_1} + C^m_{iq_1hj}\,N^{(1,0)}_{hpq_2,j}\right] = \frac{1}{2}\left\langle C^m_{iq_1pq_2} + C^m_{iq_2hj}\,N^{(1,0)}_{hpq_1,j} + \right.\\ &\left. + \quad C^m_{iq_2pq_1} + C^m_{iq_1hj}\,N^{(1,0)}_{hpq_2,j}\right\rangle,\end{aligned} \tag{2.45a}$$

$$\begin{aligned}&\left(C^m_{ijhk}\,\tilde{N}^{(2,1)}_{hq_1,k}\right)_{,j} + \left[\left(C^m_{ijhq_1}\,\tilde{N}^{(1,0)}_{h}\right)_{,j} + C^m_{iq_1hj}\,\tilde{N}^{(1,0)}_{h,j} - \left(\alpha^m_{ij}\,M^{(1,0)}_{q_1}\right)_{,j} - \right.\\ &\left. + \quad \alpha^m_{iq_1}\right] = \left\langle C^m_{iq_1hj}\,\tilde{N}^{(1,0)}_{h,j} - \alpha^m_{iq_1}\right\rangle\end{aligned} \tag{2.45b}$$

$$\left(C^m_{ijhk}\,N^{(2,2)}_{hp,k}\right)_{,j} - \rho^m\delta_{ip} = -\left\langle\rho^m\right\rangle\delta_{ip}, \tag{2.45c}$$

with interface conditions in terms of perturbation functions as

$$\left[\left[N^{(2,0)}_{hpq_1q_2}\right]\right]\Big|_{\boldsymbol{\xi}\in\Sigma_1} = 0, \tag{2.46a}$$

$$\left[\left[\left[C^m_{ijhk}N^{(2,0)}_{hpq_1q_2,k} + \frac{1}{2}\left(C^m_{ijhq_2}N^{(1,0)}_{hpq_1} + C^m_{ijhq_1}N^{(1,0)}_{hpq_2}\right)\right]n_j\right]\right]\Big|_{\boldsymbol{\xi}\in\Sigma_1} = 0, \tag{2.46b}$$

$$\left[\left[\tilde{N}^{(2,1)}_{hq_1}\right]\right]\Big|_{\boldsymbol{\xi}\in\Sigma_1} = 0, \tag{2.46c}$$

$$\left[\left[\left(C^m_{ijhk}\tilde{N}^{(2,1)}_{hq_1,k} + \left(C^m_{ijhq_2}\,\tilde{N}^{(1,0)}_{h}\delta_{kq_1} - \alpha^m_{ij}M^{(1,0)}_{q_1}\right)\right)n_j\right]\right]\Big|_{\boldsymbol{\xi}\in\Sigma_1} = 0, \tag{2.46d}$$

$$\left[\left[N^{(2,2)}_{hp}\right]\right]\Big|_{\boldsymbol{\xi}\in\Sigma_1} = 0, \tag{2.46e}$$

$$\left[\left[\left(C^m_{ijhk}N^{(2,2)}_{hp,k}\right)n_j\right]\right]\Big|_{\boldsymbol{\xi}\in\Sigma_1} = 0. \tag{2.46f}$$

Analogously, for the thermal homogenized field at the order ϵ^0, replacing solution (2.40*b*) into the differential problem (2.36*b*), one gives the next three cell problems

$$\left(K^m_{ij}\,M^{(2,0)}_{q_1q_2,j}\right)_{,i} + \frac{1}{2}\left[\left(K^m_{iq_2}\,M^{(1,0)}_{q_1}\right)_{,i} + K^m_{q_1q_2} + K^m_{iq_2}\,M^{(1,0)}_{q_1,i} + \left(K^m_{iq_1}\,M^{(1,0)}_{q_2}\right)_{,i} + \right.$$
$$\left. + K^m_{q_2q_1} + K^m_{q_1i}\,M^{(1,0)}_{q_2,i}\right] = \frac{1}{2}\left\langle K^m_{q_1q_2} + K^m_{q_2i}\,M^{(1,0)}_{q_1,i} + K^m_{q_2q_1} + K^m_{q_1i}\,M^{(1,0)}_{q_2,i}\right\rangle, \tag{2.47a}$$

$$\left(K^m_{ij}\,\tilde{M}^{(2,1)}_{pq_1,j}\right)_{,i} - \left[\alpha^m_{ij}\,N^{(1,0)}_{ipq_1,j} + \alpha^m_{pq_1}\right] = -\left\langle \alpha^m_{ij}\,N^{(1,0)}_{ipq_1,j} + \alpha^m_{pq_1}\right\rangle, \tag{2.47b}$$

$$\left(K^m_{ij}\,M^{(2,1)}_{,j}\right)_{,i} - \left[\alpha^m_{ij}\,\tilde{N}^{(1,0)}_{i,j} + p^m\right] = -\left\langle \alpha^m_{ij}\,\tilde{N}^{(1,0)}_{i,j} + p^m\right\rangle, \tag{2.47c}$$

and, in terms of perturbation functions, the interface conditions become

$$\left[\left[M^{(2,0)}_{q_1q_2}\right]\right]\Big|_{\boldsymbol{\xi}\in\Sigma_1} = 0, \tag{2.48a}$$

$$\left[\left[\left[K^m_{ij}M^{(2,0)}_{q_1q_2,j} + \frac{1}{2}\left(K^m_{iq_2}\,M^{(1,0)}_{q_1} + K^m_{iq_1}\,M^{(1,0)}_{q_2}\right)\right]n_i\right]\right]\Big|_{\boldsymbol{\xi}\in\Sigma_1} = 0. \tag{2.48b}$$

$$\left[\left[\tilde{M}^{(2,1)}_{pq_1}\right]\right]\Big|_{\boldsymbol{\xi}\in\Sigma_1} = 0, \tag{2.48c}$$

$$\left[\left[\left(K^m_{ij}(s)\tilde{M}^{(2,1)}_{pq_1,j}\right)n_i\right]\right]\Big|_{\boldsymbol{\xi}\in\Sigma_1} = 0. \tag{2.48d}$$

$$\left[\left[M^{(2,1)}\right]\right]\Big|_{\boldsymbol{\xi}\in\Sigma_1} = 0, \tag{2.48e}$$

$$\left[\left[\left(K^m_{ij}(s)M^{(2,1)}_{,j}\right)n_i\right]\right]\Big|_{\boldsymbol{\xi}\in\Sigma_1} = 0. \tag{2.48f}$$

2.3.2 Down-scaling and up-scaling relations

On one hand, the feasibility of expressing the microscopic fields $\hat{u}_h(\mathbf{x},\boldsymbol{\xi},s)$ and $\hat{\theta}(\mathbf{x},\boldsymbol{\xi},s)$ as asymptotic expansions of powers of the microscopic length ϵ in terms of the macroscopic fields $\hat{U}_h^M(\mathbf{x},s)$, $\hat{\Theta}^M(\mathbf{x},s)$, their gradients and in terms of the $\mathcal{Q}$-periodic perturbation functions arises from the solution of the cell problems at different orders of ϵ developed in Sec. 2.3.1. From the expansions (2.16*b*) and (2.16*a*), and considering the solutions in (2.28), (2.29), (2.34a), (2.34b), (2.40a) and (2.40b) of cell problems at the different orders of ϵ, one derives the down-scaling relations of the transformed micro-displacement field and the transformed micro-temperature field, respectively,

$$\begin{aligned}\hat{u}_h\left(\mathbf{x},\frac{\mathbf{x}}{\epsilon},s\right) = \Bigg[&\hat{U}_h^M(\mathbf{x},s) + \epsilon\left(N_{hpq_1}^{(1,0)}(\boldsymbol{\xi})\frac{\partial\hat{U}_h^M}{\partial x_{q_1}} + \tilde{N}_h^{(1,0)}(\boldsymbol{\xi})\hat{\Theta}^M\right) + \\ &+\epsilon^2\left(N_{hpq_1q_2}^{(2,0)}(\boldsymbol{\xi})\frac{\partial^2\hat{U}_h^M}{\partial x_{q1}\partial x_{q2}} + \tilde{N}_{hq_1}^{(2,1)}(\boldsymbol{\xi})\frac{\partial\hat{\Theta}^M}{\partial x_{q_1}} + s^2N_{hp}^{(2,2)}(\boldsymbol{\xi})\hat{U}_h^M\right) + \\ &+\ \mathcal{O}(\epsilon^3)\Big]\Big|_{\boldsymbol{\xi}=\frac{\mathbf{x}}{\epsilon}},\end{aligned} \tag{2.49a}$$

$$\begin{aligned}\hat{\theta}\left(\mathbf{x},\frac{\mathbf{x}}{\epsilon},s\right) = \Bigg[&\hat{\Theta}^M(\mathbf{x},s) + \epsilon\left(M_{q_1}^{(1,0)}(\boldsymbol{\xi})\frac{\partial\hat{\Theta}^M}{\partial x_{q_1}}\right) + \\ &+\epsilon^2\left(M_{pq_1q_2}^{(2,0)}(\boldsymbol{\xi})\frac{\partial^2\hat{\Theta}^M}{\partial x_{q1}\partial x_{q2}} + s\tilde{M}_{pq_1}^{(2,1)}(\boldsymbol{\xi})\frac{\partial\hat{\Theta}^M}{\partial x_{q_1}} + s^2M_{hp}^{(2,1)}(\boldsymbol{\xi})\hat{\Theta}^M\right) + \\ &+\ \mathcal{O}(\epsilon^3)\Big]\Big|_{\boldsymbol{\xi}=\frac{\mathbf{x}}{\epsilon}}.\end{aligned} \tag{2.49b}$$

Noteworthy, the $\mathcal{Q}$-periodic perturbation functions $N_{hpq_1}^{(1,0)}, \tilde{N}_h^{(1,0)}, N_{hpq_1q_2}^{(2,0)}, \tilde{N}_{hq_1}^{(2,0)}$, $N_{hp}^{(2,2)}$, $M_{q_1}^{(1,0)}$, $M_{q_1q_2}^{(2,0)}$, $\tilde{M}_{pq_1}^{(2,1)}$, $M^{(2,1)}$, cast the effect of microstructural inhomogeneities of the material through their dependency on the fast variable $\boldsymbol{\xi} = \mathbf{x}/\epsilon$, whereas the macro-fields $\hat{\boldsymbol{u}}(\mathbf{x},s)$, and $\hat{\theta}(\mathbf{x},s)$ are $\mathfrak{L}$-periodic functions and therefore rely only on the slow variable $\mathbf{x}$ [130].

On the other hand, also known as the up-scaling relations, they allow the definition of the macroscopic fields in terms of the microscopic ones. This means that the macroscopic fields may be defined as the mean values of microscopic Eqs. (2.49*a*) and (2.49*b*) over the unit cell $\mathcal{Q}$, thus it follows that

$$\hat{U}_h(\mathbf{x},s) \doteq \left\langle \hat{u}_h\left(\mathbf{x},\frac{\mathbf{x}}{\epsilon}+\boldsymbol{\zeta},s\right)\right\rangle = \frac{1}{|\mathcal{Q}|}\int_{\mathcal{Q}} \hat{u}_h\left(\mathbf{x},\frac{\mathbf{x}}{\epsilon}+\boldsymbol{\zeta},s\right)d\boldsymbol{\zeta} = \\ = \frac{1}{|\mathcal{Q}|}\int_{\mathcal{Q}} u_h\left(\mathbf{x},\boldsymbol{\xi},s\right)d\boldsymbol{\xi} = \left\langle \hat{u}_h\left(\mathbf{x},\boldsymbol{\xi},s\right)\right\rangle, \tag{2.50a}$$

$$\hat{\Theta}(\mathbf{x},s) \doteq \left\langle \hat{\theta}\left(\mathbf{x},\frac{\mathbf{x}}{\epsilon}+\boldsymbol{\zeta},s\right)\right\rangle = \frac{1}{|\mathcal{Q}|}\int_{\mathcal{Q}} \hat{\theta}\left(\mathbf{x},\frac{\mathbf{x}}{\epsilon}+\boldsymbol{\zeta},s\right)d\boldsymbol{\zeta} = \\ = \frac{1}{|\mathcal{Q}|}\int_{\mathcal{Q}} \hat{\theta}\left(\mathbf{x},\boldsymbol{\xi},s\right)d\boldsymbol{\xi} = \left\langle \hat{\theta}\left(\mathbf{x},\boldsymbol{\xi},s\right)\right\rangle, \tag{2.50b}$$

where the variable $\boldsymbol{\zeta} \in \mathcal{Q}$ has been introduced and the vector $\epsilon\boldsymbol{\zeta} \in \mathcal{A}$ defines all the possible translations of the heterogeneous medium compared to a grid of cells having characteristic size ϵ, with respect to the $\mathfrak{L}$-periodic body force $\hat{\mathbf{b}}(\mathbf{x})$ [35, 171]. Besides, the mean value operator of the left hand side is taken over the variable $\boldsymbol{\zeta}$, whereas the mean value operator of the right hand side has become over $\boldsymbol{\xi}$.

2.4 Average field equation of infinite order

Recalling the structure of the field Eqs. (2.24*a*) and (2.24*b*) and substituting each $f_i^{(l)}(\mathbf{x})$ and $g^{(l)}(\mathbf{x})$, obtained from each relative recursive differential problem into them, one derives the average field equations of infinite order

$$n^{(2,0)}_{ipq_1q_2}\frac{\partial^2 \hat{U}_h^M}{\partial x_{q_1}\partial x_{q_2}} + \tilde{n}^{(2,0)}_{iq_1}\frac{\partial \hat{\Theta}^M}{\partial x_{q_1}} - n^{(2,2)}_{ip}s^2\hat{U}_h^M + \mathcal{O}(\epsilon) + \hat{b}_i = 0, \tag{2.51a}$$

$$w^{(2,0)}_{q_1q_2}\frac{\partial^2 \hat{\Theta}^M}{\partial x_{q_1}\partial x_{q_2}} - \tilde{w}^{(2,1)}_{pq_1}s\frac{\partial \hat{U}_h^M}{\partial x_{q_1}} - w^{(2,1)}s\hat{\Theta}^M + \mathcal{O}(\epsilon) + \hat{r} = 0, \tag{2.51b}$$

where the constant global constitutive tensors factors are

$$n^{(2,0)}_{ipq_1q_2} = \frac{1}{2}\left\langle C^m_{iq_1pq_2} + C^m_{iq_2hj}N^{(1,0)}_{hpq_1,j} + C^m_{iq_2pq_1} + C^m_{iq_1hj}N^{(1,0)}_{hpq_2,j}\right\rangle, \tag{2.52a}$$

$$\tilde{n}^{(2,0)}_{iq_1} = \left\langle C^m_{iq_1hj}\tilde{N}^{(1,0)}_{h,j} - \alpha^m_{iq_1}\right\rangle, \tag{2.52b}$$

$$n^{(2,2)}_{ip} = \langle \rho^m \rangle \, \delta_{ip}, \tag{2.52c}$$

$$w^{(2,0)}_{q_1q_2} = \frac{1}{2}\left\langle K^m_{q_1q_2} + K^m_{q_2i}M^{(1,0)}_{q_1,i} + K^m_{q_2q_1} + K^m_{q_1i}M^{(1,0)}_{q_2,i}\right\rangle, \tag{2.52d}$$

$$\tilde{w}^{(2,1)}_{pq_1} = \left\langle \alpha^m_{ij}N^{(1,0)}_{ipq_1,j} + \alpha^m_{pq_1}\right\rangle, \tag{2.52e}$$

$$w^{(2,1)} = \left\langle \alpha^m_{ij}\tilde{N}^{(1,0)}_{i,j} - p^m_{iq_1}\right\rangle. \tag{2.52f}$$

In the interest of deriving explicit solutions of the Eqs. (2.51a) and (2.51b), the macroscopic variables $\hat{U}^M_h$ and $\hat{\Theta}^M$ are asymptotically expanded as follows

$$\hat{U}^M_h(\mathbf{x}, s) = \sum_{j=0}^{+\infty} \epsilon^j \hat{U}^{(j)}_h(\mathbf{x}, s), \tag{2.53a}$$

$$\hat{\Theta}^M(\mathbf{x}, s) = \sum_{j=0}^{+\infty} \epsilon^j \hat{\Theta}^{(j)}(\mathbf{x}, s). \tag{2.53b}$$

By plugging the solutions (2.53a) and (2.53b), into the Eqs. (2.51a) and (2.51b), the asymptotic expansions of the average field equations of infinite order become

$$\begin{aligned} &n^{(2,0)}_{ipq_1q_2}\left(\frac{\partial^2\hat{U}^{(0)}_h}{\partial x_{q_1}\partial x_{q_2}} + \epsilon\frac{\partial^2\hat{U}^{(1)}_h}{\partial x_{q_1}\partial x_{q_2}} + \epsilon^2\frac{\partial^2\hat{U}^{(2)}_h}{\partial x_{q_1}\partial x_{q_2}} + \cdots\right) + \\ &\tilde{n}^{(2,0)}_{iq_1}\left(\frac{\partial\hat{\Theta}^{(0)}}{\partial x_{q_1}} + \epsilon\frac{\partial\hat{\Theta}^{(1)}}{\partial x_{q_1}} + \epsilon^2\frac{\partial\hat{\Theta}^{(2)}}{\partial x_{q_1}} + \cdots\right) + \\ &- n^{(2,2)}_{ip}s^2\left(\hat{U}^{(0)}_h + \epsilon\hat{U}^{(1)}_h + \epsilon^2\hat{U}^{(2)}_h\right) + \cdots + \hat{b}_i = 0, \end{aligned} \tag{2.54a}$$

$$\begin{aligned} &w^{(2,0)}_{q_1q_2}\left(\frac{\partial^2\hat{\Theta}^{(0)}}{\partial x_{q_1}\partial x_{q_2}} + \epsilon\frac{\partial^2\hat{\Theta}^{(1)}}{\partial x_{q_1}\partial x_{q_2}} + \epsilon^2\frac{\partial^2\hat{\Theta}^{(2)}}{\partial x_{q_1}\partial x_{q_2}} + \cdots\right) - \\ &+ \tilde{w}^{(2,1)}_{pq_1}s\left(\frac{\partial\hat{U}^{(0)}_h}{\partial x_{q_1}} + \epsilon\frac{\partial\hat{U}^{(1)}_h}{\partial x_{q_1}} + \epsilon^2\frac{\partial\hat{U}^{(2)}_h}{\partial x_{q_1}} + \cdots\right) + \\ &- w^{(2,1)}s\left(\hat{\Theta}^{(0)} + \epsilon\hat{\Theta}^{(1)} + \epsilon^2\hat{\Theta}^{(2)}\right) + \cdots + \hat{r} = 0. \end{aligned} \tag{2.54b}$$

Rearranging the terms at the same order of ϵ in (2.54a) and (2.54b), an infinite set of macroscopic hierarchical differential problems expressed in terms of the sensitivities $\hat{U}_h^{(j)}$ and $\hat{\Theta}^{(j)}$ of both macroscopic displacement $\hat{U}_h^M$ and macroscopic temperature $\hat{\Theta}^M$ fields can be determined. Thus,

$$\begin{aligned}
&\epsilon^0 \left(n^{(2,0)}_{ipq_1q_2} \frac{\partial^2 \hat{U}_h^{(0)}}{\partial x_{q_1} \partial x_{q_2}} + \tilde{n}^{(2,0)}_{iq_1} \frac{\partial \hat{\Theta}^{(0)}}{\partial x_{q_1}} - n^{(2,2)}_{ip} s^2 \hat{U}_h^{(0)} + \hat{b}_i \right) + \\
&+ \epsilon \left(n^{(2,0)}_{ipq_1q_2} \frac{\partial^2 \hat{U}_h^{(1)}}{\partial x_{q_1} \partial x_{q_2}} + \tilde{n}^{(2,0)}_{iq_1} \frac{\partial \hat{\Theta}^{(1)}}{\partial x_{q_1}} - n^{(2,2)}_{ip} s^2 \hat{U}_h^{(1)} + s_i^{(1)}(\mathbf{x}, s) \right) + \\
&+ \epsilon^2 \left(n^{(2,0)}_{ipq_1q_2} \frac{\partial^2 \hat{U}_h^{(2)}}{\partial x_{q_1} \partial x_{q_2}} + \tilde{n}^{(2,0)}_{iq_1} \frac{\partial \hat{\Theta}^{(2)}}{\partial x_{q_1}} - n^{(2,2)}_{ip} s^2 \hat{U}_h^{(2)} + s_i^{(2)}(\mathbf{x}, s) \right) + \mathcal{O}(\epsilon^3) = 0,
\end{aligned} \tag{2.55a}$$

$$\begin{aligned}
&\epsilon^0 \left(w^{(2,0)}_{q_1q_2} \frac{\partial^2 \hat{\Theta}^{(0)}}{\partial x_{q_1} \partial x_{q_2}} - \tilde{w}^{(2,1)}_{pq_1} s \frac{\partial \hat{U}_h^{(0)}}{\partial x_{q_1}} - w^{(2,1)} s \hat{\Theta}^{(0)} + \hat{r} \right) + \\
&+ \epsilon \left(w^{(2,0)}_{q_1q_2} \frac{\partial^2 \hat{\Theta}^{(1)}}{\partial x_{q_1} \partial x_{q_2}} - \tilde{w}^{(2,1)}_{pq_1} s \frac{\partial \hat{U}_h^{(1)}}{\partial x_{q_1}} - w^{(2,1)} s \hat{\Theta}^{(1)} + \upsilon^{(1)}(\mathbf{x}, s) \right) + \\
&+ \epsilon^2 \left(w^{(2,0)}_{q_1q_2} \frac{\partial^2 \hat{\Theta}^{(2)}}{\partial x_{q_1} \partial x_{q_2}} - \tilde{w}^{(2,1)}_{pq_1} s \frac{\partial \hat{U}_h^{(2)}}{\partial x_{q_1}} - w^{(2,1)} s \hat{\Theta}^{(2)} + \upsilon^{(2)}(\mathbf{x}, s) \right) + \mathcal{O}(\epsilon^3) = 0,
\end{aligned} \tag{2.55b}$$

Therefore, the recursive problem at the macroscopic scale at order ϵ^0 reads

$$n^{(2,0)}_{ipq_1q_2} \frac{\partial^2 \hat{U}_h^{(0)}}{\partial x_{q_1} \partial x_{q_2}} + \tilde{n}^{(2,0)}_{iq_1} \frac{\partial \hat{\Theta}^{(0)}}{\partial x_{q_1}} - n^{(2,2)}_{ip} s^2 \hat{U}_h^{(0)} + \hat{b}_i = 0, \tag{2.56a}$$

$$w^{(2,0)}_{q_1q_2} \frac{\partial^2 \hat{\Theta}^{(0)}}{\partial x_{q_1} \partial x_{q_2}} - \tilde{w}^{(2,1)}_{pq_2} s \frac{\partial \hat{U}_h^{(0)}}{\partial x_{q_1}} - w^{(2,1)} s \hat{\Theta}^{(0)} + \hat{r} = 0, \tag{2.56b}$$

while the generic recursive problem at the macroscopic scale of order ϵ^r with $l \in \mathbb{Z}$, $l \geq 1$ is found as

$$n^{(2,0)}_{ipq_1q_2} \frac{\partial^2 \hat{U}_h^{(l)}}{\partial x_{q_1} \partial x_{q_2}} + \tilde{n}^{(2,0)}_{iq_1} \frac{\partial \hat{\Theta}^{(l)}}{\partial x_{q_1}} - n^{(2,2)}_{ip} s^2 \hat{U}_h^{(l)} + s_i^{(l)}(\mathbf{x}, s) = 0, \tag{2.57a}$$

$$w^{(2,0)}_{q_1q_2} \frac{\partial^2 \hat{\Theta}^{(l)}}{\partial x_{q_1} \partial x_{q_2}} - \tilde{w}^{(2,1)}_{pq_2} s \frac{\partial \hat{U}_h^{(l)}}{\partial x_{q_1}} - w^{(2,1)} s \hat{\Theta}^{(l)} - \upsilon^{(l)}(\mathbf{x}, s) = 0, \tag{2.57b}$$

where the functions $s_i^{(l)}(\mathbf{x}, s)$ and $\upsilon^{(l)}(\mathbf{x}, s)$ are the source terms $\mathcal{Q}$-periodic fields, which depend both on the higher order constant tensors that appear in the terms at orders equal or higher than ϵ^m of the Eqs. (2.51a) and (2.51b), and on the sensitivities $\hat{U}_h^{(j)}$ and $\hat{\Theta}^{(j)}$ from macroscopic hierarchical differential problems of an order lower than ϵ^m.

2.5 Approximation of the power-like functional via truncation of its asymptotic expansion

A variational-asymptotic procedure [35, 105] is exploited to furnish a finite order governing equation to establish an equivalence among the Eqs. (2.11a) and (2.11b) at the macro-scale. For this matter, on the periodic domain $\mathfrak{L}$, let the power-like functional Λ be expressed in terms of the energy-like density λ_m at the micro-scale

$$\begin{aligned}\Lambda(\boldsymbol{u},\theta) &= \frac{\partial}{\partial t}\int_{\mathfrak{L}} \lambda_m\left(\mathbf{x},\frac{\mathbf{x}}{\epsilon}\right) d\mathbf{x} = \\ &= \frac{\partial}{\partial t}\int_{\mathfrak{L}} \left(\frac{1}{2}\rho^m \dot{\boldsymbol{u}} * \dot{\boldsymbol{u}} + \frac{1}{2}\nabla\boldsymbol{u} * (\boldsymbol{\mathfrak{C}}^m \nabla\boldsymbol{u}) - \frac{1}{2}\nabla\boldsymbol{u} * (\boldsymbol{\alpha}^m\theta) - \boldsymbol{u} * \boldsymbol{b}\right) d\mathbf{x} \quad + \\ &- \int_{\mathfrak{L}} \left(\frac{1}{2}\nabla\theta * \left(\mathcal{L}^{-1}\left\{\mathbf{K}^m\right\} * \nabla\theta\right) + \frac{1}{2}\theta * (\boldsymbol{\alpha}^m \nabla\dot{\boldsymbol{u}}) + \frac{1}{2}\theta * (p^m\dot{\theta}) - \theta * r\right) d\mathbf{x}\,.\end{aligned} \tag{2.58}$$

Now, applying the Laplace transform on $\mathcal{L}(\Lambda)$, the functional above is taken to the Laplace domain and expressed in terms of the power-like density $\hat{\lambda}_m$ as follows

$$\begin{aligned}\mathcal{L}\{\Lambda\} = \hat{\Lambda}(\hat{\boldsymbol{u}},\hat{\theta}) &= \int_{\mathfrak{L}} \hat{\lambda}_m\left(\mathbf{x},\frac{\mathbf{x}}{\epsilon}\right) d\mathbf{x} = \\ &= \int_{\mathfrak{L}} s\left(\frac{1}{2}\rho^m s^2 \hat{\boldsymbol{u}}\cdot\hat{\boldsymbol{u}} + \frac{1}{2}\nabla\hat{\boldsymbol{u}} : (\boldsymbol{\mathfrak{C}}^m\nabla\hat{\boldsymbol{u}}) - \frac{1}{2}\nabla\hat{\boldsymbol{u}} : (\boldsymbol{\alpha}^m\hat{\theta}) - \hat{\boldsymbol{u}}\cdot\hat{\boldsymbol{b}}\right) d\mathbf{x} \quad + \\ &- \int_{\mathfrak{L}} \left(\frac{1}{2}\nabla\hat{\theta}\cdot\left(\mathbf{K}^m\nabla\hat{\theta}\right) + \frac{1}{2}s\hat{\theta}\,(\boldsymbol{\alpha}^m : \nabla\hat{\boldsymbol{u}}) + \frac{1}{2}s\hat{\theta}(p^m\hat{\theta}) - \hat{\theta}\hat{r}\right) d\mathbf{x}\,,\end{aligned} \tag{2.59}$$

where the symbol : indicates the tensor double inner product. Note that the Euler-Lagrange equation from the functional (2.59) agrees with the demonstration presented in the Appendix A which leads to the field equations at the micro-scale (2.11a) and (2.11b).

As it was introduced at the Eqs. (2.50a) and (2.50b), the transformed power-like functional $\hat{\Lambda}$ and its corresponding power-like density $\hat{\lambda}_m$ are dependent by the translation parameter $\boldsymbol{\zeta} \in \mathcal{Q}$. Which means, the perturbation functions $N^{(1,0)}_{hpq_1}$, $\tilde{N}^{(1,0)}_{h}, N^{(2,0)}_{hpq_1q_2}$, $\tilde{N}^{(2,0)}_{hq_1}, N^{(2,2)}_{hp}$, $M^{(1,0)}_{q_1}$, $M^{(2,0)}_{q_1q_2}$, $\tilde{M}^{(2,1)}_{pq_1}$, $M^{(2,1)}$, determined from the cell problems in Sec. 2.3.1, also depend on the translation variable $\boldsymbol{\zeta}$. Besides, the power-like density $\hat{\lambda}_m$ in the Laplace domain complies with the property

$$\hat{\lambda}^{\zeta}_m\left(\mathbf{x}, \frac{\mathbf{x}}{\epsilon}\right) = \hat{\lambda}_m\left(\mathbf{x}, \frac{\mathbf{x}}{\epsilon} + \boldsymbol{\zeta}\right), \tag{2.60}$$

implying that the Laplace transformed of the power-like functional $\hat{\Lambda}$, depends on the parameter $\boldsymbol{\zeta}$, one has

$$\hat{\Lambda}^{\zeta} = \hat{\Lambda}(\boldsymbol{\zeta}) = \int_{\mathfrak{L}} \hat{\lambda}^{\zeta}_m\left(\mathbf{x}, \frac{\mathbf{x}}{\epsilon}\right) d\mathbf{x} = \int_{\mathfrak{L}} \hat{\lambda}_m\left(\mathbf{x}, \frac{\mathbf{x}}{\epsilon} + \boldsymbol{\zeta}\right) d\mathbf{x}. \tag{2.61}$$

Let $\hat{\Lambda}_m$ be the average transformed power-like functional at the micro-scale

$$\begin{aligned} \hat{\Lambda}_m \doteq \langle \hat{\Lambda}^{\zeta} \rangle &= \frac{1}{|\mathcal{Q}|} \int_{\mathcal{Q}} \left[\int_{\mathfrak{L}} \hat{\lambda}_m\left(\mathbf{x}, \frac{\mathbf{x}}{\epsilon} + \boldsymbol{\zeta}\right) d\mathbf{x} \right] d\boldsymbol{\zeta} = \\ &= \int_{\mathfrak{L}} \left[\frac{1}{|\mathcal{Q}|} \int_{\mathcal{Q}} \hat{\Lambda}(\boldsymbol{\zeta}) d\boldsymbol{\zeta} \right] d\mathbf{x} = \int_{\mathfrak{L}} \left\langle \hat{\lambda}_m\left(\mathbf{x}, \frac{\mathbf{x}}{\epsilon}\right) \right\rangle d\mathbf{x}, \end{aligned} \tag{2.62}$$

where the Fubini's theorem was applied in the third equality.

Since the power-like functional $\hat{\Lambda}^{\zeta}$ is averaged by the translated realizations of the microstructure, which entails that the transformed power-like density at the micro-scale satisfies

$$\begin{aligned} \left\langle \hat{\lambda}_m\Big(\mathbf{x}, \frac{\mathbf{x}}{\epsilon} + \boldsymbol{\zeta}\Big) \right\rangle &= \frac{1}{|\mathcal{Q}|} \int_{\mathcal{Q}} \hat{\lambda}_m\Big(\mathbf{x}, \frac{\mathbf{x}}{\epsilon} + \boldsymbol{\zeta}\Big) d\boldsymbol{\zeta} = \\ &= \frac{1}{|\mathcal{Q}|} \int_{\mathcal{Q}} \hat{\lambda}_m\Big(\mathbf{x}, \boldsymbol{\xi}\Big) d\boldsymbol{\xi} = \langle \hat{\lambda}_m(\mathbf{x}, \xi) \rangle, \end{aligned} \tag{2.63}$$

consequently, this ensures that the average transformed power-like functional $\langle \hat{\Lambda}^{\zeta} \rangle$ at the micro-scale does not rely on the translation variable $\boldsymbol{\zeta}$.

Through a similar variational approach made in the Appendix A, we will determine the governing field equations at the macro-scale and the overall constitutive tensors, finding the Euler-Lagrange equation of the power-like function from the down-scaling relations (2.49a) and (2.49b). So, let us once again introduce the

down-scaling relations related to the transformed micro-displacement $\hat{\boldsymbol{u}}(\mathbf{x}, \boldsymbol{\xi}, s)$, and to the transformed micro-temperature $\hat{\theta}(\mathbf{x}, \boldsymbol{\xi}, s)$, i.e.

$$\hat{u}_h\left(\mathbf{x}, \frac{\mathbf{x}}{\epsilon}, s\right) = \hat{U}_h^M(\mathbf{x}, s) + \epsilon\left(N_{hpq_1}^{(1,0)}(\boldsymbol{\xi})\frac{\partial \hat{U}_h^M}{\partial x_{q_1}} + \tilde{N}_h^{(1,0)}(\boldsymbol{\xi})\hat{\Theta}^M\right) + \mathcal{O}(\epsilon^2), \quad (2.64a)$$

$$\hat{\theta}\left(\mathbf{x}, \frac{\mathbf{x}}{\epsilon}, s\right) = \hat{\Theta}^M(\mathbf{x}, s) + \epsilon\left(M_{q_1}^{(1,0)}(\boldsymbol{\xi})\frac{\partial \hat{\Theta}^M}{\partial x_{q_1}}\right) + \mathcal{O}(\epsilon^2), \quad (2.64b)$$

and applying the gradients (2.18a) and (2.18b) to the down-scaling relations above, one gives

$$\begin{aligned}\frac{D\hat{u}_h}{Dx_k} &= \frac{\partial \hat{U}_h^M}{\partial x_k} + N_{hpq_1,k}^{(1,0)}\frac{\partial \hat{U}_p^M}{\partial x_{q_1}} + \tilde{N}_{h,k}^{(1,0)}\hat{\Theta}^M + \epsilon\left(N_{hpq_1}^{(1,0)}\frac{\partial^2 \hat{U}_p^M}{\partial x_{q_1}\partial x_k} + \tilde{N}_h^{(1,0)}\frac{\partial \hat{\Theta}^M}{\partial x_k}\right) + \\ &+ \mathcal{O}(\epsilon^2) = B_{hkpq_1}^{(1,0)}\frac{\partial \hat{U}_h^M}{\partial x_{q_1}} + \tilde{B}_{hk}^{(1,0)}\hat{\Theta}^M + \mathcal{O}(\epsilon),\end{aligned} \quad (2.65)$$

where $B_{hkpq_1}^{(1,0)} = \delta_{hp}\delta_{kq_1} + N_{hpq_1,k}^{(1,0)}$ and $\tilde{B}_{hk}^{(1,0)} = \tilde{N}_{h,k}^{(1,0)}$, and

$$\begin{aligned}\frac{D\hat{\theta}_h}{Dx_j} &= \frac{\partial \hat{\Theta}^M}{\partial x_j} + M_{q_1,j}^{(1,0)}\frac{\partial \hat{\Theta}^M}{\partial x_{q_1}} + \epsilon M_{q_1}^{(1,0)}\frac{\partial^2 \hat{\Theta}^M}{\partial x_{q_1}\partial x_j} + \mathcal{O}(\epsilon^2) = \\ &= A_{jq_1}^{(1,0)}\frac{\partial \hat{\Theta}^M}{\partial x_{q_1}} + \mathcal{O}(\epsilon),\end{aligned} \quad (2.66)$$

where $A_{jq_1}^{(1,0)} = \delta_{jq_1} + M_{q_1,j}^{(1,0)}$. The tensors $B_{hkpq_1}^{(1,0)}$, $\tilde{B}_{hk}^{(1,0)}$ and $A_{jq_1}^{(1,0)}$ are called localization tensors and are also $\mathcal{Q}$-periodic functions in relation to the fast variable $\boldsymbol{\xi}$, once the perturbation functions and their gradients are $\mathcal{Q}$-periodic functions.

Thus, plugging the down-scaling relations truncated at the first order (2.64a), (2.64b) and their gradients (2.65), (2.66), into the transformed power-like functional (2.59), it results

$$
\begin{aligned}
\hat{\Lambda}_m(\hat{U}_h^M, \hat{\Theta}^M) = \int_{\mathfrak{L}} \langle \hat{\lambda}_m(\mathbf{x}, \boldsymbol{\xi}) \rangle d\mathbf{x} = \\
= & s \left[\frac{1}{2} s^2 \langle \rho^m \rangle \int_{\mathfrak{L}} \hat{U}_h^M \hat{U}_h^M d\mathbf{x} + \quad + \right. \\
& + \left\langle \frac{1}{2} B_{ijlr_1}^{(1,0)} C_{ijhk}^m B_{hkpq_1}^{(1,0)} \right\rangle \int_{\mathfrak{L}} \frac{\partial \hat{U}_l^M}{\partial x_{r_1}} \frac{\partial \hat{U}_p^M}{\partial x_{q_1}} d\mathbf{x} \quad + \\
& + \left\langle \frac{1}{2} B_{ijlr_1}^{(1,0)} C_{ijhk}^m \tilde{B}_{hk}^{(1,0)} \right\rangle \int_{\mathfrak{L}} \frac{\partial \hat{U}_l^M}{\partial x_{r_1}} \hat{\Theta}^M d\mathbf{x} \quad + \\
& + \left\langle \frac{1}{2} \tilde{B}_{ij}^{(1,0)} C_{ijhk}^m B_{hkpq_1}^{(1,0)} \right\rangle \int_{\mathfrak{L}} \hat{\Theta}^M \frac{\partial \hat{U}_l^M}{\partial x_{q_1}} d\mathbf{x} \quad + \\
& + \left\langle \frac{1}{2} \tilde{B}_{ij}^{(1,0)} C_{ijhk}^m \tilde{B}_{hk}^{(1,0)} \right\rangle \int_{\mathfrak{L}} \hat{\Theta}^M \hat{\Theta}^M d\mathbf{x} \quad + \\
& - \left\langle B_{ijlr_1}^{(1,0)} \alpha_{ij}^m \right\rangle \int_{\mathfrak{L}} \frac{\partial \hat{U}_l^M}{\partial x_{r_1}} \hat{\Theta}^M d\mathbf{x} \quad + \\
& \left. - \left\langle \tilde{B}_{ij}^{(1,0)} \alpha_{ij}^m \right\rangle \int_{\mathfrak{L}} \hat{\Theta}^M \hat{\Theta}^M d\mathbf{x} - \int_{\mathfrak{L}} \hat{U}_h^M \hat{b}_h d\mathbf{x} \right] \quad + \\
& - \left\langle \frac{1}{2} A_{ir_1}^{(1,0)} K_{ij}^m A_{jq_1}^{(1,0)} \right\rangle \int_{\mathfrak{L}} \frac{\partial \hat{\Theta}^M}{\partial x_{r_1}} \frac{\partial \hat{\Theta}^M}{\partial x_{q_1}} d\mathbf{x} \quad + \\
& - \frac{1}{2} s \langle p^m \rangle \int_{\mathfrak{L}} \hat{\Theta}^M \hat{\Theta}^M d\mathbf{x} \quad + \int_{\mathfrak{L}} \hat{r} \hat{\Theta}^M d\mathbf{x} + \mathcal{O}(\epsilon^2).
\end{aligned}
\tag{2.67}
$$

Using the concept of the variation of a functional to use the necessary condition for a functional to have an extremum [175], the stability condition of the transformed power-like functional $\hat{\Lambda}_m$ is given by the governing equation of a non-local homogeneous continuum, in other words, one arises to the first variation of the average transformed power-like functional $\delta\hat{\Lambda}_m(\hat{U}_h^M, \delta\hat{U}_h^M, \hat{\Theta}^M, \delta\hat{\Theta}^M)$, thus

$$
\begin{aligned}
\delta\hat{\Lambda}_m = \int_{\mathfrak{L}} s \Bigg[& s^2\langle\rho^m\rangle\hat{U}_l^M - \left\langle B_{ijlr_1}^{(1,0)} C_{ijhk}^m B_{hkpq_1}^{(1,0)} \right\rangle \frac{\partial^2 \hat{U}_p^M}{\partial x_{q_1}\partial x_{r_1}} \quad + \\
& - \left\langle \frac{1}{2} B_{ijlr_1}^{(1,0)} C_{ijhk}^m \tilde{B}_{hk}^{(1,0)} \right\rangle \frac{\partial \hat{\Theta}^M}{\partial x_{r_1}} \quad + \\
& - \left\langle \frac{1}{2} \tilde{B}_{ij}^{(1,0)} C_{ijhk}^m B_{hklq_1}^{(1,0)} \right\rangle \frac{\partial \hat{\Theta}^M}{\partial x_{q_1}} + \left\langle B_{ijlr_1}^{(1,0)} \alpha_{ij}^m \right\rangle \frac{\partial \hat{\Theta}^M}{\partial x_{r_1}} - \hat{b}_l \Bigg] \delta\hat{U}_l^M d\mathbf{x} \quad + \\
& + \int_{\mathfrak{L}} \Bigg[s \Bigg(\left\langle \frac{1}{2} B_{ijlr_1}^{(1,0)} C_{ijhk}^m \tilde{B}_{hk}^{(1,0)} \right\rangle \frac{\partial \hat{U}_l^M}{\partial x_{r_1}} + \left\langle \frac{1}{2} \tilde{B}_{ij}^{(1,0)} C_{ijhk}^m B_{hkpq_1}^{(1,0)} \right\rangle \frac{\partial \hat{U}_p^M}{\partial x_{q_1}} \quad + \\
& - \left\langle \tilde{B}_{ij}^{(1,0)} C_{ijhk}^m \tilde{B}_{hk}^{(1,0)} \right\rangle \hat{\Theta}^M - \left\langle B_{ijlr_1}^{(1,0)} \alpha_{ij}^m \right\rangle \frac{\partial \hat{U}_l^M}{\partial x_{r_1}} - 2 \left\langle \tilde{B}_{ij}^{(1,0)} \alpha_{ij}^m \hat{\Theta}^M \right\rangle \Bigg) \quad + \\
& + \left\langle A_{ir_1}^{(1,0)} K_{ij}^m A_{jq_1}^{(1,0)} \right\rangle \frac{\partial^2 \hat{\Theta}^M}{\partial x_{r_1} x_{q_1}} - s\langle p^m\rangle\hat{\Theta}^M + \hat{r} \Bigg] \delta\hat{\Theta}^M d\mathbf{x},
\end{aligned}
\tag{2.68}
$$

where the divergence theorem has been applied in the first variation of the transformed power-like functional (2.68).

As previously mentioned, such first variation must vanish for all admissible $\delta\hat{U}_h^M$, $\delta\hat{\Theta}^M$ i.e, $\delta\hat{\Lambda}_m(\hat{U}_h^M, \delta\hat{U}_h^M, \delta\hat{\Theta}^M, \delta\hat{\Theta}^M) = 0$, and hence the Euler-Lagrange differential equation associated to the variational problem (2.68), by truncating at the zeroth order, it leads to the following two equations

$$
\begin{aligned}
& s^2\langle\rho^m\rangle\hat{U}_l^M - \left\langle B_{ijlr_1}^{(1,0)} C_{ijhk}^m B_{hkpq_1}^{(1,0)} \right\rangle \frac{\partial^2 \hat{U}_p^M}{\partial x_{q_1}\partial x_{r_1}} \quad + \\
& + \left\langle B_{ijlq_1}^{(1,0)} \alpha_{ij}^m - B_{hklq_1}^{(1,0)} C_{ijhk}^m \tilde{B}_{ij}^{(1,0)} \right\rangle \frac{\partial \hat{\Theta}^M}{\partial x_{q_1}} - \hat{b}_l = 0,
\end{aligned}
\tag{2.69a}
$$

$$
\begin{aligned}
& \left\langle A_{ir_1}^{(1,0)} K_{ij}^m A_{jq_1}^{(1,0)} \right\rangle \frac{\partial^2 \hat{\Theta}^M}{\partial x_{r_1} x_{q_1}} \quad + \\
& + s \left(\left\langle B_{hkpq_1}^{(1,0)} C_{ijhk}^m \tilde{B}_{ij}^{(1,0)} \right\rangle \frac{\partial \hat{U}_l^M}{\partial x_{q_1}} - \left\langle B_{ijpq_1}^{(1,0)} \alpha_{ij}^m \right\rangle \frac{\partial \hat{U}_l^M}{\partial x_{q_1}} \right) \quad + \\
& - s\langle p^m + 2\tilde{B}_{ij}^{(1,0)} \alpha_{ij}^m + \tilde{B}_{ij}^{(1,0)} C_{ijhk}^m \tilde{B}_{hk}^{(1,0)} \rangle \hat{\Theta}^M + \hat{r} = 0,
\end{aligned}
\tag{2.69b}
$$

which are clearly developed in terms of the Laplace transformed macro-temperature and macro-displacement among with their gradients. Since the Eqs. (2.69a) and

(2.69b) are set by positive definite constitutive tensors, one implies that the existence and the uniqueness of their solutions are endorsed by the Legendre-Hadamard condition [176].

Rearranging and rewriting the Eqs. (2.69a) and (2.69b) in terms of the constitutive tensors, one gives

$$C_{lr_1pq_1}\frac{\partial^2\hat{U}_p^M}{\partial x_{q_1}\partial x_{r_1}} - \alpha_{lq_1}\frac{\partial\hat{\Theta}^M}{\partial x_{q_1}} + \hat{b}_l = \rho s^2\hat{U}_l^M, \tag{2.70a}$$

$$K_{r_1q_1}\frac{\partial^2\hat{\Theta}^M}{\partial x_{r_1}x_{q_1}} - s\alpha_{lq_1}\frac{\partial\hat{U}_l^M}{\partial x_{q_1}} + \hat{r} = ps\hat{\Theta}^M, \tag{2.70b}$$

where the overall constitutive tensors are defined as

$$C_{lr_1pq_1} = \left\langle B_{ijlr_1}^{(1,0)}C_{ijhk}^m B_{hkpq_1}^{(1,0)}\right\rangle, \tag{2.71a}$$

$$K_{r_1q_1} = \left\langle A_{ir_1}^{(1,0)}K_{ij}^m A_{jq_1}^{(1,0)}\right\rangle, \tag{2.71b}$$

$$\alpha_{lq_1} = \left\langle B_{ijlq_1}^{(1,0)}\alpha_{ij}^m - B_{hklq_1}^{(1,0)}C_{ijhk}^m\tilde{B}_{ij}^{(1,0)}\right\rangle, \tag{2.71c}$$

$$p = \langle p^m + 2\tilde{B}_{ij}^{(1,0)}\alpha_{ij}^m + \tilde{B}_{ij}^{(1,0)}C_{ijhk}^m\tilde{B}_{hk}^{(1,0)}\rangle, \tag{2.71d}$$

$$\rho = \langle\rho^m\rangle. \tag{2.71e}$$

Note that, at this stage, the Eqs. (2.70a) and (2.70b) are the macro-scale equivalent to the field Eqs. (2.11a) and (2.11b) on the transformed Laplace space. Moreover, by applying the inverse Laplace transform (2.9) to them, and recalling the identity (2.14), the field equations at the macro-scale corresponding to the Eqs. (2.7a) and (2.7b) are recast on the time domain as

$$C_{lr_1pq_1}\frac{\partial^2 U_p^M}{\partial x_{q_1}\partial x_{r_1}} - \alpha_{lq_1}\frac{\partial\dot{\Theta}^M}{\partial x_{q_1}} + \hat{b}_l = \rho\ddot{U}_l^M, \tag{2.72a}$$

$$\mathcal{L}^{-1}\left\{K_{r_1q_1}\right\} * \frac{\partial^2\Theta^M}{\partial x_{r_1}x_{q_1}} - \alpha_{lq_1}\frac{\partial\dot{U}_l^M}{\partial x_{q_1}} + r = p\dot{\Theta}^M. \tag{2.72b}$$

In addition, Sec. 2.4 considers higher order terms in the asymptotic expansions at the microscopic scale, along with the macroscopic constitutive tensors and source terms, states an alternative path to obtain higher order field equations and the possibility of a more precise modeling of the thermoelastic heterogeneous continuum.

2.6 Wave propagation in homogenized continuum

In this Section, we exploit the wave propagation along the homogenized continuum, which is equivalent to the heterogeneous thermoelastic periodic material. Such procedure consists in applying the Fourier transform to Eqs. (2.70a) and (2.70b), with respect to the macroscopic variable $\mathbf{x} \in \mathbb{R}^3$, in order to derive these field equations at the macro-scale defined over the complex frequency s, and also defined over the wave vector $\boldsymbol{k} = (k_1, k_2, k_3)^T \in \mathbb{C}^3$ ((k_1, k_2, k_3) are the wave numbers and T identifies transpose vector), in other terms, the thermoelastic field Eqs. (2.7a) and (2.7b), initially defined on the space-time domain $(\mathbf{x}, t) \in \mathbb{R}^3 \times \mathbb{R}$, will be taken to the wave vector-frequency domain $(\boldsymbol{k}, s) \in \mathbb{C}^3 \times \mathbb{C}$ [177].

Proceeding the same way as made in Sec. 2.1, we begin defining the space Fourier transform and its properties that will be used throughout the work [172]. Let $f : \mathbb{R}^3 \to \mathbb{R}$ be an arbitrary function defined over the domain $\mathbf{x} \in \mathbb{R}^3$, the complex space Fourier transform is defined as,

$$\mathcal{F}(f(\mathbf{x})) = \check{f}(\boldsymbol{k}) = \int_{\mathbb{R}^3} f(\mathbf{x}) \mathrm{e}^{-\mathrm{i}\boldsymbol{k}\cdot\mathbf{x}} \mathrm{d}\mathbf{x}, \quad \boldsymbol{k} \in \mathbb{C}^3, \tag{2.73}$$

where $\check{f} : \mathbb{C}^3 \to \mathbb{C}$.

The Fourier transform of the derivative of order $n+m$ of f with respect to x_j^n and x_r^m is given by the identity$\mathcal{F}\left\{\partial^{n+m} f(\mathbf{x}) \partial x_j^n \partial x_r^m\right\} = (\mathrm{i}k_j)^n (\mathrm{i}k_r)^m \check{f}(\boldsymbol{k})$.

Transforming the macro-scale field Eqs. (2.70a) and (2.70b) into the Fourier transformed space, one has

$$C_{lr_1pq_1}(\mathrm{i}k_{q_1})(\mathrm{i}k_{r_1})\check{U}_p^M - \alpha_{lq_1}(\mathrm{i}k_{q_1})\check{\hat{\Theta}}^M + \check{b}_l = \rho s^2 \check{U}_l^M, \tag{2.74a}$$

$$K_{r_1q_1}(\mathrm{i}k_{q_1})(\mathrm{i}k_{r_1})\check{\hat{\Theta}}^M - s\alpha_{lq_1}(\mathrm{i}k_{q_1})\check{U}_l^M + \check{r} = ps\check{\hat{\Theta}}^M. \tag{2.74b}$$

In case of free wave propagation, we take the external influences (source terms) being zero, such as the heat source equivalent $\check{r}$, and the body force equivalent $\check{\hat{\boldsymbol{b}}}$, so the equations above might be rephrased to the compact form as

$$\left[\bar{\mathfrak{C}}(\boldsymbol{k} \otimes \boldsymbol{k}) + \rho s^2 \boldsymbol{I}\right] \cdot \check{\boldsymbol{U}}^M + \mathrm{i}(\boldsymbol{\alpha}\boldsymbol{k})\check{\hat{\Theta}}^M = \mathbf{0}, \tag{2.75a}$$

$$\left[\mathbf{K} : (\boldsymbol{k} \otimes \boldsymbol{k}) + ps\right]\check{\hat{\Theta}}^M + \mathrm{i}s(\boldsymbol{\alpha}\boldsymbol{k}) \cdot \check{\boldsymbol{U}}^M = 0, \tag{2.75b}$$

where the tensor $\bar{\mathfrak{C}}$ corresponds to the shift $\bar{\mathfrak{C}} = \bar{C}_{lpr_1q_1}\mathbf{e}_l \otimes \mathbf{e}_p \otimes \mathbf{e}_{r_1} \otimes \mathbf{e}_{q_1}$, with

$\bar{C}_{lpr_1q_1} = C_{lpr_1q_1}$. Note that, the system of linear equations formed by Eqs. (2.75a) and (2.75b) may be rewritten in a matricial form as

$$\left[\begin{array}{cc} \bar{\mathfrak{C}}(\boldsymbol{k}\otimes\boldsymbol{k}) + \rho s^2 \boldsymbol{I} & \mathrm{i}\boldsymbol{k}\boldsymbol{\alpha} \\ \mathrm{i}s\boldsymbol{k}\boldsymbol{\alpha} & \mathbf{K}:(\boldsymbol{k}\otimes\boldsymbol{k}) + ps \end{array} \right] \left[\begin{array}{c} \check{\boldsymbol{U}}^M \\ \check{\Theta}^M \end{array} \right] = \left[\begin{array}{c} \mathbf{0} \\ 0 \end{array} \right]. \tag{2.76}$$

The matricial system (2.76), is an eigenproblem that provides the frequency spectrum as an implicit function of the wave vector $\boldsymbol{k}$ and the complex frequency s, which is given by the frequency equation $F(\boldsymbol{k}, s) = \det([\boldsymbol{H}(\boldsymbol{k}, s)]) = 0$, also known as implicit dispersion relation, where the matrices in the system (2.76) are named as $[\boldsymbol{H}(\boldsymbol{k}, s)][\boldsymbol{V}] = [\mathbf{0}]$. Since the implicit function $F(\boldsymbol{k}, s) = 0$ is a complex function, it can be rephrased in terms of its real part and imaginary part as $F(\boldsymbol{k}, s) = \Re e(F(\boldsymbol{k}, s)) + \mathrm{i}\Im m(F(\boldsymbol{k}, s)) = 0$, or simply

$$\left\{ \begin{array}{rcl} \Re e(F(\boldsymbol{k}, s)) & = & 0 \\ \Im m(F(\boldsymbol{k}, s)) & = & 0 \end{array} \right. , \tag{2.77}$$

which represents the collection of branches (frequency spectrum) by the hyper-surfaces $\Re e(F(\boldsymbol{k}, s))$ and $\Im m(F(\boldsymbol{k}, s))$ into the space $(\boldsymbol{k}, s) \in \mathbb{C}^4$, such hyper-surface $F(\boldsymbol{k}, s)$ is also seen in mathematics as a level set of the complexed-valued function F. As [177] pinpoints, from a mathematical standpoint, there is no reason to choose real over complex values for either the frequency or the wave vector. What matters is actually the physical meaning that might be associated to them. Having described the implicit dispersion function, from this stage on we emphasize two possible lanes that might provide us the dispersion spectrum, and finally analyse the wave propagation either with spatial damping or with the damping in time, [178].

Particularly, before presenting the time damping path to analyse the wave propagation, we briefly introduce the concepts of inhomogeneous waves and homogeneous waves, for more details see [178]. An harmonic homogeneous wave is defined when $\boldsymbol{n}_r = \boldsymbol{n}_i = \boldsymbol{n}$ occurs, this scenario means that the direction $\boldsymbol{n}$ leads both the real wave vector direction and the attenuation factor direction to become an unique direction of propagation. When $\gamma \equiv 0$, the wave is called homogeneous, in other words the angle γ being zero implies that the real wave vector and the attenuation directions coincide. Moreover, physically it can also be quoted as [179] does, homogeneous waves have the property that their surfaces of constant phase are parallel to their surfaces of constant amplitude whereas inhomogeneous waves have the property that their surfaces of constant phase are perpendicular to their surfaces of constant amplitude.

In these circumstances, for the first case, let us consider the complex angular frequency as $s = \mathrm{i}\omega$ with $\omega \in \mathbb{R}$ in the implicit dispersion relation (2.77). Thus the dispersion relation dependence goes over to the complex wave vector $\boldsymbol{k}$ and the angular frequency ω. Therefore, the dispersion relation associated to generic inhomogeneous harmonic waves holds

$$\left\{ \begin{array}{rcl} \Re e(F(\Re e(\boldsymbol{k}), \Im m(\boldsymbol{k}), \omega)) & = & 0 \\ \Im m(F(\Re e(\boldsymbol{k}), \Im m(\boldsymbol{k}), \omega)) & = & 0 \end{array} \right. , \tag{2.78}$$

where the intersection between these two hyper-surfaces defines the frequency spectrum of the material as an hyper-curve immersed in $\mathbb{R}^7$. More specifically, such hyper-curve describes the relation between the angular frequency ω and the complex vector $\boldsymbol{k}$, which can be expressed as $\boldsymbol{k} = \Re e(\boldsymbol{k}) + \mathrm{i}\Im m(\boldsymbol{k}) = \|\Re e(\boldsymbol{k})\|\boldsymbol{n}_r + \mathrm{i}\|\Im m(\boldsymbol{k})\|\boldsymbol{n}_i$, where $\boldsymbol{n}_r$, $\boldsymbol{n}_i$ are versors (i.e $\|\boldsymbol{n}_r\| = \|\boldsymbol{n}_i\| = 1$ and $\boldsymbol{n}_r, \boldsymbol{n}_i \in \mathbb{R}^3$), representing the direction of the normal to planes of constant phase and planes of constant amplitude of the propagating wave, respectively. Moreover, in the particular case of the homogeneous harmonic waves characterized by $\boldsymbol{n}_r = \boldsymbol{n}_i = \boldsymbol{n}$ and for the complex wave expressed in the form $\boldsymbol{k} = (\|\Re e(\boldsymbol{k})\| + i\|\Im m(\boldsymbol{k})\|)\boldsymbol{n} = \kappa\boldsymbol{n}$, the dispersion relation is obtained by specializing (2.78) in the form

$$\left\{ \begin{array}{rcl} \Re e(F(\Re e(\kappa), \Im m(\kappa), \omega)) & = & 0 \\ \Im m(F(\Re e(\kappa), \Im m(\kappa), \omega)) & = & 0 \end{array} \right. , \tag{2.79}$$

a three dimensional hyper-surface whose intersection is a curve immersed in $\mathbb{R}^3$.

Nonetheless, in the second case of wave propagation with attenuation in time, let us assume in the set of Eqs. (2.77) the complex frequency being as $s = \Re e(s) + \mathrm{i}\Im m(s)$, the wave vector such that $\boldsymbol{k} \in \mathbb{R}^3$, and let us also fix a direction of the wave vector $\boldsymbol{k} = \kappa\boldsymbol{n}$, where $\boldsymbol{n}$ is its versor and $\kappa = ||\boldsymbol{k}|| \in \mathbb{R}$, thus (2.77) becomes

$$\left\{ \begin{array}{rcl} \Re e(F(\kappa, \Re e(s), \Im m(s))) & = & 0 \\ \Im m(F(\kappa, \Re e(s), \Im m(s))) & = & 0 \end{array} \right. , \tag{2.80}$$

and hence taking the intersection between the two hyper-surfaces from (2.80), one yields a hyper-curve $s(\kappa)$-curves immersed in $\mathbb{R}^3$, given a certain propagation direction $\boldsymbol{n}$.

2.7 Illustrative example: homogenization procedure on a bi-phase orthotropic layered material

In this section, in order to contrast the results found by the analysis of the heterogeneous approach stressed in Appendix B, the homogenized formulation obtained in Sec. 2.7 is now applied for a layered two-dimensional infinite thermoelastic body with orthotropic phases having the orthotropy axes parallel to the layering direction $\boldsymbol{e_1}$. Analytical precise formulae for the overall elastic, thermal dilatation and thermal conduction tensors are determined. Subsequently, we compare the results of the heterogeneous model developed in Appendix B, against those from the model obtained proceeding with the first order homogenization technique, both under the same hypothesis, by finding their dispersions spectrum seen in Sec. 2.6.

2.7.1 Perturbation functions and overall constitutive tensors

Let us assume a layered body composed by two phases where the first order homogenization process will be applied on the system. As may seen in Fig. 13, let the domain $\mathcal{A}$ made by two layered materials be defined having thickness $\mathfrak{s}_1$ and $\mathfrak{s}_2$, where $d_2 = \epsilon = \mathfrak{s}_1 + \mathfrak{s}_2$, and $\eta = \mathfrak{s}_1/\mathfrak{s}_2$. Also the domain displays orthotropic phases, which it coincides with the axis that determines the layering direction $\boldsymbol{e}_1$. The perturbation functions at the order ϵ^{-1}, $N^{(1,0)}_{hpq_1}$ $\tilde{N}^{(1,0)}_{h}$, $M^{(1,0)}_{q_1}$ are analytically obtained by the solutions of the three cell problems presented in (2.43) formulated in Sec. 2.7, along with the interface conditions in (2.44). Due to the microstructure symmetry, these functions rely exclusively on the microscopic (fast) component ξ_2, which is perpendicular to the layering direction $\boldsymbol{e}_1$. Considering only non-zero perturbations functions, they are given by

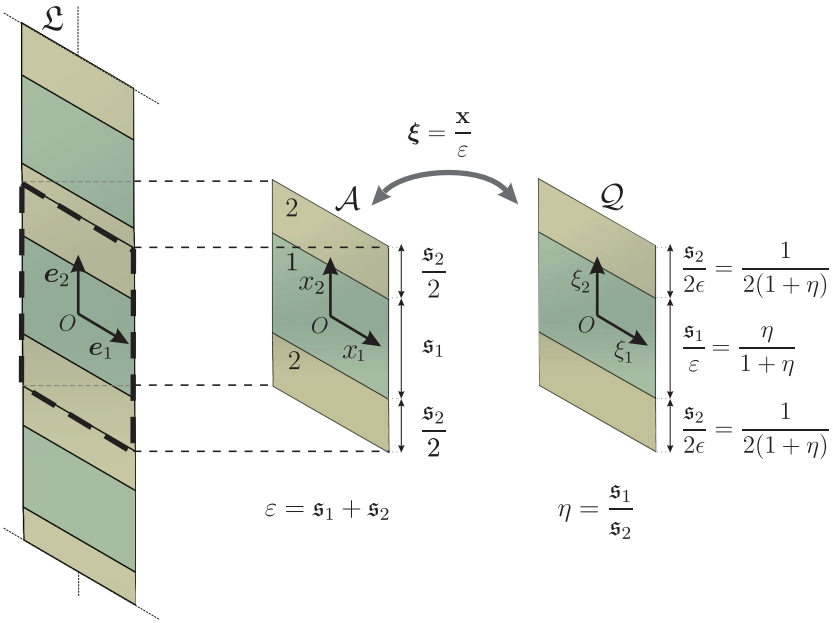

Figure 13: Heterogeneous bi-dimensional domain bi-phase layered periodic cell.

$$N_{112}^{(1,0)_1} = N_{121}^{(1,0)_1} = \frac{\left(C_{1212}^{(2)} - C_{1212}^{(1)}\right)\xi_2^{(1)}}{C_{1212}^{(2)}\eta + C_{1212}^{(1)}}, \qquad N_{112}^{(1,0)_2} = N_{121}^{(1,0)_2} = \frac{\eta\left(C_{1212}^{(2)} - C_{1212}^{(1)}\right)\xi_2^{(2)}}{C_{1212}^{(2)}\eta + C_{1212}^{(1)}}, \tag{2.81a}$$

$$N_{211}^{(1,0)_1} = \frac{\left(C_{1122}^{(2)} - C_{1122}^{(1)}\right)\xi_2^{(1)}}{C_{2222}^{(2)}\eta + C_{2222}^{(1)}}, \qquad N_{211}^{(1,0)_2} = \frac{\eta\left(C_{1122}^{(2)} - C_{1122}^{(1)}\right)\xi_2^{(2)}}{C_{2222}^{(2)}\eta + C_{2222}^{(1)}}, \tag{2.81b}$$

$$N_{222}^{(1,0)_1} = \frac{\left(C_{2222}^{(2)} - C_{2222}^{(1)}\right)\xi_2^{(1)}}{C_{2222}^{(2)}\eta + C_{2222}^{(1)}}, \qquad N_{222}^{(1,0)_2} = \frac{\eta\left(C_{2222}^{(2)} - C_{2222}^{(1)}\right)\xi_2^{(2)}}{C_{2222}^{(2)}\eta + C_{2222}^{(1)}}, \tag{2.81c}$$

$$\tilde{N}_2^{(1,0)_1} = \frac{\left(\alpha_{22}^{(1)} - \alpha_{22}^{(2)}\right)\xi_2^{(1)}}{C_{2222}^{(2)}\eta + C_{2222}^{(1)}}, \qquad \tilde{N}_2^{(1,0)_2} = \frac{\eta\left(\alpha_{22}^{(2)} - \alpha_{22}^{(1)}\right)\xi_2^{(2)}}{C_{2222}^{(2)}\eta + C_{2222}^{(1)}}, \tag{2.81d}$$

$$M_2^{(1,0)_1} = \frac{\left(K_{22}^{(2)} - K_{22}^{(1)}\right)\xi_2^{(1)}}{K_{22}^{(2)}\eta + K_{22}^{(1)}}, \qquad M_2^{(1,0)_2} = \frac{\eta\left(K_{22}^{(1)} - K_{22}^{(2)}\right)\xi_2^{(2)}}{K_{22}^{(2)}\eta + K_{22}^{(1)}}, \tag{2.81e}$$

where the superscript $i = \{1, 2\}$ denotes for the phase 1 and the phase 2, respectively. Moreover, the dimensionless vertical variables $\xi_2^{(1)}$ and $\xi_2^{(2)}$ centered in each layer are such that, $\xi_2^{(1)} \in [-\eta/2(\eta+1), \eta/2(\eta+1)]$ and $\xi_2^{(2)} \in [-1/2(\eta+1), 1/2(\eta+1)]$,

agreeing with the Fig. 13.

In particular, once the perturbation functions $M_{q1}^{(1,0)}$ depend on the complex angular frequency s (see Eqs. (2.12) and (2.34b)), such dependency is evaluated, but dimensionless. As may be seen in Fig. 14, the complex absolute value of the dimensionless perturbation function, which is $\|M_2^{(1,0)}\|$, is analytically computed by the Eqs. in (2.81e), with respect to the phase 1 and the phase 2, taking the following values for dimensionless parameters $\eta = 1$, $\tau^{(2)}/\tau^{(1)} = 3$ and $\bar{K}_{22}^{(2)}/\bar{K}_{22}^{(1)} = 10$. Such a function depends on the fast variable ξ_2, which is perpendicular to the transversal direction $\boldsymbol{e}_1$ and to the dimensionless complex parameter $s\tau^{(1)} = \Re e(s\tau^{(1)}) + \mathrm{i}\Im m(s\tau^{(1)})$. It must be noted in Fig. 14(a) that the function $\|M_2^{(1,0)}(\xi_2, \Re e(s\tau^{(1)}))\|$ presents a singularity along the variable ξ_2, whereas the function $\|M_2^{(1,0)}(\xi_2, \Im m(s\tau^{(1)}))\|$ displays the absence of any sort of singularities regardless the variable.

As previously mentioned, we also derive the non-vanishing overall elastic, thermal dilatation and thermal conduction tensors corresponding to a first order equivalent continuum. Thus, from the perturbation functions (2.81a), (2.81b) and (2.81c) are used into Eq. (2.71a), hence the overall elastic tensors $C_{lr_1pq_1}$ are expressed as

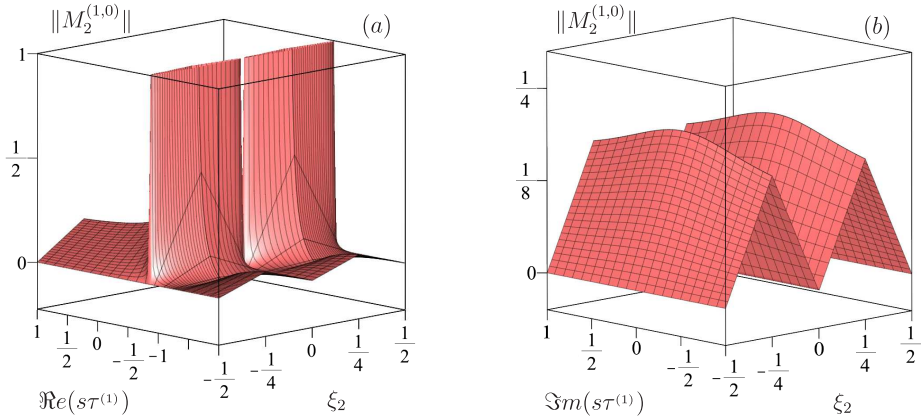

Figure 14: Dimensionless complex absolute value of the perturbation function $M_2^{(1,0)}$ for the dimensionless parameters assumed $\eta = 1$, $\tau^{(2)}/\tau^{(1)} = 3$ and $\bar{K}_{22}^{(2)}/\bar{K}_{22}^{(1)} = 10$. ($a$) $\|M_2^{(1,0)}\|$ vs. $\Re e(s\tau^{(1)})$ and ξ_2; (b) $\|M_2^{(1,0)}\|$ vs. $\Im m(s\tau^{(1)})$ and ξ_2.

$$C_{1111} = \frac{\eta^2 C^{(1)}_{1111} C^{(2)}_{2222} + + C^{(2)}_{1111} C^{(1)}_{2222}}{(\eta+1)\left(C^{(1)}_{2222} + \eta C^{(2)}_{2222}\right)} \quad + \\ + \frac{\eta\left(C^{(2)}_{1111} C^{(2)}_{2222} + C^{(2)}_{1111} C^{(1)}_{2222} - \left(C^{(1)}_{1122} - C^{(2)}_{1122}\right)^2\right)}{(\eta+1)\left(C^{(1)}_{2222} + \eta C^{(2)}_{2222}\right)}, \tag{2.82a}$$

$$C_{1122} = \frac{\eta C^{(1)}_{1122} C^{(2)}_{2222} + C^{(2)}_{1122} C^{(1)}_{2222}}{C^{(1)}_{2222} + \eta C^{(2)}_{2222}}, \tag{2.82b}$$

$$C_{1212} = \frac{(\eta+1) C^{(1)}_{1212} C^{(2)}_{1212}}{C^{(1)}_{1212} + \eta C^{(2)}_{1212}}, \tag{2.82c}$$

$$C_{2222} = \frac{(\eta+1) C^{(1)}_{2222} C^{(2)}_{2222}}{C^{(1)}_{2222} + \eta C^{(2)}_{2222}}. \tag{2.82d}$$

Similarly, for the thermal dilatation components follows that from the perturbation functions (2.81a) to (2.81d) into Eqs. (2.71a) and (2.71c), one provides

$$\alpha_{11} = \frac{\eta^2 C^{(2)}_{2222} \alpha^{(1)}_{11} + C^{(1)}_{2222} \alpha^{(2)}_{11}}{(\eta+1)(C^{(1)}_{2222} + \eta C^{(2)}_{2222})} \quad + \\ + \frac{\eta\left(C^{(1)}_{2222} \alpha^{(1)}_{11} + C^{(2)}_{2222} \alpha^{(2)}_{11} - \left(\alpha^{(1)}_{22} - \alpha^{(2)}_{22}\right)\left(C^{(1)}_{1122} - C^{(2)}_{1122}\right)\right)}{(\eta+1)(C^{(1)}_{2222} + \eta C^{(2)}_{2222})}, \tag{2.83a}$$

$$\alpha_{22} = \frac{\eta C^{(2)}_{2222} \alpha^{(1)}_{22} + \alpha^{(2)}_{22} C^{(1)}_{2222}}{\eta C^{(2)}_{2222} + C^{(1)}_{2222}}. \tag{2.83b}$$

The specific heat p and the mass density ρ in the Eqs. (2.71d) and (2.71e) respectively, are obtained following the same steps made latter for the elastic, and thermal dilatations tensors, giving

$$p = \frac{p^{(1)} \eta^2 C^{(2)}_{2222} + \left(p^{(1)} C^{(1)}_{2222} + p^{(2)} C^{(2)}_{2222} + 2\left(\alpha^{(1)}_{22} - \alpha^{(2)}_{22}\right)^2\right)\eta + p^{(2)} C^{(1)}_{2222}}{\left(\eta C^{(2)}_{2222} + C^{(1)}_{2222}\right)(\eta+1)}, \tag{2.84a}$$

$$\rho = \frac{\eta \rho^{(1)} + \rho^{(2)}}{\eta+1}. \tag{2.84b}$$

Still in this matter, from the perturbation functions (2.81e) and Eq. (2.71b), the components of the overall thermal conduction tensor are

$$K_{11}(s) = \frac{\eta K_{11}^{(1)}(s) + K_{11}^{(2)}(s)}{\eta + 1}, \tag{2.85a}$$

$$K_{22}(s) = \frac{(\eta + 1) K_{22}^{(1)}(s) K_{22}^{(2)}(s)}{\eta K_{22}^{(2)}(s) + K_{22}^{(1)}(s)}. \tag{2.85b}$$

Consequently, from Eq. (2.12), the corresponding parts of the overall thermal conduction tensor namely $K_{11}(s)$ and $K_{22}(s)$, are also dependent on the complex angular frequency s, which ends up being rewritten in terms of the relaxation times $\tau^{(1)}$, $\tau^{(2)}$, the specific heat T_0 and also the thermal conductivity tensors defined at the begining of the theory. After the respective substitutions of Eq. (2.12) into both equations in Eqs. (2.85), the equivalent components for overall thermal conduction tensor are, respectively:

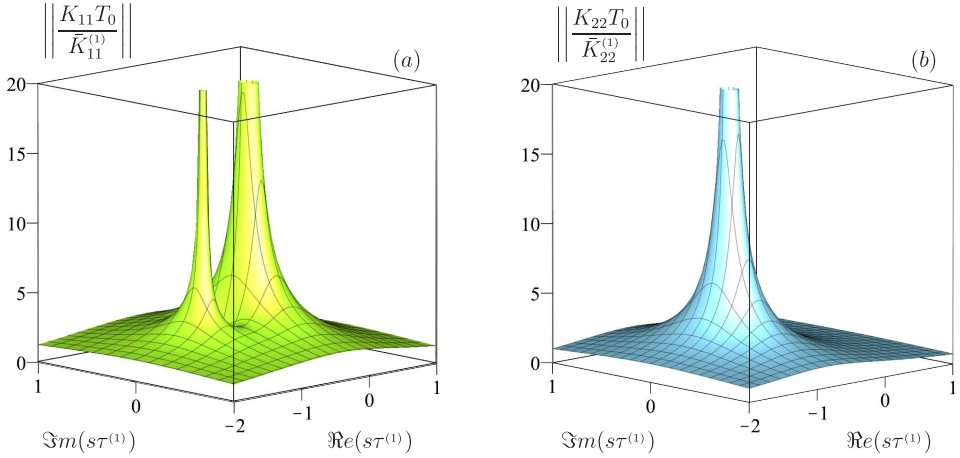

Figure 15: Dimensionless complex absolute value of the non-vanishing overall thermal conduction tensor components with $\eta = 1$, $\tau^{(2)}/\tau^{(1)} = 3$ and $\bar{K}_{22}^{(2)}/\bar{K}_{22}^{(1)} = 10$. (*a*) $\|K_{11}T_0/\bar{K}_{11}^{(1)}\|$ vs. $\Re e(s\tau^{(1)}) \times \Im m(s\tau^{(1)})$; (*b*) $\|\bar{K}_{22}T_0/K_{22}^{(1)}\|$ vs. $\Re e(s\tau^{(1)}) \times \Im m(s\tau^{(1)})$.

$$K_{11}(s) = \frac{\eta \bar{K}_{11}^{(1)}(s\tau^{(2)} + 1) + \bar{K}_{11}^{(2)}(s\tau^{(1)} + 1)}{T_0(\eta + 1)(s\tau^{(1)} + 1)(s\tau^{(2)} + 1)}, \tag{2.86a}$$

$$K_{22}(s) = \frac{(\eta + 1)\bar{K}_{22}^{(1)}\bar{K}_{22}^{(2)}}{T_0\left(\eta \bar{K}_{22}^{(2)}(s\tau^{(1)} + 1) + \bar{K}_{22}^{(1)}(s\tau^{(2)} + 1)\right)}. \tag{2.86b}$$

The Fig. 15 displays the complex absolute value of the dimensionless overall thermal conduction tensor components $\|K_{11}T_0/\bar{K}_{11}^{(1)}\|$ and $\|K_{22}T_0/\bar{K}_{22}^{(1)}\|$ in terms

of the dimensionless complex frequency $(\Re e(s\tau^{(1)}), \Im m(s\tau^{(1)}))$, for the same dimensionless parameters $\eta = 1$, $\tau^{(2)}/\tau^{(1)} = 3$ and $\bar{K}_{22}^{(2)}/\bar{K}_{22}^{(1)} = 10$ already assumed when it was analyzed the perturbation function $M_2^{(1,0)}$. Still in the regard of the Fig. 15, note that the Eq. (2.86a) presents a quadratic behaviour in its denominator and hence, as expected, it does display two poles, whereas the equation for K_{22}, namely Eq. (2.86b), has a linear nature in its denominator, giving only one pole.

2.7.2 Comparative analysis: heterogeneous material vs. homogenized solid

Under the same hypothesis assumed in the beginning of this Section, herein we proceed with a comparative analysis between the results obtained from the heterogeneous modelling procedure developed in the Sec. B via Floquet-Bloch theory, and the homogenized first order model approached in the previous sections of the generalized thermoelastic problem with the derived overall elastic, thermal dilatation and thermal conduction constants.

For the considered two-dimensional body with the orthotropy axes perpendicular to the layering direction $\boldsymbol{e_2}$ and the wave vector taken such as $k_1 = 0$, i.e the propagation axes is exclusively along the $\boldsymbol{e_2}$. For this scenario we consider an uncoupled problem which means that the dilatation tensor is assumed zero. Having said so, on the one hand by plugging overall constitutive tensors displayed in the set of Eqs. (2.82), (2.84) and (2.86) into the homogenized specialized governing equations from (2.70a), (2.70b) and following the procedure reported in Sec. 2.6, the dispersive relation (2.80) (for $\kappa = k_2$) provides the explicit functions

$$k_2(s) = \pm \frac{\mathrm{i}s\sqrt{C_{1212}^{(1)} C_{1212}^{(2)} \left(\eta\rho^{(1)} + \rho^{(2)}\right)\left(\eta C_{1212}^{(2)} + C_{1212}^{(1)}\right)}}{C_{1212}^{(1)} C_{1212}^{(2)}(\eta + 1)}, \tag{2.87}$$

or in its inverse form

$$s(k_2) = \pm \frac{\mathrm{i}k_2(\eta + 1)\sqrt{C_{1212}^{(1)} C_{1212}^{(2)} \left(\eta\rho^{(1)} + \rho^{(2)}\right)\left(\eta C_{1212}^{(2)} + C_{1212}^{(1)}\right)}}{\left(\eta\rho^{(1)} + \rho^{(2)}\right)\left(\eta C_{1212}^{(2)} + C_{1212}^{(1)}\right)}, \tag{2.88}$$

corresponding to the dispersion relation associated to the shear waves, giving rise to the standard non-dispersive behaviour. Similarly

$$k_2(s) = \pm \frac{\mathrm{i}s\sqrt{C_{2222}^{(1)} C_{2222}^{(2)} \left(\eta\rho^{(1)} + \rho^{(2)}\right)\left(\eta C_{2222}^{(2)} + C_{2222}^{(1)}\right)}}{C_{2222}^{(1)} C_{2222}^{(2)}(\eta + 1)}, \tag{2.89}$$

with the inversion function as

$$s(k_2) = \pm \frac{\mathrm{i}k_2(\eta+1)\sqrt{C^{(1)}_{2222}C^{(2)}_{2222}\left(\eta\rho^{(1)}+\rho^{(2)}\right)\left(\eta C^{(2)}_{2222}+C^{(1)}_{2222}\right)}}{\left(\eta\rho^{(1)}+\rho^{(2)}\right)\left(\eta C^{(2)}_{2222}+C^{(1)}_{2222}\right)}, \tag{2.90}$$

corresponding to the dispersion relation associated to the compressional waves, providing once again the standard non-dispersive behaviour. Finally, for dispersion relation associated to the thermal waves,

$$k_2(s) = \pm \frac{\mathrm{i}\sqrt{\mathscr{Z}_0\left[s^2\left(\eta\bar{K}^{(2)}_{22}\tau^{(1)}+\bar{K}^{(1)}_{22}\tau^{(2)}\right)+s\left(\eta\bar{K}^{(2)}_{22}+\bar{K}^{(1)}_{22}\right)\right]}}{\bar{K}^{(1)}_{22}\bar{K}^{(2)}_{22}(\eta+1)\left(\eta C^{(2)}_{2222}+C^{(1)}_{2222}\right)}, \tag{2.91}$$

where $\mathscr{Z}_0 = T_0\left(\eta^2 p^{(1)}C^{(2)}_{2222}+\eta\left(p^{(1)}C^{(1)}_{2222}+2\left(\alpha^{(1)}_{22}-\alpha^{(2)}_{22}\right)^2\right)+p^{(2)}C^{(1)}_{2222}\right)$, or in its inverse form

$$s(k_2) = \frac{\mathscr{Z}_0\left(\eta\bar{K}^{(2)}_{22}+\bar{K}^{(1)}_{22}\right) \pm \sqrt{\mathscr{Z}_1(k_2)}}{2\mathscr{Z}_0\left(\eta\bar{K}^{(2)}_{22}\tau^{(1)}+\bar{K}^{(1)}_{22}\tau^{(2)}\right)}, \tag{2.92}$$

with the function $\mathscr{Z}_1(k_2)$ defined as

$$\begin{aligned}\mathscr{Z}_1(k_2) = {} & \mathscr{Z}_0^2\left(\eta\bar{K}^{(2)}_{22}+\bar{K}^{(1)}_{22}\right)^2 \quad + \\ & - 4k_2^2\mathscr{Z}_0\left(\eta\bar{K}^{(2)}_{22}\tau^{(1)}+\bar{K}^{(1)}_{22}\tau^{(2)}\right)(\eta+1)^2\left(\eta C^{(2)}_{2222}+C^{(1)}_{2222}\right)^2\left(\bar{K}^{(1)}_{22}\bar{K}^{(2)}_{22}\right)^2.\end{aligned} \tag{2.93}$$

It is important to notice here that, the dispersion relations (2.91) and (2.92) are expressed, as expected, in terms of both phases of the micro-thermal-conductivity tensor components $\bar{K}^{(1)}_{22}$ and $\bar{K}^{(2)}_{22}$, as well as the relaxation times $\tau^{(1)}$ and $\tau^{(2)}$.

In respect of characterizing harmonic waves in the homogenized continuum, it is worth noting that for these above equations and their respective inverse forms allow us to either describe them by spatial damping or time damping as previously seen in Sec. 2.6.

On the other hand, followed from the Appendices B and C, the dispersion relations for the heterogeneous bi-dimensional body with the orthotropy axes perpendicular to the layering direction $\boldsymbol{e_2}$ and the wave vector taken such as $k_1 = 0$, with $d_2 = d^{(1)} + d^{(2)}$ are given by

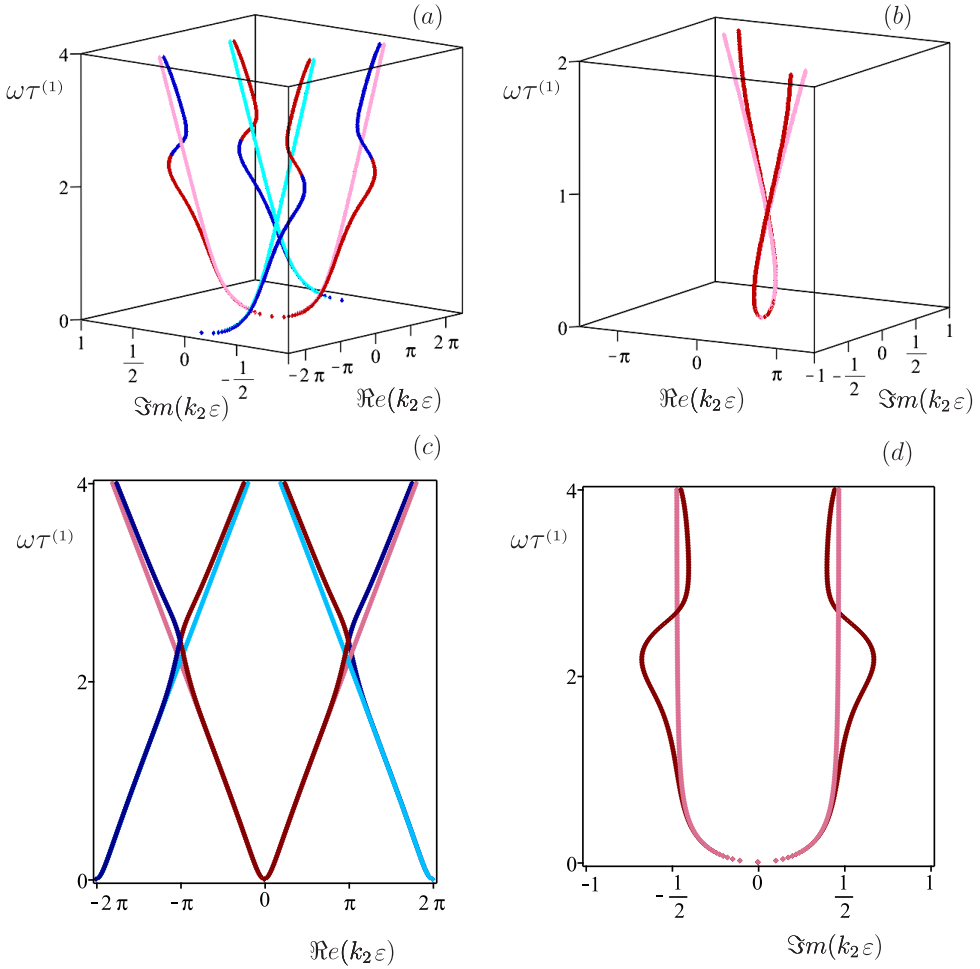

Figure 16: Dimensionless dispersion functions associated to thermal waves when $k_1 = 0$. Comparison between a first order homogenized model (light blue curve and light red curve) with its respective heterogeneous one (dark blue curve and dark red curve), and assuming the numerical values for the dimensionless parameters as $\eta = 1$, $\tau^{(2)}/\tau^{(1)} = 3$, $\bar{K}_{22}^{(2)}/\bar{K}_{22}^{(1)} = 3$, $p^{(2)}/p^{(1)} = 3$ and $p^{(1)}T_0/\left(\tau^{(1)}\bar{K}_{22}^{(1)}\right) = 1$. (a) $\omega\tau^{(1)}$ vs. $\Re e(k_2\epsilon) \times \Im m(k_2\epsilon)$; (b) zoomed view of the angular frequency spectrum $\omega\tau^{(1)}$ vs. $\Re e(k_2\epsilon) \times \Im m(k_2\epsilon)$; (c) view of the plane $\omega\tau^{(1)} \times \Re e(k_2\epsilon)$; (d) view of the plane $\omega\tau^{(1)} \times \Im m(k_2\epsilon)$.

$$k_2(s) = \frac{1}{\mathrm{i}d_2}\left[\ln\left(\frac{-\tilde{I}_1^j(s) \pm \sqrt{\left(\tilde{I}_1^j(s)\right)^2 - 4}}{2}\right) - 2\pi\mathrm{i}n\right], \text{ with } n \in \mathbb{Z}, j = 1, 2, 3, \tag{2.94}$$

where the details about the invariants $\tilde{I}_1^j(s)$ are brought in Appendix D.

For the case in which the wave number k_1 is assumed zero and when $s = \mathrm{i}\omega$, the Fig. 16 exhibits the behaviour of the thermal wave propagation given by Eqs. (2.92) and (2.93) for the homogenized material represented in light blue and light red curves, while the thermal wave function (2.94) for the heterogeneous solid via Floquet-Bloch theory is presented in dark blue and light red curves, where the parameters have been set as $\eta = 1$, $\tau^{(2)}/\tau^{(1)} = 3$, $\bar{K}_{22}^{(2)}/\bar{K}_{22}^{(1)} = 3$, $p^{(2)}/p^{(1)} = 3$ and $p^{(1)}T_0/\left(\tau^{(1)}\bar{K}_{22}^{(1)}\right) = 1$. Both light and dark blue lines stand for the translations of their respective dispersion curves due to the periodicity of the material along $\boldsymbol{e}_2$ around $\Re e(k_2\epsilon) = 2\pi n$, which they go all along the real wave number axis $\Re e(k_2\epsilon)$. The dispersion relations of the homogenized model can also be determined seeking solutions from the governing Eqs. (2.70a) and (2.70b) (with source terms assumed zero) of the forms $\hat{\boldsymbol{U}}^M = \check{\boldsymbol{U}}^M \exp[\mathrm{i}(\boldsymbol{k}\cdot\mathbf{x} + 2\pi n)]$ and $\hat{\Theta}^M = \check{\Theta}^M \exp[\mathrm{i}(\boldsymbol{k}\cdot\mathbf{x} + 2\pi n)]$ (with $n \in \mathbb{Z}$) for the displacement and temperature, respectively. When $n = 0$ one arrives to the functions (2.88), (2.90), (2.91), while when $n = -1$, $n = 1$ one produces the translated curves drawn in light blue displayed in the Figs. $16(a)$ and $16(c)$. Besides, since a first order homogenization was applied one may notice an accurate approximation between the light curves and dark ones along the thermal wave propagation, in other words the dispersion function derived from the homogenization process shows a very good agreement with the dispersion function obtained taking advantage of the Floquet–Bloch theory, seen in Appendixes B, C and D, for the interval $2\pi(1-n)/3 < \Re e(k_2\epsilon) < 2\pi(1+n)/3, \forall n \in \mathbb{Z}$. The Figs. $16(a)$ and $16(c)$ show the dispersion functions associated to $n = -1$, $n = 0$ and $n = 1$, where may be observed that for a low frequency the curves of the heterogeneous continuum (dark red) are quite precise in respect to those obtained from the homogenization process of the material (light red). For a high frequency can be noticed that the curves of the heterogeneous continuum (dark red) are well approximated with a tiny deviation when compared to the translated curves ($n = -1$ and $n = 1$) gotten from the homogenization process of the material (light blue). Fig. $16(b)$ shows a zoom of the thermal wave propagation by attenuation in space seen in Fig. $16(a)$. The dimensionless angular frequency $\omega\tau^{(1)}$ by the dimensionless real wave number $\Re e(k_2\epsilon)$ plane and the dimensionless angular frequency $\omega\tau^{(1)}$ by the dimensionless attenuation factor $\Im m(k_2\epsilon)$ plane are represented in $16(c)$ and $16(d)$, respectively.

For a better understanding of the first order homogenization facing its heterogeneous version, the Fig. 17 has been made varying some parameters, where dark curves represent the heterogeneous material obtained via Floquet-Bloch the-

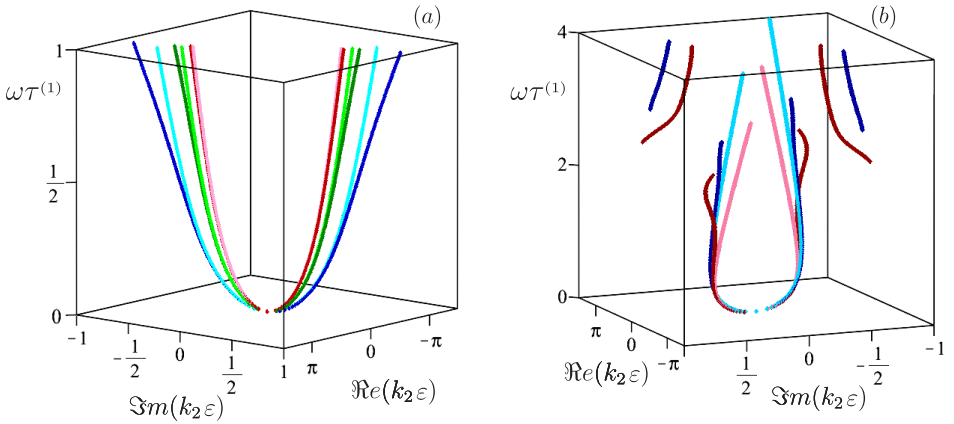

Figure 17: Dimensionless dispersion functions associated to thermal waves when $k_1 = 0$. Comparison between homogenized models (light curves) and their respective heterogeneous ones (dark curves) given different values of the parameters. (a) fixed parameters $\eta = 1$, $p^{(1)}T_0/\left(\tau^{(1)}\bar{K}_{22}^{(1)}\right) = 1$ with $\tau^{(2)}/\tau^{(1)} = 3$, $\bar{K}_{22}^{(2)}/\bar{K}_{22}^{(1)} = 3$, $p^{(2)}/p^{(1)} = 3$ (red curves); $\tau^{(2)}/\tau^{(1)} = 5$, $\bar{K}_{22}^{(2)}/\bar{K}_{22}^{(1)} = 5$, $p^{(2)}/p^{(1)} = 5$ (green curves); $\tau^{(2)}/\tau^{(1)} = 10$, $\bar{K}_{22}^{(2)}/\bar{K}_{22}^{(1)} = 10$, $p^{(2)}/p^{(1)} = 10$ (blue curves); (b) fixed parameters $\tau^{(2)}/\tau^{(1)} = 3$, $\bar{K}_{22}^{(2)}/\bar{K}_{22}^{(1)} = 3$, $p^{(2)}/p^{(1)} = 3$, $p^{(1)}T_0/\left(\tau^{(1)}\bar{K}_{22}^{(1)}\right) = 1$, thickness as $\eta = 1$ (red curves), $\eta = 10$ (blue curves).

ory, whereas light curves are for the first order homogenized model. Essentially, Fig. 17(a) displays three zoomed different situations for the thermal wave propagation when $\eta = 1$ and $p^{(1)}T_0/\left(\tau^{(1)}\bar{K}_{22}^{(1)}\right) = 1$, namely the curves in red were plotted setting $\tau^{(2)}/\tau^{(1)} = 3$, $\bar{K}_{22}^{(2)}/\bar{K}_{22}^{(1)} = 3$, $p^{(2)}/p^{(1)} = 3$, for the second scenario the curves in green were generated choosing $\tau^{(2)}/\tau^{(1)} = 5$, $\bar{K}_{22}^{(2)}/\bar{K}_{22}^{(1)} = 5$, $p^{(2)}/p^{(1)} = 5$, and for the third situation the curves in blue were plotted choosing the parameters $\tau^{(2)}/\tau^{(1)} = 10$, $\bar{K}_{22}^{(2)}/\bar{K}_{22}^{(1)} = 10$, $p^{(2)}/p^{(1)} = 10$. Furthermore, regarding the behaviour led by the different values of the dimensionless parameters taken, it can be noted in the Fig. 17(a) that an increase in the parameters $\tau^{(2)}/\tau^{(1)}$, $\bar{K}_{22}^{(2)}/\bar{K}_{22}^{(1)}$ and $p^{(2)}/p^{(1)}$, produces curves that bend less sharply, and hence have smaller curvatures. With an analogous idea, Fig. 17(b) displays two scenarios varying the thickness that are $\eta = 1$ represented by the red curves and $\eta = 10$ represented by the blue curves, while the parameters $\tau^{(2)}/\tau^{(1)} = 3$, $\bar{K}_{22}^{(2)}/\bar{K}_{22}^{(1)} = 3$, $p^{(2)}/p^{(1)} = 3$ and $p^{(1)}T_0/\left(\tau^{(1)}\bar{K}_{22}^{(1)}\right) = 1$, are fixed. Analysing the Fig. 17(b), it is notable that a decrease in the dimensionless thickness induce to bigger curvatures along the wave propagation. From these comparisons between the wave for the heterogeneous solid and their respectives for the

homogenized model illustrated in Fig. 17, it may be verified a good matching for the wave propagation between the two models exemplified considering the interval $2\pi(1-n)/3 < \Re e(k_2\epsilon) < 2\pi(1+n)/3, \forall n \in \mathbb{Z}$.

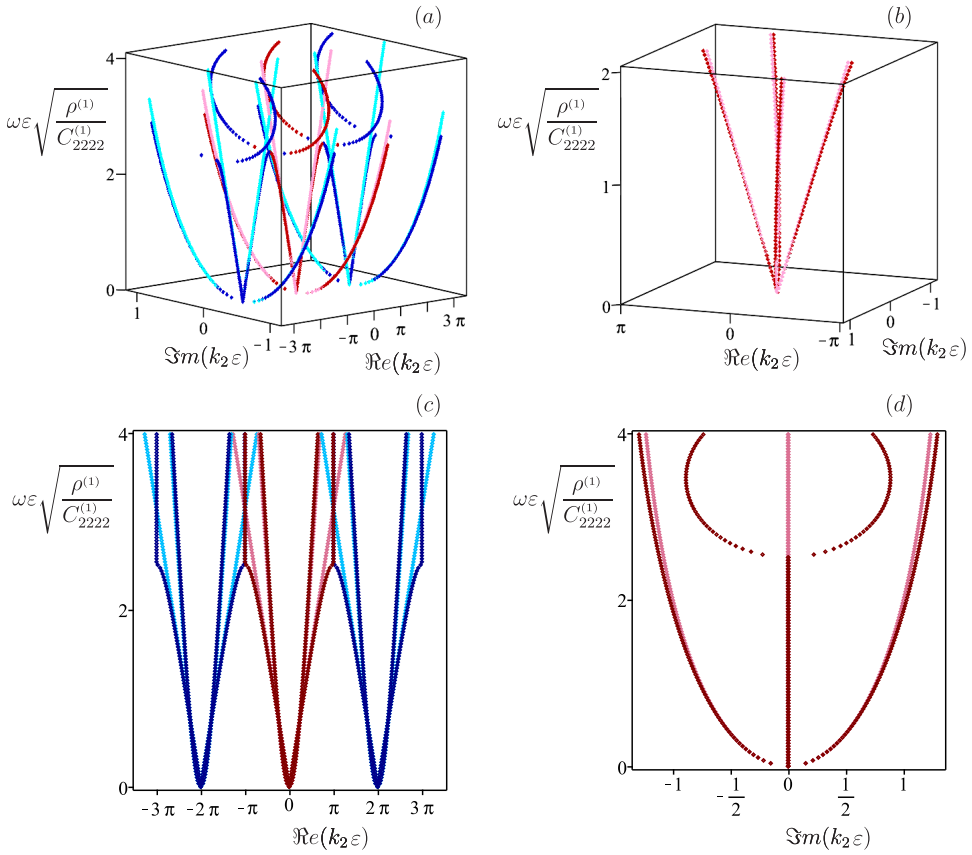

Figure 18: Dimensionless dispersion functions associated to compressional-thermal waves when $k_1 = 0$, $\eta = 1$, $\tau^{(2)}/\tau^{(1)} = 3$, $C^{(2)}_{2222}/C^{(1)}_{2222} = 3$, $\bar{K}^{(2)}_{22}/\bar{K}^{(1)}_{22} = 3$, $p^{(2)}/p^{(1)} = 3$, $\rho^{(2)}/\rho^{(1)} = 2$, $(\alpha^{(1)}_{22}T_0)/C^{(1)}_{2222} = 1/100$, $\alpha^{(2)}_{22}T_0/C^{(2)}_{2222} = 1/10$, $\alpha^{(1)}_{22}\eta\sqrt{C^{(1)}_{2222}/\rho^{(1)}}/\bar{K}^{(1)}_{22} = 1/100$, $\alpha^{(2)}_{22}\eta\sqrt{C^{(1)}_{2222}/\rho^{(1)}}/\bar{K}^{(2)}_{22} = 1/10$, $p^{(1)}T_0\eta\sqrt{C^{(1)}_{2222}/\rho^{(1)}}/\bar{K}^{(1)}_{22} = 1$ and $\tau^{(1)}\sqrt{C^{(1)}_{2222}/\rho^{(1)}}/\epsilon = 1/10$.
(*a*) $\omega\epsilon\sqrt{\rho^{(1)}/C^{(1)}_{2222}}$ vs. $\Re e(k_2\epsilon) \times \Im m(k_2\epsilon)$; (*b*) zoomed view of the angular frequency spectrum $\omega\epsilon\sqrt{\rho^{(1)}/C^{(1)}_{2222}}$ vs. $\Re e(k_2\epsilon) \times \Im m(k_2\epsilon)$; (*c*) view of the plane $\omega\epsilon\sqrt{\rho^{(1)}/C^{(1)}_{2222}} \times \Re e(k_2\epsilon)$; (*d*) view of the plane $\omega\epsilon\sqrt{\rho^{(1)}/C^{(1)}_{2222}} \times \Im m(k_2\epsilon)$.

Likewise the previous comparative test, under the hypothesis when the wave

number k_1 is assumed zero and the complex frequency is taken as $s = \mathrm{i}\omega$, the compressional-thermal wave function of the heterogeneous continuum via Floquet-Bloch theory and the compressional-thermal waves of the first order homogenized material are illustrated in the Fig. 18 by the dark blue and red lines, and the light blue and red lines, respectively. The dimensionless parameters were chosen as $\eta = 1$, $\tau^{(2)}/\tau^{(1)} = 3$, $C^{(2)}_{2222}/C^{(1)}_{2222} = 3$, $\bar{K}^{(2)}_{22}/\bar{K}^{(1)}_{22} = 3$, $p^{(2)}/p^{(1)} = 3$, $\rho^{(2)}/\rho^{(1)} = 2$, $(\alpha^{(1)}_{22}T_0)/C^{(1)}_{2222} = 1/100$, $\alpha^{(2)}_{22}T_0/C^{(2)}_{2222} = 1/10$, $\alpha^{(1)}_{22}\eta\sqrt{C^{(1)}_{2222}/\rho^{(1)}}/\bar{K}^{(1)}_{22} = 1/100$, $p^{(1)}T_0\eta\sqrt{C^{(1)}_{2222}/\rho^{(1)}}/\bar{K}^{(1)}_{22} = 1$, $\alpha^{(2)}_{22}\eta\sqrt{C^{(1)}_{2222}/\rho^{(1)}}/\bar{K}^{(2)}_{22} = 1/10$ and $\tau^{(1)}\sqrt{C^{(1)}_{2222}/\rho^{(1)}}/\epsilon = 1/10$. Figs. 18($a$) and 18($c$), both light and dark blue lines stand for the translations of their respective dispersion curves due to the periodicity of the material along $\boldsymbol{e}_2$ around $\Re e(k_2\epsilon) = 2\pi n$, which they go all along the real wave number axis $\Re e(k_2\epsilon)$. Moreover, one may observe a precise estimation between the light lines and dark ones along the compressional-thermal wave propagation. This means that the dispersion function derived from the first order homogenization process yield to a quite good matching when contrasted against the dispersion function determined with the Floquet–Bloch theory for the heterogeneous solid, elucidated in Appendixes B, C and D, for the interval $2\pi(1-n)/3 < \Re e(k_2\epsilon) < 2\pi(1+n)/3, \forall n \in \mathbb{Z}$. The Figs. 18($a$) and 18($c$), exhibit the dispersion functions when $n = -1$, $n = 0$ and $n = 1$, where may be noted that for a low frequency the curves of the heterogeneous continuum (dark red) are matched very well for those obtained from the homogenization process of the material (light red), in addition the same observation may be seen for the translated blue lines. Fig. 18(b) shows a zoom of the compressional-thermal wave propagation by spatial damping seen in Fig. 18(a). A bi-dimensional view of the dimensionless angular frequency $\omega\epsilon\sqrt{\rho^{(1)}/C^{(1)}_{2222}}$ by the dimensionless real wave number $\Re e(k_2\epsilon)$ plane and the dimensionless angular frequency $\omega\epsilon\sqrt{\rho^{(1)}/C^{(1)}_{2222}}$ by the dimensionless attenuation factor $\Im m(k_2\epsilon)$ plane are represented in 18(c) and 18(d), respectively. It is worthy of note that, the branches of the spectrum characterized when the real part $\Re e(k_2\epsilon)$ is set fixed as $\Im m(k_2\epsilon)$ varies, as expected, which characterize the first frequency stop-band for quasi-compressional waves and which propagate perpendicularly to the layering direction, they are unable to be approximated by the frequency spectrum obtained from the homogenized first order model, as showed in the Fig. 18(d). In order to overcome such encumbrance, it is feasible to use a perturbative technique, which will lead to a local asymptotic approximation of the compressional-thermal wave through local explicit and closed-form parametric expressions in the space of complex wave number and the angular

frequency [137, 180].

The Fig. 19 compares some cases of the compressional-thermal wave assuming different values of the dimensionless parameters, where the dark lines represent the waves obtained for the heterogeneous material via Floquet-Bloch theory, while the light lines are for the first order homogenized model. The Figs. 19(a) and 19(b) were generated taking the following values for dimensionless parameters $(\alpha_{22}^{(1)}T_0)/C_{2222}^{(1)} = 1/100$, $\alpha_{22}^{(2)}T_0/C_{2222}^{(2)} = 1/10$, $\alpha_{22}^{(1)}\eta\sqrt{C_{2222}^{(1)}/\rho^{(1)}}/\bar{K}_{22}^{(1)} = 1/100$, $\alpha_{22}^{(2)}\eta\sqrt{C_{2222}^{(1)}/\rho^{(1)}}/\bar{K}_{22}^{(2)} = 1/10$, $\tau^{(1)}\sqrt{C_{2222}^{(1)}/\rho^{(1)}}/\epsilon = 1/10$ and $p^{(1)}T_0\eta\sqrt{C_{2222}^{(1)}/\rho^{(1)}}/\bar{K}_{22}^{(1)} = 1$. Assuming $\eta = 1$, Fig. 19(a) shows three zoomed different cases for the compressional-thermal wave propagation. Therefore, the red lines were plotted setting $\tau^{(2)}/\tau^{(1)} = 3$, $C_{2222}^{(2)}/C_{2222}^{(1)} = 3$, $\bar{K}_{22}^{(2)}/\bar{K}_{22}^{(1)} = 3$, $p^{(2)}/p^{(1)} = 3$, $\rho^{(2)}/\rho^{(1)} = 2$, the green lines were drawn choosing $\tau^{(2)}/\tau^{(1)} = 5$, $C_{2222}^{(2)}/C_{2222}^{(1)} = 5$, $\bar{K}_{22}^{(2)}/\bar{K}_{22}^{(1)} = 5$, $p^{(2)}/p^{(1)} = 5$, $\rho^{(2)}/\rho^{(1)} = 4$, and finally the lines in blue represent the situation in which $\tau^{(2)}/\tau^{(1)} = 10$, $C_{2222}^{(2)}/C_{2222}^{(1)} = 10$, $\bar{K}_{22}^{(2)}/\bar{K}_{22}^{(1)} = 10$, $p^{(2)}/p^{(1)} = 10$, $\rho^{(2)}/\rho^{(1)} = 6$. Taking a look closely at the curvatures of the compressional-thermal waves plotted in the Fig. 19(a), it may be affirmed that increasing the numerical values of $\tau^{(2)}/\tau^{(1)}$, $C_{2222}^{(2)}/C_{2222}^{(1)}$, $\bar{K}_{22}^{(2)}/\bar{K}_{22}^{(1)}$, $p^{(2)}/p^{(1)}$ and $\rho^{(2)}/\rho^{(1)}$, the curves show a tendency of having smaller curvatures. The compressional-thermal waves behaviour is foretold in matters of different values of the thickness η, the Fig. 19(b) displays two scenarios where is fixed $\tau^{(2)}/\tau^{(1)} = 3$, $C_{2222}^{(2)}/C_{2222}^{(1)} = 3$, $\bar{K}_{22}^{(2)}/\bar{K}_{22}^{(1)} = 3$, $p^{(2)}/p^{(1)} = 3$, $\rho^{(2)}/\rho^{(1)} = 2$, and varying the thickness that are $\eta = 1$ and $\eta = 20$ represented by the red and blue lines, respectively. Such comparisons provided by the Fig. 19 shows a good agreement of the compressional-thermal wave propagation between the two models exemplified considering the interval $2\pi(1-n)/3 < \Re e(k_2\epsilon) < 2\pi(1+n)/3, \forall n \in \mathbb{Z}$.

Some plots of the shear waves may be seen in Fig. 20, where red lines stand for the central shear wave, blue lines for the translated shear waves, and the nuances in the color distinguish the shear curve of the heterogeneous continuum (dark lines) from the shear wave first order homogenized (light lines). In regards to de capability of the first order homogenization process for the shear wave, it also shows itself in a good agreement with its heterogeneous continuum from the Floquet-Bloch theory. The Fig. 20 was drawn adopting the dimensionless parameters as $\eta = 1$, $C_{1212}^{(2)}/C_{1212}^{(1)} = 1$ and $\rho^{(2)}/\rho^{(1)} = 2$. Note that, as verified for the compressional-thermal wave, and with a cleaner comprehension looking at the Fig. 20(d), also the frequency stop-bands of the shear wave propagating perpendicularly to the layering direction is not well

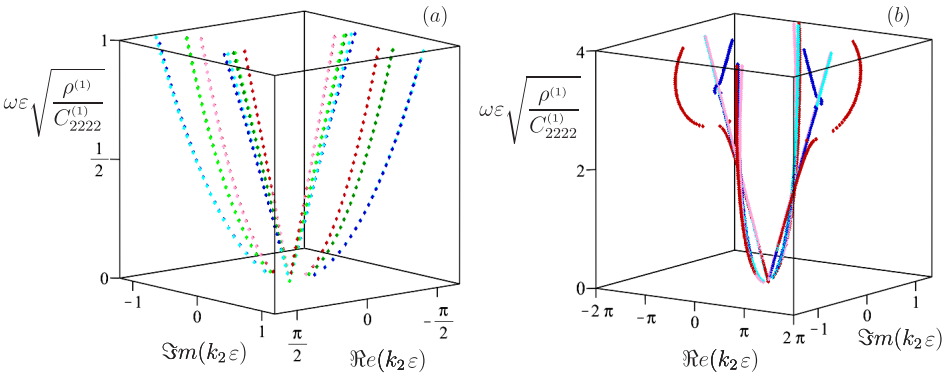

Figure 19: Dimensionless dispersion functions associated to compressional-thermal waves when $k_1 = 0$, $(\alpha^{(1)}_{22}T_0)/C^{(1)}_{2222} = 1/100$, $\alpha^{(2)}_{22}T_0/C^{(2)}_{2222} = 1/10$, $\alpha^{(1)}_{22}\eta\sqrt{C^{(1)}_{2222}/\rho^{(1)}}/\bar{K}^{(1)}_{22} = 1/100$, $\alpha^{(2)}_{22}\eta\sqrt{C^{(1)}_{2222}/\rho^{(1)}}/\bar{K}^{(2)}_{22} = 1/10$, $p^{(1)}T_0\eta\sqrt{C^{(1)}_{2222}/\rho^{(1)}}/\bar{K}^{(1)}_{22} = 1$ and $\tau^{(1)}\sqrt{C^{(1)}_{2222}/\rho^{(1)}}/\epsilon = 1/10$. (a) $\eta = 1$, with $\tau^{(2)}/\tau^{(1)} = 3$, $C^{(2)}_{2222}/C^{(1)}_{2222} = 3$, $\bar{K}^{(2)}_{22}/\bar{K}^{(1)}_{22} = 3$, $p^{(2)}/p^{(1)} = 3$, $\rho^{(2)}/\rho^{(1)} = 2$, (red curves); $\tau^{(2)}/\tau^{(1)} = 5$, $C^{(2)}_{2222}/C^{(1)}_{2222} = 5$, $\bar{K}^{(2)}_{22}/\bar{K}^{(1)}_{22} = 5$, $p^{(2)}/p^{(1)} = 5$, $\rho^{(2)}/\rho^{(1)} = 4$, (green curves); $\tau^{(2)}/\tau^{(1)} = 10$, $C^{(2)}_{2222}/C^{(1)}_{2222} = 10$, $\bar{K}^{(2)}_{22}/\bar{K}^{(1)}_{22} = 10$, $p^{(2)}/p^{(1)} = 10$, $\rho^{(2)}/\rho^{(1)} = 6$, (blue curves); (b) fixed parameters $\tau^{(2)}/\tau^{(1)} = 3$, $C^{(2)}_{2222}/C^{(1)}_{2222} = 3$, $\bar{K}^{(2)}_{22}/\bar{K}^{(1)}_{22} = 3$, $p^{(2)}/p^{(1)} = 3$, $\rho^{(2)}/\rho^{(1)} = 2$, thickness as $\eta = 1$ (red curves), $\eta = 20$ (blue curves).

described by the first order homogenization technique developed. As aforementioned, to remedy this issue the shear waves may be approached by a perturbative method through explicit and closed-form parametric expressions, in which will approximate locally the real spectrum of the non-homogeneous material [137, 180].

The Fig. $21(a)$ exhibits three zoomed different cases for the shear wave propagation for a fixed thickness $\eta = 1$. The red lines represent the choices for the parameters as $C^{(2)}_{1212}/C^{(1)}_{1212} = 1$, $\rho^{(2)}/\rho^{(1)} = 2$, the green lines stand for $C^{(2)}_{1212}/C^{(1)}_{1212} = 5$, $\rho^{(2)}/\rho^{(1)} = 5$, and lastly, the lines that approximate locally the real spectrum of the heterogeneous material in blue correspond to the case when $C^{(2)}_{1212}/C^{(1)}_{1212} = 10$, $\rho^{(2)}/\rho^{(1)} = 10$. From a quick analysis over the Fig. $21(a)$, it can be assured that the curvatures of the shear waves are reduced numerically due to a rise in the values of the non-dimensional parameters $C^{(2)}_{1212}/C^{(1)}_{1212}$ and $\rho^{(2)}/\rho^{(1)}$. Varying the thickness η namely $\eta = 1$ (red curves) and $\eta = 20$ (blue curves), and adopting the dimensionless parameters as $C^{(2)}_{1212}/C^{(1)}_{1212} = 1$, $\rho^{(2)}/\rho^{(1)} = 2$, both shear waves for these assumptions are contrasted in the Fig. $21(b)$. Essentially, the Fig. 21 illustrates the good estimation of the shear wave propagation between the two models developed

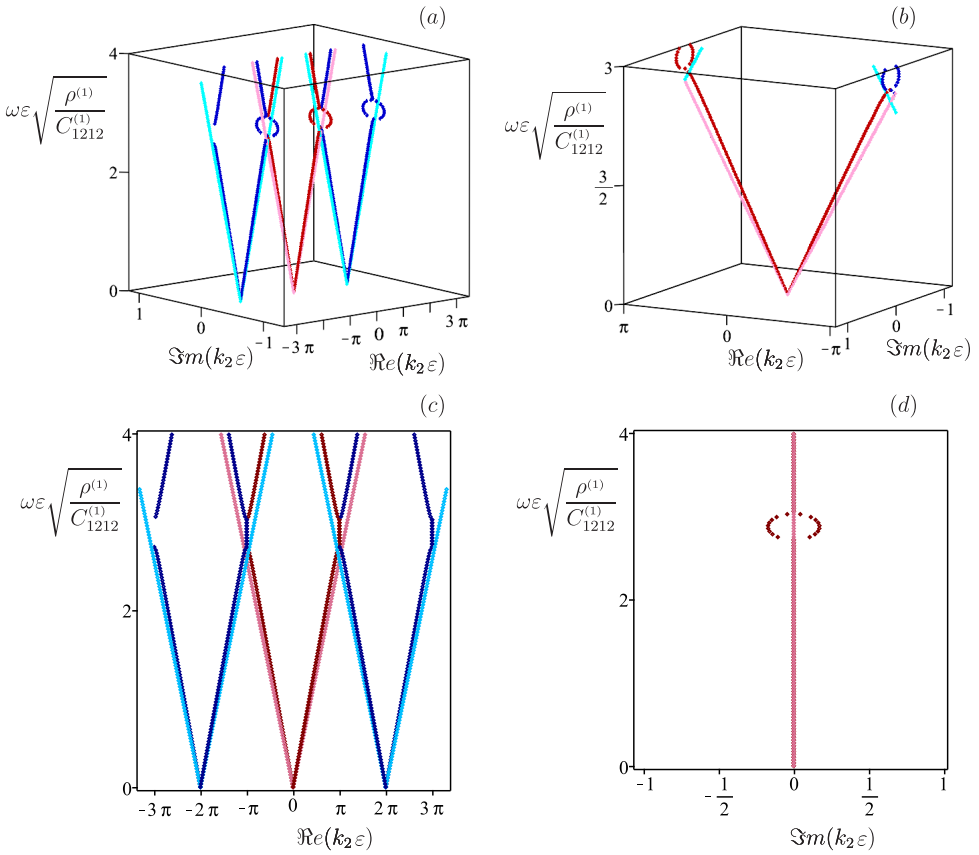

Figure 20: Dimensionless dispersion functions associated to shear waves when $k_1 = 0$, $\eta = 1$, $C^{(2)}_{1212}/C^{(1)}_{1212} = 1$ and $\rho^{(2)}/\rho^{(1)} = 2$. (a) $\omega\epsilon\sqrt{\rho^{(1)}/C^{(1)}_{1212}}$ vs. $\Re e(k_2\epsilon)\times\Im m(k_2\epsilon)$; (b) zoomed view of the angular frequency spectrum $\omega\epsilon\sqrt{\rho^{(1)}/C^{(1)}_{1212}}$ vs. $\Re e(k_2\epsilon)\times\Im m(k_2\epsilon)$; (c) view of the plane $\omega\epsilon\sqrt{\rho^{(1)}/C^{(1)}_{1212}}\times\Re e(k_2\epsilon)$; (d) view of the plane $\omega\epsilon\sqrt{\rho^{(1)}/C^{(1)}_{1212}}\times\Im m(k_2\epsilon)$.

considering the interval $2\pi(1-n)/3 < \Re e(k_2\epsilon) < 2\pi(1+n)/3, \forall n \in \mathbb{Z}$.

In order to analyse the effects of the presence of the relaxation time in the thermoelastic equation of Lord-Shulman, Fig. 22 displays a few compressional-thermal waves for four different values of the dimensionless relaxation time $\tau^{(1)}\sqrt{C^{(1)}_{2222}/\rho^{(1)}}/\epsilon$ of the phase 1 of the layered material and choosing the dimensionless relaxation time parameter between the layers as $\tau^{(2)}/\tau^{(1)} = 1$, while the other parameters were set fixed throughout the curves as $\eta = 1$, $C^{(2)}_{2222}/C^{(1)}_{2222} = 3$, $\bar{K}^{(2)}_{22}/\bar{K}^{(1)}_{22} =$

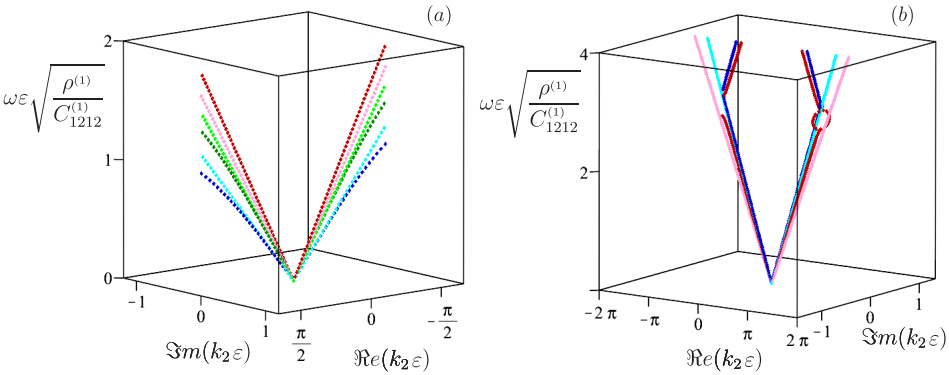

Figure 21: Dimensionless dispersion functions associated to shear waves when $k_1 = 0$. (a) setting $\eta = 1$, with $C^{(2)}_{1212}/C^{(1)}_{1212} = 1$, $\rho^{(2)}/\rho^{(1)} = 2$, (red curves); $C^{(2)}_{1212}/C^{(1)}_{1212} = 5$, $\rho^{(2)}/\rho^{(1)} = 5$, (green curves); $C^{(2)}_{1212}/C^{(1)}_{1212} = 10$ and $\rho^{(2)}/\rho^{(1)} = 10$, (blue curves); (b) fixed $C^{(2)}_{1212}/C^{(1)}_{1212} = 1$, $\rho^{(2)}/\rho^{(1)} = 2$, thickness as $\eta = 1$ (red curves); $\eta = 20$ (blue curves).

3, $p^{(2)}/p^{(1)} = 3$, $\rho^{(2)}/\rho^{(1)} = 2$, $(\alpha^{(1)}_{22}T_0)/C^{(1)}_{2222} = 1/100$, $\alpha^{(2)}_{22}T_0/C^{(2)}_{2222} = 1/10$, $\alpha^{(1)}_{22}\eta\sqrt{C^{(1)}_{2222}/\rho^{(1)}}/\bar{K}^{(1)}_{22} = 1/100$, $\alpha^{(2)}_{22}\eta\sqrt{C^{(1)}_{2222}/\rho^{(1)}}/\bar{K}^{(2)}_{22} = 1/10$ and $p^{(1)}T_0\eta\sqrt{C^{(1)}_{2222}/\rho^{(1)}}/\bar{K}^{(1)}_{22} = 1$. For such a comparison, once again, the light curves represent the homogenized model, whereas the dark curves indicate the waves characterized by the heterogeneous continuum. The red curves stand for $\tau^{(1)}\sqrt{C^{(1)}_{2222}/\rho^{(1)}}/\epsilon = 0$, the green lines represent the waves for $\tau^{(1)}\sqrt{C^{(1)}_{2222}/\rho^{(1)}}/\epsilon = 1/10$, the waves in blue are representing the case in which $\tau^{(1)}\sqrt{C^{(1)}_{2222}/\rho^{(1)}}/\epsilon = 1$, and the lines with a yellow color indicate the scenario where $\tau^{(1)}\sqrt{C^{(1)}_{2222}/\rho^{(1)}}/\epsilon = 10$. Over this analysis, as expected, it can be seen that the red lines, the ones where the dimensionless relaxation time were set zero, have smaller curvature as compared to the rest of the curves, and of course as the relaxation time increases, the curvature of the curves also increases. This implies that on one hand for low frequencies the dispersion curves associated with the quasi-thermal waves present an imaginary part of the dimensionless wave number (which characterizes the spatial damping of the wave) that in modulus tends to decrease as the dimensionless relaxation time increases. On the other hand, we observe the real part of the dimensionless wave number that in modulus tends to increase as the dimensionless relaxation time increases. Specifically, it is possible to observe very different qualitatively scenarios of the frequency

band structure of the layered material as the dimensionless relaxation time of phase 1 varies, often obtaining phenomena of increasingly complex and dense frequency band structures at low frequencies as the dimensionless relaxation time grows. Furthermore, a good accuracy of the dispersion curves obtained from the homogenized model is also found here.

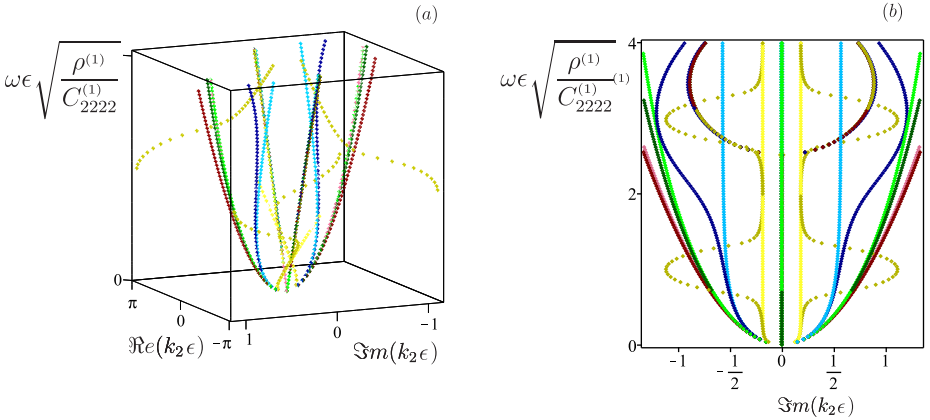

Figure 22: Dimensionless dispersion functions associated to compressional-thermal waves when $k_1 = 0$, $\eta = 1$, $\tau^{(2)}/\tau^{(1)} = 1$, $C^{(2)}_{2222}/C^{(1)}_{2222} = 3$, $\bar{K}^{(2)}_{22}/\bar{K}^{(1)}_{22} = 3$, $p^{(2)}/p^{(1)} = 3$, $\rho^{(2)}/\rho^{(1)} = 2$, $(\alpha^{(1)}_{22}T_0)/C^{(1)}_{2222} = 1/100$, $\alpha^{(2)}_{22}T_0/C^{(2)}_{2222} = 1/10$, $\alpha^{(1)}_{22}\eta\sqrt{C^{(1)}_{2222}/\rho^{(1)}}/\bar{K}^{(1)}_{22} = 1/100$, $\alpha^{(2)}_{22}\eta\sqrt{C^{(1)}_{2222}/\rho^{(1)}}/\bar{K}^{(2)}_{22} = 1/10$, $p^{(1)}T_0\eta\sqrt{C^{(1)}_{2222}/\rho^{(1)}}/\bar{K}^{(1)}_{22} = 1$, $\tau^{(1)}\sqrt{C^{(1)}_{2222}/\rho^{(1)}}/\epsilon = 0$ (red curves); $\tau^{(1)}\sqrt{C^{(1)}_{2222}/\rho^{(1)}}/\epsilon = 1/10$ (green curves); $\tau^{(1)}\sqrt{C^{(1)}_{2222}/\rho^{(1)}}/\epsilon = 1$ (blue curves); $\tau^{(1)}\sqrt{C^{(1)}_{2222}/\rho^{(1)}}/\epsilon = 10$ (yellow curves); (a) $\omega\epsilon\sqrt{\rho^{(1)}/C^{(1)}_{2222}}$ vs. $\Re e(k_2\epsilon) \times \Im m(k_2\epsilon)$; (b) view of the plane $\omega\epsilon\sqrt{\rho^{(1)}/C^{(1)}_{2222}} \times \Im m(k_2\epsilon)$.

Lastly, it is noteworthy that in the case where the dimensionless relaxation time of phase 1 is $\tau^{(1)}\sqrt{C^{(1)}_{2222}/\rho^{(1)}}/\epsilon = 0$, and the parameter between the relaxation times is $\tau^{(2)}/\tau^{(1)} = 1$, we find the particular case of classical thermoelasticity. In fact, in this situation, the relaxation times of the phases are zero (i.e. $\tau^m = 0$), and the field equations of the periodic material in the Laplace transformed space (2.11a) and (2.11b) return to be those of the standard thermoelastic problem, since the thermal conduction constitutive tensor $\mathbf{K}^m$ from Eq. (2.12) becomes $s-$independent again. In this particular scenario, the asymptotic variational homogenization technique proposed here leads to the same global constitutive tensors that are obtained by applying the multi-field asymptotic homogenization procedure proposed in [137], focused exclusively in the study of the classical thermoelasticity without considering

the phenomenon of mass diffusion.

Chapter 3

Fracture characterization in Triply Periodic Minimal Surfaces unit cell foams via Phase Field theory

This Chapter is mainly taken from [17]. Firstly, the definition and generation of TPMS is introduced, so the issue of numerically characterize the occurrences of fracture, as well as the propagation paths in TPMS sheet networks by means of the regularization theory of phase field is then derived. The present endeavour is complemented by the validation of the results along several experimental studies present in literature.

3.1 Definition of minimal surfaces and mathematical characterization of TPMS structures

3.1.1 Minimal surfaces and soap films

Before introducing the definition of Triply Periodic Minimal Surfaces, let be defined the concept of a Minimal Surface. Minimal Surfaces are surfaces of minimal area subject to certain boundary conditions, which relates to a variational problem. Nevertheless, they can also be geometrically characterized by their mean curvature, which is

$$H(q) = \frac{k_2 + k_1}{2}, \tag{3.1}$$

with q a point on the surface $q \in S_X$ and k_1 and k_2 are the principal curvatures for some regular surface S_X, defined for some parametrization X in $\mathbb{R}^3$, which are determined by taking the maximum and minimum values of the curvatures of the curves formed by the intersection of the surface S_X with the orthogonal planes perpendicular to the tangent plane to the surface on a given point on S_X (see Fig. 23). The principal curvatures may also be obtained by finding the eigenvalues of the Gauss map of the surface S_X [38]. Geometrically, such curvatures of these intrinsic curves measure the change in direction of the tangent plane of that surface at a given point. On a minimal surface, the curvature along the principal curvature planes are equal and opposite at all point of the surface S_X, i.e

$$H(q) = 0, \quad \forall q \in S_X. \tag{3.2}$$

hence, if its mean curvature is identically zero, the surface S_X it is called minimal.

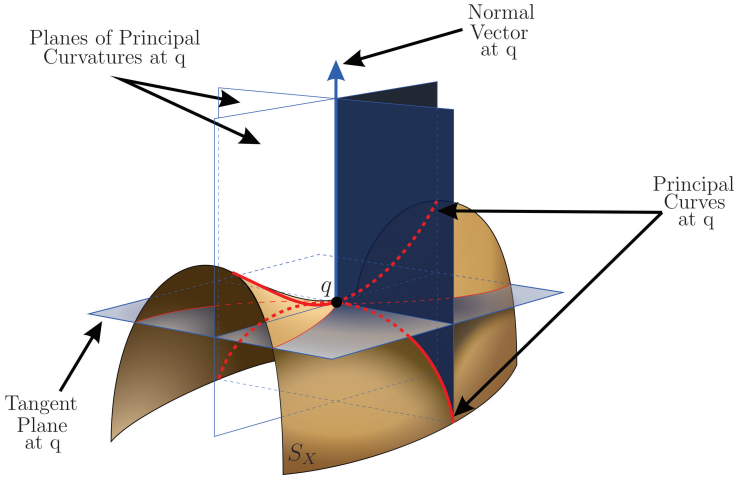

Figure 23: Curvature planes and principal curvatures. Adapted from [11].

Intuitively, mean curvature zero can be interpreted as Hoffman et al. [181] quoted *'Loosely speaking, one imagines the surface as made up of very many rubber bands, stretched out in all directions; on a minimal surface the forces due to the rubber bands balance out, and the surface does not need to move to reduce tension'.*

At this stage, it is worth mentioning that the definition of mean curvature does not depend on the parameterization X of the surface S_X taken. Given the definition above, the trivial example of a minimal surface is the plane, since the curvature of any intrinsic curve lying on the plane is always zero, therefore $H(q) = (k_1 + k_2)/2 = 0$.

Another essential geometric quantity in the description of surfaces is the Gaussian curvature, which is defined as

$$K(q) = k_1 k_2, \text{ with } q \in S_X, \tag{3.3}$$

that is, the product of the principal curvatures of S_X. Analogously, the Gaussian curvature is also independent of the parametrization X of S_X. An interesting feature of the minimal surfaces is that there are no compact minimal surfaces. A quick remark, a surface is compact if it is a compact topological space, since the surface is a subset of $\mathbb{R}^3$, if the surface is closed and bounded, then it is a compact set. [38]. In fact, let S_X be a minimal surface, then $H \equiv 0$, and so $k_1 = -k_2$. Thus, from the Gaussian curvature one has $K(q) = k_1 k_2 = k_1(-k_1) = -(k_1)^2 \leq 0$ for all $q \in S_X$, and given the fact that the Gaussian curvature function defined over the minimal surface S_X is continuous, one entails that the Gaussian curvature is always non-positive, implying that a minimal surface is unbounded.

The problem of finding a surface that has the smallest area bounded by a given closed curve is the Plateau's Problem [40]. From the standing point of the calculus of variations, where the mean curvature H appears naturally in the first variation of area [38, 182], the problem can be seen as follows

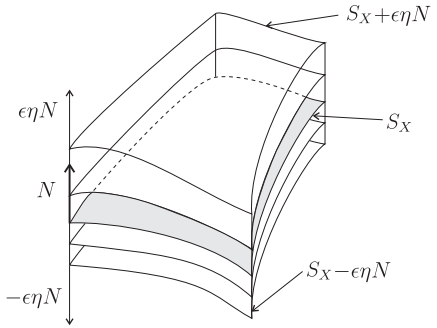

Figure 24: Normal variation of the surface S_X.

$$A(\epsilon) = \iint_{\Omega} \sqrt{EG - F^2}\sqrt{1 - 4H\epsilon\eta(u,v) + Q(\epsilon)}dudv, \tag{3.4}$$

where $Q'(0) = 0$, and thus $\lim_{\epsilon \to 0}(Q(\epsilon)/\epsilon) = 0$.

Therefore, $A'(0) = 0$ if and only if $H \equiv 0$. This fact guarantees that for any variation of the surface S in the direction of the normal vector, if the mean curvature vanishes everywhere, it entails that S_X is minimal, with the initial definition [38, 183]. It can be concluded that any bounded and closed region of a minimal surface is a critical point for the area functional at any normal variation of that bounded and closed region. Note that, the critical point provides a relative minimum, which makes the word *minimal* be inadequate in this context, even though such terminology is enshrined throughout history.

As aforementioned, the great notoriety of minimal surfaces came with the possibility of interpret them as soap films, which has leveraged studies over time in various areas of mathematics and other science fields. As such, consider drowning a thin wire frame that shapes a sharp curve in a mixture of soap and water, after removing it from the solution, a thin film of soap will appear having the wire frame as its boundary, which is in equilibrium under the action of the surface tension of the liquid [184]. It is worth emphasizing that every minimal surface can be represented as a soap film from a wire frame, however, not every soap film is a minimal surface in the sense of the present definition, for instance, a soap bubble, which is nothing more but a sphere, it can easily be shown that the mean curvature of a sphere is always positive for the entire sphere [185].

Several well known examples of minimal surfaces and their soap films forms are frequently mentioned namely, the helicoid Fig. 25, and the catenoid Fig. 26. The helicoid, which is shaped by a double helix curve, the same design shown in the DNA's shape [186], posses the property of being the only ruled minimal surface, i.e. generated by straight lines, in addition to the plane [183]. Whereas, the catenoid, formed between two axial rings, is the only minimal surface of revolution, beside the plane. Fig. 27 display the famous minimal surface of Scherk, which can be obtained by the minimal surface differential equation, assuming a parametrized solution in which the variables can be separated [183, 187].

Notwithstanding, beyond the classical definition of a vanishing mean curvature, and Plateau's Problem, there is a plethora of different ways, yet equivalent, to define minimal surfaces, and therefore TPMS, as described in the forthcoming.

3.1.2 Characterization of Triply Periodic Minimal Surfaces

Mathematically, a TPMS is a minimal surface in $\mathbb{R}^3$ that is invariant under a rank-3 lattice of translations, meaning that a TPMS is periodic along all three dimensional

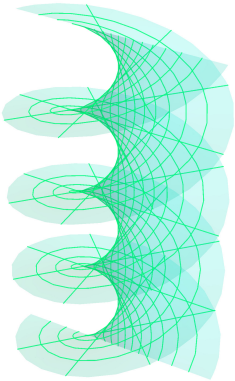

(a) Helicoid minimal surface.

(b) Helicoid soap film. Source [188].

Figure 25: Helicoid.

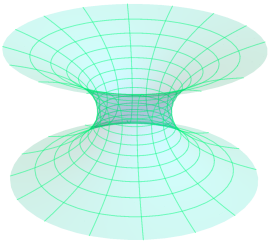

(a) Catenoid minimal surface.

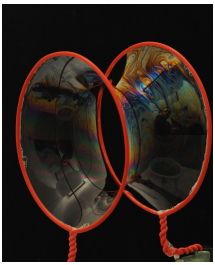

(b) Catenoid soap film. Source [189].

Figure 26: Catenoid.

directions. Figs. 28 and 29 depict some well known TPMS examples. Fig. 28a and Fig. 28b, display respectively, the unit cell and a three cells cluster of the Schwarz Primitive minimal surface. Whereas Fig. 29a and Fig. 29b, display respectively, the unit cell and a three cells cluster of the Schoen Gyroid minimal surface [191].

Minimal surfaces, and consequently TPMS can be precisely defined by the

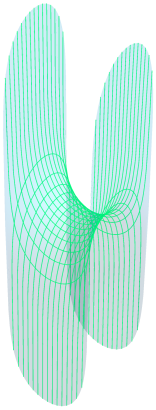

(a) Minimal surface of Scherk.

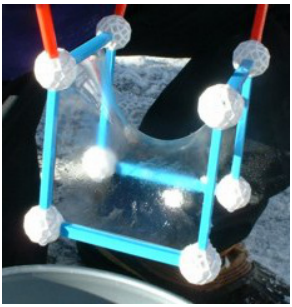

(b) Surface of Scherk soap film. Source [190].

Figure 27: Surface of Scherk.

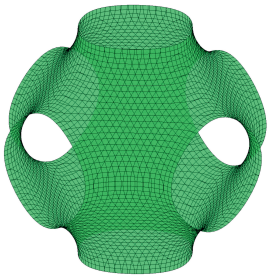

(a) Schwarz Primitive unit cell surface.

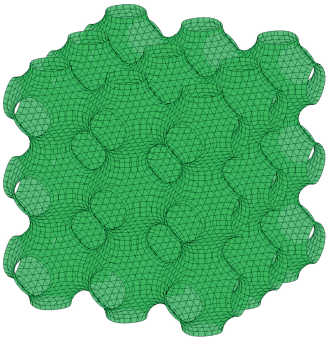

(b) Schwarz Primitive three cells cluster surface.

Figure 28: Schwarz Primitive minimal surface.

Weierstrass-Enneper representation [38, 39, 182], as in the following: let $w = u + iv$ be the complex variable defined on a open set $\mathcal{D} \in \mathbb{C}$, thus the Weierstrass-Enneper parametrization is

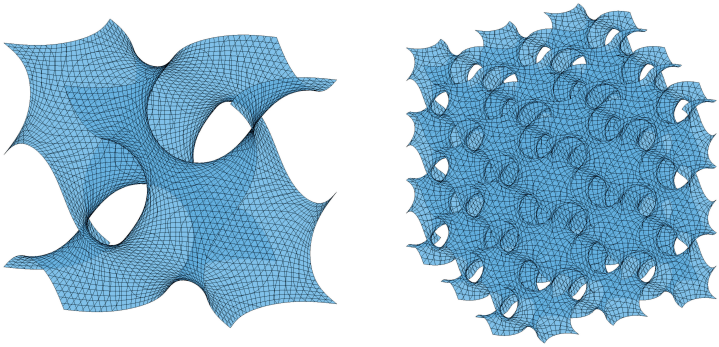

(a) Schoen Gyroid unit cell surface. (b) Schoen Gyroid three cells cluster surface.

Figure 29: Schoen Gyroid minimal surface.

$$
\begin{aligned}
x(w) &= \Re e\left(\int_{w_0}^{w} e^{\mathrm{i}\theta}(1-\tau^2)R(\tau)d\tau\right),\\
y(w) &= \Re e\left(\int_{w_0}^{w} e^{\mathrm{i}\theta} i(1-\tau^2)R(\tau)d\tau\right),\\
z(w) &= \Re e\left(\int_{w_0}^{w} e^{\mathrm{i}\theta} 2\tau R(\tau)d\tau\right),
\end{aligned}
\tag{3.5}
$$

where $R(\tau)$ (Weierstrass function) is a non vanishing analytic function defined on a simply connected domain in $\mathbb{C}$, and the multiplication by a complex number of unit magnitude is known as the Bonnet transformation by the Bonnet angle θ [192, 193], which has been an useful tool in generating new TPMS by converting the free boundary problem to the Plateau's problem [194–196]. The minimal surfaces are determined by integrating the coordinates in Eqs. (3.5), which analytical solutions constructed by reflection or rotation (through the Bonnet angle) about the patch boundary entirely generates the surface for some TPMS [197–199]. Nonetheless, in practice, computing the complex integrals using Weierstrass-Enneper representation (3.5) can be rather worrisome to be tackled, and by consequence evaluate their effective properties.

As matter of fact, once the TPMS are characterized for its periodicity in the three independent Cartesian directions, such surfaces can be approximated by the periodic nodal surfaces (PNS) of a sum defined in terms of the Fourier series [51, 200, 201],

$$\Psi(\boldsymbol{r}) = \sum_{\mathbf{k}} F(\mathbf{k}) \cos[\mathbf{k} \cdot \boldsymbol{r} - \alpha(\mathbf{k})] = C, \tag{3.6}$$

where $\boldsymbol{r} \in \mathbb{D} \subset \mathbb{R}^3$, $\mathbb{D}$ a closed set dependent of $\mathbf{k}$, which are the TPMS function periodicities, $\alpha(\mathbf{k})$ is a phase shift, and the structure factor $F(\mathbf{k})$ is an amplitude associated with a given $\mathbf{k}-$vector. Naturally, the quality of the approximation of a TPMS by nodal surfaces depends on the number of terms in the Fourier series (3.6). However, the minimal surface is satisfactorily reproduced by truncating such series to the leading point and setting the level surface $C = 0$, where the resulting minimal surface will split the space into two sub-domains of equal volumes [202, 203]. For a nodal surface described by the Eq. (3.6), the mean curvature and the Gaussian curvature are given in terms of the unit normal vector field $\mathbf{n}$ [182, 203, 204], respectively, as

$$\mathrm{H} = \nabla \cdot \mathbf{n}, \tag{3.7}$$

$$\mathrm{K} = \frac{\mathbf{n} \cdot \nabla^2 \mathbf{n} + [\nabla \cdot \mathbf{n}]^2 + [\nabla \times \mathbf{n}]^2}{2}, \tag{3.8}$$

with $\mathbf{n} = \nabla\Psi(\boldsymbol{r})/\|\nabla\Psi(\boldsymbol{r})\|$.

In the present work, the decision of taking a specific definition among all relies on how the mathematical description of the surface will unravel the analytical, numerical and experimental steps. It is noteworthy that although representing the TPMS through a truncation of the Fourier series (3.6) does not give a surface with an exact zero mean curvature in Eq. (3.7), the viability is quite simple and accessible [201, 202, 205], once the truncated series to the leading term give rise to an implicit function (as known as isosurface) essentially formed of a combination of trigonometric functions. Such an approach has been capable of producing several numerical studies in the area of mechanics showing the multi-functionality of the TPMS [52, 206, 207], their mechanical properties by means of finite elements analysis (FEA) [73, 208], and additive manufactured TPMS prototypes [13, 57, 60, 71, 75, 161], as well as in tissue engineering via AM in order to predict experimentally, with the aid of FEA, responses of cellular TPMS models [61, 63, 64, 160, 209].

3.2 Phase Field approach to fracture: Variational formulation and weak form model

Let us consider an arbitrary n-dimensional solid body Ω in the Euclidean space $\mathbb{R}^n$, with its external boundary $\partial\Omega \in \mathbb{R}^{n-1}$, in which an evolving internal discontinuity $\Gamma \in \mathbb{R}^{n-1}$ is postulated. The position of a material point is denoted by the vector $\mathbf{x}$ in the global Cartesian frame within the bulk. The body is characterized by the kinematic displacement field $\mathbf{u}(\mathbf{x})$ and the strain field is defined as a symmetric gradient ($\nabla^s(\cdot)$) of the displacement field, i.e. $\boldsymbol{\varepsilon}(\mathbf{x}) := \nabla^s(\mathbf{u}(\mathbf{x}))$ for all $\mathbf{x} \in \Omega$. The external boundary of the body $\partial\Omega \in \mathbb{R}^{n-1}$ is split into two disjoint sets, namely $\partial\Omega_{\mathbf{u}} \subset \partial\Omega$ and $\partial\Omega_{\mathbf{t}} \subset \partial\Omega$, with $\overline{\partial\Omega_{\mathbf{t}} \cup \partial\Omega_{\mathbf{u}}} = \partial\Omega$ and $\partial\Omega_{\mathbf{t}} \cap \partial\Omega_{\mathbf{u}} = \emptyset$, such that the displacement boundary conditions are prescribed as $\bar{\mathbf{u}}(\mathbf{x})$ for $\mathbf{x} \in \partial\Omega_{\mathbf{u}}$, and traction conditions are given by $\boldsymbol{\sigma} \cdot \mathbf{n} = \bar{\mathbf{t}}(\mathbf{x})$ for $\mathbf{x} \in \partial\Omega_{\mathbf{t}}$, where $\mathbf{n}$ denotes the outward normal unit vector to the body, and $\boldsymbol{\sigma}$ is the Cauchy stress tensor, as shown in Fig. 30a. Therefore, the external potential energy functional is defined by

$$\Pi_{\text{ext}}(\mathbf{u}) = \int_{\partial\Omega} \bar{\mathbf{t}} \cdot \mathbf{u} \, \mathrm{d}\mathbf{S} + \int_{\Omega} \mathbf{b} \cdot \mathbf{u} \, \mathrm{d}\mathbf{V}, \tag{3.9}$$

where $\mathbf{b} : \Omega \longrightarrow \mathbb{R}^n$ is the distributed body force.

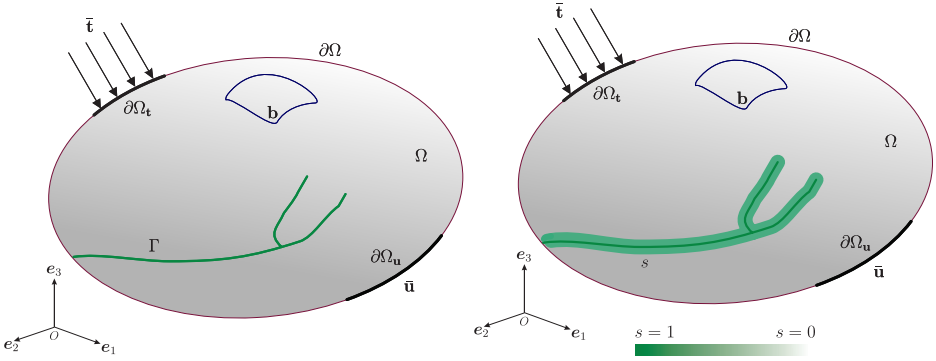

(a) Sharp crack in the bulk.

(b) Phase field regularization.

Figure 30: Schematic illustration of diffusive cracks.

The variational approach to fracture governing crack nucleation, propagation and branching according to Griffith's theory [142, 144, 210] is set up through the definition of the following total energy functional [144, 145, 211] in a quasi-elastic loading regime

$$\Pi(\mathbf{u},\Gamma) = \Pi_{\Omega}(\mathbf{u},\Gamma) + \Pi_{\Gamma}(\Gamma) + \Pi_{\text{ext}}(\mathbf{u}), \tag{3.10}$$

where $\Pi_{\Omega}(\mathbf{u},\Gamma)$ identifies the elastic energy stored in the damaged body given by a volume integral, while the energy required to create the crack complying with the Griffith criterion is denoted by $\Pi_{\Gamma}(\Gamma)$ given by a surface integral. Therefore, the total energy functional (3.10) reads

$$\Pi(\mathbf{u},\Gamma) = \int_{\Omega\setminus\Gamma} \psi^{e}(\boldsymbol{\varepsilon})\ \mathrm{d}\mathbf{V} + \int_{\Gamma} \mathcal{G}_c \mathrm{d}\mathbf{S} + \Pi_{\text{ext}}(\mathbf{u}), \tag{3.11}$$

where $\psi^{e}(\boldsymbol{\varepsilon})$ is the elastic energy density function that depends upon the strain field $\boldsymbol{\varepsilon}(\mathbf{u})$, and $\mathcal{G}_c$ is the fracture energy. In this scenario, at any given pseudo-time step $t \in [0,T]$, minimizing the functional (3.11) results in a crack set $\Gamma_t \subset \Omega$ ($\Gamma_t \supset \Gamma_t$), and a quasi-static displacement field $\mathbf{u}^t : \Omega \longrightarrow \mathbb{R}^n$, which is discontinuous over Γ_t. However, the path to solve this problem is very tortuous since the crack surface Γ is unknown a *priori* [143, 148].

To regularize the problem, i.e. the replacement of the crack surface variable by the phase field variable, introduces a smooth continuous bounded scalar field damage function $s(\mathbf{x},t)$ with $s \in [0,1]$, [143, 144, 149], where $s = 0$ represents an intact material, and $s = 1$ identifies the fully damaged state (see Fig.30b). Hence, the dissipated surface energy associated with the crack in the bulk Ω is approximated by

$$\Pi_{\Gamma} = \int_{\Gamma} \mathcal{G}_c(\mathbf{x},s)\mathrm{d}\mathbf{S} \cong \int_{\Omega} \mathcal{G}_c \gamma^{l}(s,\nabla s)\ \mathrm{d}\mathbf{V}. \tag{3.12}$$

where $\gamma^{l}(s,\nabla s)$ stands for the so-called crack surface energy density function. According to [145], the function $\gamma^{l}(s,\nabla s)$ is given by

$$\gamma^{l}(s,\nabla s) = \frac{1}{2l}s^2 + \frac{l}{2}|\nabla s|^2, \tag{3.13}$$

where $l \in \mathbb{R}^{+}$ stands for a regularization parameter related to the smeared crack width, responsible for controlling the width of the transition zone of the regularized crack. Thus, when the characteristic regularization parameter tends to zero ($l \to 0$), then the formulation outlined in Eq. (3.12) tends to its respective term in Eq. (3.10) in the sense of the so-called Γ-convergence [212–214].

In what regards the dependency of the energy density of the bulk $\psi(\boldsymbol{\varepsilon},s)$ in Eq. (3.11), is split in a tension/compression to prevent cracking under compresses loads,

and due to the regularization of the crack Γ by the phase field variable s, it also becomes $s(\mathbf{x})$ dependent, which means that

$$\psi^e(\mathbf{u}, s) = g(s)\psi_+(\varepsilon(\mathbf{u})) + \psi_-(\varepsilon(\mathbf{u})), \tag{3.14}$$

where $g(s)$ is a monotonically decreasing function representing the energetic degradation function characterized by the initial elastic energy function applied only in tension ψ_+, as proposed in [145].

Note that, since the phase field variable s is bounded, the degradation function chosen $g(s) = (1-s)^2 + k_l$ [143] is bounded as well, mapping $g(s) : [0,1] \to [1,0]$, with $k_l = \mathcal{O}(l) > 0$ a parameter that defines a residual stiffness to prevent numerical instabilities in the computational implementation, and simultaneously preventing that the resulting system of equations becomes ill-conditioned and $\psi_\pm$ the tensile and compressive part of the strain energy density as defined in [145]. Besides, the energetic degradation function $g(s)$ satisfies the following phase field conditions, which are

- The intact solid happens when $g(0) = 1$, while $g(1) = 0$ provides the fully broken state of the initial elastic energy.
- The function $g(s)$ is indeed monotonically decreasing. In fact, $g'(s) = dg/ds < 0$.
- When the material is completely broken, $g(s)$ is forced to stay complying $g'(1) = 0$. This condition avoids the localization band to grow orthogonally.

Hence, based on the previous regularizing assumptions within the framework of the phase field approach [143–145], the potential energy of the system in Eq. (3.10) can be recast as

$$\begin{aligned}\Pi_l(\mathbf{u}, s) = &\int_\Omega [(1-s)^2 + k_l]\psi_+(\varepsilon(\mathbf{u})) + \psi_-(\varepsilon(\mathbf{u}))\ \mathrm{d}\mathbf{V} + \\ &+ \int_\Omega \frac{\mathcal{G}_c}{2}\left[\frac{s^2}{l} + l|\nabla s|^2\right]\mathrm{d}\mathbf{V} + \Pi_{\text{ext}}(\mathbf{u}).\end{aligned} \tag{3.15}$$

The Eq. (3.15) regularizes the energy functional from Griffith's theory in Eq. (3.11) in the sense of $\Gamma-$convergence under the following restated Griffith's criteria [142, 143],

- **Irreversibility:** The cracks only grow in time, meaning that $\dot{\Gamma}(t) \geq 0$ or $\Gamma_t \subseteq \Gamma_{t+1}$. Over the regularized framework, one must have the function $g(s)$ monotonically decreasing, i.e $g'(s) = dg/ds < 0$.

- **Optimality Condition :** The first variation of the total energy functional, with the variation $(\delta\mathbf{u}, \delta s)$ of $(\mathbf{u}, s)$, gives

  - $\delta\Pi = 0$ for each $(\delta\mathbf{u}, \delta s) > 0$,
  - $\delta\Pi > 0$ for $(\delta\mathbf{u}, \delta s) = 0$.

- **Energy Conservation:** The regularized energy functional Eq. (3.15) (and of course Eq. (3.10)) must preserve the energy in time $t \in [0, T]$ as the cracks evolve, which means

$$\dot{\Pi} = \int_{\partial\Omega} (\boldsymbol{\sigma} \cdot \boldsymbol{n}) \cdot \dot{\mathbf{u}} \mathrm{d}\mathbf{S} - \int_{\Omega} \dot{\mathbf{b}} \cdot \mathbf{u} \mathrm{d}\mathbf{V} - \int_{\partial\Omega_t} \dot{\bar{\mathbf{t}}} \cdot \mathbf{u} \mathrm{d}\mathbf{S}, \tag{3.16}$$

  with stress $\boldsymbol{\sigma}$ defined as usual rate change of total energy with respect to strain $\boldsymbol{\varepsilon}$. i.e $\boldsymbol{\sigma} = \partial\psi^e(\boldsymbol{\varepsilon})/\partial\boldsymbol{\varepsilon}$.

Furthermore, the solution $(\mathbf{u}, s)$ of the total regularized energy functional in Eq. (3.15) along with the restated Griffith's criteria [142, 143], is then obtained by minimizing the first variation of the functional in Eq. (3.15) ($\delta\Pi_l(\mathbf{u}, s)$) in terms of Gateaux derivative for the variation $(\delta\mathbf{u}, \delta s)$ of $(\mathbf{u}, s)$, which also derives the phase field Euler-Lagrangian governing equations under quasi-static conditions, giving

$$\left[(1-s)^2 + k_l\right] \nabla \cdot \boldsymbol{\sigma}(\mathbf{x}) + \boldsymbol{b} = 0 \quad \text{on } \Omega, \tag{3.17a}$$

$$\text{with } \boldsymbol{\sigma} \cdot \mathbf{n} = \bar{\mathbf{t}} \quad \text{on } \partial\Omega_t, \tag{3.17b}$$

$$\mathcal{G}_c(\mathbf{x}) \left[\frac{s}{l} - l\boldsymbol{\Delta}s\right] - 2(1-s)\left(\psi_+(\varepsilon(\mathbf{u})) + \psi_-(\varepsilon(\mathbf{u}))\right) = 0 \quad \text{on } \Omega, \tag{3.17c}$$

$$\text{with } \nabla s \cdot \mathbf{n} = 0 \quad \text{on } \partial\Omega, \tag{3.17d}$$

where $\mathbf{n}$ is the outward normal vector on $\partial\Omega$.

The weak form corresponding to the phase field model for brittle fracture numerically implemented in the TPMS unite cell open lattices can be derived from Eqs. (3.17) following a standard Galerkin procedure. In particular, a standard derivation [143–145] leads Eq. (3.14) to the Cauchy stress tensor from the strain energy density,

$$\boldsymbol{\sigma}(\mathbf{u}, s) = g(s)\boldsymbol{\sigma}_+ + \boldsymbol{\sigma}_- = g(s)\frac{\partial\psi_+(\boldsymbol{\varepsilon})}{\partial\boldsymbol{\varepsilon}} + \frac{\partial\psi_-(\boldsymbol{\varepsilon})}{\partial\boldsymbol{\varepsilon}} \ , \tag{3.18}$$

and the weak form of the coupled displacement and phase field damage problem according to Eq. (3.15) [145] is

$$\begin{aligned}\delta\Pi_l = &\int_\Omega \boldsymbol{\sigma}(\mathbf{u}) : \boldsymbol{\varepsilon}(\mathbf{v})\mathrm{d}\mathbf{V} - \int_\Omega 2H_+(\boldsymbol{\varepsilon})(1-s)\phi \ \mathrm{d}\mathbf{V} + \\ &+ \int_\Omega \mathcal{G}_c \left\{ \frac{s\phi}{l} + l\nabla s \cdot \nabla\phi \right\} \mathrm{d}\mathbf{V} + \delta\Pi_{\text{ext}},\end{aligned} \tag{3.19}$$

where $H_+(\boldsymbol{\varepsilon}) = \max_{\tau\in[0,t]} \left\{ \psi_+^e(\boldsymbol{\varepsilon}(\tau)) \right\}$ is the strain history function, accounting for the irreversibility of crack formation [145], $\mathbf{v}$ is the vector of the displacement test functions defined on $\mathbf{H}_0^1(\Omega)$, ϕ stands for the phase field test function defined on $\mathbf{H}_0^1(\Omega)$. Eq. (3.19) holds for every test functions $\mathbf{v}$ and ϕ. The external contribution to the variation of the bulk functional in Eq. (3.19) is defined as follows,

$$\delta\Pi_{\text{ext}}(\mathbf{u},\mathbf{v}) = \int_{\partial\Omega_{\mathbf{t}}} \bar{\mathbf{t}} \cdot \mathbf{v} \ \mathrm{d}\mathbf{S} + \int_\Omega \mathbf{b} \cdot \mathbf{v} \ \mathrm{d}\mathbf{V}. \tag{3.20}$$

Given the prescribed loading condition $\overline{\mathbf{u}}_n$ and $\bar{\mathbf{t}}_n$ at step n, the mechanical problem and the phase field problem are formulated, respectively, as finding $\mathbf{u} \in \mathbf{U} = \left\{ \mathbf{u} \,|\, \mathbf{u} = \overline{\mathbf{u}}_n \text{ on } \quad \partial\Omega_u, \mathbf{u} \in \mathbf{H}^1(\Omega) \right\}$, such that

$$\int_\Omega \boldsymbol{\sigma}(\mathbf{u}) : \boldsymbol{\varepsilon}(\mathbf{v})\mathrm{d}\mathbf{V} - \int_{\partial\Omega} \bar{\mathbf{t}} \cdot \mathbf{v}\mathrm{d}\mathbf{S} - \int_\Omega \mathbf{b} \cdot \mathbf{v}\mathrm{d}\mathbf{V} = 0, \quad \forall \mathbf{v} \in \mathbf{H}_0^1(\Omega), \tag{3.21}$$

and by finding $s \in S$ where $S = \left\{ s \,|\, s = 0 \text{ on } \Gamma, s \in \mathbf{H}^1(\Omega) \right\}$ such that $\forall \phi \in \mathbf{H}_0^1(\Omega)$, gives

$$\int_\Omega \mathcal{G}_c l \nabla s \cdot \nabla\phi \mathrm{d}\mathbf{V} + \int_\Omega \left(\frac{\mathcal{G}_c}{l} + 2H_+(\boldsymbol{\varepsilon}) \right) s\phi \mathrm{d}\mathbf{V} - \int_\Omega 2H_+(\boldsymbol{\varepsilon})\phi \mathrm{d}\mathbf{V} = 0. \tag{3.22}$$

The quasi-static evolution problem for brittle fracture was performed using isoparametric linear triangular finite elements for the spatial discretization of the domain, and a staggered solution scheme is considered. Staggered schemes based on alternate minimization explore the convexity of the energy functional with respect to each individual variable, namely $\mathbf{u}$ and s, see also Cavuoto et al. [215] for more details. The schematic staggered pseudo-code for the mechanical and phase field model based on the weak form in Eqs. (3.21) and (3.22), is displayed in Scheme (1).

At this stage, it is fundamental to remark that, in order to predict crack trajectories in TPMS unit cell open foams under tensile/compressive stress states, the phase

Algorithm 1 Staggered iterative scheme for multi-phase field fracture at a step $n \geq 1$

Input: Displacements and phase fields $(\mathbf{u}^{n-1}, s^{n-1})$ and prescribed loads $(\overline{\mathbf{u}}^n, \overline{\mathbf{T}}^n)$:
Initialize $(\mathbf{u}^0, s^0) := (\mathbf{u}^{n-1}, s^{n-1})$;
for $k \geq 1$ staggered iteration **do**:
    Given s^{k-1}, solve the mechanical problem: $\mathcal{E}_{\mathbf{u}}(\mathbf{u}, s^{k-1}; \mathbf{v}) = 0$ for $\mathbf{u}$, set $\mathbf{u} := \mathbf{u}^k$;
    Given $\mathbf{u}^k$, solve the phase field problem $\mathcal{E}_s(\mathbf{u}^k, s; \phi) = 0$ and set $s := s^k$;
    if $\max\{||\mathbf{u}^k - \mathbf{u}^{k-1}||/||\mathbf{u}^{k-1}||, |s^k - s^{k-1}|/|s^k|\} <$ tol: **then**
        set $(\mathbf{u}^k, s^k) := (\mathbf{u}^n, s^n)$;
    else $k + 1 \to k$.
    end if
end for
Output: $(\mathbf{u}^n, s^n)$.

field finite element method was formulated by decomposing the strain energy density $\psi^e(\mathbf{u}, s)$ in Eq. (3.14), based on the spectral diagonalization according to [145], in active and passive parts, in order to apply the degradation of the material response only in tension. The variational formulation is then implemented on `FEniCS` [166] environment.

The length scale l is deeply inserted for modelling phase field, considering that for a sufficiently small length scale l_0, the functional (3.15) converges to the total potential energy functional (3.10), in the sense that the global minimizers of Π_l will also converge to that of Π. This entails that the length scale must be carefully chosen, rather than setting it arbitrarily. In the context of the uniaxial tension of a homogeneous bar, the length scale l was experimentally determined in [211, 216–218], and well summarized in [219]. Thereby, the length scale l value is linked to the apparent material strength. Particularly, as proposed in [220], once these material properties such as Young's modulus E, critical energy release rate $\mathcal{G}_c$ are known, then the characteristic length l can be set as

$$l = \frac{27}{256} \left(\frac{\mathcal{G}_c E}{\sigma_{\max}^2} \right). \tag{3.23}$$

The failure stress $\sigma_{\max}$ can either be obtained by using the closed-form relation $\sigma_{\max} = \sqrt{\mathcal{G}_c E / L}$ where L is the characteristic size of the specimen, or obtained through tensile tests, and afterwards the length scale l can be evaluated through Eq. (3.23).

3.3 TPMS modelling in the Phase Field FEM and analysis on compressive regime

In order to apply the phase field scheme to the TPMS lattices, the computer-aided design (CAD) modelling is performed assuming the approximated isosurface established by the truncation of the Fourier series (3.6) to generate unit cells of the TPMS topologies. Using the software developed at the University of Nottingham, namely FLatt-Pack [221], printable triangular mesh struts spatially discretized by the parameter μ, are then generated as STL files by offsetting ($-C \leq \Psi(x, y, z) \leq C$) the minimal surface controllable by its volume fraction (or relative density) $\rho^* = V_{latt}/V$ of the lattice, which is the ratio between the inner volume of the TPMS unit open cell lattice V_{latt} and the enclosing cubic unit open cell volume V, controllable by the level set C. The spatial discretization factor μ divides the cell size L into μ elements of size L/μ, in each direction. The relationship between the volume fraction of the TPMS cell ρ^* and the level set C can be seen in [71, 222, 223]. Usually, the level set C indicates an offset (thickness) of the surface in the normal direction and/or in the opposite direction to vary the volume fraction ρ^* at each TPMS lattice type.

Additionally, before importing them to the finite element environment `FEniCS`, uniform tetrahedral meshes are constructed by transferring the STL triangular meshes into the pre-processing software HyperMesh [224], producing the necessary tetrahedral solid assessed and converted to MSH file by Gmsh software [225]. As stated in [226], it is recommended that uniform meshes should be used for phase field models, in particular for brittle fracture simulation. Even though 3D continuum tetrahedral-like meshes might present less accuracy over the edges of the surface when a phase field finite element technique is playing a role (contact problems for instance [227, 228]), the choice of working with them rather than using hexahedral solid shells is based on the complexity that the topology of a TPMS type may take, thus facilitating the representation of the surface curvatures more accurately [157, 229–231].

The TPMS types chosen to have the phase field scheme applied are the Schwarz Primitive (P) (Fig. 31a), Schoen Gyroid (G) (Fig. 31b), Schoen-I-WP (IWP) (Fig. 31c), Schwarz Diamond (D) (Fig. 31d) and Neovius (N) (Fig. 31e) expressed as isosurfaces, respectively, as

$$\Psi_{\mathrm{P}}(x,y,z) = \cos(\mathrm{k}_x x) + \cos(\mathrm{k}_y y) + \cos(\mathrm{k}_z z) - C, \tag{3.24a}$$

$$\Psi_{\mathrm{G}}(x,y,z) = \cos(\mathrm{k}_x x)\sin(\mathrm{k}_y y) + \cos(\mathrm{k}_y y)\sin(\mathrm{k}_z z) + \cos(\mathrm{k}_z z)\sin(\mathrm{k}_x x) - C, \tag{3.24b}$$

$$\begin{aligned}\Psi_{\mathrm{IWP}}(x,y,z) =& 2(\cos(\mathrm{k}_x x)\cos(\mathrm{k}_y y) + \cos(\mathrm{k}_y y)\cos(\mathrm{k}_z z) + \cos(\mathrm{k}_x x)\cos(\mathrm{k}_z z)) \\ &- (\cos(2\mathrm{k}_x x) + \cos(2\mathrm{k}_y y) + \cos(2\mathrm{k}_z z)) - C,\end{aligned} \tag{3.24c}$$

$$\Psi_{\mathrm{D}}(x,y,z) = \cos(\mathrm{k}_x x)\cos(\mathrm{k}_y y)\cos(\mathrm{k}_z z) - \sin(\mathrm{k}_x x)\sin(\mathrm{k}_y y)\sin(\mathrm{k}_z z) - C, \tag{3.24d}$$

$$\begin{aligned}\Psi_{\mathrm{N}}(x,y,z) =& 3(\cos(\mathrm{k}_x x) + \cos(\mathrm{k}_y y) + \cos(\mathrm{k}_z z)) \\ &+ 4(\cos(\mathrm{k}_x x)\cos(\mathrm{k}_y y)\cos(\mathrm{k}_z z)) - C,\end{aligned} \tag{3.24e}$$

where the periodicity components are $\mathrm{k}_i = 2\pi n_i / L_i$ for each direction $i = x, y, z$, having n_i as the number of cell repetitions, and L_i correspond to the absolute length of the structure.

3.3.1 Boundary conditions for quasi-static uniaxial compressive loading

Let $\mathbf{u}(\mathbf{x}) = (\mathrm{u}_x(\mathbf{x}), \mathrm{u}_y(\mathbf{x}), \mathrm{u}_z(\mathbf{x}))$, with $\mathbf{x} = (x, y, z) \in \partial\Omega$, be the displacement field, and let u_0 be the magnitude of the applied displacement. The brittle fracture phase field, deformation behaviour and mechanical properties of the TPMS structures are investigated under the boundary conditions subjected to an uniaxial compressive loading of the quasi-static phase field model having on the top face $\mathrm{u}_z = \mathrm{u}_0$ in the normal direction together with free u_x, u_y, and $\mathbf{u}$ free on the lateral faces. In order to avoid any rigid body movement, such as slipping, the bottom face has been constrained by $\mathrm{u}_z = 0$, and on a small region of the bottom by $\mathrm{u}_x = \mathrm{u}_y = 0$. Namely, the lateral free boundary condition set up allows the open celled lattices to deform without any interference due to the absence of neither neighbor cells nor walls. The finite element meshes of all TPMS topologies, with the described boundary conditions, are depicted in Fig. 31.

3.3.2 Mesh sensitivity analysis

With the aim of reducing the computation time of numerical simulations, which are demanding in 3D, a mesh sensitivity analysis has been carried out throughout the analysis of the outcomes of the compressive stress-strain curves for different mesh

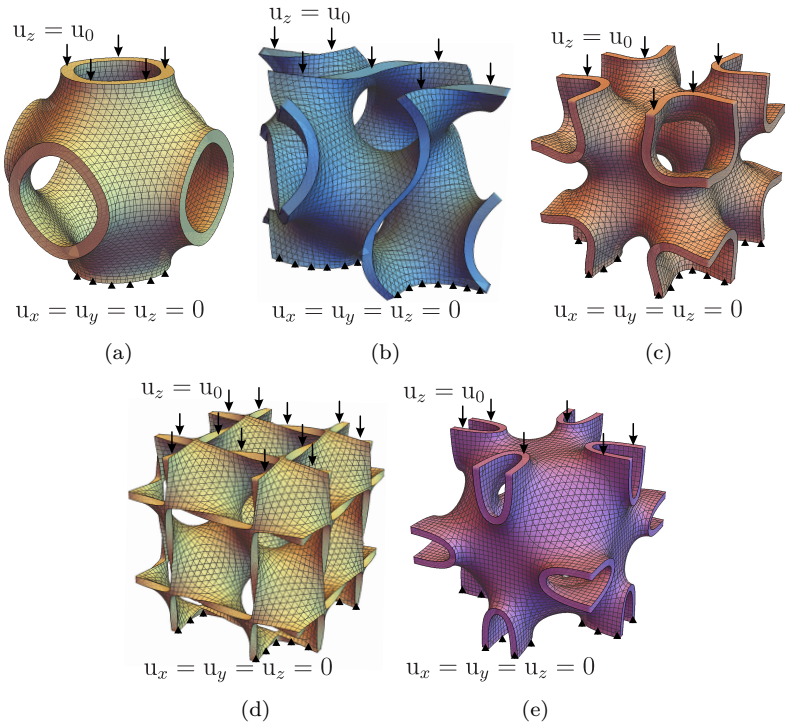

Figure 31: Unit cells of TPMS structures, boundary conditions and applied uniaxial load: (a) Schwarz Primitive; (b) Schoen Gyroid; (c) Schoen-I-WP; (d) Schwarz Diamond; (e) Neovius.

refinements of a single unit cell of the Primitive, Gyroid, IWP, Diamond and Neovius TPMS. The outcomes from the present analysis are assessed in Secs. 3.4 and 3.5. For such a purpose, the material adopted for the lattices was Aluminium alloy [13]. The Young's modulus and Poisson's ratio of this material are, respectively, $E = 82\text{GPa}$ and $\nu = 0.33$. The fracture toughness $\mathcal{G}_c$, and the apparent tensile strength $\sigma_{\max}$, are taken from a broad range of previous evaluations through AM [232–236]. In accordance, from Eq. (3.23), a length scale l_0 is the order of 10^{-4}mm. The fracture toughness $\mathcal{G}_c$ is set in the order of 10^{-4}J/mm^2.

The unit cells were generated with dimensions of $8\text{mm} \times 8\text{mm} \times 8\text{mm}$ each, which means that the enclosing cubic unit cell volume is $V = L^3 = 512\text{mm}^3$, and the percentage volume fraction, ρ^*, was 20%. Force-displacement curves were numerically predicted to compute the stress-strain curves by dividing the force by the apparent

cross-sectional area $A = L^2$ and the displacement by L. A maximum quasi-static compressive displacement of 10^{-3}mm was applied along all the simulations of the lattices. The spatial discretization values μ taken to perform the mesh analysis for the Primitive unit cells were $\mu = 15$ to $\mu = 70$, for the Gyroid unit cell meshes were $\mu = 20$ to $\mu = 75$, and for the IWP, Neovius and Diamond meshes were $\mu = 25$ to $\mu = 75$, in increments of 5.

The stress-strain curves of the series of Primitive, Gyroid, IWP, Diamond and Neovius lattices are plotted in Figs. 32a, 33a, 34a, 35a and 36a. During loading, it can be noted a linear elastic behaviour at low strains up to the critical stress point.

The stress-strain curves of the unit cells begin to show significant deformations right after the peak compressive stress is reached, followed by a drastic drop in the curves, losing their load-bearing capacity. This characteristic is also observed in compressive tests with clusters of TPMS additively fabricated [150, 151, 164], although clusters of TPMS are employed and their global collapse may different from the local failure of a single cell.

Here, the apparent Young's modulus of the different discretized TPMS was found by calculating the slope of the first linear elastic region, i.e. up to $0,2\%$ strain level. Figs. 32b, 33b, 34b, 35b and 36b depict how the apparent Young's modulus varies depending on mesh refinement (corresponding to a different value of μ). A synthesis of the mesh sensitivity analysis for the different TPMS is provided in Tabs. 1 to 5, with the value of μ, the number of finite elements, the apparent Young's modulus E^*, and the apparent strength $\sigma_{max,c}$.

Although to ensure an accurate estimation of fracture patterns it is necessary to have a finite element size $h = L/\mu$ of the order of $h << (1/5{\sim}1/10)l_0$ [144, 237]. It can be noted from the previous results that the absolute error deviations from the finest meshes is quite stable even for coarser discretizations. In particular, in order to improve computational efficiency of the herein model and to ensure an accurate estimation of the crack as it evolves, a dual-mesh adaptive approach proposed in [238] can also be implemented to avoid the analysis of too fine meshes requesting very long simulations. The finest mesh discretizations chosen ensure apparent Young's moduli and maximum compressive stresses as tabulated in Table 6, together with their respective standard deviations based on the above series of simulations at different discretizations calculated from Tabs. 1 to 5. It is also observed that among the five TPMS unit cells studied at 20% of volume fraction, the Neovius structure gives the stiffest topology, giving an average Young's modulus of $\bar{E}^* = 6.98$GPa, and an average maximum stress of $\sigma_{\max,c} = 52.1$MPa, followed by IWP, Diamond,

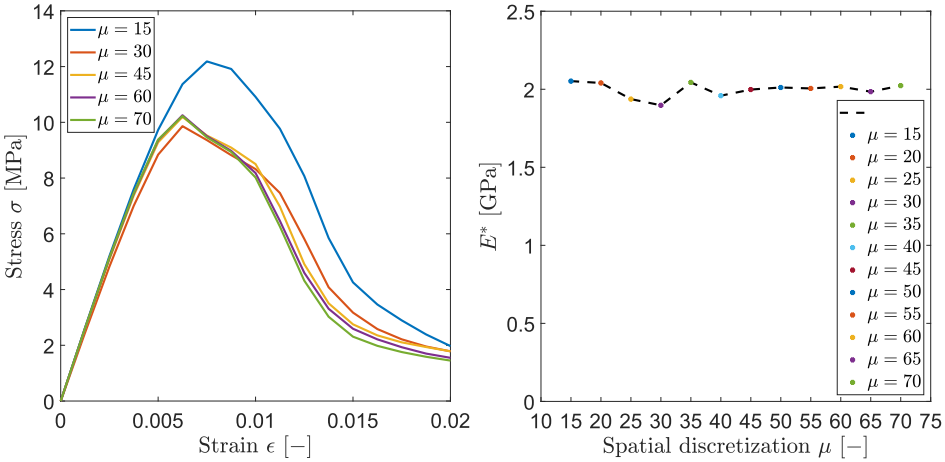

(a) Stress–strain curves for different spatial discretizations.

(b) Young's modulus dependency on the spatial discretization.

Figure 32: Mesh sensitivity analysis of the Primitive unit cells at 20% volume fraction.

μ	N. of elements	$E^*(\mu)$ [GPa]	$\sigma_{\max,c}(\mu)$ [MPa]
15	21875	2.05	12.2
20	48045	2.04	10.7
25	68945	1.93	10.2
30	133611	1.89	9.9
35	194478	2.04	10.6
40	298375	1.95	10.0
45	394161	1.99	10.2
50	495644	2.01	10.3
55	621951	2.00	10.1
60	783464	2.01	10.3
65	904353	1.98	10.0
70	1157245	2.02	10.2

Table 1: Primitive: spatial discretization μ; number of finite elements; apparent Young's modulus E^*; ultimate compressive stress $\sigma_{\max,c}$.

Gyroid, and Primitive, the latter being the less stiff strut among all five TPMS studied, having averages of $\bar{E}^* = 1.99$GPa and $\sigma_{\max,c} = 10.4$MPa. In order to map and to compare the stiffness among all the five kinds of TPMS under the

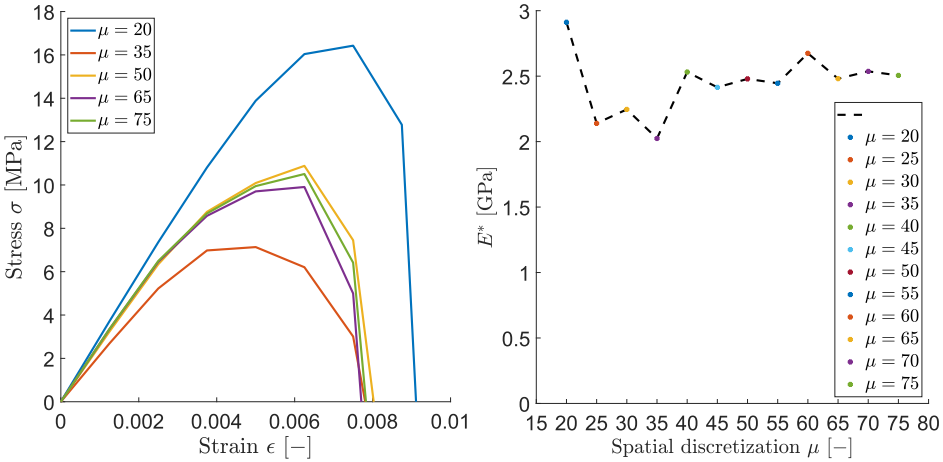

(a) Stress–strain curves for different spatial discretizations.

(b) Young's modulus dependency on the spatial discretization.

Figure 33: Mesh sensitivity analysis of the Gyroid unit cells at 20% volume fraction.

μ	N. of elements	$E^*(\mu)$ [GPa]	$\sigma_{\max,c}(\mu)$ [MPa]
20	50425	2.91	16.43
25	90900	2.13	9.73
30	146380	2.24	10.33
35	229317	2.02	7.13
40	306548	2.53	10.82
45	434392	2.41	10.21
50	550416	2.47	10.88
55	715508	2.44	10.68
60	788926	2.67	12.49
65	1056405	2.48	9.91
70	1257132	2.53	10.88
75	1537369	2.50	10.51

Table 2: Gyroid: spatial discretization μ; number of finite elements; apparent Young's modulus E^*; ultimate compressive stress $\sigma_{\max,c}$.

developed phase field scheme, in Sec. 3.5, unit cells with different volume fractions have been generated by setting one single value of discretization for each TPMS topology. Table 6 will also be helpful as an additional guideline when setting the proper spatial discretization μ that better optimizes the relation between finer mesh

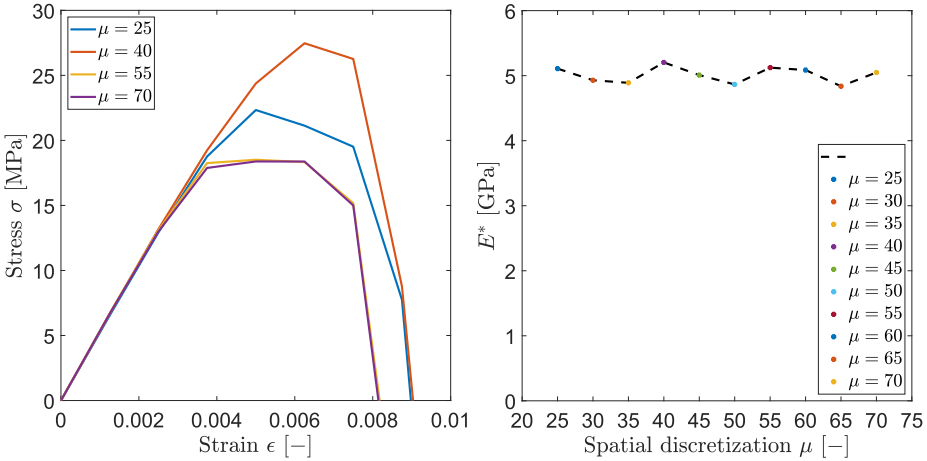

(a) Stress–strain curves of the simulated IWP unit cells at different spatial discretizations.

(b) Spatial discretization × Derived Young's modulus.

Figure 34: Mesh sensitivity analysis of the IWP unit cells at 20% volume fraction.

μ	N. of elements	$E^*(\mu)$ [GPa]	$\sigma_{\max,c}(\mu)$ [MPa]
25	80317	5.10	22.3
30	141942	4.92	17.4
35	230306	4.88	20.9
40	294595	5.20	27.5
45	405429	5.00	18.3
50	558742	4.86	16.9
55	678209	5.12	18.5
60	871902	5.08	21.5
65	1057063	4.83	16.5
70	1230149	5.04	18.4

Table 3: IWP: spatial discretization μ; number of finite elements; apparent Young's modulus E^*; ultimate compressive stress $\sigma_{\max,c}$.

and computational time in the following volume fraction analysis in Sec. 3.5, for each of the five TPMS. It can be highlighted that crack patterns through all five TPMS were independent of the spatial discretization μ simulated, nonetheless, one also can observe that the finer the meshes became, the thinner the smeared crack region became, as expected for a phase field model.

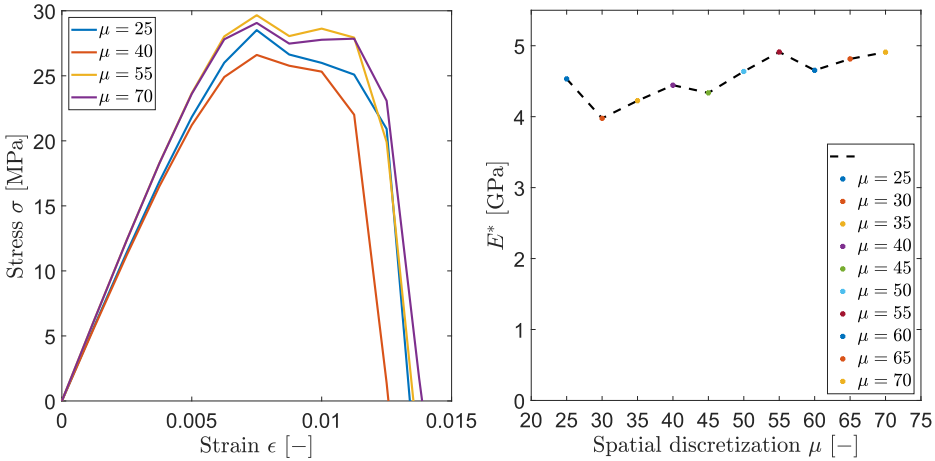

(a) Stress–strain curves for different spatial discretizations.

(b) Young's modulus dependency on the spatial discretization.

Figure 35: Mesh sensitivity analysis of the Diamond unit cells at 20% volume fraction.

μ	N. of elements	$E^*(\mu)$ [GPa]	$\sigma_{\max,c}(\mu)$ [MPa]
25	101166	4.53	28.5
30	151999	3.97	23.0
35	227730	4.22	25.0
40	309889	4.44	26.6
45	473513	4.33	23.1
50	584342	4.63	26.7
55	716617	4.91	29.7
60	925827	4.65	259
65	1073706	4.81	27.1
70	1386746	4.90	29.1

Table 4: Diamond: spatial discretization μ; number of finite elements; apparent Young's modulus E^*; ultimate compressive stress $\sigma_{\max}$.

The simulations were run in parallel with a MPI implementation of FEniCS. Throughout, for the coarsest meshes, a server with 100GB of RAM and from 4 to 6 cores has been used to run from 4 to 6 MPI simulations in parallel. Simulations run from 30 minutes up to 20 hours. For the finest meshes, different partitions have been considered. On the medium memory partition, the average RAM utilized was

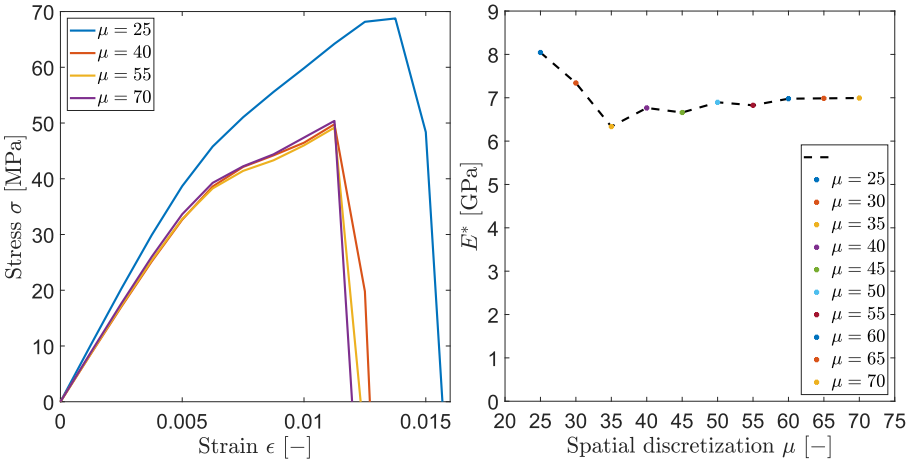

(a) Stress–strain curves for different spatial discretizations.

(b) Young's modulus dependency on the spatial discretization.

Figure 36: Mesh sensitivity analysis of the Neovius unit cells at 20% volume fraction.

μ	N. of elements	$E^*(\mu)$ [GPa]	$\sigma_{max,c}(\mu)$ [MPa]
25	95363	8,04	68,8
30	124734	7.37	55.5
35	174635	6.33	48.2
40	266917	6.76	49.8
45	352847	6.65	48.6
50	465175	6.89	50.1
55	607940	6.82	49.2
60	752578	6.95	49.9
65	864469	6.92	50.1
70	1085643	6.99	50.4

Table 5: Neovius: spatial discretization μ; number of finite elements; apparent Young's modulus E^*; ultimate compressive stress $\sigma_{\max}$.

200GB and from 4 to 6 cores were used, whereas the standard memory partition utilized 125GB and from 8 to 10 cores, which CPU time varying from 20 up to roughly 72 hours, for both machine partitions.

Having established the present analysis, one might notice that throughout the simulations, the phase field pattern and deformation behaviour of the five TPMS unit

TPMS	$\bar{E}^*$ [GPa]	$\sigma_{\max,c}$ [MPa]
Primitive	1.99 ± 0.04	10.4 ± 0.6
Gyroid	2.44 ± 0.23	10.8 ± 2.5
IWP	5.01 ± 0.12	19.8 ± 3.3
Diamond	4.54 ± 0.30	26.5 ± 2.3
Neovius	6.98 ± 0.45	52.1 ± 6.2

Table 6: Apparent Young's modulus and ultimate compressive stresses for a volume fraction of 20% from simulations, average values and standard deviations.

cells studied are essentially the same for the several spatial discretizations analysed, and therefore the phase field model proposed well captures and characterizes the crack nucleation, branching, propagation and deformation mechanism. Additionally, choosing meshes near $300,000$ tetrahedral elements are capable to pursuit the further analyses on volume fraction in unit cell TPMS specimens with dimensions of $8\text{mm} \times 8\text{mm} \times 8\text{mm}$ made in Sec. 3.5. A similar approach was taken in [165], whereas along other investigative studies [158, 231, 239], TPMS unit cell meshes of around $50,000$ elements were sufficient to ensure finite element mesh independent results.

Moreover, one might wonder the reasons on conducting simulations only over unit cells of TPMS. In order to optimize the computational cost, elastic and yield properties of TPMS struts can be investigated using single unit cells for various set ups of boundary conditions given the periodicity of the structures. As quoted in [5], the periodicity fact allows the derivation of the elastic compressive responses on a single unit cell, but in order to evaluate post-yield properties, an analysis on TPMS clusters rather than single unit cells is necessary, although it is computationally more expensive. A plethora of studies have used a single unit cell to derive deformation behaviour, failure, plateau stress, among other properties and validate the experimental tests. Although experimental tests were conducted on TPMS clusters in [151, 154], a compressive uniaxial finite element method was applied on the TPMS unit cells to extract mechanical properties of the unit cell TPMS microlattices, and thus validating the experimental tests taken on TPMS cluster lattices. In [208] interpenetrating phase composites (IPC) TPMS unit cells were studied using a finite element method in order to predict effective electrical/thermal conductivity and elastic moduli of a couple of types of TPMS-based IPC's. Also, a full numerical work by [157] derived the elastic parameters and deformation behaviour of the Primitive structure and its variation.

Concerning to TPMS clusters, elastic mechanical properties and post-yield char-

acterizations, namely deformation and failure mechanisms, energy absorption are being investigated and captured utilizing specimens with enough unit cells (clusters) of TPMS (please see [9, 60, 164]). Throughout, it can be observed deformation through the development of shear bands with a certain angle with respect to the loading direction, bulging, barrelling and failure by horizontal layer-by-layer collapse. More importantly, the after failure behavioural features have been brought to attention when functionally graded TPMS are being evaluated either experimentally or numerically [12, 64, 163, 223]. In essence, various works structurally derived elastic and plastic properties and responses of TPMS, however no numerical crack characterization on TPMS has taken place in literature, which is performed in the next section.

3.4 Phase Field prediction of fracture patterns

Based on the careful mesh sensitivity analysis made in Sec. 3.3.2, the following phase field characterizations of the TPMS unit cells have the spatial discretization corresponding to $\mu = 65$. TPMS parameters and dimensions as well as phase field finite element parameters selected to pursue the following estimations are the same assumed in Sec. 3.3.2. For the sake of spotting crack initiation sites, propagation and nucleation the contour plots of the phase field damage variable in the post-peak regime are shown in the sequence of Figs. 37, 39, 41, 42 and 43 for an increasing level of strain, for all TPMS analyzed. Figs. 37a, 39a, 41a, 42a and 43a are displaying front views (yz-plane) of the TPMS lattices under the phase field model, whereas Figs. 37b, 39b, 41b, 42b and 43b. Meanwhile, the deformation behaviour of the TPMS unit cells can be seen in Fig. 44.

Fig. 37 shows cracks appearing in the directions either parallel or perpendicular to the loading of the Primitive strut, with failure occurring under the form of arch bridges, bifurcating to sub-cracks on the top and bottom of the unit cell. Crack formation in the direction to the loading was observed coming from the inside of the unit cell, in agreement with the experimental results derived in [68]. Whereby the cracks in the perpendicular direction nucleate from outside and propagate towards inside. Analogously, the crack pattern over the Primitive unit cell right above described is also in very good agreement with the results obtained in [12] (see Fig. 38a). In particular, for the cracks nucleating parallel to the loading direction, they occur after the failure of the hollows, then the arch bridge like semicircular parts were loaded, concentrating the stress in the top of the arch bridge. Some sub-cracks

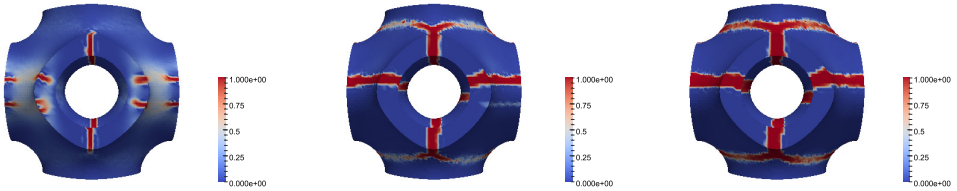

(a) Phase field P65 front view at 1%, 2%, 3% strains.

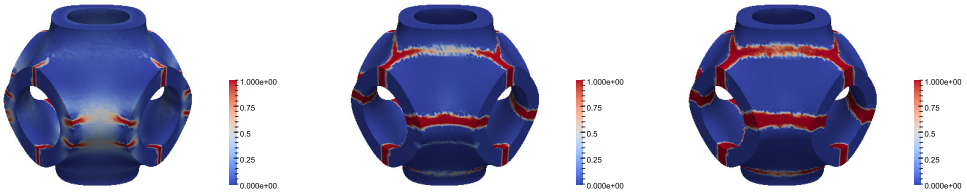

(b) Phase field P65 perspective view at 1%, 2%, 3% strains.

Figure 37: Primitive unit cell crack sites, nucleation, propagation and branching, for 1%, 2%, and 3% of strain.

are formed by the propagation of these parallel cracks along the top and bottom of Primitive, as a kind of *crown* like, perpendicular to the loading direction, thereby descried as sub-hollow layers. Even though the material utilized in [12] is different from the Aluminium alloy used here, the crack patterning is similar. As observed and summarized in [14], regardless of the base material, the topology of the unit cell dictates the stress/strain distribution within the TPMS unit cell under loading regimes, but post-yield properties depend on the material.

Still in Fig. 37, at a strain of 1%, two horizontal cracks appear and further nucleate at higher strain levels. Based on this scenario, it is conjectured that when fatigue takes place and the lattice collapses, both initial cracks meet, assembling to one branch on the exact deformed/broken spot. The deformation mechanism (see Fig. 44a) relates to barrelling behaviour (barrel-shaped), which is in good agreement with previous works [68, 152].

For the Gyroid, nucleation, propagation, and branching are shown in Fig. 39, at strains of 0.75% and 1.5%. Cracks are predominantly seen inside of the unit cell, however fractures are also spotted on the boundaries, propagating towards the inside of the cell, resembling a pattern seen in the cluster lattices of the Gyroid in [12]. A contrast of this patterning is shown in Fig. 38b. Fig. 40 compares the crack initiation and propagation in the aluminium alloy based Gyroid lattice

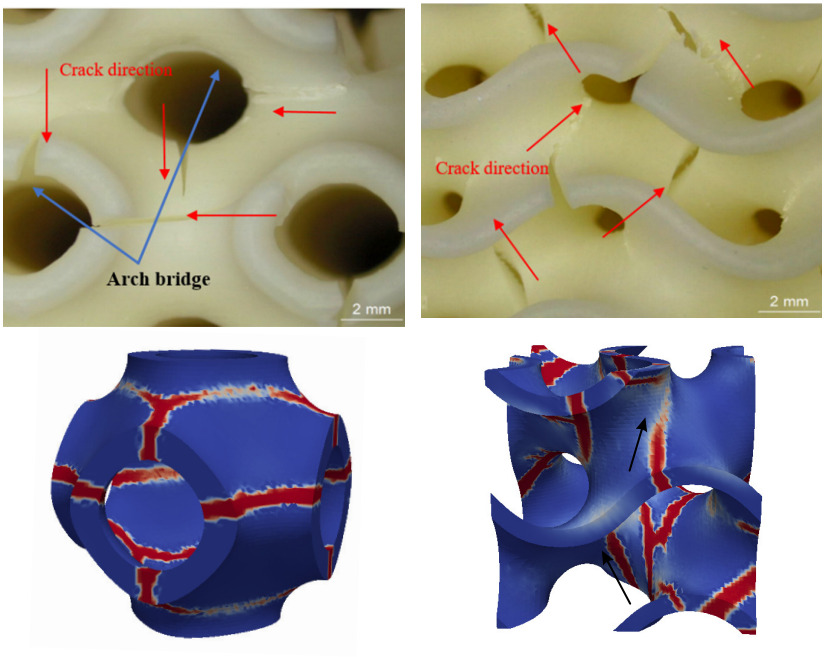

(a) (b)

Figure 38: Comparative illustration of the crack pattern in compressive regime derived in [12] (above lattices), and the developed phase field model (below cells). (a) Primitive; (b) Gyroid. Subfigures on experiments adapted from [12].

from compressive experimental tests made in [13], against the present phase field model Gyroid unit cell. It can be noted that the phase field crack initiates at in-parts of the unit cell, in agreement with the characterization previously made. As the strain grows, fractures begin to initiate also on the curved band boundaries of the Gyroid. Notwithstanding, the TPMS clusters studied throughout literature are made of ductile material, which may also experience ovalization and instabilities that cannot be predicted from compressive tests on single cells.

IWP phase field characterization is beheld in Fig. 41. The deformation and fracture process of IWP cell shows a dominated expansion on top and bottom of the surface, forming four handles-like, observed in Fig. 44c at 1.5% strain. In the upcoming section, it will be remarked that as the volume fraction of IWP cell increases, these handle features become thicker enough to contain this stretching behaviour, letting the deformation stress be dislocated to the mid height region of

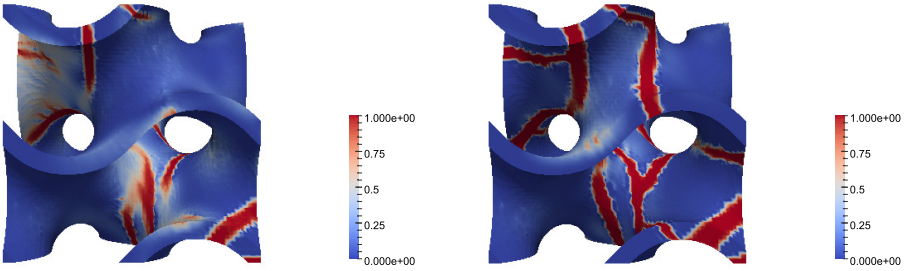

(a) Phase field G65 front view at $0,75\%$, $1,5\%$ strains.

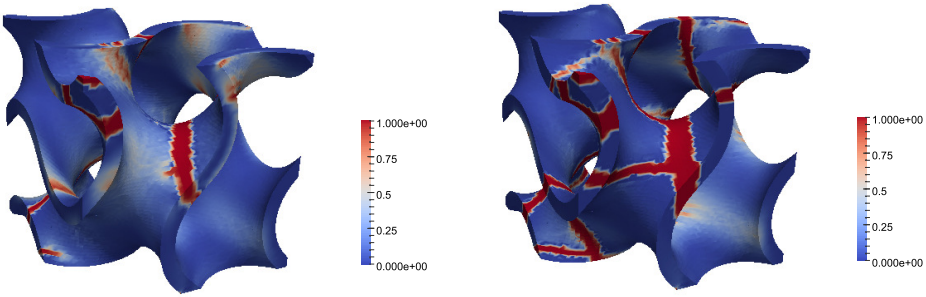

(b) Phase field G65 perspective view at $0,75\%$, $1,5\%$ strains.

Figure 39: Gyroid unit cell crack sites, nucleation, propagation and branching, for 0.75% and 1.5% of strain.

the strut.

Phase field behaviour of Diamond and Neovius unit cells are depicted at increasing strains of 0.88% and 1.75%, in Figs. 42 and 43, respectively. Diamond phase field is characterized by cracks nucleating with a small inclined angle to the loading direction. as the strain grows, crack initiate over the top of the cell, propagating along the surface curvature perpendicular to the bottom (xy-plane). Cracking on Neovius cells form and evolve in the parallel direction to the loading, secondary cracks nucleate perpendicular to the loading direction when high strain values are reached. A bloating-like deformation behaviour is seen in both Diamond, which is in good agreement with the outcomes seen in [153], and Neovius samples, both depicted at strains of 1.75% in Figs. 44d and 44e.

Notably, during the compression simulations performed, a couple of cracks spread

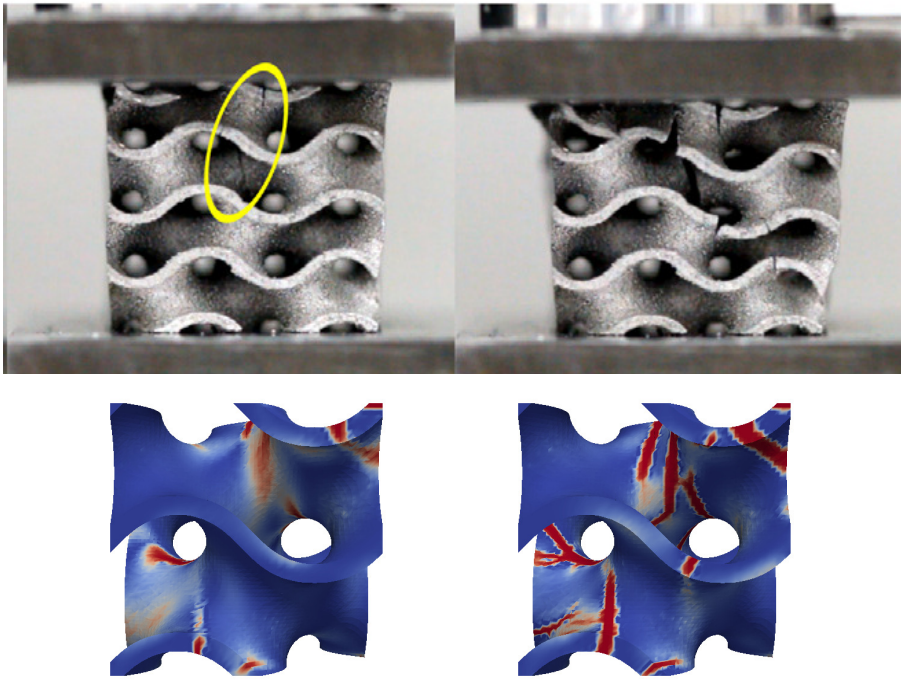

Figure 40: Comparison at low strains between the crack initiation and propagation in the aluminium alloy based Gyroid lattice from experimental tests made in [13], and the present phase field simulated Gyroid unit cell. Subfigures on experiments adapted from [13].

and get connected as the load continues, succeeding in the collapse of the cells and consequently the drop of the stress. Furthermore, the propagation of the cracks within the TPMS lattices exhibit a particular characteristic as consequence of the overall property of self similarity of TPMS. As such, in what regards to the phase field propagation and cell bending, Primitive, IWP, Diamond and Neovius present an uniform pattern led by their geometry design. On the other hand, Gyroid clusters would need to undergo through the phase field scheme to identify and characterize patterns coming from its geometric nature, since a solo unit cell analyzed was not sufficient to infer any pattern.

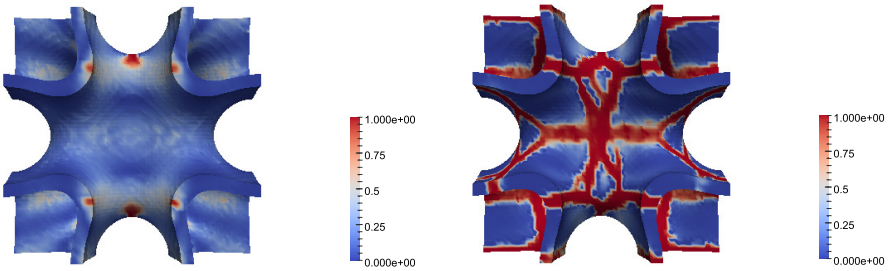

(a) Phase field IWP65 front view at $0,75\%$, $1,5\%$ strains.

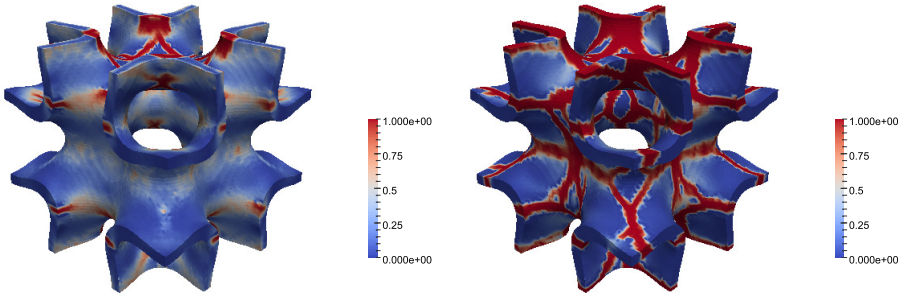

(b) Phase field IWP65 perspective view at $0,75\%$, $1,5\%$ strains.

Figure 41: IWP unit cell crack sites, nucleation, propagation and branching, for 0.75% and 1.5% of strain.

3.5 Effect of the volume fraction on mechanical properties

Guided by the derived numerical results on the mesh sensitivity analysis conducted in Sec. 3.3.2) for a volume fraction of 20%, the study is herein extended to assess the effect of the volume fraction (or, analogously, the porosity) on the apparent mechanical properties. Here we set the discretization parameter $\mu = 35$ for the Primitive surfaces, $\mu = 40$ for the Gyroid, IWP and Neovius unit cells, while $\mu = 50$ is used for the Diamond lattices. Figs. 45 to 49 depict the TPMS unit cells for different volume fractions.

The volume fraction, which is also related to the porosity as its complement to unity, plays an important role in determining the mechanical properties of porous foams, as typically plotted in Ashby plots [152, 168, 169]. Here, the quantities

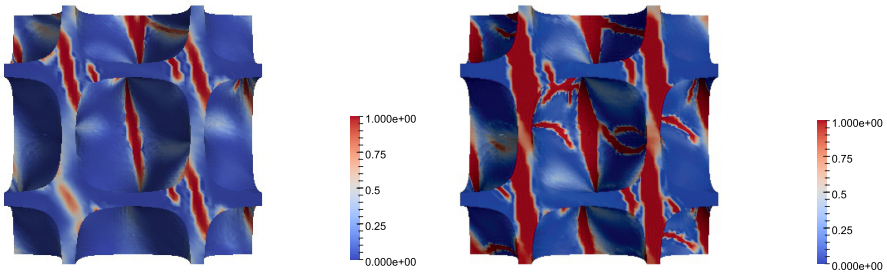

(a) Phase field D65 front view at $0,88\%$, $1,75\%$ strains.

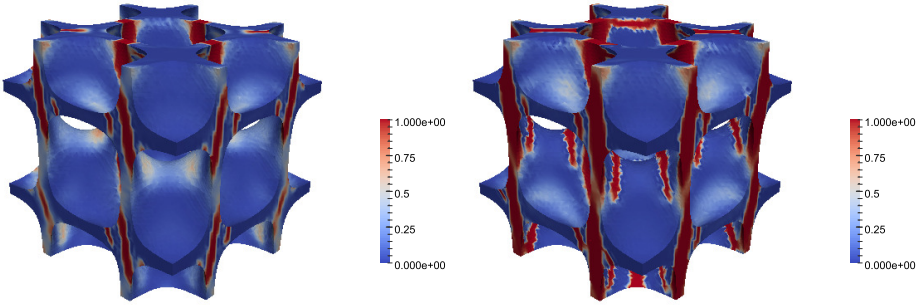

(b) Phase field D65 perspective view at $0,88\%$, $1,75\%$ strains.

Figure 42: Diamond unit cell crack sites, nucleation, propagation and branching, for 0.88% and 1.75% of strain.

of interest for the Ashby plots (apparent Young's modulus, compressive strength, and volume fraction) of lattice TPMS structures are extracted from numerical simulations and examined, see the charts provided in linear, seen in Fig. 50, and bi-logarithmic scales, depicted in Fig. 51.

It is noteworthy that the compressive strength of the open unit cells is an increasing function of the volume fraction. The trend in the stiffness of the TPMS discussed in Sec. 3.3.2 for a volume fraction of 20%, is confirmed as the volume fraction increases, i.e. Neovius being the stiffest, followed by IWP, Diamond, Gyroid and Primitive. The same trend occurs for the load carrying capacity in compression, see Fig.50a or 51a.

It can be observed that in between the volume fraction interval of $[35\%, 40\%]$ the Primitive unit cell overtakes the Gyroid unit cell in terms of the apparent Young's modulus E^*. Moreover, the results are in reasonable agreement with the findings

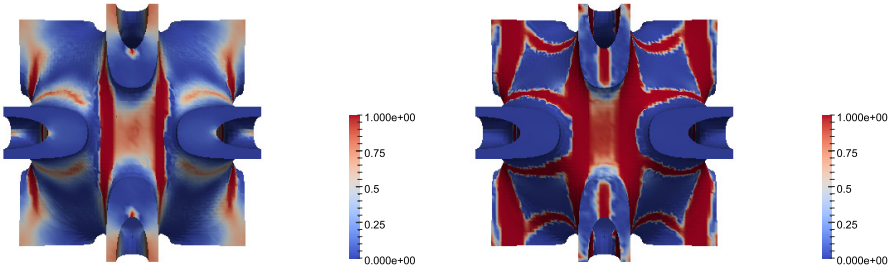

(a) Phase field N65 front view at $0,88\%$, $1,75\%$ strains.

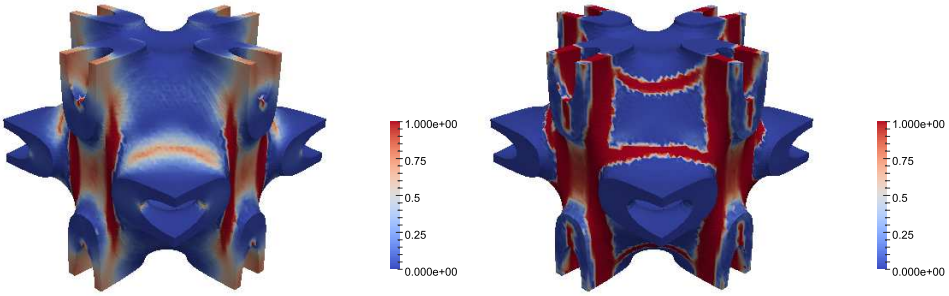

(b) Phase field N65 perspective view at 0%, $0,88\%$, $1,75\%$ strains.

Figure 43: Neovius unit cell crack sites, nucleation, propagation and branching, for 0.88% and 1.75% of strain.

presented in [158, 164], where the latter stated that for low volume fractions, the more relative discrepancy regarding to the elastic properties through the manipulation of the unit cells was found, such a behaviour being clearly evidenced in the bi-logarithmic charts, Figs. 51a, 51b and 51c. Particularly, Fig. 51b highlights that, for low volume fractions, the Gyroid cell underperforms all the other TPMS in terms of supported maximum compressive stress $\sigma_{\max,c}$. O the other hand, for higher volume fractions, the less performant TPMS becomes the Primitive one.

In what regards the nucleation sites and deformation for the Primitive cells, the crack initiation sites and their branching seem to happen at the same regions seen in the Primitive at $\rho^* = 20\%$, as the volume fraction increases. Meanwhile, the fracture tips tend to primarily appear at arch bridges of the Primitive geometry, among with barrelling, but uniform, deformation behaviour. From the deformed cells, crumbled regions at the fractured zones perpendicular to the loading are seen,

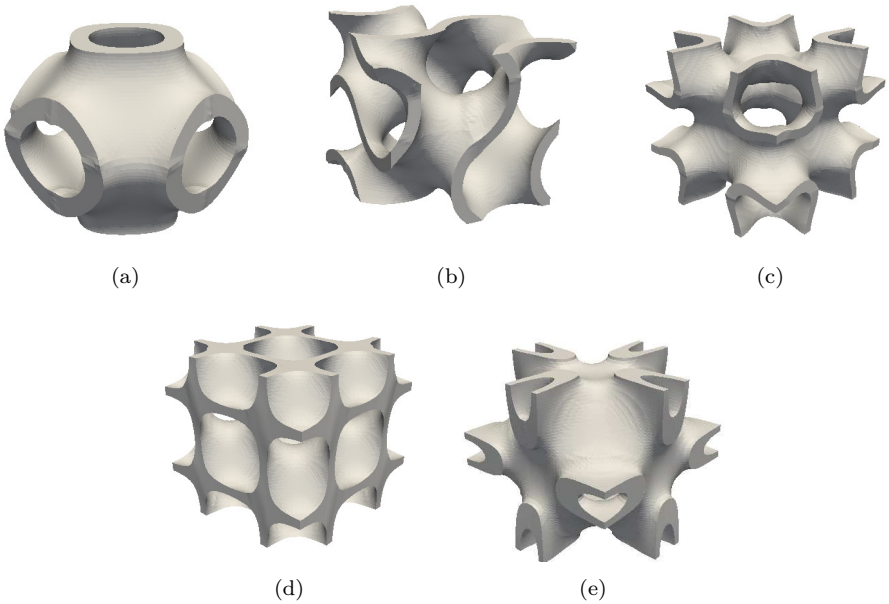

(a) (b) (c)

(d) (e)

Figure 44: Deformed unit cell TPMS structures at strains of: (a) Schwarz Primitive 3%; (b) Schoen Gyroid 1.5%; (c) Schoen-I-WP 1.5%; (d) Schwarz Diamond 1.75%; (e) Neovius 1.75%.

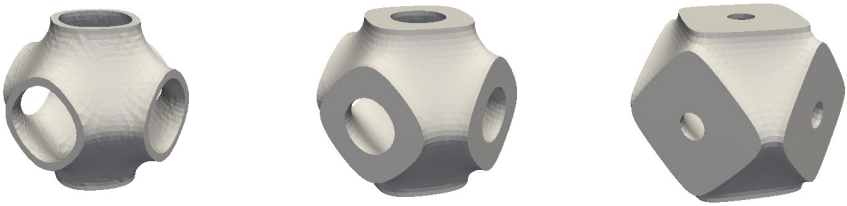

(a) $\rho^* = 10\%$. (b) $\rho^* = 30\%$. (c) $\rho^* = 50\%$.

Figure 45: Primitive unit cell at different values of volume fraction.

which interconnect the arch bridges of the lateral faces. Interestingly, at lower strains, the cracks initiate firstly and propagate more rapidly for the cells with higher volume fractions. The Primitive with $\rho^* = 55\%$, for instance, is almost entirely crushed, while the Primitive at $\rho^* = 10\%$ resembles the original minimal

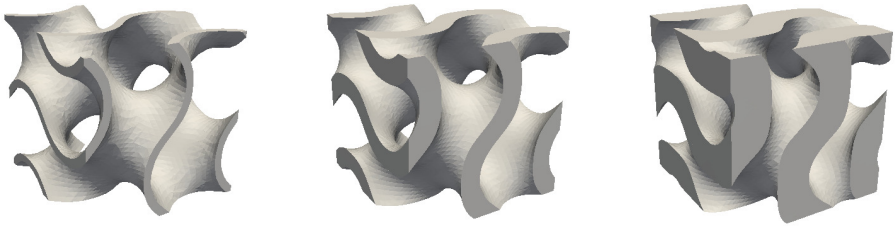

(a) $\rho^* = 15\%$. (b) $\rho^* = 35\%$. (c) $\rho^* = 55\%$.

Figure 46: Gyroid unit cell at different values of volume fraction.

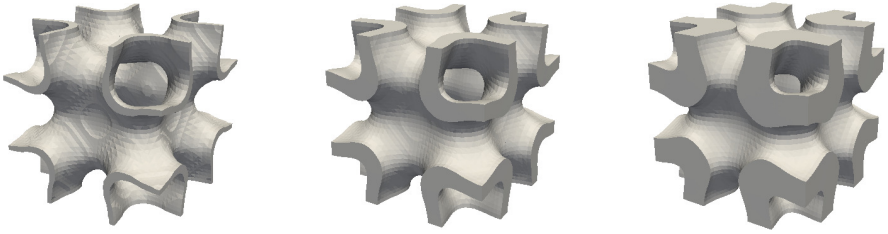

(a) $\rho^* = 15\%$. (b) $\rho^* = 35\%$. (c) $\rho^* = 55\%$.

Figure 47: IWP unit cell at different values of volume fraction.

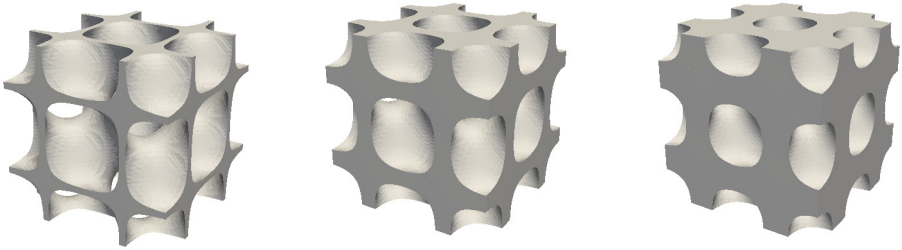

(a) $\rho^* = 15\%$. (b) $\rho^* = 35\%$. (c) $\rho^* = 55\%$.

Figure 48: Diamond unit cell at different values of volume fraction.

surface, at mid strain values.

The crack pattern predicted by the phase field model for the Gyroid type unit cells is essentially similar for all the volume fractions, meaning that crack sites

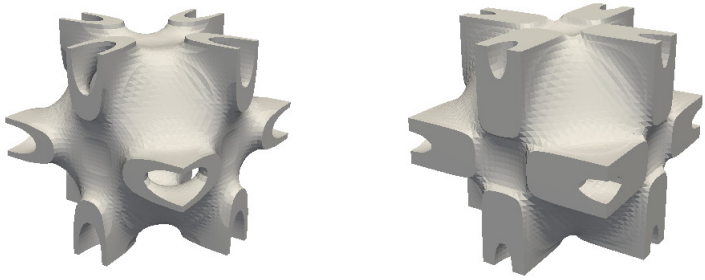

(a) $\rho^* = 15\%$. (b) $\rho^* = 30\%$.

Figure 49: Neovius unit cell at different values of volume fraction.

formed fairly correspond to the ones described at $\rho^* = 20\%$. However, cracks tend to expand quicker on the Gyroid geometries with higher volume fractions. A stretching deformation behaviour mostly concentrates on the bottom boundary of the Gyroid lattices. The ratio between the surface areas of the stretched deformed bottom and the deformed top, indicates a slightly bigger expanded area on the bottom plan of the open cell.

In Diamond cells, crack nucleation begins on the boundaries of the faces. In this case, cracks originated on the lateral faces initiate angled to loading direction and propagate to the inside of the cells. Subsequently, secondary cracks nucleating on the top of the cells propagate downward parallel to loading, guided by Diamond's surface curvature. On the contrary of what is spotted for the Primitive cells, crack development firstly appears on Diamond lattices at lower volume fractions. Under compressive loading, a uniform expansion of the Diamond unit cells can be noticed in all volume fractions as the strain varies.

IWP struts differ in the cracking pattern as volume fractions varies. Up to $\rho^* = 25\%$, nucleation first appears over top and bottom of the surfaces, propagating parallel to the loading direction. In spite of this trend, IWP cells with volume fraction above 25% show a surrounding crack nucleation at the middle region of the surfaces, perpendicular to the loading direction, which could be relevant for fatigue failure. The compressive deformation behaviour predicted by the phase field model verified that the IWP unit cell lattices have a uniform and smooth stretching deformation perpendicular to the loading at all volume fractions registered, which is in good matching with the finding made in [240].

Phase field characterization and deformation mechanisms of the Neovius cells at increasing volume fraction do not present significant differences from those observed for $\rho^* = 20\%$ in Sec. 3.4.

Figs. 52 and 53 compare the TPMS unit cell responses with experimental data from metallic TPMS currently available in the literature [14]. For a certain level set C in Eq. (3.6), a solid-network (skeleton-network) is defined as being the solid of one of the sub-domains divided by the resulting surface, while the remaining sub-domain is assumed to be a void. Sheet-network is considered to be the thickened resulting minimal surface, as described in Sec. 3.3. Sheet-networks TPMS show improved mechanical properties as compared to solid-networks. As expected, from Fig. 52, over the volume fraction interval studied, the various apparent Young's moduli of the five TPMS unit cells analyzed by the present phase field framework lie majorly on the sheet-networks region, represented by the black color, showing reasonable agreement with the existing experimental compressive works on metallic TPMS lattices.

Despite a bigger overlapping of the regions in Fig. 53, revealing that the superiority of TPMS sheet-networks over solid-networks is less evident when compressive peak stresses are examined, the ultimate compressive stress predicted by the phase field approach lie in good agreement with the experimental data of the metallic TPMS samples. Evidently, although the simulations performed by the phase field numerical model were on single unit cells, the numerical results showed great potential among the studies in the literature.

An open cell foam is comprehended as a porous structure in which its pores are interconnected to each other forming a network scaffold. In this instance, once TPMS based lattices split the three dimensional space into two intertwined domains by their porous topologies, and in the absence of solid cell walls, TPMS are systematically studied as open cellular foams. Therefore, the mechanical properties derived in the previous sections are now compared against the available data concerning compressive quasi-static uniaxial regime on open cell aluminium alloy foams. The major results to be compared with the actual outcomes are taken from the extensive review made in [15].

Fig. 54 shows the structural stiffness values of open cell Aluminium alloy foams, represented by the derived Young's modulus of the equivalent continuum, plotted against the volume fraction. Whereby, the results from the phase field for the Primitive, Gyroid, IWP, Diamond and Neovius are plotted with the data grouped in [15]. It can be noted that, over the comparable range of volume fraction, TPMS

foams exhibit considerably superior stiffness increasing with the volume fraction, as compared to the majority of the other existing Aluminium foams. The compressive strength of the various Aluminium alloy foams available in literature and TPMS as a function of volume fraction are presented in Fig. 55. Over the comparable range of volume fraction, the load bearing capacity of the five TPMS specimens studied by the phase field model are higher than the other listed foams, which can indicate superior advantage to be chosen in engineering problems where the load bearing capability plays an important role.

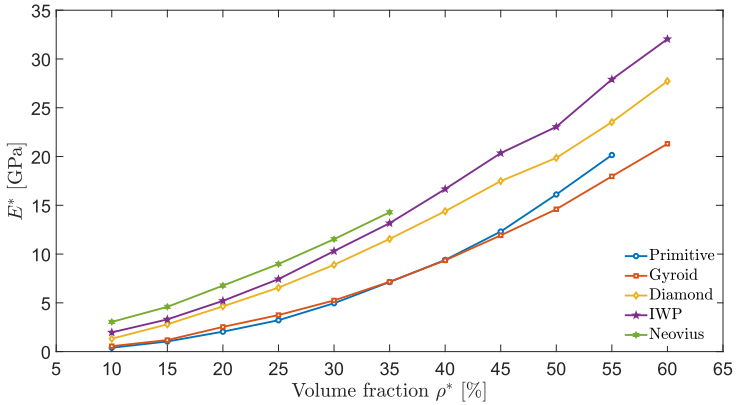

(a) Apparent Young's modulus E^* vs. volume fraction ρ^*.

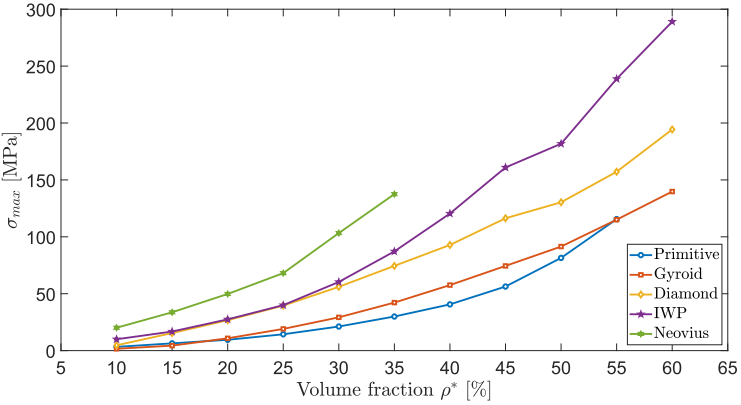

(b) Ultimate compressive stress $\sigma_{\max,c}$ vs. volume fraction ρ^*.

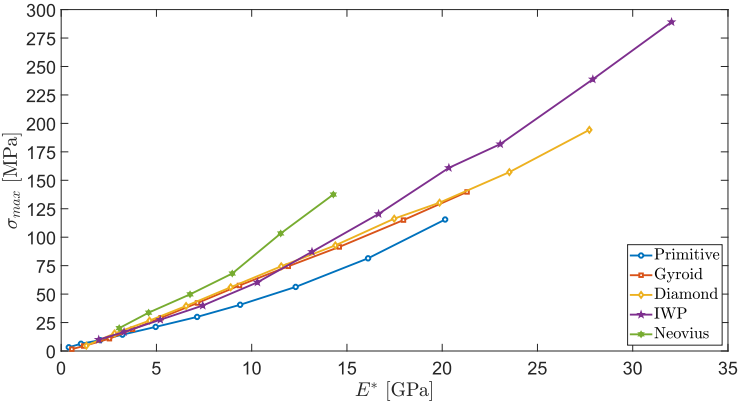

(c) $\sigma_{\max,c}$ vs. E^*.

Figure 50: Ashby charts (linear scales).

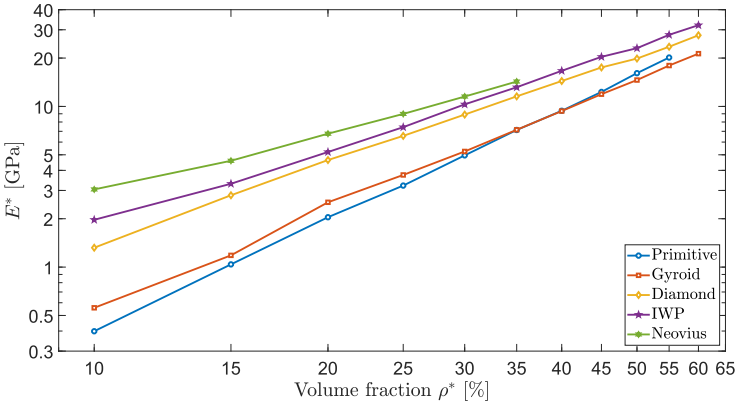

(a) Apparent Young's modulus E^* vs. volume fraction ρ^*.

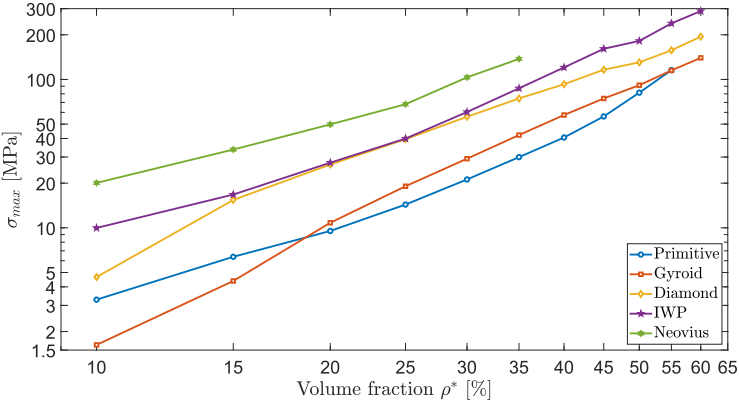

(b) Ultimate compressive stress $\sigma_{\max,c}$ vs. volume fraction ρ^*.

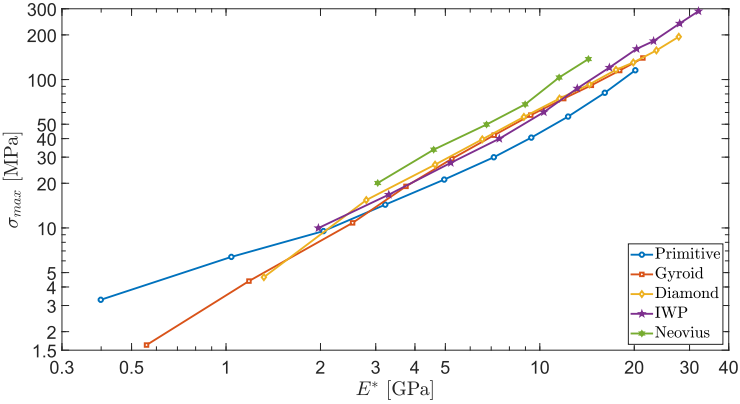

(c) $\sigma_{\max,c}$ vs. E^*.

Figure 51: Ashby charts (bi-logarithmic scales).

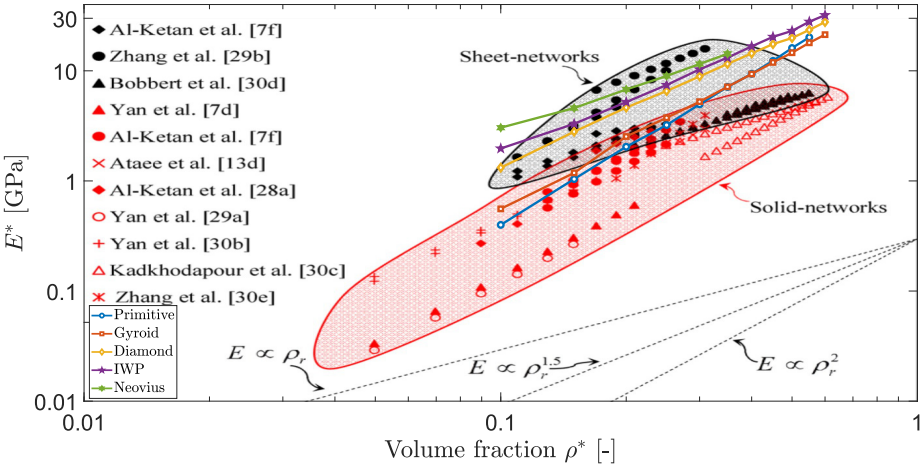

Figure 52: Ashby bi-logarithmic diagram comparing the numerically predicted Young's modulus E^* vs. volume fraction ρ^* of the tested TPMS, with experimental data from metallic TPMS [14]. For details in the legends please see references in Fig. 17(a) in [14].

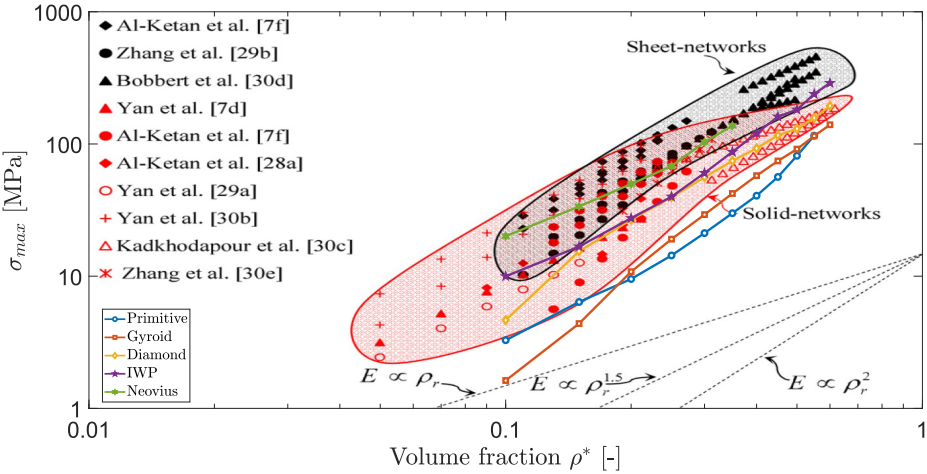

Figure 53: Ashby bi-logarithmic diagram comparing the numerically predicted ultimate compressive stress $\sigma_{\max,c}$ vs. volume fraction ρ^* of the tested TPMS, with experimental data from metallic TPMS [14]. For details in the legends please see references in Fig. 17(b) in [14].

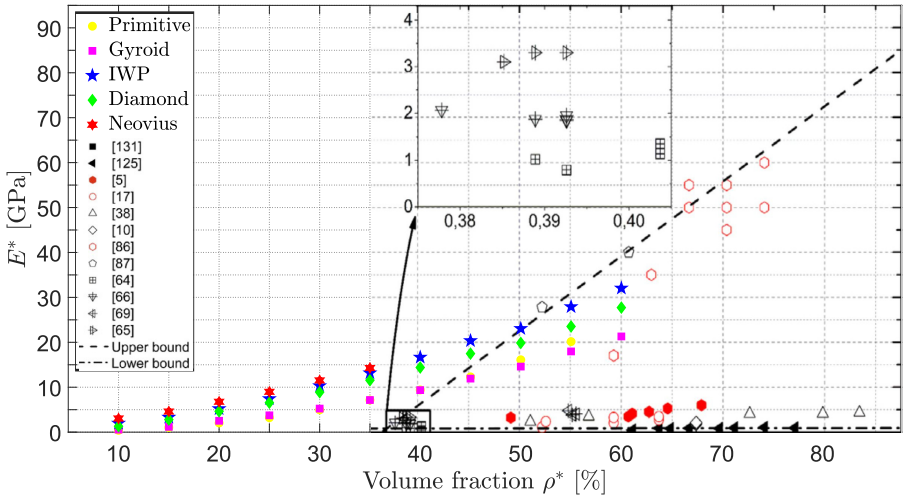

Figure 54: Comparison between the predicted Young's modulus E^* of TPMS foams and those of the open cell Aluminium alloy foams, vs. the volume fraction ρ^*. Experimental data of Aluminium foams are taken from [15]. For details in the legends please see references in Fig. 6 in [15]

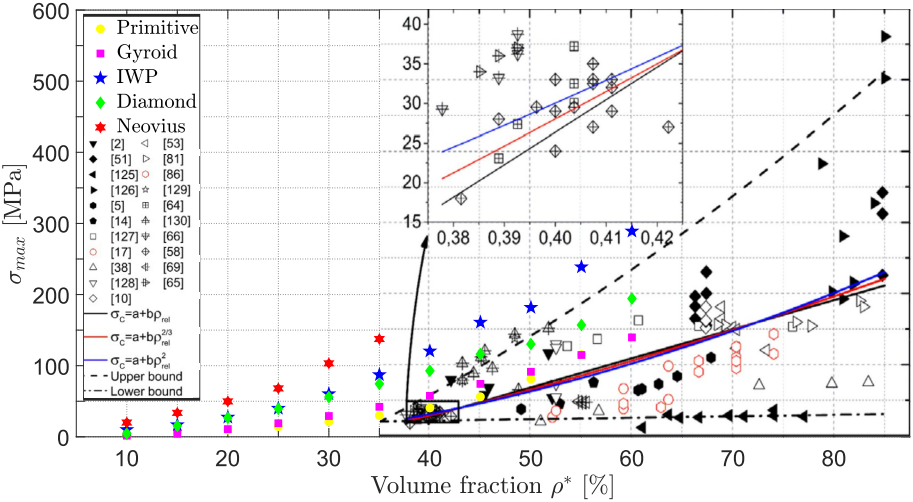

Figure 55: Comparison between the predicted compressive strength $\sigma_{\max,c}$ of TPMS foams and those of the open cell Aluminium alloy foams, vs. the volume fraction ρ^*. Experimental data of Aluminium foams are taken from [15]. For details in the legends please see references in Fig. 3 in [15].

Chapter 4

Conclusion and future developments

4.1 Conclusions

The present thesis has successfully dealt with the development of two mathematical frameworks in order to computationally exploit and characterize physical and mechanical responses of periodic materials. The conclusions, highlights and future prospective stated in the present section have been mainly taken from [16, 17].

4.1.1 Conclusions on Variational-Asymptotic Homogenization of Lord-Shulman thermoelastic theory in laminated materials

In what regards to the variational homogenization procedure applied to the Lord-Shulman thermoelasticity phenomenon, Chapter 2 has successfully formulated an asymptotic homogenization approach for describing composites that have a periodic microstructure in presence of the generalized thermoelasticity theory with a single periodic spatially dependent relaxation time [94], by which the results reached on layered periodic material could be therefore validated by comparing them with the ones obtained by solving the micromechanical problem in accordance to the Floquet-Bloch theory. The layered material provides suitable conditions to analytically control and manage both the micromechanical solution and the solution of the problem at the macro-scale. Meaning that, the method emerges as a significant tool to synthetically but also accurately characterize the behaviour of a periodic material

governed by the field equations of the unconventional Lord-Shulman thermoelasticity.

The mathematical procedure throughout developed begins by giving rise to the down-scaling relations, allowing such technique to express the micro-fields namely, displacement and temperature, in terms of the macroscopic fields and their derivatives, through the $\mathcal{Q}$-periodic perturbation functions. The cell problems i.e, a cascade of inhomogeneous recursive differential problems defined on the unit cell $\mathcal{Q}$ and having zero mean values over this unit cell, gave the availability to seek for those perturbation functions.

Still, the cell problems were derived substituting series expansions for both of the micro-fields in powers of the microstructural characteristic size ϵ into the micro governing equations and rearranging the outcomes as asymptotic expansions in terms of ϵ exponents. Inserting the down-scaling relations into the microscopic thermoelastic field equations has led to the average field equations of infinite order, which are asymptotically equivalent to the initial governing equations of the heterogeneous continuum, in which the formal solutions might be derived by plugging an asymptotic infinite series of the macro fields in powers of the microstructural size ϵ. Particularly, by a perturbative technique the solution of the average field equations of infinite order over the complex frequency-space domain are derived, followed by truncating the asymptotic expansion to the zeroth order, it is obtained the field equations at the macro-scale formally identical to those obtained through the variational procedure, also truncated to the zeroth order. Consequently, the higher the order of the truncated asymptotic expansions of the macro fields the better the estimation for solutions of the heterogeneous problem. It is important to note that, the overall thermal conductivity tensor depends on the complex frequency and the relaxation time of the phases, and in the scenario where the relaxation time is zero everywhere, the problem turns into the conventional thermoelasticity.

The reliability of such analysis has been evaluated through a benchmark test between the presented first order homogenized model and the heterogeneous continuum over an illustrative example of a bi-dimensional two-phase periodic layered material endowed with an orthotropy axis parallel to the layering direction, by comparing the wave propagation from their dispersion spectrum. The eigenproblem provides an imaginary implicit function and a real implicit function of the complex frequency and wave vector, where the intersection between them defines the frequency spectrum. The choice of considering a layered material as a key test case is endorsed by literature where can be found a vast number of engineering problems and techno-

logical applications. In what regards the investigation of the dispersion properties of the heterogeneous thermoelastic medium, the Floquet-Bloch theory has been analytically developed by means of the transfer matrix theory. Such path has led to a sixth order differential eigenproblem problem in terms of the Floquet multipliers, solved over the periodic cell subjected to Floquet-Bloch periodic boundary conditions, which throughout the comparative analysis were considered the uncoupled and coupled scenarios. In both eigenproblems, which give the dispersion relations of the layered material, the Floquet-Bloch approach characterizing the heterogeneous material, and the first order homogenized approximation, the thermal waves from the uncoupled problem as well as the compressional-thermal waves from the coupled problem, and the shear waves were compared against their respectives. Over the comparisons carried out in this work, it has been achieved a very good agreement between the dispersion curves computed from the two different methods i.e., thermal, compressional-thermal and shear waves along and normal direction to the layering. The lack of the relaxation time was also evaluated by the wave propagation comparing it with waves originated by assuming a few different values for the relaxation time. In essence, such strong connection observed between the methods confirms that the multi-field homogenization technique of the first order herein developed has been shown itself to be a quite good tool to estimate the macroscopic elastic and thermal overall properties of the equivalent heterogeneous body having periodic microstructure under thermoelastic phenomena with effective accuracy.

The outcome dispersion functions associated to the thermal-elastic waves from the homogenized model are fully derived in terms of the physico-mechanical properties of the periodic layered material at the micro-scale were analytically determined in closed form, so they can be compared with those of the heterogeneous thermoelastic material obtained from the solutions of the Floquet–Bloch theory by applying the transfer matrix method, leading to the solution of an eigenproblem in terms of the Floquet multiplier [241–243].

4.1.2 Conclusion on Phase Field modelling to Triply Periodic Minimal Surfaces

In Chapter 3, it was conducted an original exploitation of the phase field approach to simulate complex crack patterns in five types of TPMS open cells under compression, which the length scale parameter that regulates the sharpness of the crack has been considered as a characteristic feature of the material. The phase field approximation of fracture was derived from the weak form by a robust implementation based on

the spectral decomposition of the strain energy tensor. The TPMS unit cell lattices of Schwarz Primitive, Schoen Gyroid, Schoen-I-WP, Schwarz Diamond and Neovius were mathematically generated and virtually tested in a compressive regime. By choosing an aluminium alloy as base material of the open foams, an extensive mesh sensitivity evaluation was carried out for an increasing spatial discretization refinement via stress-strain responses. Consequently, crack sites, nucleation, propagation, branching and deformation behaviour of TPMS unit cells were computationally predicted and characterized.

Since a minimal surface is mainly characterized by its mean curvature, which is zero everywhere, and the Gaussian curvature, which is always non-positive, similar TPMS differing for the value of the volumetric content possess the same Gaussian curvature, which entails that the dependency on the volume fraction is the key aspect to be investigated. In this context, from the numerical campaign, the relationship between the role of the volume fraction against the mechanical responses have been carefully analysed. For this purpose, detailed comparative analyses were finally proposed within the Ashby diagrams relating the apparent Young's modulus in compression and the apparent maximum compressive stress to the volume fraction of the five TPMS unit cells. The comparisons have been displayed in standard and bi-logarithmic Ashby diagrams.

In addition to the analysis of the five TPMS open foams against themselves, throughout the investigation, cracking phase field pattern have been assessed and contrasted with the recent literature in AM experiments. By so, the numerical predictions showed good agreement concerning sites for crack nucleation and propagation in the Primitive and Gyroid open cells. Furthermore, it is well known that the deformation of the studied TPMS lattices is dependent on the topology, material and unit cell size. The outcomes of the present research work also exhibited deformation behaviour driven by their specific topology, and demonstrated volume fraction independency, which is in good accordance with previous literature. Additionally, through Ashby plots, a comparison with other type of cell aluminium alloy open foams with data taken from the literature was accomplished. It must be highlighted that predictions for TPMS unit cells showed the highest compressive properties as compared to standard aluminium alloys open foams. The predicted mechanical responses as functions of the volume fraction were contrasted as well with experimental results of other metallic based TPMS sheet networks existing in literature. The derived outcomes showed good agreement by lying over the hatched regions from the AM experimental data available in literature.

4.2 Future developments

From the standpoint of the homogenization technique herein proposed, it is an efficient and rigorous tool for the study of the static and dynamic behaviour of periodic medium in the presence of thermal-mechanical phenomena in the scenario where the separation of the scales is fully satisfied. In the case which non-local effects come into play, the homogenized first order models are not adequate. Meaning that, either higher-order approximations of the average infinite-order equation must be carried out, or higher-order non-local homogenization techniques must be derived, truncating the power-like functional to a desired higher order, thus identifying a non-local continuum of higher orders.

In what concerns to future research directions, the present asymptotic variational homogenization technique can be efficiently applied to other complex topologies, which may have great interest in technological applications for instance, thermoelastic wave propagation within TPMS could be a promising research field. On this behalf, the numerical solutions of the differential cell problems and the evaluation of the global constitutive tensors are required, which the latter a new finite element formulation in the field of unconventional thermoelasticity would be needed. Succinctly, the application of the novel described method to other geometries will require a wide analysis regarding the effect of numerical discretization that must be deeply developed and described in detail. Another topic that could be relevant for future works is a rigorous and complete justification of the formal asymptotics, having a more theoretical framework aimed at the study of the error that the solution of the average equation of infinite order attached with a perturbative approach and truncated at a defined order with respect to the current solution of the micro-scale problem and therefore aimed to demonstrate that the formal asymptotics proposed is close to the exact solution of the problem.

With respect to the phase field method hereby developed and achieved results, they provide together a cutting-edge tool to evaluate and estimate brittle fracture on TPMS structures, which can hasten applications of these structures in a variety of fields. For instance, it can be a useful tool on identifying weakest regions where fracture might occur in TPMS, with the aim of improving these critical sites before production by additive manufacturing techniques. Moreover, the present phase field model can diminish the uncertainty between crack occurrence caused by defects generated from the manufacturing processes, from crack nucleation driven by the TPMS topology. Notwithstanding, the phase field method derived can be utilized

to estimate and characterize fracture patterns as well as evaluate the load-bearing capacity in different 3D complex structures, under compression regimes, such as osseointegration and applications in bone tissue engineering.

In future works, an investigation of fracture in clusters of TPMS open foams, to assess emergent behaviours resulting from multiple unit cell interactions. Giving the complexity of the TPMS geometries, in order to reduce the computational time and ensure crack estimations in the vicinity of the crack, the developed phase field model can also be adapted and improved by utilizing a dual-mesh adaptive refinement method. In addition, the present phase field approach can be exploited to study the effect of the base material used to manufacture these structures, through virtual testing. As such, preliminary simulations showed differences regarding crack nucleation, propagation and branching in the Gyroid unit cell structure made out of a titanium alloy (which is commonly used in load-bearing bone replacement testing procedures), from the present characterized aluminium Gyroid, which may indicate that the material used can also play an important role on TPMS reliability. Particularly, through experimental tests in recent literature, it has been observed that post-yield mechanical properties, for instance plastic deformation and plateau stress response, are dictated by the base material of the TPMS unit cells, in spite of this fact, the presented phase field model can be further derived to exploit and validate these findings.

Appendices

The Appendices are mainly dedicated in developing the necessary tools to derive the benchmark analysis pursuit in Sec. 2.7. Based on the Floquet-Bloch theory, the dispersion relations of the periodic heterogeneous thermoelastic layered media are obtained via the transfer matrix decomposition. In particular, Appendix A focuses on showing the equivalence between the governing field equations at the micro-scale and the power-like functional through its Euler-Lagrange first variation. The content of the this Appendix is taken from the Supplementary Material of [16].

A Euler-Lagrange equation via power-like functional at micro-scale

Regarding the obtained governing field equations at the macro-scale, namely (2.72a) and (2.72b), and the overall constitutive tensors (2.71a) to (2.71d) in Sec. 2.5, the procedure only holds true in case that the variational approach at the micro-scale also holds. Having said that, this Appendix will provide an equivalence between the governing field equations at the micro-scale (2.11a), (2.11b) and the power-like functional (2.59) through the first variation of it, a similar procedure may be seen also in [244].

If the functional $\hat{\Lambda}$ in Eq. (2.59) attains a local minimum at $(\hat{\boldsymbol{u}}, \hat{\theta})$, δ is an arbitrary functions that has at least one derivative and vanishes at the boundary of $\mathfrak{L}$, and then defining here η as any number close to 0, yields

$$
\begin{aligned}
\delta\hat{\Lambda}_m(\hat{\boldsymbol{u}},\delta\hat{\boldsymbol{u}},\hat{\theta},\delta\hat{\theta}) = \frac{d}{d\eta}\Bigg[\int_{\mathfrak{L}} s\Bigg(&\frac{1}{2}\rho^m s^2(\hat{\boldsymbol{u}}+\eta\delta\hat{\boldsymbol{u}})\cdot(\hat{\boldsymbol{u}}+\eta\delta\hat{\boldsymbol{u}}) \quad + \\
&+\frac{1}{2}\nabla(\hat{\boldsymbol{u}}+\eta\delta\hat{\boldsymbol{u}}) : (\mathfrak{C}^m\nabla(\hat{\boldsymbol{u}}+\eta\delta\hat{\boldsymbol{u}})) \quad + \\
&-\frac{1}{2}\nabla(\hat{\boldsymbol{u}}+\eta\delta\hat{\boldsymbol{u}}) : (\boldsymbol{\alpha}^m(\hat{\theta}+\eta\delta\hat{\theta})) - (\hat{\boldsymbol{u}}+\eta\delta\hat{\boldsymbol{u}})\cdot\hat{\boldsymbol{b}}\Bigg)\, d\mathbf{x} \quad + \\
&-\int_{\mathfrak{L}}\Bigg(\frac{1}{2}\nabla(\hat{\theta}+\eta\delta\hat{\theta})\cdot\Big(\mathbf{K}^m\nabla(\hat{\theta}+\eta\delta\hat{\theta})\Big) \quad + \\
&+\frac{1}{2}s(\hat{\theta}+\eta\delta\hat{\theta})\,(\boldsymbol{\alpha}^m : \nabla(\hat{\boldsymbol{u}}+\eta\delta\hat{\boldsymbol{u}})) \quad + \\
&+\ \frac{1}{2}s(\hat{\theta}+\eta\delta\hat{\theta})(p^m(\hat{\theta}+\eta\delta\hat{\theta}) - (\hat{\theta}+\eta\delta\hat{\theta})\hat{r}\Bigg)\, d\mathbf{x}\Bigg]\Bigg|_{\eta=0},
\end{aligned}
\tag{1}
$$

where it must be highlighted that η as defined in this Appendix does not stand for thickness.

Reckon that the divergence theorem, the symmetry of the tensors $\mathfrak{C}^m$, $\mathbf{K}^m$, $\boldsymbol{\alpha}^m$ and evaluating the Eq. (1) on $\eta = 0$, the first variation of the power-like functional lying on the Laplace transform space at the micro-scale takes the form

$$
\begin{aligned}
\delta\hat{\Lambda}_m = &\int_{\mathfrak{L}}\Big[s\Big(\rho^m s^2\hat{\boldsymbol{u}} - \nabla\cdot(\mathfrak{C}^m\nabla\hat{\boldsymbol{u}}) + \nabla\cdot(\boldsymbol{\alpha}^m\hat{\theta}) - \hat{\boldsymbol{b}}\Big)\,\delta\hat{\boldsymbol{u}}\Big]\, d\mathbf{x} \quad + \\
&+\int_{\mathfrak{L}}\Big[\Big(\nabla\cdot\Big(\mathbf{K}^m\nabla\hat{\theta}\Big) - s\,(\boldsymbol{\alpha}^m\nabla\hat{\boldsymbol{u}}) - sp^m\hat{\theta} + \hat{r}\Big)\,\delta\hat{\theta}\Big]\, d\mathbf{x}\,,
\end{aligned}
\tag{2}
$$

and since $\delta\hat{\Lambda}_m(\hat{\boldsymbol{u}},\delta\hat{\boldsymbol{u}},\hat{\theta},\delta\hat{\theta}) = 0$, the Euler-Lagrange equations corresponding to the power-like functional at the micro-scale are

$$
\rho^m s^2\hat{\boldsymbol{u}} - \nabla\cdot(\mathfrak{C}^m\nabla\hat{\boldsymbol{u}}) + \nabla\cdot(\boldsymbol{\alpha}^m\hat{\theta}) - \hat{\boldsymbol{b}} = \mathbf{0}, \tag{3a}
$$

$$
\nabla\cdot\Big(\mathbf{K}^m\nabla\hat{\theta}\Big) - s\,(\boldsymbol{\alpha}^m\nabla\hat{\boldsymbol{u}}) - sp^m\hat{\theta} + \hat{r} = 0, \tag{3b}
$$

hence the variational approach at the micro-scale gives exactly the field equations defined over the Laplace transform space seen in Eqs. (2.11a) and (2.11b). By consequence, the thermoelasticity governing field equations (2.15a) and (2.15b) over the time space t emerge once again after applying the inverse Laplace transform.

B Thermoelastic wave propagation modelling: Wave propagation in heterogeneous periodic material

On one hand, Sec. 2.6 studied the wave propagation an homogenized continuum, taking advantage of the thermoelastic field equations on the complex frequency space s at the macro-scale, provided by the asymptotic homogenization process seen previously in the present work. Now, on the other hand, this Appendix is focused on investigate the heterogeneous material to determine the frequency spectrum via Floquet-Bloch theory [241–243], from the thermoelastic field equations at the micro-scale over Laplace transformed space.

To this aim, firstly we recall the thermoelastic field equations (3a) and (3b), without the source terms $\hat{\boldsymbol{b}}$ and $\hat{r}$, i.e.,

$$\nabla \cdot (\mathfrak{C}^m \nabla \hat{\boldsymbol{u}}) - \nabla \cdot (\boldsymbol{\alpha}^m \hat{\theta}) = \rho^m s^2 \hat{\boldsymbol{u}}, \tag{4a}$$

$$\nabla \cdot \left(\mathbf{K}^m \nabla \hat{\theta}\right) - s\,(\boldsymbol{\alpha}^m \nabla \hat{\boldsymbol{u}}) = s p^m \hat{\theta}. \tag{4b}$$

Secondly, from Floquet-Bloch theory, the decompositions for the thermoelastic medium are given by

$$\hat{\boldsymbol{u}}\,(\mathbf{x}, s) = \hat{\boldsymbol{U}}^B(\mathbf{x}, s)\mathrm{e}^{\mathrm{i}(\boldsymbol{k}\cdot\mathbf{x})}, \tag{5a}$$

$$\hat{\theta}\,(\mathbf{x}, s) = \hat{\Theta}^B(\mathbf{x}, s)\mathrm{e}^{\mathrm{i}(\boldsymbol{k}\cdot\mathbf{x})}, \tag{5b}$$

where $\hat{\boldsymbol{U}}^B(\mathbf{x}, s)$ and $\hat{\Theta}^B(\mathbf{x}, s)$ are $\mathcal{A}$-periodic Bloch amplitudes of the displacement field and temperature field, on the Laplace transformed space, respectively. Eqs. (5a) and (5b) satisfy the Floquet-Bloch periodicity boundary conditions, in which they arose by the $\mathcal{Q}$-periodicity of the medium. Let $\boldsymbol{k} \in \mathbb{C}^3$ be the wave vector, the Floquet-Bloch boundary conditions read

$$\hat{\boldsymbol{u}}(\mathbf{x} + \boldsymbol{v}_p, s) = \mathrm{e}^{\mathrm{i}(\boldsymbol{k}\cdot\boldsymbol{v}_p)}\hat{\boldsymbol{u}}\,(\mathbf{x}, s)\,, \tag{6a}$$

$$\hat{\theta}(\mathbf{x} + \boldsymbol{v}_p, s) = \mathrm{e}^{\mathrm{i}(\boldsymbol{k}\cdot\boldsymbol{v}_p)}\hat{\theta}\,(\mathbf{x}, s)\,, \tag{6b}$$

where $\boldsymbol{v}_p$ is the periodicity vector ($p = 1, 2, 3$).

Finally, coupling the Floquet-Bloch decompositions above into the field equations (4a) and (4b), and making some simplifications, the tensorial form yields

$$\nabla^B \cdot (\mathfrak{C}^m \nabla^B \hat{\boldsymbol{U}}^B) - \nabla^B \cdot (\boldsymbol{\alpha}^m \hat{\Theta}^B) - \rho^m s^2 \hat{\boldsymbol{U}}^B = \boldsymbol{0}, \tag{7a}$$

$$\nabla^B \cdot \left(\mathbf{K}^m \nabla^B \hat{\Theta}^B\right) - s\left(\boldsymbol{\alpha}^m \nabla^B \hat{\boldsymbol{U}}^B\right) - s p^m \hat{\Theta}^B = 0, \tag{7b}$$

where the differential operator ∇^B was defined as

$$\nabla \hat{\boldsymbol{u}} = \left(\nabla \hat{\boldsymbol{U}}^B + \mathrm{i}\boldsymbol{k} \otimes \hat{\boldsymbol{U}}^B\right) \mathrm{e}^{\mathrm{i}(\boldsymbol{k}\cdot\mathbf{x})} = \nabla^B \left(\hat{\boldsymbol{U}}^B\right) \mathrm{e}^{\mathrm{i}(\boldsymbol{k}\cdot\mathbf{x})}, \tag{8a}$$

$$\nabla \hat{\theta} = \left(\nabla \hat{\Theta}^B + \mathrm{i}\boldsymbol{k} \otimes \hat{\Theta}^B\right) \mathrm{e}^{\mathrm{i}(\boldsymbol{k}\cdot\mathbf{x})} = \nabla^B \left(\hat{\Theta}^B\right) \mathrm{e}^{\mathrm{i}(\boldsymbol{k}\cdot\mathbf{x})}. \tag{8b}$$

Particularly, we may also represent the field equations in terms of the components

$$\begin{aligned} &\left(C^m_{ijhk} \hat{U}^B_{h,k}\right)_{,j} + \mathrm{i}k_j \left[\left(C^m_{ijhk} + C^m_{ikhj}\right) \hat{U}^B_{h,k} + C^m_{ikhj,k} \hat{U}^B_h - \alpha^m_{ij} \hat{\Theta}^B\right] + \\ &- \left(k_k k_j C^m_{ijhk} + \rho^m s^2 \delta_{ih}\right) \hat{U}^B_h - \left(\alpha^m_{ij} \hat{\Theta}^B\right)_{,j} = 0, \end{aligned} \tag{9a}$$

$$\begin{aligned} &\left(K^m_{ij} \hat{\Theta}^B_{,j}\right)_{,i} + \mathrm{i}k_j \left[\left(K^m_{ij} + K^m_{ji}\right) \hat{\Theta}^B_{,i} + K^m_{ij,i} \hat{\Theta}^B - s\alpha^m_{ij} \hat{U}^B_i\right] + \\ &- \left(k_i k_j K^m_{ij} + s p^m\right) \hat{\Theta}^B - s\alpha^m_{ij} \hat{U}^B_{i,j} = 0, \end{aligned} \tag{9b}$$

although the derivative $(\cdot)_{,j}$ was once defined as the microscopic derivative, for convenience here it represents the partial derivative in x_j, i.e. $\partial/\partial x_j = (\cdot)_{,j}$

Recalling the spatial damping method in the Sec. 2.6, let the conditions of an homogeneous wave be plugged into the field equations (9a) and (9b), so given a direction $\boldsymbol{n}$ of the wave vector $\boldsymbol{k} = \kappa \boldsymbol{n}$ one obtains an eigenvector-eigenvalue problem where κ is the eigenvalue and the $\mathcal{Q}$-periodic Bloch amplitudes $\hat{\boldsymbol{U}}^B$, $\hat{\Theta}^B$ are the eigenfunctions associated to it, while the angular frequency ω might be a fixed parameter. Consequently to the study of harmonic waves over a layered media in the next Sec. C, it arrives to the frequency spectrum $\kappa\omega$ (2.79).

Similarly through the time damping path seen in Sec. 2.6 together with the results from the Sec. C, it is possible to find an eigenproblem, where once resolved in this scenario it allows to determine the eigenvalues corresponding to the dispersion surfaces $s(\boldsymbol{k})$, that is writing the complex angular frequency s as functions of the wave vector $\boldsymbol{k}$ and also the eigenfunctions corresponding to the wave polarization, with the Bloch amplitudes being its components [245].

C Frequency-band structure for periodic heterogeneous thermoelastic layered material

In the present Appendix, it is outlined the procedure followed to obtain the frequency spectrum corresponding to the spatial damping over a periodic heterogeneous thermoelastic orthotropic layered material, which has led us to evaluate the benchmark test detailed in Sec. 2.7.2, where the corresponding method drives into the dispersion relation (2.78). Specifically, this procedure is based on the transfer matrix method [246].

Initially, let us consider a body made of a given number n of overlapped layers bonded at their interfaces and stacked normal to the axis $\boldsymbol{e}_2$ of the plane $(\boldsymbol{e}_1, \boldsymbol{e}_2)$ ($\boldsymbol{\xi} = \xi_1 \boldsymbol{e}_1 + \xi_2 \boldsymbol{e}_2$). By assumption, the line boundary of each layer must be parallel to the $\boldsymbol{e}_1$ vector which is chosen to coincide whit the exact half of the layered plate. We also assign for each layer the number j (with $j = 1, 2, \ldots, n$) a local coordinate $\mathfrak{s}_i^{(j)}$ such that its origin is located in the barycentre of the layer with $\mathfrak{s}_2^{(j)}$ normal to it. Thus layer j occupies the region $-d^{(j)}/2 \leq \mathfrak{s}_3^{(j)} \leq d^{(j)}/2$, where $d^{(j)}$ is its thickness, and hence d, the sum of the thickness of all individual layers $d_2 = d^{(1)} + \cdots + d^{(j)} + \cdots + d^{(n)}$ must be equal to the total height of the layered body, where the body occupies the region $-d_2/2 \leq \xi_2 \leq d_2/2$.

Let us assume the same hypothesis taken in the Sec. 2.7.1 for the heterogeneous thermoelastic problem, this means an orthotropic bi-phase layered material with the orthotropy axes perpendicular to the layering direction $\boldsymbol{e_2}$ and the wave vector as $\boldsymbol{k} = (k_1, k_2)^T = (0, k_2)^T$, which make the field equations (9a) and (9b) only dependent on the variable ξ_2, therefore for each layer j we have a set of following governing equations

$$C_{1212}^{(j)} \hat{U}_{1,22}^B + \mathrm{i}2k_2 C_{1212}^{(j)} \hat{U}_{1,2}^B - \left(k_2^2 C_{1212}^{(j)} + \rho^m s^2\right) \hat{U}_1^B = 0, \tag{10a}$$

$$C_{2222}^{(j)} \hat{U}_{2,22}^B + \mathrm{i}2k_2 \left(C_{2222}^{(j)} \hat{U}_{2,2}^B - \alpha_{22}^{(j)} \hat{\Theta}^B\right) - \left(k_2^2 C_{2222}^{(j)} + \rho^{(j)} s^2\right) \hat{U}_2^B - \alpha_{22}^{(j)} \hat{\Theta}_{,2}^B = 0, \tag{10b}$$

$$K_{22}^{(j)} \hat{\Theta}_{,22}^B + \mathrm{i}2k_2 \left(K_{22}^{(j)} \hat{\Theta}_{,2}^B - s\alpha_{22}^{(j)} \hat{U}_2^B\right) - \left(k_2^2 K_{22}^{(j)} + sp^{(j)}\right) \hat{\Theta}^B - s\alpha_{22}^{(j)} \hat{U}_{2,2}^B = 0. \tag{10c}$$

In order to arrive at the transfer matrix, the solutions in the Floquet-Bloch form (5a) and (5b) of the specialized governing equations (10a), (10b) and (10c) for each layer j are obtained and are evaluated for both the upper $(+)$ and lower $(-)$

boundary surfaces of layer j. Among them, from the constitutive relations (2.1a) and (2.1b) transformed in the Floquet-Bloch form as well, the components $\hat{\sigma}_{12}^{B}$, $\hat{\sigma}_{22}^{B}$ and $\hat{q}_{2}^{B}$ are derived, which are also evaluated for the upper $(+)$ and lower $(-)$ boundary surfaces of layer j. Proceeding with some algebraic manipulations over them, the transformed components specialized for the upper $(+)$ boundary of layer j can be written in terms of the same components but specialized for the lower $(-)$ boundary of layer j.

In the following, by applying the above procedure to a single layer, one obtains

$$[\boldsymbol{P}]_{j}^{+} = [\boldsymbol{A}]_{j}[\boldsymbol{P}]_{j}^{-}, \quad j = 1, 2, \ldots, n, \tag{11}$$

where the vector $[\boldsymbol{P}]_{j}^{\pm} = \left(\left[\hat{U}_{1}^{B}, \hat{U}_{2}^{B}, \hat{\Theta}^{B}, \hat{\sigma}_{12}^{B}, \hat{\sigma}_{22}^{B}, \hat{q}_{2}^{B} \right]_{j}^{\pm} \right)^{T}$ (T here is for transpose) defines the column vectors of the displacement $\hat{\boldsymbol{U}}^{B}$, temperature $\hat{\boldsymbol{\Theta}}^{B}$, stress $\hat{\boldsymbol{\sigma}}^{B}$ and heat flux $\hat{\boldsymbol{q}}^{B}$, specialized to the upper $(+)$ and lower $(-)$ boundary surfaces of layer j, and the matrix $[\boldsymbol{A}]_{j}$ constitutes the local transfer matrix for layer j.

Finding the Eq. (11) to each layer, followed by the individual matrix multiplication $[\boldsymbol{A}] = [\boldsymbol{A}]_{n} \ldots [\boldsymbol{A}]_{2}[\boldsymbol{A}]_{1}$ and reminding the continuity of the thermoelastic solutions and constitutive tensors at the layer interfaces namely, $[\boldsymbol{P}]_{j+1}^{-} = [\boldsymbol{P}]_{j}^{+}$, one relates the solutions and tensors at the upper boundary, to those at its lower boundary, this results in $[\boldsymbol{P}]^{+} = [\boldsymbol{A}][\boldsymbol{P}]^{-}$, where $[\boldsymbol{P}]^{-}$ and $[\boldsymbol{P}]^{+}$ are now the displacement, temperature and tensor column vectors specialized to the upper and lower faces of the total plate, respectively and $[\boldsymbol{A}]$ is the global transfer matrix of the total cell. Finally, imposing the Floquet-Bloch periodic boundary conditions namely, Eqs. (6a) and (6b), one gives $[\boldsymbol{P}]^{+} = \mathrm{e}^{\mathrm{i}(\boldsymbol{k}\cdot\mathbf{x})}[\boldsymbol{P}]^{-}$, and therefore one arises the linear problem

$$\mathrm{e}^{\mathrm{i}(\boldsymbol{k}\cdot\mathbf{x})}[\boldsymbol{P}]^{-} = [\boldsymbol{A}][\boldsymbol{P}]^{-}. \tag{12}$$

At this point, even though both the local and global transfer matrices show themselves with several properties, which are discussed and listed in [246], we only exploit them computationally herein. Such properties classify the transfer matrix as being a symplectic matrix, and the characteristic polynomial attached to its respective eigenproblem i.e. $([\boldsymbol{A}] - \mathrm{e}^{\mathrm{i}(\boldsymbol{k}\cdot\mathbf{x})}[\boldsymbol{I}])[\boldsymbol{P}]^{-} = ([\boldsymbol{A}] - \lambda[\boldsymbol{I}])[\boldsymbol{P}]^{-} = [\mathbf{0}]$, is a palindromic polynomial [247].

The palindromic polynomial $\mathscr{P}(\lambda) = \det([\boldsymbol{A}] - \lambda[\boldsymbol{I}]) = 0$ to our bi-layered material problem given by the field equations (10a), (10b) and (10c), wrote in terms of the invariants I_{k} of $[\boldsymbol{A}]$ as

$$\mathscr{P}(\lambda) = I_6 + I_5\lambda + I_4\lambda^2 + I_3\lambda^3 + I_2\lambda^4 + I_1\lambda^5 + I_0\lambda^6, \tag{13}$$

it has the following symmetric relations

$$I_0 = I_6 = 1, \quad I_1 = I_5, \quad I_2 = I_4. \tag{14}$$

In addition, once recognized that $\mathrm{e}^{i(\boldsymbol{k}\cdot\mathbf{x})}$ is an eigenvalue of the transfer matrix $[\boldsymbol{A}]$, via the transformation $\mathfrak{z} = \lambda + 1/\lambda$ its palindromic polynomial (13) can still be formally rephrased as

$$\mathscr{P}(\mathfrak{z}) = \mathfrak{z}^3 + I_1\mathfrak{z}^2 + (I_2 - 3)\mathfrak{z} + (I_3 - 2I_1). \tag{15}$$

Last but not least, it is possible to invoke the transfer matrix structure and rewrite the invariants I_1, I_2, and I_3 in terms of the trace of $[\boldsymbol{A}]$ as established in [248], so

$$I_1 = -\mathrm{tr}([\boldsymbol{A}]), \tag{16a}$$

$$I_2 = -\frac{1}{2}\mathrm{tr}([\boldsymbol{A}]^2) + \frac{1}{2}(\mathrm{tr}([\boldsymbol{A}]))^2, \tag{16b}$$

$$I_3 = -\frac{1}{3}\mathrm{tr}([\boldsymbol{A}]^3) + \frac{1}{2}\mathrm{tr}([\boldsymbol{A}]^2)\mathrm{tr}([\boldsymbol{A}]) - \frac{1}{6}(\mathrm{tr}([\boldsymbol{A}]))^3. \tag{16c}$$

Still at the same assumptions made in the beginning of this Appendix, it is also feasible factorize the polynomial (13) into two minor factors, namely one of a second degree polynomial associated to the Eq. (10a) and another of a fourth degree polynomial associated to the Eqs. (10b) and (10c). Each sub-polynomial will also be a palindromic polynomial and therefore governed by invariants of its sub-matrices. Furthermore, choosing the right changing of variables, after a similar process as made before, one will have factorized the third degree polynomial (15) into two sub-polynomials a linear one and a quadratic one.

D Invariants of the dispersive wave propagation in the periodic heterogeneous thermoelastic layered material

Throughout this Appendix it is presented the invariants that characterize the wave propagation along the heterogeneous material. So, for the uncoupled hypothesis

of the thermoelastic problem taken in Sec. 2.7.2 for the comparative analysis and among the latter theories written in the Secs. B and C, the invariants may be obtained with the following analytical expressions

$$\tilde{I}_1^1(s) = -\frac{\sqrt{A_{1212}}B_{1212}+2A_{1212}}{4A_{1212}}\left(\mathrm{e}^{-s\left(\sum_{r=1}^{2}\varpi_{1212}^{(r)}\right)}+\mathrm{e}^{s\left(\sum_{r=1}^{2}\varpi_{1212}^{(r)}\right)}\right)+ \\ +\frac{\sqrt{A_{1212}}B_{1212}-2A_{1212}}{4A_{1212}}\left(\mathrm{e}^{-s\left(\sum_{r=1}^{2}(-1)^r\varpi_{1212}^{(r)}\right)}+\mathrm{e}^{s\left(\sum_{r=1}^{2}(-1)^r\varpi_{1212}^{(r)}\right)}\right), \tag{17}$$

where $A_{1212} = C_{1212}^{(2)}\rho^{(2)}C_{1212}^{(1)}\rho^{(1)}$, $B_{1212} = C_{1212}^{(1)}\rho^{(1)} + C_{1212}^{(2)}\rho^{(2)}$,
$\varpi_{1212}^{(j)} = \mathfrak{s}_j\sqrt{C_{1212}^{(j)}\rho^{(j)}}/C_{1212}^{(j)}$ with $j = 1, 2$.

Analogously, for the compressional wave the associate dispersion relation provides the wave number k_2 as an explicit function of the complex frequency s,

$$\tilde{I}_1^2(s) = -\frac{\sqrt{A_{2222}}B_{2222}+2A_{2222}}{4A_{2222}}\left(\mathrm{e}^{-s\left(\sum_{r=1}^{2}\varpi_{1212}^{(r)}\right)}+\mathrm{e}^{s\left(\sum_{r=1}^{2}\varpi_{1212}^{(r)}\right)}\right)+ \\ +\frac{\sqrt{A_{2222}}B_{2222}-2A_{2222}}{4A_{2222}}\left(\mathrm{e}^{-s\left(\sum_{r=1}^{2}(-1)^r\varpi_{1212}^{(r)}\right)}+\mathrm{e}^{s\left(\sum_{r=1}^{2}(-1)^r\varpi_{1212}^{(r)}\right)}\right), \tag{18}$$

where $A_{2222} = C_{2222}^{(2)}\rho^{(2)}C_{2222}^{(1)}\rho^{(1)}$, $B_{2222} = C_{2222}^{(1)}\rho^{(1)} + C_{2222}^{(2)}\rho^{(2)}$,
$\varpi_{2222}^{(j)} = \mathfrak{s}_j\sqrt{C_{2222}^{(j)}\rho^{(j)}}/C_{2222}^{(j)}$ with $j = 1, 2$.

Lastly, for the thermal wave propagation follows that

$$\tilde{I}_1^3(s) = -\left(\frac{|s|\sum\limits_{r=1}^{2}\left(s\tau^{(r)}+1\right)\mu_{22}^{(r)}}{4s\sqrt{\left(\prod_{r=1}^{2}\left(s\tau^{(r)}+1\right)\mu_{22}^{(r)}\right)}}+\frac{1}{2}\right)\left(\begin{matrix}\mathrm{e}^{-\sum\limits_{r=1}^{2}\left(s\tau^{(r)}+1\right)\varphi_{22}^{(r)}} \\ \\ \end{matrix}+\mathrm{e}^{\sum\limits_{r=1}^{2}\left(s\tau^{(r)}+1\right)\varphi_{22}^{(r)}}\right)+$$
$$+\left(\frac{|s|\sum\limits_{r=1}^{2}\left(s\tau^{(r)}+1\right)\mu_{22}^{(r)}}{4s\sqrt{\left(\prod_{r=1}^{2}\left(s\tau^{(r)}+1\right)\mu_{22}^{(r)}\right)}}-\frac{1}{2}\right)\left(\begin{matrix}\mathrm{e}^{-\sum\limits_{r=1}^{2}(-1)^r\left(s\tau^{(r)}+1\right)\varphi_{22}^{(r)}} \\ \\ \end{matrix}+\mathrm{e}^{\sum\limits_{r=1}^{2}(-1)^r\left(s\tau^{(r)}+1\right)\varphi_{22}^{(r)}}\right), \tag{19}$$

where $\mu_{22}^{(r)} = 1/\bar{K}_{22}^{(r)}p^{(r)}$, $\varphi_{22}^{(r)} = T_0\mathfrak{s}_r\sqrt{\bar{K}_{22}^{(r)}p^{(r)}}/\bar{K}_{22}^{(r)}$.

Bibliography

[1] Anand Krishna Asundi and Alta YN Choi. Fiber metal laminates: an advanced material for future aircraft. *Journal of Materials processing technology*, 63(1-3):384–394, 1997.

[2] Jeremy W Galusha, Lauren R Richey, John S Gardner, Jennifer N Cha, and Michael H Bartl. Discovery of a diamond-based photonic crystal structure in beetle scales. *Physical Review E*, 77(5):050904, 2008.

[3] Jeremy W Galusha, Lauren R Richey, Matthew R Jorgensen, John S Gardner, and Michael H Bartl. Study of natural photonic crystals in beetle scales and their conversion into inorganic structures via a sol–gel bio-templating route. *Journal of Materials Chemistry*, 20(7):1277–1284, 2010.

[4] Katarina Monkova, Peter Monka, Ivana Zetkova, Pavel Hanzl, and Dusan Mandulak. Three approaches to the gyroid structure modelling as a base of lightweight component produced by additive technology. *DEStech Trans. Comput. Sci. Eng. CMSAM*, 2017.

[5] Liping Wu, Wanlin Wang, Wang Zhang, Huilan Su, Jiajun Gu, Qinglei Liu, Di Zhang, Dejan Pantelić, and Branislav Jelenković. Optical performance study of gyroid-structured tio2 photonic crystals replicated from natural templates using a sol-gel method. *Advanced Optical Materials*, 6(21):1800064, 2018.

[6] Jiaqing He, Nicolò Simone Villa, Zhen Luo, Shun An, Qingchen Shen, Peng Tao, Chengyi Song, Jianbo Wu, Tao Deng, and Wen Shang. Integrating plasmonic nanostructures with natural photonic architectures in pd-modified morpho butterfly wings for sensitive hydrogen gas sensing. *RSC advances*, 8(57):32395–32400, 2018.

[7] *File:*munih-olimpiyat-stadyumu-13.jpg. (visited on 29/09/2022). URL: https://www.arkitektuel.com/wp-content/uploads/2017/10/munih-olimpiyat-stadyumu-13.jpg.

[8] Dong J Yoo. Porous scaffold design using the distance field and triply periodic minimal surface models. *Biomaterials*, 32(31):7741–7754, 2011.

[9] Sara AlMahri, Rafael Santiago, Dong-Wook Lee, Henrique Ramos, Haleimah Alabdouli, Mohamed Alteneiji, Zhongwei Guan, Wesley Cantwell, and Marcilio Alves. Evaluation of the dynamic response of triply periodic minimal surfaces subjected to high strain-rate compression. *Additive Manufacturing*, 46:102220, 2021.

[10] Mathew Speirs, Brecht Van Hooreweder, Jan Van Humbeeck, and J-P Kruth. Fatigue behaviour of niti shape memory alloy scaffolds produced by slm, a unit cell design comparison. *Journal of the mechanical behavior of biomedical materials*, 70:53–59, 2017.

[11] *File:*Minimal_surface_curvature_planes-en.svg. (visited on 29/09/2022). URL: https://commons.wikimedia.org/wiki/File:Minimal_surface_curvature_planes-en.svg.

[12] Shixiang Yu, Jinxing Sun, and Jiaming Bai. Investigation of functionally graded tpms structures fabricated by additive manufacturing. *Materials & Design*, 182:108021, 2019.

[13] Ian Maskery, Nesma T Aboulkhair, AO Aremu, CJ Tuck, and IA Ashcroft. Compressive failure modes and energy absorption in additively manufactured double gyroid lattices. *Additive Manufacturing*, 16:24–29, 2017.

[14] Oraib Al-Ketan and Rashid K Abu Al-Rub. Multifunctional mechanical metamaterials based on triply periodic minimal surface lattices. *Advanced Engineering Materials*, 21(10):1900524, 2019.

[15] Imre Norbert Orbulov and Attila Szlancsik. On the mechanical properties of aluminum matrix syntactic foams. *Advanced Engineering Materials*, 20(5):1700980, 2018.

[16] Deison Préve, Andrea Bacigalupo, and Marco Paggi. Variational-asymptotic homogenization of thermoelastic periodic materials with thermal relaxation. *International Journal of Mechanical Sciences*, 205:106566, 2021.

[17] Deison Préve, Pietro Lenarda, Ian Maskey, and Marco Paggi. A comprehensive characterization of fracture in unit cell open foams generated from triply periodic minimal surfaces. *Engineering Fracture Mechanics*, .:108949, 2022.

[18] Ronald F Gibson. *Principles of composite material mechanics*. CRC press, 2016.

[19] Jack R Vinson and Robert L Sierakowski. *The behavior of structures composed of composite materials*, volume 105. Springer, 2006.

[20] M Ruzzene and A Baz. Active control of wave propagation in periodic fluid-loaded shells. *Smart Materials and Structures*, 10(5):893, 2001.

[21] *File:*portiera-aperta-koenigsegg-agera-s-hundra_145115.jpg. (visited on 29/09/2022). URL: `https://www.allaguida.it/wp-content/uploads/np-gallery/2013/03/portiera-aperta-koenigsegg-agera-s-hundra_145115.jpg`.

[22] *File:*NASA's Composite Crew Module-660982main_ELG8245_226x170.jpg. (visited on 29/09/2022). URL: `https://www.nasa.gov/centers/marshall/images/content/660982main_ELG8245_226x170.jpg`.

[23] Manvir S Kushwaha, Peter Halevi, Leonard Dobrzynski, and Bahram Djafari-Rouhani. Acoustic band structure of periodic elastic composites. *Physical review letters*, 71(13):2022, 1993.

[24] J Prunty. Dimensionally stable graphite composites for spacecraft structures. *SAMPE Quarterly*, 9(2):41–51, 1978.

[25] Kelly J Dodson and John E Rule. Thermal stability considerations for space flight optical benches. *sampe*, pages 1578–1589, 1989.

[26] Jeffery T Farmer, Deborah M Wahls, Robert L Wright, and A Louis Tahernia. Thermal distortion analysis of an antenna-support truss in geosynchronous orbit. *Journal of Spacecraft and Rockets*, 29(3):386–393, 1992.

[27] Ran Y Kim, Allan S Crasto, and Gregory A Schoeppner. Dimensional stability of composite in a space thermal environment. *Composites science and technology*, 60(12-13):2601–2608, 2000.

[28] RP Zhu and CT Sun. Effects of fiber orientation and elastic constants on coefficients of thermal expansion in laminates. *Mechanics of Advanced Materials and Structures*, 10(2):99–107, 2003.

[29] Marco Paggi, Sarah Kajari-Schröder, and Ulrich Eitner. Thermomechanical deformations in photovoltaic laminates. *The Journal of Strain Analysis for Engineering Design*, 46(8):772–782, 2011.

[30] Adnan Nayfeh and S Nemat-Nasser. Thermoelastic waves in solids with thermal relaxation. *Acta Mechanica*, 12(1-2):53–69, 1971.

[31] Muhammad A Hawwa and Adnan H Nayfeh. The general problem of thermoelastic waves in anisotropic periodically laminated composites. *Composites Engineering*, 5(12):1499–1517, 1995.

[32] Enrique Sanchez-Palencia. Comportements local et macroscopique d'un type de milieux physiques hétérogènes. *International Journal of Engineering Science*, 12(4):331–351, 1974.

[33] George Papanicolau, Alain Bensoussan, and J-L Lions. *Asymptotic analysis for periodic structures*, volume 5. Elsevier, 1978.

[34] Nikolai Sergeevich Bakhvalov and Grigory Panasenko. *Homogenization: Averaging Processes in Periodic Media*. Kluwer Academic Publishers, Dordrecht-Boston-London, 1984.

[35] Valery P Smyshlyaev and KD Cherednichenko. On rigorous derivation of strain gradient effects in the overall behaviour of periodic heterogeneous media. *Journal of the Mechanics and Physics of Solids*, 48(6):1325–1357, 2000.

[36] Andrea Bacigalupo and Luigi Gambarotta. Computational dynamic homogenization for the analysis of dispersive waves in layered rock masses with periodic ures. *Computers and Geotechnics*, 56:61–68, 2014.

[37] Hussein Nassar, Q-C He, and Nicolas Auffray. On asymptotic elastodynamic homogenization approaches for periodic media. *Journal of the Mechanics and Physics of Solids*, 88:274–290, 2016.

[38] Manfredo P Do Carmo. *Differential forms and applications*. Springer Science & Business Media, 2012.

[39] Alfred Gray, Elsa Abbena, and Simon Salamon. *Modern differential geometry of curves and surfaces with Mathematica®*. Chapman and Hall/CRC, 2017.

[40] Joseph Antoine Ferdinand Plateau. *Statique expérimentale et théorique des liquides soumis aux seules forces moléculaires*, volume 2. Gauthier-Villars, 1873.

[41] Jesse Douglas. Solution of the problem of plateau. *Transactions of the American Mathematical Society*, 33(1):263–321, 1931.

[42] Hans-Ude Nissen. Crystal orientation and plate structure in echinoid skeletal units. *Science*, 166(3909):1150–1152, 1969.

[43] Stephen Hyde, Z Blum, T Landh, S Lidin, BW Ninham, S Andersson, and K Larsson. *The language of shape: the role of curvature in condensed matter: physics, chemistry and biology*. Elsevier, 1996.

[44] Gerd E Schröder-Turk, S Wickham, Holger Averdunk, Frank Brink, JD Fitz Gerald, L Poladian, MCJ Large, and ST Hyde. The chiral structure of porous chitin within the wing-scales of callophrys rubi. *Journal of structural biology*, 174(2):290–295, 2011.

[45] Sebastian C Kapfer, Stephen T Hyde, Klaus Mecke, Christoph H Arns, and Gerd E Schröder-Turk. Minimal surface scaffold designs for tissue engineering. *Biomaterials*, 32(29):6875–6882, 2011.

[46] Hiroshi Jinnai, Yukihiro Nishikawa, Masako Ito, Steven D Smith, David A Agard, and Richard J Spontak. Topological similarity of sponge-like bicontinuous morphologies differing in length scale. *Advanced Materials*, 14(22):1615–1618, 2002.

[47] Hiroshi Jinnai, Hideyukki Watashiba, Takashi Kajihara, Yukihiro Nishikawa, Masaoki Takahashi, and Masako Ito. Surface curvatures of trabecular bone microarchitecture. *Bone*, 30(1):191–194, 2002.

[48] Benjamin Winter, Benjamin Butz, Christel Dieker, Gerd E Schröder-Turk, Klaus Mecke, and Erdmann Spiecker. Coexistence of both gyroid chiralities in individual butterfly wing scales of callophrys rubi. *Proceedings of the National Academy of Sciences*, 112(42):12911–12916, 2015.

[49] Joaquín Pérez. A new golden age of minimal surfaces. *Notices of the AMS*, 64(4):347–358, 2017.

[50] Peter D Olmsted and Scott T Milner. Strong segregation theory of bicontinuous phases in block copolymers. *Macromolecules*, 31(12):4011–4022, 1998.

[51] Meinhard Wohlgemuth, Nataliya Yufa, James Hoffman, and Edwin L Thomas. Triply periodic bicontinuous cubic microdomain morphologies by symmetries. *Macromolecules*, 34(17):6083–6089, 2001.

[52] Salvatore Torquato and Aleksandar Donev. Minimal surfaces and multifunctionality. *Proceedings of the Royal Society of London. Series A: Mathematical, Physical and Engineering Sciences*, 460(2047):1849–1856, 2004.

[53] Jörg G Werner, GG Rodríguez-Calero, Hector D Abruña, and Ulrich Wiesner. Block copolymer derived 3-d interpenetrating multifunctional gyroidal nanohybrids for electrical energy storage. *Energy & Environmental Science*, 11(5):1261–1270, 2018.

[54] Reduan Asbai-Ghoudan, Sergio Ruiz de Galarreta, and Naiara Rodriguez-Florez. Analytical model for the prediction of permeability of triply periodic minimal surfaces. *Journal of the Mechanical Behavior of Biomedical Materials*, page 104804, 2021.

[55] Zahid Ahmed Qureshi, Emad Elnajjar, Oraib Al-Ketan, Rashid Abu Al-Rub, and Salah Burhan Al-Omari. Heat transfer performance of a finned metal foam-phase change material (fmf-pcm) system incorporating triply periodic minimal surfaces (tpms). *International Journal of Heat and Mass Transfer*, 170:121001, 2021.

[56] Jorge Santos, Tiago Pires, Bárbara P Gouveia, André PG Castro, and Paulo R Fernandes. On the permeability of tpms scaffolds. *Journal of the Mechanical Behavior of Biomedical Materials*, 110:103932, 2020.

[57] Zahid Ahmed Qureshi, Salah Addin Burhan Al-Omari, Emad Elnajjar, Oraib Al-Ketan, and Rashid Abu Al-Rub. Using triply periodic minimal surfaces (tpms)-based metal foams structures as skeleton for metal-foam-pcm composites for thermal energy storage and energy management applications. *International Communications in Heat and Mass Transfer*, 124:105265, 2021.

[58] Jaisree Iyer, Thomas Moore, Du Nguyen, Pratanu Roy, and Joshuah Stolaroff. Heat transfer and pressure drop characteristics of heat exchangers based on triply periodic minimal and periodic nodal surfaces. *Applied Thermal Engineering*, page 118192, 2022.

[59] Shiyi Tan, Jiafei Gu, Seung Chul Han, Dong-Weon Lee, and Kiju Kang. Design and fabrication of a non-clogging scaffold composed of semi-permeable membrane. *Materials & Design*, 142:229–239, 2018.

[60] Javad Kadkhodapour, Hossein Montazerian, Ali Cheloee Darab, Ali Zargarian, and Siegfride Schmauder. The relationships between deformation mechanisms and mechanical properties of additively manufactured porous biomaterials. *Journal of the mechanical behavior of biomedical materials*, 70:28–42, 2017.

[61] Songhua Ma, Kaile Song, Jing Lan, and Li Ma. Biological and mechanical property analysis for designed heterogeneous porous scaffolds based on the refined tpms. *Journal of the mechanical behavior of biomedical materials*, 107:103727, 2020.

[62] Kaile Song, Zhaohui Wang, Jing Lan, and Songhua Ma. Porous structure design and mechanical behavior analysis based on tpms for customized root analogue implant. *Journal of the Mechanical Behavior of Biomedical Materials*, 115:104222, 2021.

[63] Dongjin Yoo. New paradigms in internal architecture design and freeform fabrication of tissue engineering porous scaffolds. *Medical engineering & physics*, 34(6):762–776, 2012.

[64] M Afshar, A Pourkamali Anaraki, Hossein Montazerian, and Javad Kadkhodapour. Additive manufacturing and mechanical characterization of graded porosity scaffolds designed based on triply periodic minimal surface architectures. *Journal of the mechanical behavior of biomedical materials*, 62:481–494, 2016.

[65] Arash Ataee, Yuncang Li, Milan Brandt, and Cuie Wen. Ultrahigh-strength titanium gyroid scaffolds manufactured by selective laser melting (slm) for bone implant applications. *Acta Materialia*, 158:354–368, 2018.

[66] Pedram Karimipour-Fard, Amir H Behravesh, Holly Jones-Taggart, Remon Pop-Iliev, and Ghaus Rizvi. Effects of design, porosity and biodegradation

on mechanical and morphological properties of additive-manufactured triply periodic minimal surface scaffolds. *Journal of the Mechanical Behavior of Biomedical Materials*, 112:104064, 2020.

[67] Dong-Jin Yoo. Computer-aided porous scaffold design for tissue engineering using triply periodic minimal surfaces. *International Journal of Precision Engineering and Manufacturing*, 12(1):61–71, 2011.

[68] FSL Bobbert, Karel Lietaert, Ali Akbar Eftekhari, Behdad Pouran, Seyed Mohammad Ahmadi, Harrie Weinans, and Amir A Zadpoor. Additively manufactured metallic porous biomaterials based on minimal surfaces: A unique combination of topological, mechanical, and mass transport properties. *Acta biomaterialia*, 53:572–584, 2017.

[69] André PG Castro, Tiago A Pires, Jorge E Santos, BP Gouveia, and Paulo Rui Fernandes. Permeability versus design in tpms scaffolds. *Materials*, 12(8):1313, 2019.

[70] Tiago Pires, Jorge Santos, Rui B Ruben, Bárbara P Gouveia, André PG Castro, and Paulo R Fernandes. Numerical-experimental analysis of the permeability-porosity relationship in triply periodic minimal surfaces scaffolds. *Journal of Biomechanics*, 117:110263, 2021.

[71] Ian Maskery, L Sturm, AO Aremu, Ajit Panesar, CB Williams, CJ Tuck, Ricky D Wildman, IA Ashcroft, and Richard JM Hague. Insights into the mechanical properties of several triply periodic minimal surface lattice structures made by polymer additive manufacturing. *Polymer*, 152:62–71, 2018.

[72] M Maxim Sychov, Lev A Lebedev, SV Dyachenko, and Liubov A Nefedova. Mechanical properties of energy-absorbing structures with triply periodic minimal surface topology. *Acta Astronautica*, 150:81–84, 2018.

[73] Dong-Wook Lee, Kamran A Khan, and Rashid K Abu Al-Rub. Stiffness and yield strength of architectured foams based on the schwarz primitive triply periodic minimal surface. *International Journal of Plasticity*, 95:1–20, 2017.

[74] André PG Castro, Jorge Santos, Tiago Pires, and Paulo R Fernandes. Micromechanical behavior of tpms scaffolds for bone tissue engineering. *Macromolecular Materials and Engineering*, 305(12):2000487, 2020.

[75] Jiawei Feng, Bo Liu, Zhiwei Lin, and Jianzhong Fu. Isotropic porous structure design methods based on triply periodic minimal surfaces. *Materials & Design*, 210:110050, 2021.

[76] José Reinoso, Marco Paggi, and Christian Linder. Phase field modeling of brittle fracture for enhanced assumed strain shells at large deformations: formulation and finite element implementation. *Computational Mechanics*, 59(6):981–1001, 2017.

[77] Aamir Dean, PK Asur Vijaya Kumar, José Reinoso, Christian Gerendt, Marco Paggi, Elsadig Mahdi, and Raimund Rolfes. A multi phase-field fracture model for long fiber reinforced composites based on the puck theory of failure. *Composite Structures*, 251:112446, 2020.

[78] Pavan Asur Vijaya Kumar, Aamir Dean, José Reinoso, Pietro Lenarda, and Marco Paggi. Phase field modeling of fracture in functionally graded materials: γ-convergence and mechanical insight on the effect of grading. *Thin-Walled Structures*, 159:107234, 2021.

[79] Fatemeh Amiri, Daniel Millán, Yongxing Shen, Timon Rabczuk, and Marino Arroyo. Phase-field modeling of fracture in linear thin shells. *Theoretical and Applied Fracture Mechanics*, 69:102–109, 2014.

[80] Maurice Anthony Biot. Thermoelasticity and irreversible thermodynamics. *Journal of applied physics*, 27(3):240–253, 1956.

[81] Viktor D Kupradze, TG Gegelia, Mo Oo Basheleishvili, To V Burchuladze, and E Sternberg. Three-dimensional problems of the mathematical theory of elasticity and thermoelasticity. *North-Holland Series. In Applied Mathematics and Mechanics*, 1979.

[82] José M Carcione, Zhi-Wei Wang, Wenchang Ling, Ettore Salusti, Jing Ba, and Li-Yun Fu. Simulation of wave propagation in linear thermoelastic media. *Geophysics*, 84(1):T1–T11, 2019.

[83] Daniel D Joseph and Luigi Preziosi. Heat waves. *Reviews of Modern Physics*, 61(1):41, 1989.

[84] Jing Liu, Xu Chen, and Lisa X Xu. New thermal wave aspects on burn evaluation of skin subjected to instantaneous heating. *IEEE transactions on biomedical engineering*, 46(4):420–428, 1999.

[85] Józef Ignaczak and Martin Ostoja-Starzewski. *Thermoelasticity with finite wave speeds*. Oxford University Press, 2010.

[86] DS Chandrasekharaiah. Hyperbolic thermoelasticity: a review of recent literature. *Applied Mechanics Reviews*, 51(12):705–729, 1998.

[87] Arash Zamani, Richard B Hetnarski, and M Reza Eslami. Second sound in a cracked layer based on lord–shulman theory. *Journal of Thermal Stresses*, 34(3):181–200, 2011.

[88] W Kaminski. Hyperbolic heat conduction equation for materials with a nonhomogeneous inner structure. *Journal of Heat Transfer*, 112(3):555–560, 1990.

[89] Koyel Mitra, S Kumar, A Vedevarz, and MK Moallemi. Experimental evidence of hyperbolic heat conduction in processed meat. *Journal of Heat Transfer*, 117(3):568–573, 1995.

[90] Venkatesh Narayanamurti and RC Dynes. Observation of second sound in bismuth. *Physical Review Letters*, 28(22):1461, 1972.

[91] Richard B Hetnarski and Jozef Ignaczak. Generalized thermoelasticity. *Journal of Thermal Stresses*, 22(4-5):451–476, 1999.

[92] Richard B Hetnarski, M Reza Eslami, and GML Gladwell. *Thermal stresses: advanced theory and applications*, volume 41. Springer, 2009.

[93] Hany H Sherief, AMA El-Sayed, and AM Abd El-Latief. Fractional order theory of thermoelasticity. *International Journal of Solids and structures*, 47(2):269–275, 2010.

[94] Harold Wesley Lord and Y Shulman. A generalized dynamical theory of thermoelasticity. *Journal of the Mechanics and Physics of Solids*, 15(5):299–309, 1967.

[95] James Clerk Maxwell. On the dynamical theory of gases. *Philosophical transactions of the Royal Society of London, 157*, pages 49–88, 1867.

[96] Carlo Cattaneo. Sulla conduzione del calore. *Atti Sem. Mat. Fis. Univ. Modena*, 3:83–101, 1948.

[97] Ranjit S Dhaliwal and Hani H Sherief. Generalized thermoelasticity for anisotropic media. *Quarterly of Applied Mathematics*, 38(1):1–8, 1980.

[98] Barbara Gambin and E Kröner. Higher-order terms in the homogenized stress-strain relation of periodic elastic media. *physica status solidi (b)*, 151(2):513–519, 1989.

[99] Igor V Andrianov, Vladimir I Bolshakov, Vladyslav V Danishevs' kyy, and Dieter Weichert. Higher order asymptotic homogenization and wave propagation in periodic composite materials. *Proceedings of the Royal Society of London A: Mathematical, Physical and Engineering Sciences*, 464(2093):1181–1201, 2008.

[100] Andrea Bacigalupo and Luigi Gambarotta. Second-order computational homogenization of heterogeneous materials with periodic microstructure. *ZAMM-Journal of Applied Mathematics and Mechanics/Zeitschrift für Angewandte Mathematik und Mechanik*, 90(10-11):796–811, 2010.

[101] Zhiqiang Yang, Junzhi Cui, Yi Sun, Jun Liang, and Zihao Yang. Multiscale analysis method for thermo-mechanical performance of periodic porous materials with interior surface radiation. *International Journal for Numerical Methods in Engineering*, 105(5):323–350, 2016.

[102] Jacob Fish, Zhiqiang Yang, and Zifeng Yuan. A second-order reduced asymptotic homogenization approach for nonlinear periodic heterogeneous materials. *International Journal for Numerical Methods in Engineering*, 119(6):469–489, 2019.

[103] John R Willis. Variational and related methods for the overall properties of composites. In *Advances in applied mechanics*, volume 21, pages 1–78. Elsevier, 1981.

[104] Valery P Smyshlyaev. Propagation and localization of elastic waves in highly anisotropic periodic composites via two-scale homogenization. *Mechanics of Materials*, R59:434–447, 2009.

[105] Andrea Bacigalupo and Luigi Gambarotta. Second-gradient homogenized model for wave propagation in heterogeneous periodic media. *International Journal of Solids and Structures*, 51(5):1052–1065, 2014.

[106] IIia V Kamotski and Valery P Smyshlyaev. Bandgaps in two-dimensional high-contrast periodic elastic beam lattice materials. *Journal of the Mechanics and Physics of Solids*, 123:292–304, 2019.

[107] Davide Bigoni and Walter J Drugan. Analytical derivation of cosserat moduli via homogenization of heterogeneous elastic materials. *Journal of Applied Mechanics*, 74(7):741–753, 2007.

[108] Graeme W Milton and John R Willis. On modifications of newton's second law and linear continuum elastodynamics. *Proceedings of the Royal Society A: Mathematical, Physical and Engineering Sciences*, 463(2079):855–880, 2007.

[109] Mattia Bacca, Francesco Dal Corso, Daniele Veber, and Davide Bigoni. Mindlin second-gradient elastic properties from dilute two-phase cauchy-elastic composites part i: closed form expression for the effective higher-order constitutive tensor. *International Journal of Solids and Structures*, 50(24):4010–4019, 2013.

[110] Mattia Bacca, Francesco Dal Corso, Daniele Veber, and Davide Bigoni. Mindlin second-gradient elastic properties from dilute two-phase cauchy-elastic composites part ii: Higher-order constitutive properties and application cases. *International Journal of Solids and Structures*, 50(24):4020–4029, 2013.

[111] Andrea Bacigalupo, Marco Paggi, F Dal Corso, and Davide Bigoni. Identification of higher-order continua equivalent to a cauchy elastic composite. *Mechanics Research Communications*, 93:11–22, 2018.

[112] Martin Ostoja-Starzewski, Stéphane D Boccara, and Iwona Jasiuk. Couple-stress moduli and characteristic length of a two-phase composite. *Mechanics Research Communications*, 26(4):387–396, 1999.

[113] Varvara Kouznetsova, Marc GD Geers, and WA Marcel Brekelmans. Multi-scale constitutive modelling of heterogeneous materials with a gradient-enhanced computational homogenization scheme. *International journal for numerical methods in engineering*, 54(8):1235–1260, 2002.

[114] Samuel Forest. Homogenization methods and mechanics of generalized continua-part 2. *Theoretical and applied mechanics*, (28-29):113–144, 2002.

[115] TL Lew, F Scarpa, and K Worden. Homogenisation metamodelling of perforated plates. *Strain*, 40(3):103–112, 2004.

[116] Fabrizio Scarpa, Sondipon Adhikari, and A Srikantha Phani. Effective elastic mechanical properties of single layer graphene sheets. *Nanotechnology*, 20(6):065709, 2009.

[117] Maria Laura De Bellis and Daniela Addessi. A cosserat based multi-scale model for masonry structures. *International Journal for Multiscale Computational Engineering*, 9(5):543, 2011.

[118] Samuel Forest and Duy Khanh Trinh. Generalized continua and non-homogeneous boundary conditions in homogenisation methods. *ZAMM-Journal of Applied Mathematics and Mechanics/Zeitschrift fur Angewandte Mathematik und Mechanik*, 91(2):90–109, 2011.

[119] Yijin J Chen, Fabrizio Scarpa, Yaqing J Liu, and Jingsong S Leng. Elasticity of anti-tetrachiral anisotropic lattices. *International Journal of Solids and Structures*, 50(6):996–1004, 2013.

[120] Vincent Monchiet, Nicolas Auffray, and Julien Yvonnet. Strain-gradient homogenization: a bridge between the asymptotic expansion and quadratic boundary condition methods. *Mechanics of Materials*, 143:103309, 2020.

[121] Gilles A Francfort. Homogenization and linear thermoelasticity. *SIAM Journal on Mathematical Analysis*, 14(4):696–708, 1983.

[122] Ilker Temizer and Peter Wriggers. Homogenization in finite thermoelasticity. *Journal of the Mechanics and Physics of Solids*, 59(2):344–372, 2011.

[123] VL Savatorova, AV Talonov, and AN Vlasov. Homogenization of thermoelasticity processes in composite materials with periodic structure of heterogeneities. *ZAMM-Journal of Applied Mathematics and Mechanics/Zeitschrift für Angewandte Mathematik und Mechanik*, 93(8):575–596, 2013.

[124] Gildas L'Hostis and François Devries. Characterization of the thermoelastic behavior of syntactic foams. *Composites Part B: Engineering*, 29(4):351–361, 1998.

[125] Wenbin Yu and Tian Tang. A variational asymptotic micromechanics model for predicting thermoelastic properties of heterogeneous materials. *International Journal of Solids and Structures*, 44(22-23):7510–7525, 2007.

[126] Heinz E Pettermann and Subra Suresh. A comprehensive unit cell model: a study of coupled effects in piezoelectric 1–3 composites. *International Journal of Solids and Structures*, 37(39):5447–5464, 2000.

[127] Harald Berger, Sreedhar Kari, Ulrich Gabbert, Reinaldo Rodríguez-Ramos, Julián Bravo-Castillero, and Raúl Guinovart-Díaz. A comprehensive numerical homogenisation technique for calculating effective coefficients of uniaxial piezoelectric fibre composites. *Materials Science and Engineering: A*, 412(1-2):53–60, 2005.

[128] Jörg Schröder and Marc-André Keip. Two-scale homogenization of electromechanically coupled boundary value problems. *Computational mechanics*, 50(2):229–244, 2012.

[129] Dominic Zäh and Christian Miehe. Computational homogenization in dissipative electro-mechanics of functional materials. *Computer Methods in Applied Mechanics and Engineering*, 267:487–510, 2013.

[130] Francesca Fantoni, Andrea Bacigalupo, and Marco Paggi. Multi-field asymptotic homogenization of thermo-piezoelectric materials with periodic microstructure. *International Journal of Solids and Structures*, 120:31–56, 2017.

[131] Nobutada Ohno, Xu Wu, and Tetsuya Matsuda. Homogenized properties of elastic–viscoplastic composites with periodic internal structures. *International Journal of Mechanical Sciences*, 42(8):1519–1536, 2000.

[132] Zouhair Abdessamad, Ilya Kostin, Grigory Panasenko, and Valery P Smyshlyaev. Memory effect in homogenization of a viscoelastic kelvin–voigt model with time-dependent coefficients. *Mathematical Models and Methods in Applied Sciences*, 19(09):1603–1630, 2009.

[133] Qiang Chen, Guannan Wang, Xuefeng Chen, and Jia Geng. Finite-volume homogenization of elastic/viscoelastic periodic materials. *Composite Structures*, 182:457–470, 2017.

[134] Rosaria Del Toro, Andrea Bacigalupo, and Marco Paggi. Characterization of wave propagation in periodic viscoelastic materials via asymptotic-variational homogenization. *International Journal of Solids and Structures*, 172:110–146, 2019.

[135] A Salvadori, E Bosco, and D Grazioli. A computational homogenization approach for li-ion battery cells: Part 1–formulation. *Journal of the Mechanics and Physics of Solids*, 65:114–137, 2014.

[136] Andrea Bacigalupo, Lorenzo Morini, and Andrea Piccolroaz. Multiscale asymptotic homogenization analysis of thermo-diffusive composite materials. *International Journal of Solids and Structures*, 85:15–33, 2016.

[137] Francesca Fantoni and Andrea Bacigalupo. Wave propagation modeling in periodic elasto-thermo-diffusive materials via multifield asymptotic homogenization. *International Journal of Solids and Structures*, 196-197:99–128, 2020.

[138] Jacobi Aboudi, Maciej Z Pindera, and SM Arnold. Linear thermoelastic higher-order theory for periodic multiphase materials. *Journal of Applied Mechanics*, 68(5):697–707, 2001.

[139] Pascale Kanouté, Daniela Paola Boso, JL Chaboche, and BA Schrefler. Multiscale methods for composites: a review. *Archives of Computational Methods in Engineering*, 16(1):31–75, 2009.

[140] HW Zhang, Sheng Zhang, Jin Ying Bi, and BA Schrefler. Thermo-mechanical analysis of periodic multiphase materials by a multiscale asymptotic homogenization approach. *International Journal for Numerical Methods in Engineering*, 69(1):87–113, 2007.

[141] Lázaro M Sixto-Camacho, Julian Bravo-Castillero, Renald Brenner, Raúl Guinovart-Díaz, Houari Mechkour, Reinaldo Rodríguez-Ramos, and Federico J Sabina. Asymptotic homogenization of periodic thermo-magneto-electro-elastic heterogeneous media. *Computers & Mathematics with Applications*, 66(10):2056–2074, 2013.

[142] Alan Arnold Griffith. Vi. the phenomena of rupture and flow in solids. *Philosophical transactions of the royal society of london. Series A, containing papers of a mathematical or physical character*, 221(582-593):163–198, 1921.

[143] Blaise Bourdin, Gilles A Francfort, and Jean-Jacques Marigo. Numerical experiments in revisited brittle fracture. *Journal of the Mechanics and Physics of Solids*, 48(4):797–826, 2000.

[144] Blaise Bourdin, Gilles A Francfort, and Jean-Jacques Marigo. The variational approach to fracture. *Journal of elasticity*, 91(1):5–148, 2008.

[145] Christian Miehe, Martina Hofacker, and Fabian Welschinger. A phase field model for rate-independent crack propagation: Robust algorithmic implemen-

tation based on operator splits. *Computer Methods in Applied Mechanics and Engineering*, 199(45-48):2765–2778, 2010.

[146] Antonin Chambolle, Gilles A Francfort, and J-J Marigo. When and how do cracks propagate? *Journal of the Mechanics and Physics of Solids*, 57(9):1614–1622, 2009.

[147] Charlotte Kuhn. *Numerical and analytical investigation of a phase field model for fracture*. Technische Universität Kaiserslautern, 2013.

[148] Gilles A Francfort and J-J Marigo. Revisiting brittle fracture as an energy minimization problem. *Journal of the Mechanics and Physics of Solids*, 46(8):1319–1342, 1998.

[149] Luigi Ambrosio and Vincenzo Maria Tortorelli. Approximation of functional depending on jumps by elliptic functional via t-convergence. *Communications on Pure and Applied Mathematics*, 43(8):999–1036, 1990.

[150] Diab W Abueidda, Mete Bakir, Rashid K Abu Al-Rub, Jörgen S Bergström, Nahil A Sobh, and Iwona Jasiuk. Mechanical properties of 3d printed polymeric cellular materials with triply periodic minimal surface architectures. *Materials & Design*, 122:255–267, 2017.

[151] Oraib Al-Ketan, Reza Rowshan, and Rashid K Abu Al-Rub. Topology-mechanical property relationship of 3d printed strut, skeletal, and sheet based periodic metallic cellular materials. *Additive Manufacturing*, 19:167–183, 2018.

[152] Mohsen Keshavarzan, Mahmoud Kadkhodaei, Mohsen R Badrossamay, and Mohammadreza Karamooz-Ravari. Investigation on the failure mechanism of triply periodic minimal surface cellular structures fabricated by vat photopolymerization additive manufacturing under compressive loadings. *Mechanics of Materials*, 140:103150, 2020.

[153] Nejc Novak, Oraib Al-Ketan, Lovre Krstulović-Opara, Reza Rowshan, Rashid K Abu Al-Rub, Matej Vesenjak, and Zoran Ren. Quasi-static and dynamic compressive behaviour of sheet tpms cellular structures. *Composite Structures*, 266:113801, 2021.

[154] Oraib Al-Ketan, Rachid Rezgui, Reza Rowshan, Huifeng Du, Nicholas X Fang, and Rashid K Abu Al-Rub. Microarchitected stretching-dominated mechan-

ical metamaterials with minimal surface topologies. *Advanced Engineering Materials*, 20(9):1800029, 2018.

[155] Colin Bonatti and Dirk Mohr. Smooth-shell metamaterials of cubic symmetry: Anisotropic elasticity, yield strength and specific energy absorption. *Acta Materialia*, 164:301–321, 2019.

[156] Carmen Torres-Sanchez, James M Borgman, Ben Sargeant, Hugo Bell, Enrique Alabort, Craig Lindsay, and Paul P Conway. Comparison of selective laser melted commercially pure titanium sheet-based triply periodic minimal surfaces and trabecular-like strut-based scaffolds for tissue engineering. *Advanced Engineering Materials*, page 2100527, 2021.

[157] Jiaxin Cai, Yongbin Ma, and Zichen Deng. On the effective elastic modulus of the ribbed structure based on schwarz primitive triply periodic minimal surface. *Thin-Walled Structures*, 170:108642, 2022.

[158] Hossein Montazerian, Elham Davoodi, Mitra Asadi-Eydivand, Javad Kadkhodapour, and Mehran Solati-Hashjin. Porous scaffold internal architecture design based on minimal surfaces: a compromise between permeability and elastic properties. *Materials & Design*, 126:98–114, 2017.

[159] Chunze Yan, Liang Hao, Ahmed Hussein, and Philippe Young. Ti–6al–4v triply periodic minimal surface structures for bone implants fabricated via selective laser melting. *Journal of the mechanical behavior of biomedical materials*, 51:61–73, 2015.

[160] Lei Yang, Chunze Yan, Changjun Han, Peng Chen, Shoufeng Yang, and Yusheng Shi. Mechanical response of a triply periodic minimal surface cellular structures manufactured by selective laser melting. *International Journal of Mechanical Sciences*, 148:149–157, 2018.

[161] Alejandro Yánez, Alberto Cuadrado, Oscar Martel, H Afonso, and Donato Monopoli. Gyroid porous titanium structures: a versatile solution to be used as scaffolds in bone defect reconstruction. *Materials & Design*, 140:21–29, 2018.

[162] Chunze Yan, Liang Hao, Ahmed Hussein, Philippe Young, Juntong Huang, and Wei Zhu. Microstructure and mechanical properties of aluminium alloy cellular lattice structures manufactured by direct metal laser sintering. *Materials Science and Engineering: A*, 628:238–246, 2015.

[163] Oraib Al-Ketan, Dong-Wook Lee, Reza Rowshan, and Rashid K Abu Al-Rub. Functionally graded and multi-morphology sheet tpms lattices: Design, manufacturing, and mechanical properties. *Journal of the mechanical behavior of biomedical materials*, 102:103520, 2020.

[164] Qidong Sun, Jie Sun, Kai Guo, and Leishuo Wang. Compressive mechanical properties and energy absorption characteristics of slm fabricated ti6al4v triply periodic minimal surface cellular structures. *Mechanics of Materials*, page 104241, 2022.

[165] Javad Kadkhodapour, Hossein Montazerian, Ali Cheloee Darab, AP Anaraki, SM Ahmadi, AA Zadpoor, and Siegfride Schmauder. Failure mechanisms of additively manufactured porous biomaterials: Effects of porosity and type of unit cell. *Journal of the mechanical behavior of biomedical materials*, 50:180–191, 2015.

[166] Martin Sandve Alnæs, Johan Hake, Robert C Kirby, Hans Petter Langtangen, Anders Logg, and Garth N Wells. The fenics manual. *FEniCS Project, version October 31st*, 36, 2011.

[167] Stephen Wolfram. *Mathematica: a system for doing mathematics by computer*. Addison Wesley Longman Publishing Co., Inc., 1991.

[168] Michael F Ashby and Lorna J Gibson. Cellular solids: structure and properties. *Press Syndicate of the University of Cambridge, Cambridge, UK*, pages 175–231, 1997.

[169] Michael F Ashby. The properties of foams and lattices. *Philosophical Transactions of the Royal Society A: Mathematical, Physical and Engineering Sciences*, 364(1838):15–30, 2006.

[170] Raymind David Mindlin. Equations of high frequency vibrations of thermopiezoelectric crystal plates. *International Journal of Solids and Structures*, 10(6):625–637, 1974.

[171] Andrea Bacigalupo. Second-order homogenization of periodic materials based on asymptotic approximation of the strain energy: formulation and validity limits. *Meccanica*, 49(6):1407–1425, 2014.

[172] Raymond Edward Alan Christopher Paley and Norbert Wiener. *Fourier transforms in the complex domain*, volume 19. American Mathematical Soc., 1934.

[173] Balth Van der Pol and H. Bremmer. *Operational calculus based on the two-sided Laplace integral*. Cambridge University Press, 1950.

[174] Gregoire Allaire. Homogenization and two-scale convergence. *SIAM Journal of Mathematical Analisys*, 23:1482–1518, 1992.

[175] Izrail Moiseevitch Gelfand, Richard A Silverman, et al. *Calculus of variations*. Courier Corporation, 2000.

[176] Mariano Giaquinta and Stefan Hildebrandt. *Calculus of variations II*, volume 311. Springer Science & Business Media, 2013.

[177] Vincent Laude. *Phononic crystals: artificial crystals for sonic, acoustic, and elastic waves*, volume 26. Walter de Gruyter GmbH & Co KG, 2015.

[178] José Maria Carcione. *Wave fields in real media: Wave propagation in anisotropic, anelastic, porous and electromagnetic media*. Elsevier, 2007.

[179] Thomas C Chen and Leonard E Alsop. Reflection and transmission of obliquely incident rayleigh waves at a vertical discontinuity between two welded quarter-spaces. *Bulletin of the Seismological Society of America*, 69(5):1409–1423, 1979.

[180] Andrea Bacigalupo and Marco Lepidi. High-frequency parametric approximation of the floquet-bloch spectrum for anti-tetrachiral materials. *International Journal of Solids and Structures*, 97:575–592, 2016.

[181] David Hoffman and William H Meeks III. Minimal surfaces based on the catenoid. *The American Mathematical Monthly*, 97(8):702–730, 1990.

[182] Ulrich Dierkes, Stefan Hildebrandt, and Friedrich Sauvigny. Minimal surfaces. In *Minimal Surfaces*, pages 53–90. Springer, 2010.

[183] João Lucas Marques Barbosa and Antonio Gervasio Colares. *Minimal surfaces in* $\mathbb{R}^3$, volume 1195. Springer, 2006.

[184] Cyril Isenberg. *The science of soap films and soap bubbles*. Courier Dover Publications, 1992.

[185] Deison Préve and Alberto Saa. Doughnut-shaped soap bubbles. *Physical Review E*, 92(4):042402, 2015.

[186] S Hyde, S Andersson, K Larsson, Z Blum, T Landh, S Lidin, and BW Ninham. The role of curvature in condensed matter: Physics, chemistry and biology, 1997.

[187] Johannes C Nitsche. *Lectures on minimal surfaces: vol. 1*. Cambridge university press, 1989.

[188] *File:*helicoid-4-Figure4-1.png. (visited on 29/09/2022). URL: https://d3i71xaburhd42.cloudfront.net/4bbf729ea2f0e7d4ca6fc27435d3f17a10b8101b/4-Figure4-1.png.

[189] *File:*catenoid-douglas_soap-film2.jpg. (visited on 29/09/2022). URL: https://wdjoyner.files.wordpress.com/2018/04/douglas_soap-film2.jpg.

[190] *File:*scherksurface-InvisibleHandshake_7.gif. (visited on 29/09/2022). URL: https://www.macalester.edu/mscs/wp-content/uploads/sites/51/2011/04/InvisibleHandshake_7.gif.

[191] Alan H Schoen. Infinite periodic minimal surfaces without self-intersections. *National Aeronautics and Space Administration (NASA) Tech, , Washington DC*, (Note No. D-5541), 1970.

[192] Ossian Bonnet. Note sur la théorie générale des surfaces. *CR Acad. Sci. Paris*, 37:529–532, 1853.

[193] Sten Andersson, ST Hyde, Kare Larsson, and Sven Lidin. Minimal surfaces and structures: from inorganic and metal crystals to cell membranes and biopolymers. *Chemical Reviews*, 88(1):221–242, 1988.

[194] Hermann Karcher. The triply periodic minimal surfaces of alan schoen and their constant mean curvature companions. *Manuscripta mathematica*, 64(3):291–357, 1989.

[195] Ulrich Pinkall and Konrad Polthier. Computing discrete minimal surfaces and their conjugates. *Experimental mathematics*, 2(1):15–36, 1993.

[196] Hermann Karcher and Konrad Polthier. Construction of triply periodic minimal surfaces. *Philosophical Transactions of the Royal Society of London. Series A: Mathematical, Physical and Engineering Sciences*, 354(1715):2077–2104, 1996.

[197] Paul JF Gandy, Djurdje Cvijović, Alan L Mackay, and Jacek Klinowski. Exact computation of the triply periodic d (diamond') minimal surface. *Chemical physics letters*, 314(5-6):543–551, 1999.

[198] Paul JF Gandy and Jacek Klinowski. Exact computation of the triply periodic g (gyroid') minimal surface. *Chemical Physics Letters*, 321(5-6):363–371, 2000.

[199] Paul JF Gandy and Jacek Klinowski. Exact computation of the triply periodic schwarz p minimal surface. *Chemical Physics Letters*, 322(6):579–586, 2000.

[200] Hans Georg Von Schnering and Reinhard Nesper. Nodal surfaces of fourier series: fundamental invariants of structured matter. *Zeitschrift für Physik B Condensed Matter*, 83(3):407–412, 1991.

[201] Alan L Mackay. Periodic minimal surfaces from finite element methods. *Chemical physics letters*, 221(3-4):317–321, 1994.

[202] Charla A Lambert, Leonard H Radzilowski, and Edwin L Thomas. Triply periodic level surfaces as models for cubic tricontinuous block copolymer morphologies. *Philosophical Transactions of the Royal Society of London. Series A: Mathematical, Physical and Engineering Sciences*, 354(1715):2009–2023, 1996.

[203] Paul JF Gandy, Sonny Bardhan, Alan L Mackay, and Jacek Klinowski. Nodal surface approximations to the p, g, d and i-wp triply periodic minimal surfaces. *Chemical physics letters*, 336(3-4):187–195, 2001.

[204] Wojciech T GóźdŹ and Robert Hołyst. Triply periodic surfaces and multiply continuous structures from the landau model of microemulsions. *Physical Review E*, 54(5):5012, 1996.

[205] Youngjean Jung and Salvatore Torquato. Fluid permeabilities of triply periodic minimal surfaces. *Physical Review E*, 72(5):056319, 2005.

[206] Salvatore Torquato, S Hyun, and Aleksandar Donev. Multifunctional composites: optimizing microstructures for simultaneous transport of heat and electricity. *Physical review letters*, 89(26):266601, 2002.

[207] Zeyao Chen, Yi Min Xie, Xian Wu, Zhe Wang, Qing Li, and Shiwei Zhou. On hybrid cellular materials based on triply periodic minimal surfaces with extreme mechanical properties. *Materials & Design*, 183:108109, 2019.

[208] Diab W Abueidda, Rashid K Abu Al-Rub, Ahmed S Dalaq, Dong-Wook Lee, Kamran A Khan, and Iwona Jasiuk. Effective conductivities and elastic moduli of novel foams with triply periodic minimal surfaces. *Mechanics of Materials*, 95:102–115, 2016.

[209] Ferry PW Melchels, Katia Bertoldi, Ruggero Gabbrielli, Aldrik H Velders, Jan Feijen, and Dirk W Grijpma. Mathematically defined tissue engineering scaffold architectures prepared by stereolithography. *Biomaterials*, 31(27):6909–6916, 2010.

[210] Hanen Amor, Jean-Jacques Marigo, and Corrado Maurini. Regularized formulation of the variational brittle fracture with unilateral contact: Numerical experiments. *Journal of the Mechanics and Physics of Solids*, 57(8):1209–1229, 2009.

[211] Michael J Borden, Clemens V Verhoosel, Michael A Scott, Thomas JR Hughes, and Chad M Landis. A phase-field description of dynamic brittle fracture. *Computer Methods in Applied Mechanics and Engineering*, 217:77–95, 2012.

[212] Gianni Dal Maso. *An introduction to* Γ*-convergence*, volume 8. Springer Science & Business Media, 2012.

[213] Andrea Braides et al. *Approximation of free-discontinuity problems*. Number 1694. Springer Science & Business Media, 1998.

[214] Andrea Braides. γ-convergence for beginners. *Oxford Lecture Series in Mathematics and its Applications*, 22, 2002.

[215] Riccardo Cavuoto, Pietro Lenarda, Diego Misseroni, Marco Paggi, and Davide Bigoni. Failure through crack propagation in components with holes and notches: An experimental assessment of the phase field model. *International Journal of Solids and Structures*, page 111798, 2022.

[216] Kim Pham, Hanen Amor, Jean-Jacques Marigo, and Corrado Maurini. Gradient damage models and their use to approximate brittle fracture. *International Journal of Damage Mechanics*, 20(4):618–652, 2011.

[217] Kim Pham, Jean-Jacques Marigo, and Corrado Maurini. The issues of the uniqueness and the stability of the homogeneous response in uniaxial tests with gradient damage models. *Journal of the Mechanics and Physics of Solids*, 59(6):1163–1190, 2011.

[218] Emilio Martínez-Pañeda, Alireza Golahmar, and Christian F Niordson. A phase field formulation for hydrogen assisted cracking. *Computer Methods in Applied Mechanics and Engineering*, 342:742–761, 2018.

[219] Xue Zhang, Chet Vignes, Scott W Sloan, and Daichao Sheng. Numerical evaluation of the phase-field model for brittle fracture with emphasis on the length scale. *Computational Mechanics*, 59(5):737–752, 2017.

[220] Erwan Tanné, Tianyi Li, Blaise Bourdin, J-J Marigo, and Corrado Maurini. Crack nucleation in variational phase-field models of brittle fracture. *Journal of the Mechanics and Physics of Solids*, 110:80–99, 2018.

[221] Ian Maskery, LA Parry, D Padrão, RJM Hague, and IA Ashcroft. Flatt pack: A research-focussed lattice design program. *Additive Manufacturing*, 49:102510, 2022.

[222] Ban Dang Nguyen, Seung Chul Han, Yoon Chang Jung, and Kiju Kang. Design of the p-surfaced shellular, an ultra-low density material with micro-architecture. *Computational Materials Science*, 139:162–178, 2017.

[223] Seung Chul Han, Jeong Myung Choi, Gang Liu, and Kiju Kang. A microscopic shell structure with schwarz's d-surface. *Scientific reports*, 7(1):1–8, 2017.

[224] Rahul Pongiman. *HyperMesh Introduction Pre-Processing for Finite Element Analysis*. Altair University, 2014.

[225] Christophe Geuzaine and Jean-François Remacle. Gmsh: A 3-d finite element mesh generator with built-in pre-and post-processing facilities. *International journal for numerical methods in engineering*, 79(11):1309–1331, 2009.

[226] Tushar Kanti Mandal, Vinh Phu Nguyen, and Jian-Ying Wu. Length scale and mesh bias sensitivity of phase-field models for brittle and cohesive fracture. *Engineering Fracture Mechanics*, 217:106532, 2019.

[227] Guido Dhondt. Effect of contact between the crack faces on crack propagation. In *Key Engineering Materials*, volume 577, pages 61–64. Trans Tech Publ, 2014.

[228] Steve A Maas, Benjamin J Ellis, David S Rawlins, and Jeffrey A Weiss. Finite element simulation of articular contact mechanics with quadratic tetrahedral elements. *Journal of biomechanics*, 49(5):659–667, 2016.

[229] Jianzhong Z Zhu and Olgierd C Zienkiewicz. A posteriori error estimation and three-dimensional automatic mesh generation. *Finite Elements in Analysis and Design*, 25(1-2):167–184, 1997.

[230] Daniel Bremberg and Guido Dhondt. Automatic crack-insertion for arbitrary crack growth. *Engineering Fracture Mechanics*, 75(3-4):404–416, 2008.

[231] Kapil Krishnan, Dong-Wook Lee, Mohammed Al Teneji, and Rashid K Abu Al-Rub. Effective stiffness, strength, buckling and anisotropy of foams based on nine unique triple periodic minimal surfaces. *International Journal of Solids and Structures*, page 111418, 2022.

[232] Leonhard Hitzler, Johann Hirsch, Jochen Schanz, Burkhard Heine, Markus Merkel, Wayne Hall, and Andreas Öchsner. Fracture toughness of selective laser melted alsi10mg. *Proceedings of the Institution of Mechanical Engineers, Part L: Journal of Materials: Design and Applications*, 233(4):615–621, 2019.

[233] Xiaohui Tu, Arunava Ray, and Somnath Ghosh. A coupled crystal plasticity fem and phase-field model for crack evolution in microstructures of 7000 series aluminum alloys. *Engineering Fracture Mechanics*, 230:106970, 2020.

[234] Qian Liu, Hongkun Wu, Moses J Paul, Peidong He, Zhongxiao Peng, Bernd Gludovatz, Jamie J Kruzic, Chun H Wang, and Xiaopeng Li. Machine-learning assisted laser powder bed fusion process optimization for alsi10mg: New microstructure description indices and fracture mechanisms. *Acta Materialia*, 201:316–328, 2020.

[235] Moses J Paul, Qian Liu, James P Best, Xiaopeng Li, Jamie J Kruzic, Upadrasta Ramamurty, and Bernd Gludovatz. Fracture resistance of alsi10mg fabricated by laser powder bed fusion. *Acta Materialia*, 211:116869, 2021.

[236] Zhengkai Wu, Shengchuan Wu, Jianguang Bao, Weijian Qian, Suleyman Karabal, Wei Sun, and Philip J Withers. The effect of defect population on the anisotropic fatigue resistance of alsi10mg alloy fabricated by laser powder bed fusion. *International Journal of Fatigue*, 151:106317, 2021.

[237] Jian-Ying Wu. A unified phase-field theory for the mechanics of damage and quasi-brittle failure. *Journal of the Mechanics and Physics of Solids*, 103:72–99, 2017.

[238] Somdatta Goswami, Cosmin Anitescu, and Timon Rabczuk. Adaptive phase field analysis with dual hierarchical meshes for brittle fracture. *Engineering Fracture Mechanics*, 218:106608, 2019.

[239] Ian Maskery, Adedeji O Aremu, Loren Parry, Ricky D Wildman, Christopher J Tuck, and Ian A Ashcroft. Effective design and simulation of surface-based lattice structures featuring volume fraction and cell type grading. *Materials & Design*, 155:220–232, 2018.

[240] Oraib Al-Ketan, Rashid K Abu Al-Rub, and Reza Rowshan. The effect of architecture on the mechanical properties of cellular structures based on the iwp minimal surface. *Journal of Materials Research*, 33(3):343–359, 2018.

[241] Gaston Floquet. Sur les équations différentielles linéaires à coefficients périodiques. 12:47–88, 1883.

[242] Felix Bloch. Über die quantenmechanik der elektronen in kristallgittern. *Zeitschrift für physik*, 52(7):555–600, 1929.

[243] Leon Brillouin. *Wave propagation in periodic structures: electric filters and crystal lattices*. Dover: Mineola, New York, 2 edition, 2003.

[244] Mauro Fabrizio and Angelo Morro. *Mathematical problems in linear viscoelasticity*, volume 12. Siam, 1992.

[245] Anastasiia O Krushynska, Varvara G Kouznetsova, and Marc G D Geers. Visco-elastic effects on wave dispersion in three-phase acoustic metamaterials. *Journal of the Mechanics and Physics of Solids*, 96:29–47, 2016.

[246] Jan Achenbach. *Wave propagation in elastic solids*. Elsevier, 2012.

[247] Jared C Bronski and Zoi Rapti. Modulational instability for nonlinear schrödinger equations with a periodic potential. *Dynamics of Partial Differential Equations*, 2(4):335–355, 2005.

[248] Paul Horst et al. A method for determining the coefficients of a characteristic equation. *The Annals of Mathematical Statistics*, 6(2):83–84, 1935.

Unless otherwise expressly stated, all original material of whatever nature created by Deison Teixeira Préve and included in this thesis, is licensed under a Creative Commons Attribution Noncommercial Share Alike 3.0 Italy License.

Check on Creative Commons site:

https://creativecommons.org/licenses/by-nc-sa/3.0/it/legalcode/

https://creativecommons.org/licenses/by-nc-sa/3.0/it/deed.en

Ask the Deison Teixeira Préve about other uses.